Particles at Membranes and Interfaces

Inaugural-Dissertation

zur

Erlangung des Doktorgrads

der Mathematisch-Naturwissenschaftlichen Fakultät

der Universität zu Köln

vorgelegt von

Sabyasachi Dasgupta

aus Kolkata, India

Jülich 2014

Berichterstatter: Prof. Dr. Gerhard Gompper

Prof. Dr. Michael Lässig

Prof. Dr. Ulrich Schwarz

Tag der mündlichen Prüfung: 22.05.2014

Dedicated to my parents, brother and teachers.

Where The Mind Is Without Fear
Where the mind is without fear and the head is held high
Where knowledge is free
Where the world has not been broken up into fragments
By narrow domestic walls
Where words come out from the depth of truth
Where tireless striving stretches its arms towards perfection
Where the clear stream of reason has not lost its way
Into the dreary desert sand of dead habit
Where the mind is led forward by thee
Into ever-widening thought and action
Into that heaven of freedom, my Father, let my country awake.

-Rabindranath Tagore (Gitanjali)

Contents

Preface *IX*

1 Introduction *1*
1.1 Cell membranes *4*
1.2 Cellular transport *7*
1.3 Membrane mechanics at different length and time scales *8*
1.4 Continuum representation of membrane conformations and energetics *9*
1.5 Domain-induced budding *14*
1.6 Two-state model for membrane wrapping *15*
1.7 Phase diagram for wrapping of a spherical particle *16*
1.8 Capillarity at a fluid interface *20*

Part 1 Membrane wrapping *31*

2 Wrapping of ellipsoidal nano-particles by fluid membranes *33*
2.1 Abstract *33*
2.2 Introduction *33*
2.3 Theoretical model and methods *35*
2.3.1 Continuum membrane model *35*
2.3.2 Energy minimization *36*
2.3.3 Wrapping energy calculations *36*
2.4 Results *38*
2.4.1 Wrapping energy *38*
2.4.2 Wrapping diagrams *41*
2.4.3 Energy barrier *45*
2.4.4 Role of shape anisotropy *46*
2.5 Summary & conclusions *48*

3 Shape and Orientation Matter for the Cellular Uptake of Nonspherical Particles *59*
3.1 Abstract *59*
3.2 Introduction *59*
3.3 Ellipsoidal nanoparticles *62*

3.4 Cube-like nanoparticles *63*
3.5 Rod-like nanoparticles *65*
3.6 Role of shape and orientation *69*
3.7 Conclusions *71*
3.8 Supplementary material *76*
3.8.1 Spherocylinders 79
3.8.2 Rod-like particles 80
3.8.3 Ellipsoids 81
3.8.4 Wrapping diagrams for particles with same size 81

4 Membrane-wrapping contributions to malaria parasite invasion of the human erythrocyte *89*
4.1 Abstract *89*
4.2 Introduction *89*
4.3 Materials and methods *91*
4.3.1 Experimental derivation of merozoite dimensions 91
4.3.2 Deformation energy calculations and dimensionless parameters for erythrocyte-membrane wrapping 92
4.4 Results and discussions *95*
4.4.1 An archytepal merozoite 95
4.5 Merozoite attachment and reorientation via erythrocyte membrane wrapping *96*
4.6 Merozoite invasion via erythrocyte membrane wrapping *98*
4.6.1 Merozoite invasion supported by motor activity 102
4.7 A complete biophysical model for invasion incorporating membrane wrapping *104*
4.8 Supplementary material *115*

5 Interfacing Electrogenic Cells with 3D Nanoelectrodes: Position, Shape, and Size Matter *125*
5.1 Abstract *125*
5.2 Introduction *125*
5.3 HL-1 Cells on 3D Nanostructures: Position of the Engulfment like Event *126*
5.4 Nanostructures Engulfed at the Edge of the Cell Favor Engulfment and Free Membrane Deformation. *128*
5.5 Nanopillar Shape and Dimension Induce Differences in Junctional Membrane Deformation at the Cell Center. *132*
5.6 Conclusion *137*
5.7 Methods *138*
5.7.1 Fabrication of gold spines 138
5.7.2 HL-1 culture 138
5.7.3 Membrane stain and fixation of cells 138
5.7.4 Scanning Electron Microscopy and Focused Ion Beam 139
5.7.5 Image processing and analysis 139
5.7.6 Theoretical model 139

5.8 Supplementary material *145*

Part 2 Capillary interactions at interfaces *163*

6 Capillary Assembly of Microscale Ellipsoidal, Cuboidal, and Spherical Particles at Interfaces *165*
6.1 Abstract *165*
6.2 Introduction *165*
6.3 Model *167*
6.4 Method *169*
6.5 Interface Deformations *170*
6.5.1 Near-Field Interface Deformations around Single Ellipsoidal and Cuboidal particles 171
6.5.2 Comparison with Experimental Measurements 172
6.6 Two-Particle Interactions *173*
6.6.1 Capillary Interaction between Ellipsoidal Particles 174
6.6.2 Capillary interaction between cuboidal particles 176
6.6.3 Capillary Interaction between a Spherical and an Ellipsoidal Particle 177
6.7 Summary and Conclusions *178*
6.8 Supplementary material *184*

7 Summary & outlook *191*
7.1 Conclusion *191*
7.2 Future perspectives *197*

Preface

Soft surfaces experience morphological changes upon interaction with objects at various length scales. Two important classes of soft surfaces are membranes and interfaces. In presence of particles, through surface-mediated interactions soft surfaces exhibit diverse phenomena in nature. A fluid membrane which acts as a protective periphery enclosing cellular material can be described as a two dimensional mathematical surface characterized by 'bending elasticity' and 'membrane tension'. Similarly, interfaces at the boundary of two liquid phases or a liquid and a gas phase are characterized by their interface tension. Interestingly, a close interplay of the deformation energy of these soft surfaces and the geometry and form of the particles allows the particles to interact. Thus, the study of interactions of particles with membranes and interfaces forms the basis of this work.

The mechanistic aspects of cellular entry via membrane wrapping for particles of various geometries are studied theoretically and numerically. Such systems are characterized by the membrane bending rigidity κ, the membrane tension σ, and the adhesion strength w. The different wrapping states exhibited are "non wrapped", "partially wrapped" (with low and high wrapping fraction), and "completely wrapped". There are two kinds of phase boundaries: a continuous binding transition and a discontinuous transition either between two partially-wrapped states or from a partially-wrapped to a completely wrapped state. The theoretical analysis predicts stable partially wrapped states for nonspherical particles. Nonspherical particles having flat sides can show preferential initial binding though the decisive factor for encapsulation is the ratio of the width to the length of the particles and the softness of its edges. Wrapping energy contributions of the erythrocyte membrane to the invasion energetics for a malarial merozoite that has an asymmetric "egg-like" shape is assessed. Furthermore cell adhesion to nanopatterned substrates is characterized to predict optimal shapes of 3D nanoelectrodes for efficient coupling to cells using deformation energy calculations.

For a fluid interface dominated by an interfacial tension σ, self-assembly via capillary interactions for micron-sized nonspherical particles is reported. A nonspherical particle can induce interface distortion due to an undulating contact line creating excess interfacial area. Neighboring particles interact to minimize the excess area via long-range interface-mediated capillary forces. The particle-induced interface distortion due to single ellipsoidal or cuboidal particles are calculated. The near-field nature of the capillary interactions between a pair of particles in different relative orientations is characterized using power-law fits.

Zusammenfassung

Weiche Flächen erfahren bei der Wechselwirkung mit Teilchen verschiedener Größenskalen morphologische Veränderungen. Zwei wichtige Klassen weicher Flächen sind Membranen und Grenzflächen. Eine fluide Membran, die als schützende Hülle zelluläres Material einschließt, kann als zweidimensionale mathematische Fläche, deren mechanische Eigenschaften durch die Biegesteifigkeit und die Membranspannung gegeben sind, beschrieben werden. Analog hierzu wird eine Grenzfläche zwischen zwei Flüssigkeiten oder zwischen einer flüssigen Phase und einer Gasphase durch eine mathematische Fläche und die Grenzflächenspannung modelliert. Interessanterweise kann ein enges Wechselspiel der Deformationsenergie der weichen Flächen mit der Geometrie und der Form der Teilchen zu einer Wechselwirkung zwischen den Teilchen führen. Die Untersuchung der Wechselwirkung der Teilchen mit Membranen und Grenzflächen ist die gemeinsame Grundlage für alle Teile dieser Arbeit.

Die mechanischen Aspekte der Aufnahme von Teilchen in eine Zelle durch Einwickeln in die Zellmembran werden für Teilchen verschiedener Formen theoretisch und numerisch untersucht. Diese Systeme sind durch die Biegesteifigkeit κ der Membran, durch die Membranspannung σ und durch die Bindungsstärke w charakterisiert. Die Zustände des Systems können "nicht eingewickelt", "teilweise eingewickelt" (mit geringem und hohem eingewickelten Anteil) und "komplett eingewickelt" sein. Es treten zwei Arten von Phasengrenzen zwischen den Zuständen auf, kontinuierliche Bindungsübergänge und diskontinuierliche Übergänge zwischen zwei teilweise eingewickelten Zuständen oder zwischen einem teilweise eingewickelten und einem komplett eingewickelten Zustand. Die theoretischen Berechnungen in dieser Arbeit sagen für asphärische Teilchen stabile teilweise eingewickelte Zustände voraus. Asphärische Teilchen mit flachen Seiten binden leichter an Membranen als sphärische Teilchen, das komplette Einwickeln eines Teilchens wird jedoch durch dessen Aspektverhältnis und durch die Weichheit seiner Kanten bestimmt. Der energetischen Kosten der Membrandeformation der roten Blutkörperchen für das Eindringen des eiförmigen Malariaparasiten in die Zelle wird numerisch berechnet. Ebenfalls mit Hilfe von Biegeenergieberechnungen wird die optimale Form dreidimensionaler Elektroden auf nanostrukturierten Oberfächen für die beste Kopplung der Zellen an die Elektroden vohergesagt.

An Grenzfächen wird durch die Grenzflächenspannung σ die Selbstorganisation von mikrometergrossen Teilchen durch Kapillarwechselwirkungen beobachtet. Ein aspärisches Teilchen verformt durch seine undulierende Kontaktline die Grenzfläche in seiner Umgebung, wodurch die Grenzfläche vergrößert wird. Benachbarte Teilchen wechselwirken durch langreichweitige Kapillarkräfte, um diese zusätzliche Grenzfläche zu minimieren. Die durch Teilchen induzierte Grenzflächenverformung wird für ellipsoidförmige und quaderförmige Teilchen berechnet. Die Kapillarwechselwirkung zwischen zwei Teilchen mit verschiedenen relativen Orientierungen wird im Nahfeld durch Potenzgesetze charakterisiert.

1
Introduction

Sir D'Arcy Wentworth Thompson (1860-1948) a Scottish zoologist in his profound masterpiece[1], "*On Growth and Form*" first published in 1917 remarks "*the form of an object is a 'diagram of forces'*". In the same spirit, stressing the need for understanding biophysical forms using principles of mechanics, the general aims of this thesis are outlined to investigate how particles interact with soft surfaces. An interplay of the elasticity of soft surfaces with geometry and form of particles leads to a plethora of rich and interesting phenomena in nature. Biological systems exhibit diverse morphological forms at different length scales ranging from lengths as minuscule as cells to macroscopic lengths in the organismal level. Experimental and theoretical approaches revealing the principles of self-organization both in biological and soft matter systems have generated an immense interest towards understanding the role of geometry in nature and driven technological attempts in imitating natural forms for widespread applications. Delving into the interactions of particles with different soft surfaces like biological membranes or interfaces between different fluid environments, we discover fascinating aspects where shape matters !

Nanoparticle interaction with biological membranes, in particular their entry into cells, forms the basis for understanding toxicological effects of nanoparticles, and a quantification and prediction of these effects is of immense importance for health and safety. Potential applications of nanoparticles in various fields such as designing efficient drug/gene delivery agents provide further motivation for this study. In the first part of this thesis, the investigations contribute to fill the long-standing gap in the understanding of uptake pathways for different nanoparticles, viruses and bacteria into the host cell. It is well known that cellular entry pathways can vary depending on shape[2–4], size[5,6], and surface characteristics[7,8] of the cargo and membrane properties. In particular, non-spherical particles interacting with fluid membranes are studied in Chapter 2 and Chapter 3 of this thesis. Fluid membranes acts as boundaries providing mechanical protection for the cellular constituents within it as well as facilitating essential communication with the external environment. Membranes are ubiquitous structural elements in all living cells. Fluid membranes due to their inherent "softness" can easily conform to morphological changes under various physiological conditions. For instance, a cell can shed membrane in form of spherical or tubular bud-like structures which may enclose cargo molecules allowing cellular transport via membrane budding[9–11]. Particles adhering at a membrane cause the membrane to deform due to a close interplay of membrane deformation energy with the membrane-particle adhesion

energy. The aim of these calculations is to obtain "wrapping phase diagrams" [12–15] that show for which membrane bending rigidities, surface tensions, and nanoparticle adhesion strengths; the membrane binds and wraps around a particle either partially or completely. These results can aid to optimize design of suitable delivery vehicles in form of nanoparticles which may be specifically introduced to target diseased cells by releasing drugs and protect healthy tissues. Viruses [16] occur in different shapes- spherical viruses like human immunodeficiency virus (HIV) or filamentous viruses [17,18] like Ebola or Marburg which cause deaths to several million people worldwide. Future medicines can be significantly improved from investigations targeting pathogen invasion pathways. The results presented here on membrane budding for different shapes e.g. nanospheres, nanorods and nanocubes can provide valuable insight towards this goal.

A particularly interesting case of particle wrapping and ceullar uptake is the invasion of the malarial parasite into the cell. During the malaria life-cycle the parasite attains an asymmetric egg-like shape in the merozoite stage before invasion into a human erythrocyte. The malaria parasite, from the genus Plasmodium, must target and invade the circulating erythrocytes to complete its development. The molecular mechanisms that underlie this rapid and complex process have been the focus of intensive efforts for many years to develop drugs or vaccines that might block invasion and thus prevent or treat this major global disease. Several decades of research into the biological events that govern each stage of invasion, from attachment through reorientation and penetration, have made great strides towards building a molecular and cellular model of how complete entry is achieved. To date, however, models have predominantly centered on parasite contributions to the energetics of entry (seen as an extension of parasite cell movement) leaving the role played by the erythrocyte membrane largely unexplored. The perception of a passive erythrocyte in invasion has largely arisen from two sources: Firstly, the misconception that the red blood cell, as a terminally differentiated cell lacking a translation machinery, is completely inactive; and secondly, convincing data demonstrating that parasite actin-myosin motor force is essential for invasion and therefore is assumed to solely govern the whole process. Recent data, however, shows that the related parasite Toxoplasma gondii can invade host cells in the absence of its motor, suggest the role of the red cell in invasion needs reassessment. Towards this goal a complete biophysical model is presented based on membrane energetics describing the entry pathway in two main stages (i) the reorientation phase where the egg-shaped parasite orients with its pointed end towards the erythrocyte membrane followed by (ii) the invasion phase where the merozoite gradually invades within the cell. Different invasion possibilities are provided as a wrapping phase diagram for different values of mechano-elastic parameters used to describe the model. Strikingly, it is found that the entry is a delicate balance between parasite's biological machinery and the host cell contributions. Thus contrary to established views where the erythrocyte's role in invasion is largely disregarded we suggest that membrane energetics indeed plays a significant role during invasion. The parasite through evolution has therefore learned to take advantage of this and has evolved machinery like motors and other proteins to facilitate invasion. These studies which shed light on the role of the erythrocyte membrane in conjunction

to the parasite machinery shall not only help to design future biophysical experiments to unravel the "delicate balance" but also provide impetus to development of future medicines which take advantage of this balance to terminate proliferation.

Similar processes as in the wrapping of nanoparticles by cell membrane are also observed when a cell adheres to nanostructured surfaces. The response of cells at such structured interfaces are important for developing biosensors and investigating cellular signaling. For recording cellular signals at the single cell level, several established techniques exist. However, the need to understand how several cells interact in a network has caused huge interest in recent years towards developing nanostructured interfaces which can be electrically coupled to obtain information regarding intracellular communication. Multi electrode arrays[19,20] (MEAs) are nanostructures at the cellular interface which act as biosensors that allow to measure cellular signaling. There good mechanical coupling to cells makes them promising candidates for coupling biological cells to electronic devices. Previous studies[21,22], have successfully demonstrated how neuronal or cardiac cells can engulf three dimensional micro and nano structures similar to the uptake of a solid nanoparticle by a cell during endocytosis. Planar electrodes when modified into three dimensional structures like pillars due to better coupling improves the recording or stimulation of electrogenic cells. Two particular kinds of pillar geometry-cylindrical pillars and mushroom shaped pillars are investigated. Proper recording from such devices necessarily requires an optimal engulfment of the nanostructure by the cell membrane. We therefore aim to gain mechanistic insights as to how shape/dimensions of the structures, cell membrane properties, and the relative positioning between the cells to the structures affect the bio-mechanical coupling. Such characterization of an optimal shape for an individual electrode shall facilitate efficient design for future biosensors.

In the second part of the thesis, long range capillary forces of non-spherical particles at a fluid interface are investigated. A fluid interface acts as boundary between two fluid phase environments or between a fluid and vapor/gas phase. Capillary interactions between floating particles are caused due to particle-induced distortions of the fluid interface. In order to minimize the total surface energy due to interfacial tension, there arise long range interactions which cause self-assembly[23] at an interface. The particle-induced interface deformation due to a single particle is investigated numerically. We further predict the effective power-law behavior of interaction potentials between neighboring particles in the near-field. Strong capillary forces help to direct, orient and assemble anisotropic particles at an interface forming self assembled two-dimensional structures such as worm-like chains[24–26], colloidosomes[27,28], capillary arrows[29], 2D lattice crystals[26,30–32] etc. over several length scales[23,33,34]. They also help in stabilizing surfactant free or Ramsden-Pickering emulsions[35–39], bijels[40,41] and particle-stabilized foams. The self-assembly behavior displayed by these colloidal particles at a fluid interface due to the interfacial tension may even help to understand how proteins[42–44], viruses and nanoparticles may cluster at a fluid membrane which is a soft surface characterized in addition to membrane tension by bending elasticity. To unravel mysteries associated with membrane mediated interactions and the implications of geometry in these interactions at the nanoscale are questions of great significance.

1.1 Cell membranes

A plasma membrane acts as an interface separating the interior of a cell from the external environment, thereby maintaining a vital biochemical balance essential for life. Moreover it provides mechanical protection and enables communication across the membrane via exchange of molecules and ions. Several membrane bound organelles each with different functional roles are embedded within the cellular matrix or cytoplasm. Membranes thus form key building blocks for all cells. A cell membrane has a bilayer structure with a thickness of few nanometers ($\sim$ 5 nm). The upper and lower leaflets of the bilayer are formed via self-assembly of amphilic molecules called lipids as shown in the schematic Fig. 1.1 (a). An amphiphilic molecule has a polar hydrophilic head group and a non-polar hydrophobic tail group. Amphiphilic molecules in aqueous solvents at concentrations higher than the critical micellar concentration, tend to self aggregate reducing interfacial tension on by packing the non-polar tails towards the center of the aggregate while the polar heads face towards the aqueous environment, thereby forming a nearly spherical bag enclosed by a monolayer of surfactants called a micelle (in case of amphiphiles dispersed in non-polar solvents inverse micelles are formed where the non-polar tails are directed away from the center of the micellar aggregate). At even higher concentrations, the surfactants tend to form planar aggregates that eventually form vesicles; having a bilayer structure formed of the polar heads facing towards the aqueous solvent while the tails form a hydrophobic core. At physiological temperatures, membranes exist in the fluid phase[45] which is necessary for several biological functionality. General building blocks[46,47] of membranes are phospholipids, cholesterols and other sterols. Chief phospholipid classes being phosphatidylcholine (PC), phosphatidylethanolamine (PE), phosphatidylserine (PS), phosphatidylinositols (PI), sphingomyelin (SM) , cardiolipin (CL), glycolipids see Tab. 1.2. The lipid-bilayer remains associated to several other macromolecules/proteins that can be either embedded within the hydrophobic core or grafted/adsorbed on either leaflets as shown in the schematic Fig. 1.1 (b). There is a large variability in the lipid compositions of different membranes either belonging to the same cell (e.g. between the plasma membrane and the nuclear membrane) and between the plasma membranes of different cells. Compositional changes also occur between the inner and outer leaflet of the plasma membrane. Usually[45], a plasma membrane is linked with an underlying network of polymers that constitute the cell cytoskeleton which remains closely associated with the changes in shape and deformation of a membrane. An asymmetry between two leaflets of a bilayer can be introduced providing the membrane a preferred curvature. Different mechanisms[48–50] (a) due to hydrophobic mismatch[51] of different lipid constituents or integral proteins, (b) by membrane scaffolding through cytoskeletal filaments/proteins/grafted polymers[52,53], (c) by insertion of proteins like the amphiphysin helix[54], (d) in presence of intrinsically curved proteins like the bar-domains[55], and the recently attributed mechanism via (e) macromolecular crowding[56,57] are shown schematically in Fig. 1.3.

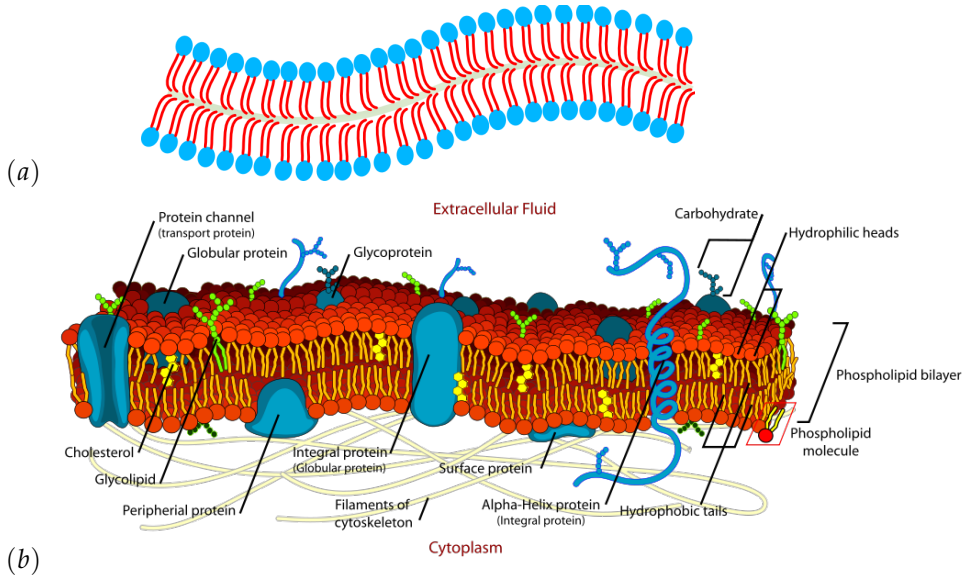

Figure 1.1: (a) A typical schematic for a lipid bilayer formed of amphiphilic lipid molecules having a polar head (in blue) and a non-polar tail (in red). (b) A cartoon of a typical fluid membrane comprising of a lipid bilayer structure associated with other macromolecules like proteins, polymer chains and an underlying polymerized network of filaments comprising the cell cytoskeleton. (Taken from public domain : Wikipedia)

Membrane	PC	PE	PS	PI	SM	CL	Glycolipid	Cholesterol	Others
Erythrocyte (human)	20	18	7	3	18	–	3	20	11
Plasma (rat liver)	18	12	7	3	12	–	8	19	21
ER	48	19	4	8	5	–	tr	6	10
Golgi	25	9	3	5	7	–	0	8	43
Lysosome	23	13	–	6	23	≈ 5	–	14	16
Nuclear membrane	44	17	4	6	3	1	tr	10	15
Mitochondria	38	29	0	3	0	14	tr	3	13
Neurons	48	21	5	7	4	–	3	11	1
Myelin	11	17	9	1	8	–	20	28	6

Table 1.2: Lipid head group composition of various membranes from some mammalian liver cells, erythrocytes, and nerve cells in weight by percentage. Abbreviations used: phosphatidylcholine (PC), phosphatidylethanolamine (PE), phosphatidylserine (PS), phosphatidylinositols (PI), sphingomyelin (SM) , cardiolipin (CL). (Taken from Ref.[58], originally published in Ref.[59]).

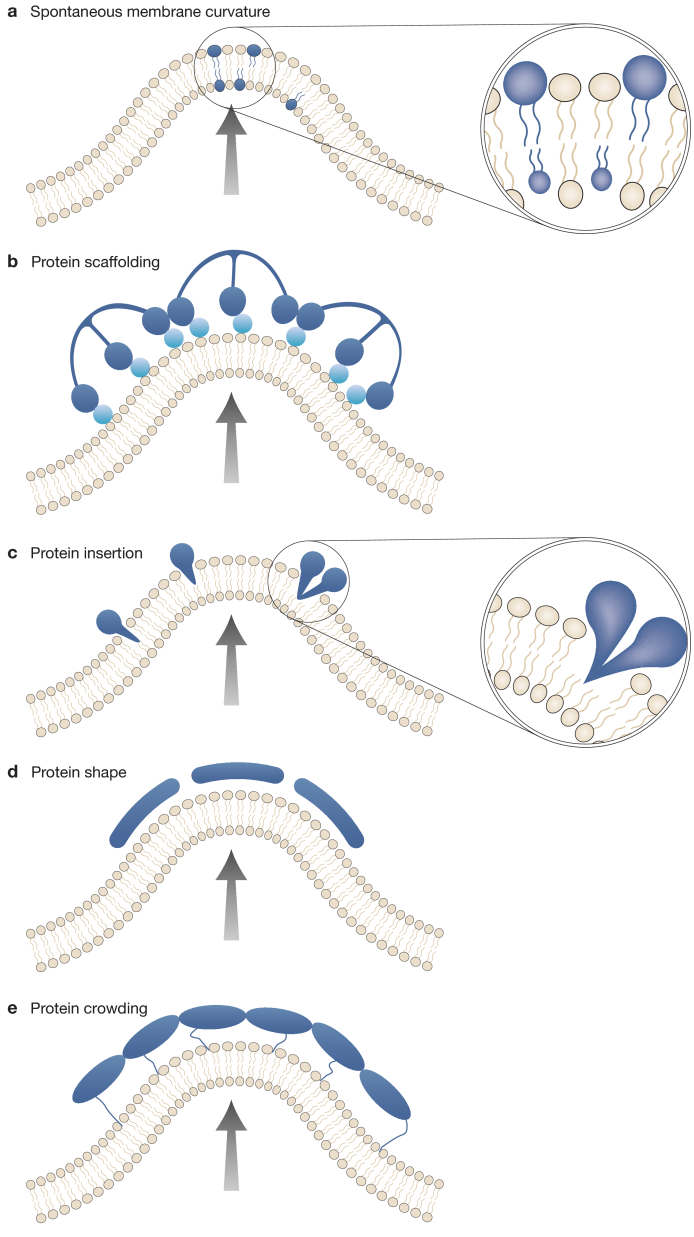

Figure 1.3: Different ways to bend a bilayer by generating a preferred curvature of the membrane due to asymmetry between the bilayer leaflets ((a),(c)) or proteins ((b),(d), and (e)). (Taken from Ref.[48])

1.2 Cellular transport

Lipid-bilayer membranes compartmentalize cells containing several membrane-bound organelles. Nevertheless, a controlled exchange of molecules and particles is required for proper functioning of a cell. Cellular trafficking involves a complex physiological process whereby this controlled exchange of cargo is accomplished- either intracellularly between different organelles like the Endoplasmic reticulum and Golgi apparatus, or across the plasma membrane with the intracellular environment. A cell continuously uptakes and releases materials within characteristic time scale of a few seconds[60,61] via membrane budding. Membrane budding[9–11,62,63] is generally the first step for intracellular transport and allows cells to exchange material with its environment while shedding a part of its membrane which is used to wrap around the cargo to form a bud. Bud-like structures which can be either spherical[64] or tubular[17,18,65] in shape and have typical dimensions which range from a few nanometer to few microns. Thus cells have devised several efficient pathways for cellular cargo transport as shown in Fig. 1.2. Smaller molecules like peptides, ions and small nanoparticles penetrate[66–69] through the membrane via diffusion or across membrane channels. Larger macromolecules are taken up via endocytosis. Despite the importance of membrane budding and wrapping of particles several aspects of this process still remain elusive. Thus how membrane budding proceeds, assisted by the biological machinery comprising of curvature-inducing proteins like clathrin[44,62,70], bar-proteins[55,71], other accessory endocytic proteins[65,72] and the cytoskeletal[4,73] contributions from actin filaments[74,75], motors[76,77] is a question of great significance.

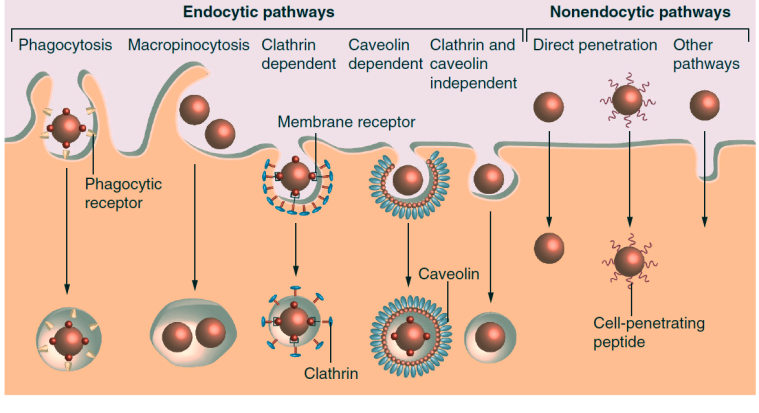

Figure 1.4: Different cellular uptake pathways[9–11,62,63] can be roughly classified as- (i) Endocytic pathways : Uptake of solid particles of sizes comparable to a micron can occur via "eating by cells" i.e., phagocytosis similar to process by which the cell takes up (extracellular) fluids via "drinking by cells" i.e., macropinocytosis. Other forms of endocytosis involve uptake of relatively smaller particle with typical dimensions ranging from 20- 200 nm via clathrin-mediated assembly or caveolae-mediated assembly or other passive endocytic pathways independent of clathrin/caveolae molecules (ii) Non-endocytic pathways usually involve uptake by direct penetration via diffusion or through translocation across membrane channels or other unknown mechanisms.(Taken from Ref.[63])

1.3 Membrane mechanics at different length and time scales

Depending on the length and time scales of interest, different membrane models have to be used, as shown schematically in Fig. 1.5(a)-(f). For example, to investigate events like membrane receptor-ligand binding or functioning of a membrane ion channel which occur in relatively small time scales of the order of few nanoseconds and where the biochemical details are relevant a fully-atomistic simulation method can be employed. For investigating biophysical events occurring at slightly longer time-scales ranging from few μs to ms; different coarse-grained models like those shown in Fig. 1.5 (b)-(d) can be used where the molecular resolution of the membrane structure is preserved but certain chemical specificity is neglected. Such methods are extensively used for studying fusion-pore dynamics[78] by characterizing the role of proteins related to exocytosis, like the SNARE complex. However, to describe conformational changes occurring at length scales comparable to the overall cell size to few microns, or investigate changes in cell shape as in endocytosis which occur at even longer time scales of the order of few seconds[60,61], such methods shall prove computationally intractable. The typical thickness of a lipid bilayer is 5 nm and is much smaller than the overall dimensions of the cells or the organelles ($\sim$ 1-10 μm), which gives the justification to describe membranes by two-dimensional mathematical surfaces with curvature-elasticity. Hence to unravel the mysteries at intermediate length scales (ranging from few nanometers up to few micrometers), mesoscopic models describing cell membranes in the continuum limit as a two-dimensional surface with associated curvature-elastic parameters as shown in Fig. 1.5 (d)-(e) prove to be extremely useful.

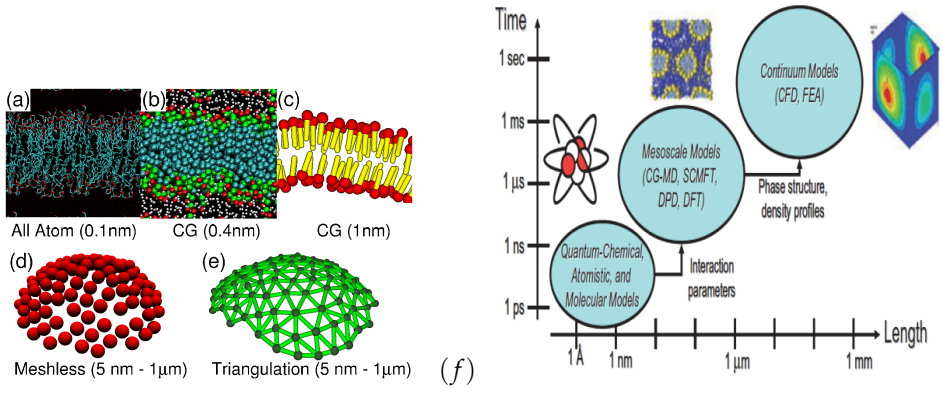

Figure 1.5: Different membrane simulation techniques used for different length scales:(a) all-atomistic model, (b) coarse-grained model with explicit solvent, (c) solvent-free molecular model, (d) meshless-membrane model, (e) dynamically-triangulated membrane description (Taken from Ref.[79]) (f) Different length and time scales relevant to membrane simulations. (Taken from Ref.[80])

1.4 Continuum representation of membrane conformations and energetics

On a curve, curvature (c), the measure for change of the normal vector is given by the inverse of the radius (r) of a circle drawn at that point. Similarly, at each point of a two-dimensional mathematical surface, there exists two principal curvatures given by c_1 and c_2, which correspond to the inverse of the radius of the circles drawn at that point having the maximum (r_1) and minimum radius (r_2), respectively, as shown in Fig. 1.6. The average sum of these two curvatures is termed as mean curvature (H) is given by, $H = (c_1 + c_2)/2 = (1/r_1 + 1/r_2)/2$. The product of the principle curvatures gives the Gaussian curvature $K = c_1 c_2 = 1/r_1 r_2$. The mean curvature H and the Gaussian curvature K are two invariants of the curvature tensor[81] which is a 3×3 matrix. Twice the mean curvature is given by the sum of the diagonal elements or the trace of the matrix. The sum of the minors of the matrix gives the Gaussian curvature K.

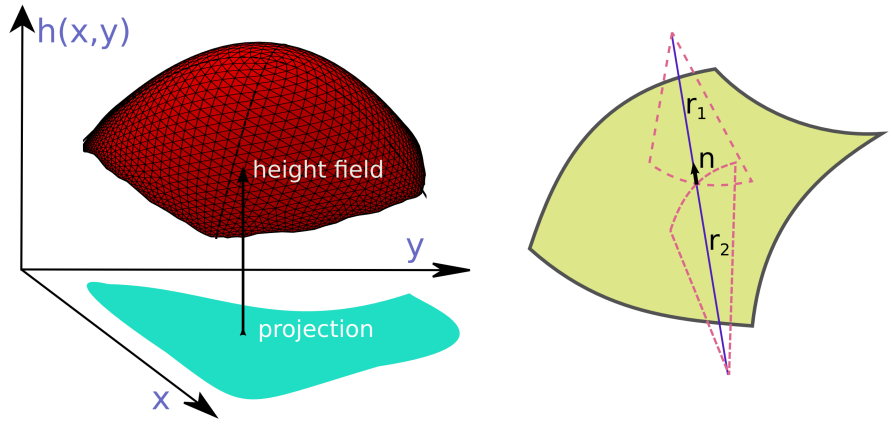

Figure 1.6: Right: A two-dimensional surface described as a height field given by , $h(x, y)$ is shown with its projection in the $x - y$ plane. Left: Two principal curvatures can be defined at each point of a surface having a normal given by, n. The curvatures are given by the inverse of the radii r_1 and r_2 of two circles having the maximum and minimum radius drawn at that point of the surface.

For certain special surfaces, the principal curvatures and thus associated mean and Gaussian curvatures as follows :

- For a sphere of radius R, $c_1 = c_2 = 1/R, H = 1/R, K = 1/R^2$.
- For a cylinder of radius R, $c_1 = 1/R, c_2 = 0, H = 1/(2R), K = 0$.
- For a saddle-like surface, $c_1 = 1/R, c_2 = -1/R, H = 0, K = -1/R^2$.
- For a plane, $c_1 = c_2 = 0, H = 0, K = 0$.

A saddle-like surface belongs to an interesting class of mathematical surfaces known as minimal surfaces. At each point on such a surface the two principal curvatures are equal in magnitude but opposite in the sign and hence the sum of these two curvatures results a null value. Thus minimal surfaces are characterized by zero mean curvature ($H = 0$). One of my personal favourite minimal surface is

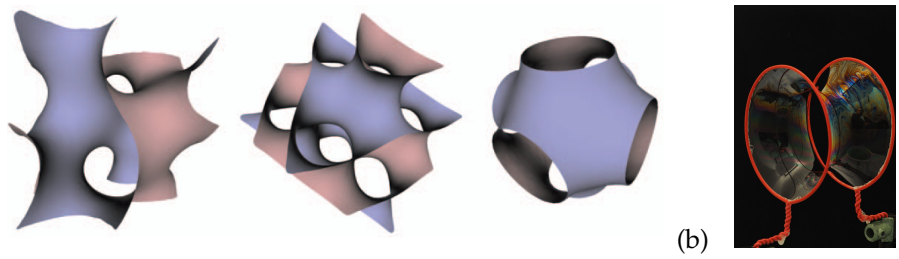

(a) (b)

Figure 1.7: (a) Minimal surfaces : Gyroid, Diamond, a Schwarz P surface (from left to right). These structures having a zero mean curvature at all points on their surfaces. (Taken from Ref. [82]) (b) The catenoid surface formed by a soap-film between two coaxial rings. The total mean curvature vanishes everywhere on such a surface since the surface has the two principal curvatures of same magnitude but opposite sign at each point on the surface. (Image credit : www.soapbubble.dk/)

a catenoid which is a form often seen in soap films enclosed between two coaxial rings, see Fig. 1.7 (b) . A catenoid is also a surface which has interesting implications in membrane budding as often the neck of a spherical bud attains a catenoidal shape which gradually shrinks and finally disappears as the bud pinches off. Some other minimal surfaces are Gyroid, Diamond and Schwarz P surfaces as shown in Fig. 1.7 (a) and often these structures are found in different systems in nature like microemulsions[1].

A mathematical statement connecting the Gaussian curvature of a surface to its global topology characterized by the Euler characteristic (χ) is given by the Gauss-Bonnet theorem [84],

$$\int_S dSK + \int_{\partial S} dsk_g = 2\pi\chi(S) = 4\pi(n-g). \tag{1.1}$$

where k_g is the geodesic curvature at the boundaries which also contributes to the integral over K for surfaces with open boundaries. The contribution of the geodesic curvature can be neglected for closed surfaces with fixed topology and for open surfaces [84–86] where the slope at the outer boundary does not change. The Euler characteristic of a surface is given by $\chi = 2(n-g)$ where n is the number of objects and g is the number of handles. The theorem states the integral of the Gaussian curvature remains unaffected as long as the global topology remains unchanged. Thus, the integral has the same value for a torus and a coffee cup with a handle since each individual object has only one handle i.e., $g = 1$ and thus an Euler characteristic of $\chi = 0$. Different vesicle morphologies like prolate, oblate, dumbbell-like [87,88], and starfish [89] geometries of giant unilammelar vesicles (GuV's) have been observed under different experimental conditions. Shape transformations of vesicles between such morphologies due to changes in the spontaneous curvature [90,91], have been studied theoretically using an elastic description for membranes. All

1) Due to massive reduction in interfacial free energy, phases with large internal surface area can become possible - like in the lamellar phase where the monolayers form a one-dimensional stack or a microemulsion [82,83] phase where the monolayers form a random isotropic array.

vesicle geometries mentioned above, can be studied as an overall perturbation of the spherical shape (as all of the forms have no handles i.e., genus zero $g = 0$) and therefore have the same Euler characteristic, $\chi = 2$. Therefore, all such forms have a (constant) Gaussian curvature contribution of 4π which can be neglected for studying shape transformations.

Helfrich and Canham in their seminal works[92,93] proposed more than 40 years ago, that fluid membranes can be described as soft surfaces characterized by an elastic deformation energy using,

$$\mathcal{E}_{\text{bend}} = \int_{A_{\text{tot}}} dS \, \left[2\kappa(H - c_0)^2 + \bar{\kappa}K\right] , \tag{1.2}$$

which is an integral over the entire membrane surface area, A_{tot}. The bending rigidity κ, is an elastic modulus of the membrane. Through various biophysical techniques like micropipette-aspiration[94] of vesicles and cells or through investigations of membrane fluctuations[95,96]values of the bending rigidity can be estimated. The bending rigidity κ, for typical membranes is found to range in the order of 10-100 k_BT. Gaussian saddle splay modulus $\bar{\kappa}$, affects the energetics of a system only if there are any global topological changes in the geometry/shape of the vesicle. From theoretical analysis[97] it can be shown that the values must be negative and range from $-2\kappa \leq \bar{\kappa} \leq 0$. Experimental measures for $\bar{\kappa}$ are difficult. An asymmetry between two leaflets of membrane may arise in different conditions as shown schematically in Fig. 1.3, providing the membrane a preferred curvature termed as spontaneous curvature, c_0. Shape transformations[90,98] (e.g. during the budding/tubulation) in vesicles and cells can result due to changes in the spontaneous curvature. For symmetric bilayers, the spontaneous curvature contribution vanishes i.e. $c_0 = 0$ and the membrane shape is then determined using the changes in squared mean curvature (H^2) and Gaussian curvature (K) terms and its associated moduli κ and $\bar{\kappa}$, respectively. For morphological transitions where there are no changes in the global topology the contribution of the Gaussian curvature can be neglected allowing us to describe the energetics using the first term in Eq. 2.2 only.

For membrane deformations characterized without any overhangs i.e., where the membrane does not cross itself or deforms strongly avoiding multiple height values when projected on to a reference plane; the membrane height can be described by the "Monge representation", where the surface is described by a height field, $h(\boldsymbol{\rho})$, where $\boldsymbol{\rho} = (x, y)$ are the coordinates in the reference plane as shown in Fig. 1.6. The bending energy for the membrane is

$$\mathcal{E}_{\text{bend}} \quad = \quad \frac{\kappa}{2} \int_{A_{\text{tot}}} dA \sqrt{1 + (\boldsymbol{\nabla} h(\boldsymbol{\rho}))^2} \left[\boldsymbol{\nabla} \cdot \frac{\boldsymbol{\nabla} h(\boldsymbol{\rho})}{\sqrt{1 + (\nabla h(\boldsymbol{\rho}))^2}} \right]^2 , \tag{1.3}$$

with $\int dA$ the integral over the reference plane. For an almost planar membrane, using small-gradient expansion of the integrand allowing to approximate the mean curvature as $H = \nabla^2 h(\boldsymbol{\rho})/2$ gives the total bending energy as

$$\mathcal{E}_{\text{bend}} \; = \int_{A_{\text{tot}}} dA \frac{\kappa}{2} (\nabla^2 h(\boldsymbol{\rho}))^2 \, . \tag{1.4}$$

Axisymmetric membrane shapes can be investigated by employing different parametrizations[93,99–102]. Such parametrizations can describe membrane overhangs as well. Some approaches using functional parametrizations for example using spherical harmonics[103], Cassini ovals[92], and Fourier functions[104] can also describe non-axisymmetric shapes. The basic strategy in these approaches is to formulate an Euler-Langrange variation of Helfrich Hamiltonian which gives a fourth-order partial non-linear differential equation[105] and then exploit the symmetry of the system to obtain solutions to the Euler-Lagrange equations in an appropriate parametrization. For example, a suitable choice of parameters which can efficiently describe shapes having axisymmetry is the arc-length parametrization. In the arc-length parametrization, the membrane shape is described using the arc-length (s) and tangent angle (ψ) at the membrane contour as shown in the schematic Fig. 1.8 and after the variation of the Helfrich Hamiltonian a set of second order non-linear ordinary differential equations is obtained. These are then solved numerically[13,14,106–108] using appropriate boundary conditions. Using this parametrization, the principal curvatures are obtained as, $c_1 = -\sin(\psi)/r$ and $c_2 = -d\psi/ds$ and thus the bending energy for a tensionless membrane is given by,

$$\mathcal{E}_{\text{bend}} = \int_0^\infty ds\, \frac{\kappa}{2} \left[\frac{d\psi}{ds} + \frac{\sin(\psi)}{r} \right]^2 . \tag{1.5}$$

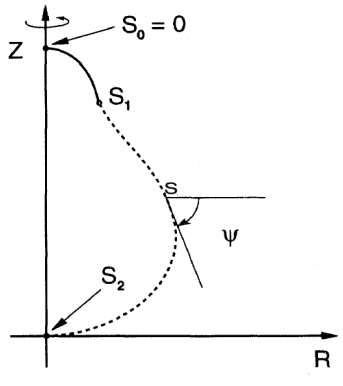

Figure 1.8: Arc-length parametrization of a membrane shape. (Adapted from Ref.[102]

Apart from the bending cost, when a fixed patch of membrane deforms there is an additional cost due to membrane tension which is proportional to the total surface area of the membrane and is given by,

$$\mathcal{E}_{\text{tension}} = \int_{A_{\text{tot}}} dS\, \sigma , \tag{1.6}$$

where membrane tension σ acts as a Lagrange parameter to the membrane surface area. Thus the total elastic deformation energy due sum of both bending and tension contributions can be written as,

$$\mathcal{E}_{\text{def}} = \mathcal{E}_{\text{bend}} + \mathcal{E}_{\text{tension}} = \int_{A_{\text{tot}}} dS \, \left[2\kappa(H - c_0)^2 + \sigma \right] , \tag{1.7}$$

assuming there are no contributions from changes in the Gaussian curvature term as the topology remain preserved.

During membrane budding as the membrane wraps around a particle, the deformation costs of the membrane must be accounted for by a competing energy. One possibility is to pay this deformation costs is through the gain in adhesion energy by virtue of contact of the particle with the membrane. For a homogeneous sticky particle of adhesion strength w, the gain due to contact is proportional to the adhered area A_{ad} and is given by,

$$\mathcal{E}_{\text{adhesion}} = -w \int_{A_{\text{ad}}} dS \ . \tag{1.8}$$

1.5 Domain-induced budding

Budding transformation can be understood as competition between different energetic terms. For example Fig. 1.9 depicts domain-induced budding[109–112] where there exists a line energy along the domain boundaries of two components α and β having different compositions like liquid ordered (L_0) and liquid disordered (L_d) phases[113]. Initially smaller circular domains of membrane coalesce to form a larger circular domains of radius R thereby reducing the energy penalty due to line tension γ given by, $\mathcal{E}_{\text{line}} = \gamma \oint_C dl = 2\pi R\gamma$. A completely budded spherical domain has a total bending energy $\mathcal{E}^{\text{bud}} = 2\kappa\,(\frac{1}{R})^2\,4\pi R^2 = 8\pi\kappa$. After smaller domains have coalesced to form a larger circular domain as shown in state (1) in Fig. 1.9, if the line energy of the domain exceeds $8\pi\kappa$ at a critical domain size $R_c = 8\pi\kappa/2\pi\gamma = 4\kappa/\gamma$ it decides to bud out like in states (2) & (3) of Fig. 1.9. Thus intramembrane domain induced budding can be understood as a competition between the $\mathcal{E}_{\text{bend}}$ vs. $\mathcal{E}_{\text{line}}$. The relevant length scale describing such a system is given by κ/γ such that domains smaller than this characteristic length shall remain flat while larger domains bud out. Thus using this simple model, it is shown how two competing energies can result in changes in membrane shape.

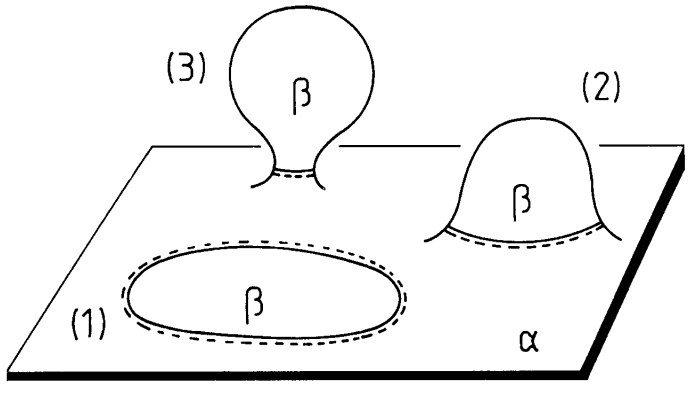

Figure 1.9: Domain-induced budding due to competition of bending energy and line energy at the domain boundary between two domains α and β. (Taken from Ref.[109])

1.6 Two-state model for membrane wrapping

Wrapping of rigid particles can be understood as a competition of the gain in the adhesion energy due to contact interaction between the particle and membrane versus deformation energy due to bending and membrane tension. Figure. 1.10, depicts a simple two-state model for wrapping of a rigid spherical particle of radius R and homogeneous adhesion strength w. For a tensionless state of the membrane the free membrane wrapped around the particle can be neglected since it attains a catenoidal deformation which is a minimal surface with null costs due to bending energy. Due to an energetic competition, the bending costs of a completely encapsulated state, $8\pi\kappa$, must be balanced by the corresponding gain due to contact energy which is $4\pi R^2 w$ for attain a complete-wrapped state; thereby giving a critical adhesion strength $w^* = 8\pi\kappa/4\pi R^2 = 2\kappa/R^2$ above which the system proceeds spontaneously without any energy barrier from a non-wrapped as in state (a) to a completely wrapped state (b), as shown in Fig. 1.10. Bending energy thus plays a significant role during uptake for typical particles sizes ranging from 20 nm to few hundred nanometers, where a competition between $\mathcal{E}_{\text{bend}}$ vs. $\mathcal{E}_{\text{adhesion}}$, determines a relevant length scale given by, $\sqrt{\kappa/w}$. However for uptake of large macroscopic particles (as in phagocytosis), the role of bending energy becomes less dominant and wrapping then is more a competition between the membrane surface tension and adhesion energy. One can describe the critical adhesion strength in terms of a dimensionless quantity called reduced adhesion $\tilde{w} = 2wR^2/\kappa$, such that the system attains a full wrapping configuration for reduced adhesion values $\tilde{w} \geq 4$. Experimental studies[5,6] have shown a size dependency for uptake of nanoparticles via endocytosis. Previous works[114–116], assuming a similar two-state description for membrane wrapping of spherical particles but accounting for the gain in contact using receptor-mediated interactions instead of a homogeneous adhesive nature estimate an optimal radius in a range between 25-30 nm. For typical values of $\kappa = 50\,k_B T$ and $w = 0.25\,k_B T/nm^2$ in $\tilde{w} = 4$, a minimal particle size of $R^* = 20$ nm is estimated above which a non-wrapped state directly jumps into a complete-wrapped state. This estimate agrees with the typical particle sizes which undergo uptake via membrane wrapping and for stiffer membranes, i.e., higher κ, or less sticky particles the estimated lower limit is larger. Using a reduced adhesion is thus advantageous since it allows us to describe both the role of particle dimension and bending stiffness of the membrane using a single dimensionless variable.

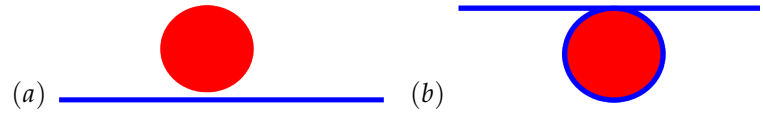

Figure 1.10: Two-state model for membrane wrapping of a spherical particle of radius R with homogeneous adhesion strength w. State (a) corresponds to no-wrapping state. State (b) corresponds to full wrapping with a total cost of bending energy $8\pi\kappa$ and a gain by contact interaction of $4\pi R^2 w$.

1.7 Phase diagram for wrapping of a spherical particle

From the two-state model described in the previous section we learn that for a "tensionless state" of the membrane there are only two possible states namely (i) non-wrapped state and (ii) complete-wrapped state and the relevant parameters for the system being adhesion strength w and bending rigidity κ. The reduced adhesion $\tilde{w}$ is a dimensionless parameter that can be constructed by choosing a length scale given by the particle radius a, and an energy scale given by, κ such that for $\tilde{w} > 4$ the system spontaneously achieves complete wrapping. It also allows to gain insight about the characteristic length scale $\sqrt{\kappa/w}$ which exists due to the energetic competition. Biological cell-membranes exhibit a wide range of membrane tensions [117] with typical values between 0.1-10 mN/m. Therefore it is important to understand the role of membrane tension in wrapping. Accounting for the deformation costs due to tension, the significance of the energetic competition between $\mathcal{E}_{\text{bend}}$ vs. $\mathcal{E}_{\text{tension}}$ is studied using a simple model presented below.

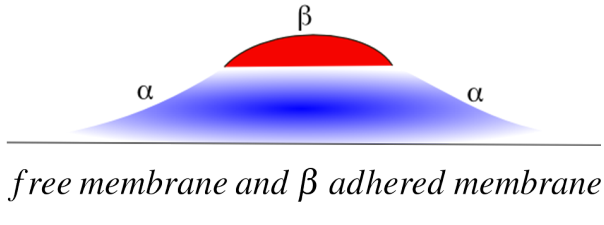

Figure 1.11: Wrapping of a particle by a fluid membrane such that the adhered membrane domain α (in red) and the free membrane β is around the particle (in blue).

In Fig. 1.11, the membrane domain α adhered on the particle is shown in red while the free membrane domain β around the particle is shown in blue. The goal is now to understand the different possible states during wrapping a system might be in for different bending rigidity κ, adhesion strength w, and membrane tension σ. The total energy of such a system is given by,

$$\mathcal{E}_{\text{total}} = \mathcal{E}^{\alpha}_{\text{bend}} + \mathcal{E}^{\beta}_{\text{bend}} + \mathcal{E}_{\text{adhesion}} + \mathcal{E}_{\text{tension}} \ , \tag{1.9}$$

where $\mathcal{E}^{\alpha}_{\text{bend}}$ and $\mathcal{E}^{\beta}_{\text{bend}}$ correspond to the bending energy due to the free membrane and adhered membrane respectively.

In Fig. 1.12, the spherical particle of radius a is wrapped partially at a wrapping angle given by θ. The wrapping fraction is defined as a ratio of the sphere wrapped to the total area of the sphere,

$$z = \frac{A_{ad}}{A_{total}} = \frac{2\pi a^2 \int_0^{\theta} d\theta \sin\,\theta}{4\pi a^2} = \frac{(1-\cos\theta)}{2} \ . \tag{1.10}$$

The height of the center of the sphere below the detachment plane is $a\cos\,\theta$ hence the height of the particle above is $a(1-cos\,\theta) = 2za$, which is the penetration depth

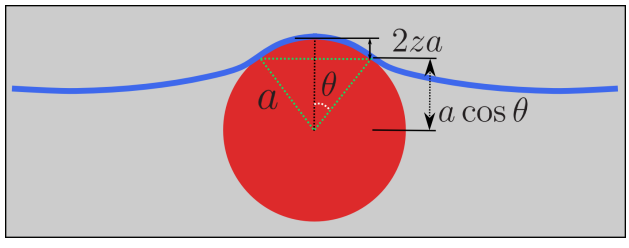

Figure 1.12: For a wrapping angle θ, a spherical particle of radius a is partially wrapped with a wrapped area, A_{ad}. The wrapping fraction z, is the ratio of the wrapped area to the total area of the sphere i.e., $z = A_{ad}/4\pi a^2$. The penetration depth (of the sphere into the membrane) given by, $2za$ as a fraction of the particle radius is described by the wrapping fraction such that for $z = 0$ the sphere is non-wrapped with null penetration while at $z = 1$, the penetration depth equal to the particle diameter of $2a$ signifies complete wrapping.

expressed as a fraction of the particle radius a which is wrapped by the membrane at a particular contact angle θ.

The free membrane for a tensionless state of the membrane can form a catenoid and thereby provides a null contribution to the deformation energy. For nonzero tension, the contribution due to the bending energy of the free membrane given by, $\mathcal{E}^{\alpha}_{\text{bend}}$ needs to be accounted for. However to estimate for this energy term accounting for membrane tension is not straightforward and requires more involved numerical approaches[12–14,106] and hence is neglected for the time being. The assumption to neglect $\mathcal{E}^{\alpha}_{\text{bend}}$ should be valid at low membrane tension values as shown using a deformed catenoid approximation calculations in our recent work[12].

Bending energy due to the adhered membrane can be written using Eq. 2.2 as

$$\mathcal{E}^{\beta}_{\text{bend}} = 2\kappa(\frac{1}{a} - c_o)^2 \left(2\pi a^2 \int_0^{\theta} d\theta \sin\theta\right) = 2\kappa(\frac{1}{a} - c_o)^2 \left[2\pi a^2(1 - \cos\theta)\right] \ . \quad (1.11)$$

Simplifying the above equation using Eq. 1.10, we get

$$\mathcal{E}^{\beta}_{\text{bend}} = 8\pi\kappa(\frac{1}{a} - c_o)^2 a^2 z \ . \quad (1.12)$$

The adhesion energy is can be written using Eq. 1.8 as,

$$\mathcal{E}_{\text{adhesion}} = -w \int_{A_{ad}} dS = -2\pi a^2 w \int_0^{\theta} d\theta \sin\theta = -2\pi a^2 w(1 - \cos\theta) \ . \quad (1.13)$$

Using Eq. 1.10, we can simplify the above equation as

$$\mathcal{E}_{\text{adhesion}} = -4\pi a^2 w z \ . \quad (1.14)$$

To evaluate the contribution of the membrane tension (due to only the part of the membrane adhered to the particle) requires to calculate the total excess area ΔA which is given as the difference of the adhered area $A_{ad} = 4\pi a^2 z$ and its projected

area in the x-y plane. The projected area A_{ad}^{proj} is equal to a the area of a circle of radius $\rho = a \sin\theta$. Thus the contribution due to membrane tension is given by

$$\mathcal{E}_{\text{tension}} = \sigma \Delta A = \sigma \left(A_{ad} - A_{ad}^{proj} \right) = \sigma (4\pi a^2 z - \pi a^2 sin^2\theta) \ . \tag{1.15}$$

Using Eq. 1.10 replacing $\sin^2\theta = 4z(1-z)$, we can simplify the above equation as

$$\mathcal{E}_{\text{tension}} = 4\pi\sigma a^2 z^2 \ . \tag{1.16}$$

Thus neglecting the free membrane bending energy contribution in Eq. 1.9, using Eqs. 1.12, 1.14, and 1.16, the total wrapping energy as a sum of the elastic energy cost due to bending of the adhered membrane, gain in adhesion energy and deformation cost due to membrane tension is given by,

$$\mathcal{E}_{\text{total}} = -\left[w - 2\kappa(\frac{1}{a} - c_0)^2 \right] 4\pi a^2 z + 4\pi\sigma a^2 z^2 \ . \tag{1.17}$$

Next, using dimensionless variables like reduced energy as $\tilde{\mathcal{E}} = \mathcal{E}_{\text{total}}/2\pi\kappa$, reduced adhesion as $\tilde{w} = 2wa^2/\kappa$, reduced spontaneous curvature as $\tilde{c}_0 = ac_0$ and reduced tension as $\tilde{\sigma} = \sigma a^2/\kappa$ we can rewrite Eq. 1.17 as,

$$\tilde{\mathcal{E}} = -\left[\tilde{w} - 4(1-\tilde{c}_0)^2 \right] z + 4\tilde{\sigma} z^2 \ . \tag{1.18}$$

For a symmetric bilayer since there is no preferred curvature i.e., $c_0 = 0$, we can describe the wrapping model using two reduced dimensionless variables $\tilde{w}$, and $\tilde{\sigma}$ given as

$$\tilde{\mathcal{E}} = -(\tilde{w} - 4)z + 2\tilde{\sigma} z^2 \ . \tag{1.19}$$

For describing a phase transition near a critical point, one can approximate the free energy of the system as a power series of the order parameters describing the system. Such an expansion is known as a Ginzburg-Landau free energy form and can be used to predict phase transitions near a critical point. Comparing Eq. 1.20 with even power of the order parameter ξ and a positive coefficient b, we obtain

$$\mathcal{F}(\xi) = a\xi^2 + \frac{b}{2}\xi^4 \ . \tag{1.20}$$

where $a = -(\tilde{w} - 4)$ and $b = 4\tilde{\sigma}$ and the order parameter of the system ξ is given by the square root of the wrapping fraction i.e., $\xi = \sqrt{z}$. The system undergoes a transition for $a > 0$ which implies $\tilde{w} > 4$. At this adhesion strength for a tensionless membrane a spherical particle undergoes a transition from a non-wrapped to a complete-wrapped state as discussed using a two state model in Sec 1.6. Next, to calculate the minimum energy condition for complete-wrapping for a non-zero membrane tension by evaluating $\tilde{\mathcal{E}}'(z)|_{z=1} = 0$ or equivalently, $\mathcal{F}'(\xi)|_{\xi=1} = 0$ we obtain $a + b = 0$ i.e $\tilde{w} = 4 + 4\tilde{\sigma}$. The wrapping fraction at which this transition occurs if given by $\xi^2|_{\xi_c} = \xi_c^2 = -a/b$ or, $z|_{z^*} = z^* = (\tilde{w} - 4)/4\tilde{\sigma}$. Fig. 1.13 (b) shows different membrane deformation profiles at different partial wrapping fractions.

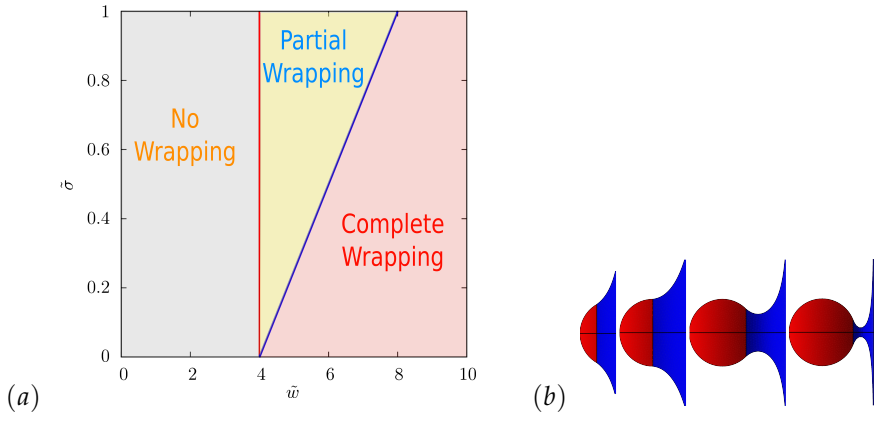

Figure 1.13: (a) A wrapping phase diagram obtained for a spherical particle of radius a adhering with a homogeneous adhesion strength w to a membrane with bending rigidity κ and membrane tension σ. We assume the contributions to the deformation energy due to the free membrane around the particle to be negligible and obtain three different wrapping behaviors namely, (i) No wrapping, (ii) Partial wrapping and (iii) Complete wrapping for different values of reduced adhesion ($\tilde{w}$) and reduced tension ($\tilde{\sigma}$). We see two kinds of transitions, a continuous binding transition which sets in at $\tilde{w} = 4$ and the particle spontaneously attains from a non-wrapped state either to a complete-wrapped state for zero membrane tension, or jumps to a bound state for systems with membrane tension. At higher adhesion values given by, $\tilde{w} = 4 + 4\tilde{\sigma}$, the partially wrapped states jump to a complete-wrapped state. This transition is a discontinuous transition and has an energy barrier associated to it; which has been calculated accounting for the free membrane deformation costs as well in Refs.[12–14]. (b) Membrane deformation profiles for a spherical particle being partially wrapped at different wrapping fractions are calculated using a triangulated membranes. At zero membrane tension, all these deformation profiles correspond to unstable states and the free membrane (shown in blue) forms catenoid-like minimal surface with null costs due bending energy.

Using this simple model one can understand the different wrapping states (no-wrapping, partial-wrapping and complete-wrapping), the characteristic length scales if the system namely, $\sqrt{\kappa/w}$ and $\sqrt{\kappa/\sigma}$ described using the two dimensionless parameters $\tilde{w}$ and $\tilde{\sigma}$, and the nature of transitions between different states having different wrapping fractions. In order to correctly estimate the phase boundaries, the energy barrier at the discontinuous transition and its associate spinodals the free membrane deformation costs needs to be taken into account and this requires a more involved numerical approach as presented in the following Chapter. 2.

1.8 Capillarity at a fluid interface

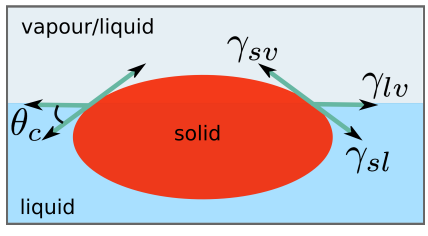

Figure 1.14: An ellipsoidal particle at a fluid-fluid or fluid-gas interface. The three interfacial tensions γ_{sv}, γ_{sl}, γ_{lv} correspond to three different phases solid (s) , liquid (l), and vapor/another liquid (v). At equilibrium, a force balance as given by the Young Dupré condition is valid at all points along the three-phase contact line for a particular wetting angle θ_c.

A fluid interface is the boundary between a two liquid phases like an oil-water interface or between a liquid and gas/vapor phase like an air-water interface. The molecular forces at an interface are different from those in the bulk environment since at an interface interactions are predominantly due to a surface energy cost per unit area of the interface or otherwise termed as surface tension. At equilibrium, the forces acting along a contact line of a solid particle at a fluid interface due to different interfacial tensions (γ_{sv}, γ_{sl}, and γ_{lv}) associated with the three different phases solid (s), liquid (l), vapor (or another liquid) (v) must balance each other for a particular wetting angle θ_c as shown schematically in Fig. 1.14. The contact angle (θ_c) of a particle at the fluid interface is given by the Young-Dupré equation[118]. At a fluid interface, micron-sized homogeneous non-spherical colloidal particles can distort the fluid interface around it. An interface in presence of particles can be distorted either due to externally directed fields like gravity/particle weight[119–121], and electromagnetic fields[122–125] or due to particle heterogeneity[126] arising due to chemical patterning[127–130] or particle roughness[131,132]. For smaller particles with sizes less than a few microns the effects due to particle weight are negligible.

Thus for a homogeneous micron-sized spherical particle at a fluid interface, to satisfy the equilibrium condition along all points of the contact line, the interface around the particle remains flat for all contact angles as shown in the experiments[133] in Fig. 1.15 (a). However, for an ellipsoidal particle[133] in similar conditions an undulating contact line causes a quadrupolar distortion of the the interface such that it rises along the flat sides of the ellipsoid and dips near the tips for $\theta_c < 90°$. Due to the induced distortion, neighboring particles can interact to self-assemble to minimize the excess interfacial area. Similarly[126], in Fig. 1.15 (b), in presence of an ellipsoidal micro-post at a fluid interface, the interface undergoes a quadrupolar distortion and then employing this curvature field they could preferentially assemble smaller cylindrical particles near the tips where the interface undergoes a depression. A biological situation where capillary forces are in action is seen in Fig. 1.15(c) where a water-strider or Gerridae distorts the water surface and uses the resulting capillary forces to effortlessly skim on the surface of the

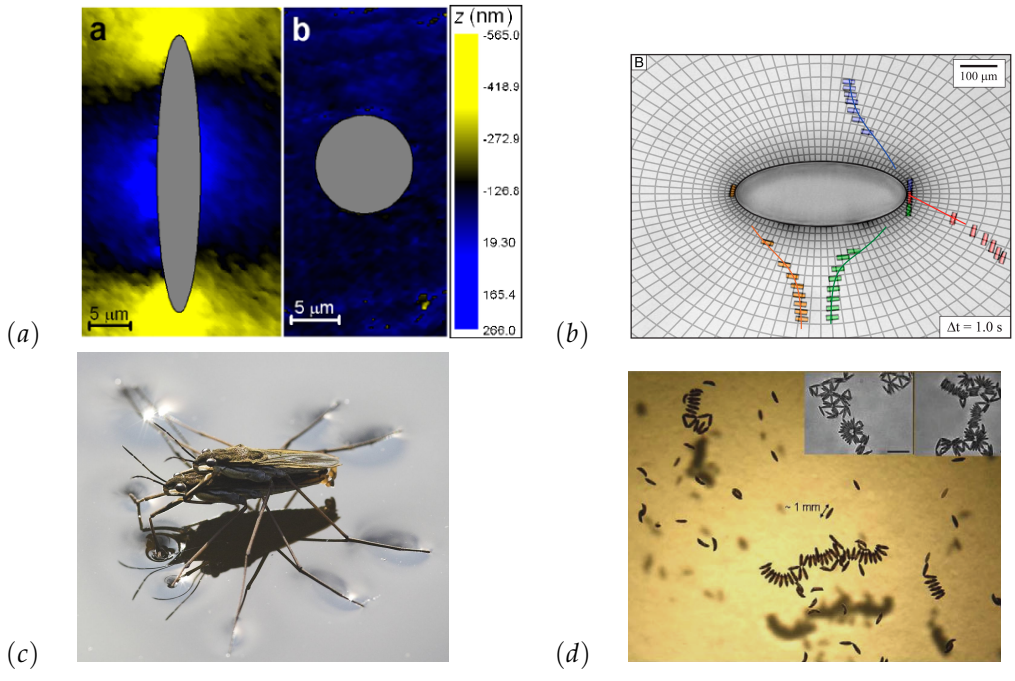

Figure 1.15: Different examples of capillarity in experiments and nature. (a) Comparison of interface deformation due to a micron-sized spherical and ellipsoidal particle. (Taken from Ref.[133]), (b) Migration of rod like particles near the tips of a an elliptical micro-post due to induced interface distortion. (Taken from Ref.[126], (c) A water strider skims the water surface. (Taken from public domain : Wikipedia), (d) Rafts formed by mosquito eggs. (Taken from Ref.[134])

water. Another biological example is seen in Fig. 1.15 (d) where millimeter sized ellipsoidal mosquito eggs[134,135] due to long-range capillarity at a water interface tend to form chains where individual eggs align mostly side-by-side. A physical motivation to study capillarity is to understand these self-assembly[23,33,34,136,137] principles for anisotropic micron-sized particles and characterize these interactions between neighboring particles approaching in different orientations. Knowledge of interaction potentials provides beautiful insight about the rheological properties of particulate monolayers[138–142] which is rich model system in soft matter science with promising applications. Capillarity within particulate suspensions[35–39] can result in striking consequences like supression of the "coffee-ring"[143–145] effect. Droplets of spherical particles on a solid surface while evaporating leave a ring-like deposition of spherical particles known as a the "coffee-ring " effect whereas droplets containing anisotropic particles like ellipsoids[146–148] can supress the ring formation and result in uniform deposition of particles due to particle aggregation on the droplet surface via capillary forces. Fundamental understanding of capillary interactions at interfaces may also facilitate a deeper understanding to self-assembly of proteins[43,44,149], viruses[16] and nanoparticles[12,15] at a biological membrane due to membrane-mediated interactions as both membranes and interfaces are dominated by surface-mediated interactions.

References: Introduction

1 D. W. Thompson, *On growth and form.*, 1942.

2 A. Schrade, Z. Cao, K. Landfester and U. Ziener, *Langmuir*, 2011, **27**, 6689–6700.

3 S. E. A. Gratton, P. A. Ropp, P. D. Pohlhaus, J. C. Luft, V. J. Madden, M. E. Napier and J. M. DeSimone, *Proc. Natl. Acad. Sci. U.S.A.*, 2008, **105**, 11613–11618.

4 J. A. Champion and S. Mitragotri, *Proc. Natl. Acad. Sci. U.S.A.*, 2006, **103**, 4930–4934.

5 B. D. Chithrani, A. A. Ghazani and W. C. W. Chan, *Nano Lett.*, 2006, **6**, 662–668.

6 B. D. Chithrani and W. C. W. Chan, *Nano Lett.*, 2007, **7**, 1542–1550.

7 S. Barua, J.-W. Yoo, P. Kolhar, A. Wakankar, Y. R. Gokarn and S. Mitragotri, *Proc. Natl. Acad. Sci. U.S.A.*, 2013, **110**, 3270–3275.

8 H. M. Ding and Y. Q. Ma, *Biomaterials*, 2012, **33**, 5798–5802.

9 J. H. Hurley, E. Boura, L.-A. Carlson and B. Różycki, *Cell*, 2010, **143**, 875–887.

10 S. Mayor and R. E. Pagano, *Nat. Rev. Mol. Cell Biol.*, 2007, **8**, 603–612.

11 I. Canton and G. Battaglia, *Chem. Soc. Rev.*, 2012, **41**, 2718–2739.

12 S. Dasgupta, T. Auth and G. Gompper, *Soft Matter*, 2013, **9**, 5473–5482.

13 M. Deserno, *Phys. Rev. E.*, 2003, **69**, 031903.

14 M. Deserno, *J. Phys.: Condens. Matter*, 2004, **16**, S2061—-S2070.

15 S. Dasgupta, T. Auth and G. Gompper, *Nano Letters*, 2014, **14**, 687–693.

16 J. Mercer, M. Schelhaas and A. Helenius, *Annu. Rev. Biochem.*, 2010, **79**, 803–833.

17 S. Welsch, L. Kolesnikova, V. Krähling, J. D. Riches, S. Becker and J. A. G. Briggs, *PLoS Pathogens*, 2010, **6**, 9.

18 T. Noda, H. Ebihara, Y. Muramoto, K. Fujii, A. Takada, H. Sagara, J. H. Kim, H. Kida, H. Feldmann and Y. Kawaoka, *PLoS Pathogens*, 2006, **2**, 9.

19 G. Panaitov, S. Thiery, B. Hofmann and A. Offenhäusser, *Microelectronic Engineering*, 2011, **88**, 1840–1844.

20 F. Santoro, J. Schnitker, G. Panaitov and A. Offenhäusser, *Nano letters*, 2013, **13**, 5379–5384.

21 A. Hai, A. Dormann, J. Shappir, S. Yitzchaik, C. Bartic, G. Borghs, J. Langedijk and M. E. Spira, *Journal of The Royal Society Interface*, 2009, **6**, 1153–1165.

22 A. Hai, J. Shappir and M. E. Spira, *Nature methods*, 2010, **7**, 200–202.

23 M. Grzelczak, J. Vermant, E. M. Furst and L. M. Liz-Marzán, *ACS Nano*, 2010, **4**, 3591–3605.

24 Z. Zhang, P. Pfleiderer, A. B. Schofield, C. Clasen and J. Vermant, *J. Am. Chem. Soc.*, 2011, **133**, 392–395.

25 J. C. Loudet, A. M. Alsayed, J. Zhang and A. G. Yodh, *Phys. Rev. Lett.*, 2005, **94**, 018301.

26 E. P. Lewandowski, J. A. Bernate, A. Tseng, P. C. Searson and K. J. Stebe, *Soft Matter*, 2009, **5**, 886–890.

27 A. Dinsmore, M. F. Hsu, M. Nikolaides, M. Marquez, A. Bausch and D. Weitz, *Science*, 2002, **298**, 1006–1009.

28 C. Zeng, H. Bissig and A. Dinsmore, *Solid State Commun.*, 2006, **139**, 547–556.

29 J. C. Loudet and B. Pouligny, *Europhys. Lett.*, 2009, **85**, 28003.

30 P. Pieranski, *Phys. Rev. Lett.*, 1980, **45**, 569–572.

31 A. Bausch, M. Bowick, A. Cacciuto, A. Dinsmore, M. Hsu, D. Nelson, M. Nikolaides, A. Travesset and D. Weitz, *Science*, 2003, **299**, 1716–1718.

32 A. B. D. Brown, C. G. Smith and A. R. Rennie, *Phys. Rev. E*, 2000, **62**, 951–960.

33 N. Bowden, A. Terfort, J. Carbeck and G. M. Whitesides, *Science*, 1997, **276**, 233–235.

34 K. J. Stebe, E. Lewandowski and M. Ghosh, *Science*, 2009, **325**, 159–160.

35 W. Ramsden, *Proc. R. Soc. London*, 1903, **72**, 156–164.

36 S. U. Pickering, *J. Chem. Soc., Trans.*, 1907, **91**, 2001–2021.

37 B. Madivala, S. Vandebril, J. Fransaer and J. Vermant, *Soft Matter*, 2009, **5**, 1717–1727.

38 R. Aveyard, B. P. Binks and J. H. Clint, *Adv. Colloid Interface Sci.*, 2003, **100**, 503–546.

39 J. W. de Folter, E. M. Hutter, S. I. Castillo, K. Klop, A. P. Philipse and W. K. Kegel, *Langmuir*, 2013, Advance online publication. doi:10.1021/la402427q.

40 K. Stratford, R. Adhikari, I. Pagonabarraga, J.-C. Desplat and M. E. Cates, *Science*, 2005, **309**, 2198–2201.

41 M. E. Cates and P. S. Clegg, *Soft Matter*, 2008, **4**, 2132–2138.

42 P. A. Kralchevsky and K. Nagayama, *Adv. Colloid Interface Sci.*, 2000, **85**, 145 – 192.

43 B. J. Reynwar and M. Deserno, *Soft Matter*, 2011, **7**, 8567–8575.

44 B. J. Reynwar, G. Illya, V. A. Harmandaris, M. M. Mueller, K. Kremer and M. Deserno, *Nature*, 2007, **447**, 461–464.

45 B. Alberts, D. Bray, K. Hopkin, A. Johnson, J. Lewis, M. Raff, K. Roberts and P. Walter, *Essential cell biology*, Garland Science, 2013.

46 D. L. Nelson, A. L. Lehninger and M. M. Cox, *Lehninger principles of biochemistry*, Macmillan, 2008.

47 O. G. Mouritsen, *Life-as a matter of fat*, Springer, 2005.

48 T. Kirchhausen, *Nature cell biology*, 2012, **14**, 906–908.

49 H. T. McMahon and J. L. Gallop, *Nature*, 2005, **438**, 590–596.

50 L. Johannes, C. Wunder and P. Bassereau, *Cold Spring Harbor perspectives in biology*, 2014, **6**, a016741.

51 M. Ø. Jensen and O. G. Mouritsen, *Biochimica et Biophysica Acta (BBA)-Biomembranes*, 2004, **1666**, 205–226.

52 T. Auth and G. Gompper, *Physical Review E*, 2003, **68**, 051801.

53 C. Hiergeist and R. Lipowsky, *Journal de Physique II*, 1996, **6**, 1465–1481.

54 F. Campelo, H. T. McMahon and M. M. Kozlov, *Biophysical journal*, 2008, **95**, 2325–2339.

55 B. Sorre, A. Callan Jones, J. Manzi, B. Goud, J. Prost, P. Bassereau and A. Roux, *Proc. Natl. Acad. Sci. U.S.A.*, 2011, **109**, 173–8.

56 J. C. Stachowiak, E. M. Schmid, C. J. Ryan, H. S. Ann, D. Y. Sasaki, M. B. Sherman, P. L. Geissler, D. A. Fletcher and C. C. Hayden, *Nature cell biology*, 2012, **14**, 944–949.

57 P. N. Dannhauser and E. J. Ungewickell, *Nature cell biology*, 2012, **14**, 634–639.

58 T. Heimburg, *Thermal biophysics of membranes*, John Wiley & Sons, 2008.

59 G. Jamieson and D. Robinson, *Mammalian Cell Membranes: Surface membranes of specific cell types*, Butterworths, 1977.

60 B. Granseth, B. Odermatt, S. J. Royle and L. Lagnado, *Neuron*, 2006, **51**, 773–786.

61 J. Balaji and T. Ryan, *Proceedings of the National Academy of Sciences*, 2007, **104**, 20576–20581.

62 H. T. McMahon and I. G. Mills, *Curr. Opin. Cell Biol.*, 2004, **16**, 379–391.

63 Z. G. Qu, X. C. He, M. Lin, B. Y. Sha, X. H. Shi, T. J. Lu and F. Xu, *Nanomedicine*, 2013, **8**, 995–1011.

64 D. R. Larson, M. C. Johnson, W. W. Webb and V. M. Vogt, *Proceedings of the National Academy of Sciences of the United States of America*, 2005, **102**, 15453–15458.

65 W. Römer, L. Berland, V. Chambon, K. Gaus, B. Windschiegl, D. Tenza, M. R. E. Aly, V. Fraisier, J. C. Florent, D. Perrais and et al., *Nature*, 2007, **450**, 670–675.

66 J. U. Sommer, M. Werner and V. A. Baulin, *Europhys. Lett.*, 2012, **98**, 18003.

67 S. Pogodin and V. A. Baulin, *ACS Nano*, 2010, **4**, 5293–5300.

68 K. Yang and Y. Q. Ma, *Nat. Nanotechnol.*, 2010, **5**, 579–583.

69 J. Lin, H. Zhang, Z. Chen and Y. Zheng, *ACS Nano*, 2010, **4**, 5421–5429.

70 T. Kohyama, D. M. Kroll and G. Gompper, *Phys. Rev. E*, 2003, **68**, 061905.

71 T. Baumgart, B. R. Capraro, C. Zhu and S. L. Das, *Annual review of physical chemistry*, 2011, **62**, 483–506.

72 P. Sens, L. Johannes and P. Bassereau, *Curr. Opin. Cell Biol.*, 2008, **20**, 476–482.

73 S. Tollis, A. E. Dart, G. Tzircotis and R. G. Endres, *BMC Syst. Biol.*, 2010, **4**, 149.

74 V. Sirotkin, J. Berro, K. Macmillan, L. Zhao and T. D. Pollard, *Molecular biology of the cell*, 2010, **21**, 2894–2904.

75 T. M. Huckaba, A. C. Gay, L. F. Pantalena, H.-C. Yang and L. A. Pon, *The Journal of cell biology*, 2004, **167**, 519–530.

76 V. Soppina, A. K. Rai, A. J. Ramaiya, P. Barak and R. Mallik, *Proceedings of the National Academy of Sciences*, 2009, **106**, 19381–19386.

77 R. Mallik and S. P. Gross, *Current Biology*, 2004, **14**, R971–R982.

78 H. Noguchi and M. Takasu, *The Journal of chemical physics*, 2001, **115**, 9547–9551.

79 H. Noguchi, *Journal of the Physical Society of Japan*, 2009, **78**, 041007.

80 V. V. Ginzburg, S. Balijepalli, K. A. Smith and A. C. Balazs, *Nanotechnologies for the Life Sciences*, 2009.

81 S. A. Safran, *Statistical thermodynamics of surfaces, interfaces, and membranes*, Addison-Wesley Reading, MA, 1994.

82 M. Belushkin and G. Gompper, *The Journal of chemical physics*, 2009, **130**, 134712.

83 G. Gompper, M. Schick and S. Milner, *Physics Today*, 2008, **48**, 91–93.

84 M. P. Do Carmo and M. P. Do Carmo, *Differential geometry of curves and surfaces*, Prentice-Hall Englewood Cliffs, 1976, vol. 2.

85 R. Capovilla, J. Guven and J. Santiago, *Physical Review E*, 2002, **66**, 021607.

86 E. Kreyszig, *Introduction to differential geometry and Riemannian geometry*, University of Toronto Press, 1968, vol. 16.

87 J. Käs and E. Sackmann, *Biophysical journal*, 1991, **60**, 825–844.

88 I. Koltover, J. O. Rädler and C. R. Safinya, *Physical review letters*, 1999, **82**, 1991.

89 W. Wintz, H.-G. Döbereiner and U. Seifert, *EPL (Europhysics Letters)*, 1996, **33**, 403.

90 R. Lipowsky and E. Sackmann, *Structure and Dynamics of Membranes: I. From Cells to Vesicles/II. Generic and Specific Interactions*, Elsevier, 1995.

91 U. Seifert, K. Berndl and R. Lipowsky, *Physical Review A*, 1991, **44**, 1182.

92 P. Canham, *J. Theor. Biol.*, 1970, **26**, 61 – 81.

93 W. Helfrich, *Z. Naturforsch. C*, 1973, **28**, 693–703.

94 E. A. Evans, *Biophysical Journal*, 1983, **43**, 27–30.

95 A. Zilker, H. Engelhardt and E. Sackmann, *Journal De Physique*, 1987, **48**, 2139–2151.

96 H.-G. Döbereiner, G. Gompper, C. K. Haluska, D. M. Kroll, P. G. Petrov and K. A. Riske, *Physical review letters*, 2003, **91**, 048301.

97 M. Deserno, *Macromolecular rapid communications*, 2009, **30**, 752–771.

98 H.-G. Döbereiner, *Current Opinion in colloid & interface science*, 2000, **5**, 256–263.

99 S. Svetina and B. Žekš, *Eur. Biophys. J.*, 1989, **17**, 101–111.

100 L. Miao, B. Fourcade, M. Rao, M. Wortis and R. K. P. Zia, *Phys. Rev. A*, 1991, **43**, 6843–6856.

101 U. Seifert, K. Berndl and R. Lipowsky, *Phys. Rev. A*, 1991, **44**, 1182–1202.

102 F. Jülicher and R. Lipowsky, *Phys. Rev. E*, 1996, **53**, 2670–2683.

103 K. Khairy and J. Howard, *Soft Matter*, 2011, **7**, 2138.

104 W. T. Góźdź, *Langmuir*, 2007, **23**, 5665–5669.

105 O.-Y. Zhong-can and W. Helfrich, *Phys. Rev. A*, 1989, **39**, 5280–5288.

106 M. Deserno and T. Bickel, *Europhys. Lett.*, 2003, **62**, 767–774.

107 S. A. Nowak and T. Chou, *Phys. Rev. E.*, 2008, **78**, 021908.

108 S. Mkrtchyan, C. Ing and J. Z. Y. Chen, *Phys. Rev. E*, 2010, **81**, 1–9.

109 R. Lipowsky, *J. Phys. II (France)*, 1992, **2**, 1825–1840.

110 R. Lipowsky, *Biophys. J.*, 1993, **64**, 1133–1138.

111 F. Jülicher and R. Lipowsky, *Phys. Rev. Lett.*, 1993, **70**, 2964–2967.

112 A. Minami and K. Yamada, *Eur. Phys. J. E*, 2007, **23**, 367–374.

113 T. Baumgart, S. T. Hess and W. W. Webb, *Nature*, 2003, **425**, 821–824.

114 S. Zhang, J. Li, G. Lykotrafitis, G. Bao and S. Suresh, *Advanced Materials*, 2009, **21**, 419–424.

115 H. Gao, W. Shi and L. B. Freund, *Proc. Natl. Acad. Sci. U.S.A.*, 2005, **102**, 9469–9474.

116 S. Zhang, J. Li, G. Lykotrafitis, G. Bao and S. Suresh, *Adv. mater.*, 2009, **21**, 419–424.

117 G. Morris, S. Neethling and J. Cilliers, *Journal of colloid and interface science*, 2011, **361**, 370–380.

118 T. Young, *Philosophical Transactions of the Royal Society of London*, 1805, 65–87.

119 D. Vella and L. Mahadevan, *Am. J. Phys.*, 2005, **73**, 817–825.

120 M. M. Nicolson, *Math. Proc. Cambridge Philos. Soc.*, 1949, **45**, 288–295.

121 W. Gifford and L. Scriven, *Chem. Eng. Sci.*, 1971, **26**, 287 – 297.

122 M. Oettel and S. Dietrich, *Langmuir*, 2008, **24**, 1425–1441.

123 M. Oettel, A. Dominguez and S. Dietrich, *Phys. Rev. E*, 2005, **71**, 051401.

124 A. Dominguez, M. Oettel and S. Dietrich, *J. Phys.: Condens. Matter*, 2005, **17**, S3387.

125 M. Nikolaides, A. Bausch, M. Hsu, A. Dinsmore, M. P. Brenner, C. Gay and D. A. Weitz, *Nature*, 2002, **420**, 299–301.

126 M. Cavallaro, L. Botto, E. P. Lewandowski, M. Wang and K. J. Stebe, *Proc. Natl. Acad. Sci. U. S. A.*, 2011, **108**, 20923–20928.

127 B. J. Park and E. M. Furst, *Soft Matter*, 2011, **7**, 7676–7682.

128 A. Kumar, B. J. Park, F. Tu and D. Lee, *Soft Matter*, 2013, **9**, 6604–6617.

129 B. J. Park, C.-H. Choi, S.-M. Kang, K. E. Tettey, C.-S. Lee and D. Lee, *Soft Matter*, 2013, **9**, 3383–3388.

130 B. J. Park and D. Lee, *ACS Nano*, 2012, **6**, 782–790.

131 L. Yao, L. Botto, M. Cavallaro, Jr, B. J. Bleier, V. Garbin and K. J. Stebe, *Soft Matter*, 2013, **9**, 779–786.

132 J. Lucassen, *Colloids and Surfaces*, 1992, **65**, 131 – 137.

133 J. C. Loudet, A. G. Yodh and B. Pouligny, *Phys. Rev. Lett.*, 2006, **97**, 018304.

134 J. Loudet and B. Pouligny, *Eur. Phys. J. E: Soft Matter Biol. Phys.*, 2011, **34**, 1–17.

135 Z. Saliternik, *Bulletin of Entomological Research*, 1942, **33**, 221–221.

136 E. P. Lewandowski, P. C. Searson and K. J. Stebe, *J. Phys. Chem. B*, 2006, **110**, 4283–4290.

137 F. Bresme and M. Oettel, *J. Phys.: Condens. Matter*, 2007, **19**, 413101.

138 E. Van Nierop, M. Stijnman and S. Hilgenfeldt, *Europhys. Lett.*, 2005, **72**, 671.

139 V. Trappe, V. Prasad, L. Cipelletti, P. Segre and D. Weitz, *Nature*, 2001, **411**, 772–775.

140 A. J. Liu and S. R. Nagel, *Nature*, 1998, **396**, 21–22.

141 J.-B. Fournier and P. Galatola, *Phys. Rev. E*, 2002, **65**, 031601.

142 B. Madivala, J. Fransaer and J. Vermant, *Langmuir*, 2009, **25**, 2718–2728.

143 R. D. Deegan, O. Bakajin, T. F. Dupont, G. Huber, S. R. Nagel and T. A. Witten, *Nature*, 1997, **389**, 827–829.

144 R. D. Deegan, O. Bakajin, T. F. Dupont, G. Huber, S. R. Nagel and T. A. Witten, *Phys. Rev. E*, 2000, **62**, 756–765.

145 H. Hu and R. G. Larson, *The Journal of Physical Chemistry B*, 2002, **106**, 1334–1344.

146 P. J. Yunker, T. Still, M. A. Lohr and A. Yodh, *Nature*, 2011, **476**, 308–311.

147 P. J. Yunker, *PhD thesis*, University of Pennsylvania, 2012.

148 P. Yunker, A. Yodh and T. Still, *Physics of Complex Colloids*, 2013, **184**, 447.

149 T. Auth and G. Gompper, *Phys. Rev. E.*, 2009, **80**, 031901.

I Membrane wrapping

2
Wrapping of ellipsoidal nano-particles by fluid membranes

2.1
Abstract

Membrane budding and wrapping of particles, such as viruses and nano-particles, play a key role in intracellular transport and have been studied for a variety of biological and soft matter systems. We study nano-particle wrapping by numerical minimization of bending, surface tension, and adhesion energies. We calculate deformation and adhesion energies as a function of membrane elastic parameters and adhesion strength to obtain wrapping diagrams. We predict unwrapped, partially-wrapped, and completely-wrapped states for prolate and oblate ellipsoids for various aspect ratios and particle sizes. In contrast to spherical particles, where partially-wrapped states exist only for finite surface tensions, partially-wrapped states for ellipsoids occur already for tensionless membranes. In addition, the partially-wrapped states are long-lived, because of an increased energy cost for wrapping of the highly-curved tips. Our results suggest a lower uptake rate of ellipsoidal particles by cells and thereby a higher virulence of tubular viruses compared with icosahedral viruses, as well as co-operative budding of ellipsoidal particles on membranes.

2.2
Introduction

Budding and subsequent vesiculation of lipid bilayer membranes is essential for transport in biological cells[1–3]. Biomembranes usually consist of a variety of lipids and proteins, therefore buds can be induced by lipid domain formation[4–7], by membrane spontaneous curvature[8–12], or by a combination of both[13–15]. For particle wrapping, in addition to the membrane properties, the particle shape and the adhesion strength have to be taken into account[16–20]. Biological examples are viral budding[21,22] and — for designing efficient drug delivery systems and other nano-engineered techniques for medical diagnosis — the uptake of small particles by cells[17,20,23,24]. Elongated viruses have been found to form patterns on cell membranes[25], and ellipsoidal nano-particles are used for drug delivery[26] and as markers[27,28] in cell biology.

Techniques to fabricate nano-particles of different shapes and sizes are well established, thus wrapping has been studied experimentally using both vesicles and cells. To gain insight into the basic mechanism of cellular uptake, the role of shape and size has been investigated both in vitro[16,17,20,23] and as well as in vivo[29–31] studies.

Computer simulations and numerical calculations are available based on coarse-grained lipid models[32–38] that are most relevant for wrapping of small particles [2], and continuum membrane models that apply if the particle size is considerably larger than the membrane thickness[39–50].

Describing the membranes as a mathematical surface with appropriate curvature-elastic constants, continuum models predict wrapping as function of bending rigidity κ, spontaneous curvature c_0, surface tension σ, and for lipid domain formation also the line tension γ at the domain boundary. Bending rigidity and surface tension oppose wrapping, whereas the adhesion strength w favors wrapping. For example, for a completely wrapped sphere of radius R and for a lipid bilayer without surface tension, an adhesion energy gain of $-4\pi R^2 w$ is opposed by a bending energy cost of $8\pi\kappa$. Complete wrapping occurs if the adhesion strength exceeds $w^* = 2\kappa/R^2$, while for smaller values the sphere remains unwrapped.

Wrapping of spherical particles has been studied systematically using continuum membranes and is well understood. A particle wrapped by an infinitely large planar membrane without surface tension is fully described by the simple calculation above. Neglecting a surface or volume constraint, also the energy of a vesicle that wraps a particle has been obtained analytically[45]. For membranes with surface tension, the deformation energy of the membrane can be calculated using approximate models[29,39] or shape equations that are evaluated numerically[41–43]. Similarly, the deformation energy for wrapping of infinitely long cylinders has been calculated[40,48], which is qualitatively different from wrapping of spheres. Regarding the example given above, the free membrane around the sphere forms a catenoid without any bending energy cost, whereas for a cylinder wrapped by an infinite planar membrane, the deformation energy of the free membrane has to be taken into account.

In this article, we investigate wrapping of ellipsoidal particles by homogeneous membranes without spontaneous curvature. In section 2.4.1, we calculate the wrapping energy as function of the wrapping fraction for membranes with and without surface tension. We obtain phase diagrams that show a non-wrapped state, a partially-wrapped state, and a fully-wrapped state, see section 2.4.2. While the transition between the unwrapped and the partially wrapped state is continuous, the partially-wrapped state is separated from the fully-wrapped state by an energy barrier. In section 2.4.3, we characterize the energy barrier and the hysteresis that is found for the transition between the partially-wrapped and the fully-wrapped state. Finally, in section 2.4.4 we discuss the role of the shape for the wrapping energy.

2) Small particles might as well cross a lipid bilayer membrane by penetration instead of wrapping

2.3 Theoretical model and methods

2.3.1 Continuum membrane model

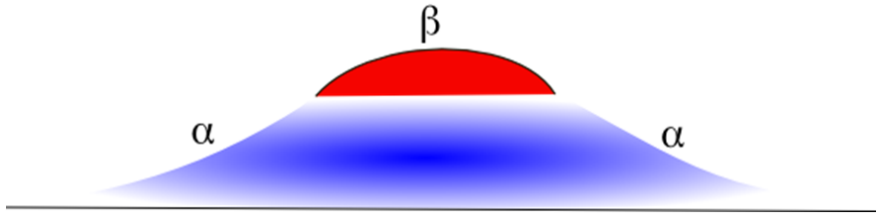

Figure 2.1: Deformation profile of membrane adhering to a rigid nano-particle. The free membrane around the particle is labeled α and the membrane adhered to the particle β.

Using the continuum membrane model, our system is constructed in order to include the minimal ingredients required to characterize wrapping of ellipsoidal particles. The uptake process can be understood as a competitive tug of war between the elastic deformation energy and the contact interaction between particle and membrane. The elastic deformation energy $\mathcal{E}_{\text{def}}$ of the lipid bilayer is [51,52]

$$\mathcal{E}_{\text{def}} = \int_{A_{\text{tot}}} dS \left[2\kappa(H - c_0)^2 + \bar{\kappa}K + \sigma \right] , \tag{2.1}$$

which is an integral over the entire membrane surface area, A_{tot}. The membrane shape is described by the mean curvature, $H = (c_1 + c_2)/2$, and the Gaussian curvature, $K = c_1 c_2$; c_1 and c_2 are the principal curvatures of the membrane. The surface tension σ is the Lagrange multiplier conjugate to the excess area that is generated due to wrapping on the particle relative to the unwrapped flat membrane. Because we assume a symmetric lipid bilayer, we use $c_0 = 0$. The integral over the Gaussian curvature with the constant saddle splay modulus $\bar{\kappa}$ is determined by the topology of the membrane (and by the geodesic curvature at a boundary). In our case of an infinite planar membrane, the integral is a constant during the wrapping process. Thus, the total energy for a membrane-particle wrapping complex is

$$\mathcal{E}_{\text{tot}} = \int_{A_{\text{tot}}} dS \left[2\kappa H^2 + \sigma \right] - w \int_{A_{\text{ad}}} dS \, . \tag{2.2}$$

The contact interaction with adhesion strength w is proportional to the membrane area A_{ad} adhered to the particle, see Fig. 2.1.

Our continuum model in Eq. (2.2) is applicable for particle sizes that are larger than a few times the thickness of a lipid bilayer, which is about 5 nm. For particle sizes smaller than $\sqrt{\kappa/\sigma}$ both bending energy and surface tension contribute, for larger particle sizes surface tension is dominant [42]. A characteristic length scale for each system is the particle size a, typically $20 - 100$ nm and a characteristic energy

scale is the bending rigidity κ, typically $10 - 100\,k_{\mathrm{B}}T$. We therefore describe our system in terms of dimensionless parameters, which we choose to be consistent with those in Refs.[42,43]. This gives

$$\tilde{E} = \frac{1}{2\pi a^2}\left(\int_{A_{\mathrm{tot}}} dS\,\left[4(aH)^2 + 2\tilde{\sigma}\right] - \tilde{w}\int_{A_{\mathrm{ad}}} dS\right), \tag{2.3}$$

with the reduced energy $\tilde{E} = \mathcal{E}_{\mathrm{tot}}/(\pi\kappa)$, the reduced surface tension $\tilde{\sigma} = \sigma a^2/\kappa$, and the reduced adhesion strength $\tilde{w} = 2wa^2/\kappa$.

2.3.2 Energy minimization

There are three approaches to calculate the membrane deformation for particle wrapping[53]. (i) Solving the Euler-Lagrange equation: the Euler-Lagrange equation is obtained from Eq. (2.2) using variational calculus; it is a fourth-order partial non-linear differential equation[54] and a general solution does not exist. Exploiting symmetry and choosing an appropriate parametrization[52,55,56] , such as the arc-length parametrization proposed in Ref.[56], one obtains a set of second order non-linear ordinary differential equations. This method has been employed both for spherical particles in Refs.[41–43,46] and for infinite cylinders in Refs.[46,48]. In the weak-wrapping limit, the Monge parametrization and the approximation for almost planar membranes can be used[40–43]. (ii) Exploiting a variational approach: minimum energy shapes are found using appropriate functional parametrization, e. g. spherical harmonics[57], Cassini ovals[51], and Fourier functions[58]. The set of parameters obtained from energy minimization describes the membrane deformation. This method has been used for wrapping in Ref.[59] and can treat non-axisymmetric shapes as well. (iii) Using triangulated membranes: the method offers a high flexibility and has been used to study both minimal energy shapes[60,61] and systems at finite temperature[62–65]. The membrane is constructed by small triangles and discretized expressions for the deformation and interaction energies are used. Triangulated membranes provide a huge amount of freedom regarding the choice of shape and local properties of the membrane and has been used to study wrapping of single as well as multiple particles[49,50,65]. We employ "Surface Evolver"[60] for our calculations, a finite-element code for surfaces formed of vertices, edges and facets; the discretization of the bending energy is discussed in appendix 3.8.

2.3.3 Wrapping energy calculations

Deformation energies are calculated such that the membrane wraps the particle starting from the lowest curvature region progressively. Therefore, ellipsoidal particles are oriented with their major axis aligned parallel to a membrane patch that is enclosed by a circular wire frame of radius $20\,a$, see Fig. 2.2. This orientation is energetically favorable until about half wrapping compared with the perpendicular orientation. It ensures a maximum gain of adhesion energy and a minimal cost due to bending and surface tension contributions. We characterize the ellipsoids

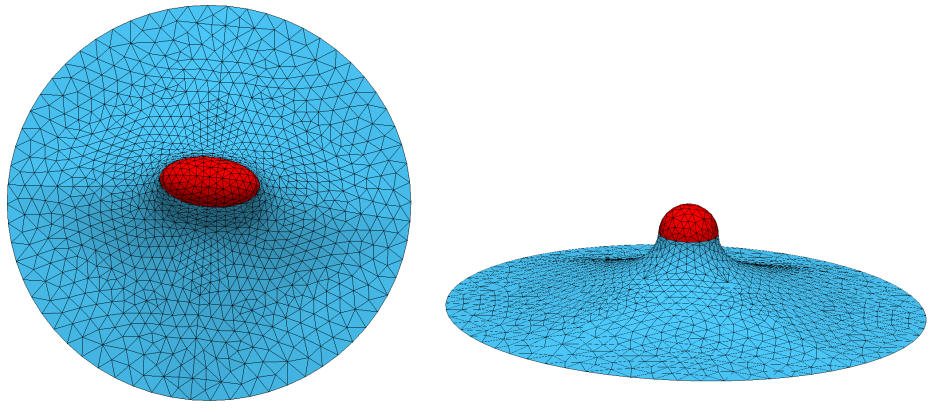

Figure 2.2: Membrane deformation for membrane-particle systems that have been discretized using triangulated surfaces.

by their polar radius a and their aspect ratio b/a. Prolate ellipsoids correspond to $b/a > 1$ and oblate ellipsoids correspond to $b/a < 1$.

From numerical calculations for ellipsoids with parallel orientation, we obtain the deformation energy as function of the fraction of the particle area that is wrapped, A_{ad}/A [3]. Snaphots of partially-wrapped particles with different wrapping fractions are shown in Figs. 2.3 (b), 2.4 (b), and 2.4 (d) [1]. The energy of the membrane relative to the unwrapped state is denoted by ΔE, which gives the wrapping energy cost $\Delta\tilde{E} = \Delta E/\pi\kappa$ in reduced units. To calculate small energy differences and derivatives with sufficient accuracy, this deformation energy profile is fit to the generalized logistic function,

$$f\left(\frac{A_{ad}}{A}\right) = c_1\left[\left(1+\exp\frac{c_2 - A_{\mathrm{ad}}/A}{c_3}\right)^{-1} - \left(1+\exp\frac{c_2}{c_3}\right)^{-1}\right], \tag{2.4}$$

with the fit parameters c_1, c_2, and c_3. This monotonic function describes the numerical data very well and vanishes for a completely detached particle, see Figs. 2.3 and 2.4. However, it cannot capture the partially-wrapped state encountered during the unwrapping transition at almost complete wrapping. This high wrapping fraction partially-wrapped state that has been found in Ref.[42] is a very shallow energy minimum, which we cannot identify in our numerical calculations. Further analysis is done using the fit function, in particular the wrapping energy at any

3) The wrapping fraction is defined as the ratio of the particle area adhered to the membrane, A_{ad}, to the total area of the particle, A. $A_{ad}/A = 0$ corresponds to the unwrapped state, while $A_{ad}/A \approx 1$ indicates a fully-wrapped state.

1) Unlike for prolate ellipsoids at a phase boundary dominated by interfacial tension[66], and although the boundary between the adhered and the free membrane is allowed to adjust freely in early stages of the energy minimization, we find an elliptical contact line in Fig. 2.4 (b) without significant variation in its height.

reduced adhesion strength is

$$\frac{\Delta E(A_{\rm ad}/A, w)}{\pi\kappa} = f\left(\frac{A_{\rm ad}}{A}\right) - \tilde{w}\frac{A_{\rm ad}}{A}\,. \tag{2.5}$$

Figs. 2.3 (a), 2.4 (a), and 2.4 (c) show energies as function of the wrapping fraction at reduced tension $\tilde{\sigma} = 1$ for wrapping of spherical, prolate, and oblate particles respectively. The open circles are the numerically calculated deformation energies that are fit by the solid line given by Eq. (2.4). The deformation energy thus increases monotonic with the wrapping fraction, the unwrapped state is stable. For finite adhesion strengths, the wrapping energies that are calculated using Eq. (2.5) are non-monotonic functions of the wrapping fraction, such that partially and fully-wrapped states can be the stable states.

2.4 Results

2.4.1 Wrapping energy

The numerical data for the deformation energy without any adhesion in Figs. 2.3 (a), 2.4 (a), and 2.4 (c) is fit by the function given in Eq. (2.4). For increased adhesion strength, the onset of wrapping occurs for the adhesion strength w_1 for that the bending-energy cost equals the adhesion-energy gain at the contact point, see appendix 2.5. For all adhesion strengths $w < w_1$ the stable state for the particle is the unwrapped state. Increasing the adhesion strength further, we find the envelopment transition from the partially-wrapped to the completely-wrapped state at adhesion strength w_2. For adhesion strengths $w_1 < w < w_2$, a global minimum of the wrapping energy is found for a small wrapping fraction, $0 < A_{\rm ad}/A \ll 1$. For adhesion strengths $w > w_2$, a stable completely-wrapped state is found. The line E, where the energy of the unwrapped state equals the energy of the completely-wrapped state is a good estimate for the binodal W_2.

Whereas there is a continuous transition from the unbound to the bound state, the envelopment transition between the partially-wrapped and completely-wrapped state is characterized by an energy barrier, $\Delta\tilde{E}_{\rm barrier}$. For $w_1 < w < w_2$, in addition to the stable partially-wrapped state at small wrapping fraction, a metastable completely-wrapped state is found; similarly at higher adhesion strengths, in addition to the completely wrapped state a metastable partially-wrapped state is found. Indicated by the spinodal S_{22} that is associated with W_2, the energy barrier between the metastable partially-wrapped state and the completely-wrapped state vanishes at an adhesion strength that is even larger than w_2. Starting from a completely-wrapped state and continuously decreasing the adhesion strength, below a threshold value w_1 a spontaneous transition between the completely-wrapped state and the unwrapped state is observed, which is in-

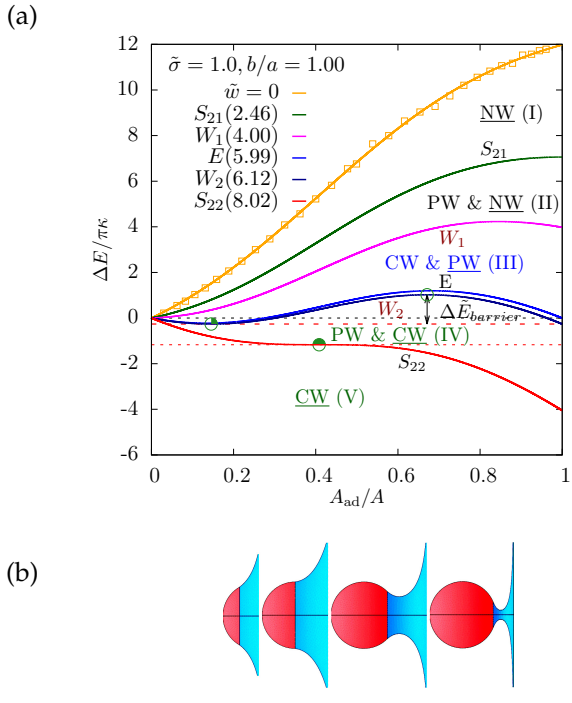

Figure 2.3: (a) Energies for wrapping a spherical particle as function of the wrapping fraction A_{ad}/A for reduced membrane tension $\tilde{\sigma} = 1$. The figure shows the wrapping energy profiles for six adhesion strengths: the numerically calculated data for zero adhesion strength and the corresponding fit function, E with equal energy for the non-wrapped and the completely-wrapped states ($\tilde{w} = 5.99$), the binding transition W_1 between the unwrapped and the partially-wrapped ($\tilde{w} = 4.00$), the binodal W_2 between the partially-wrapped and the completely-wrapped state ($\tilde{w} = 6.12$), and the spinodals S_{21} and S_{22} that are associated with W_2 (for $\tilde{w} = 2.46$ and $\tilde{w} = 8.02$ respectively). The phase boundaries separate 5 regimes in the phase diagram with stable and metastable completely wrapped (CW), partially-wrapped (PW), and and non-wrapped states (NW); the stable state is underlined. The wrapping fractions that are plotted in Fig. 2.5 are marked by circles and the energy barrier shown in Fig. 2.9 is indicated. (b) Sketches for spherical particles for wrapping fractions 0.25, 0.50, 0.85 and 0.96, with the adhered membrane in red and part of the free membrane in blue.

dicated by the second spinodal for W_2, S_{21} [4]. The system shows strong hysteresis, such that no partially wrapped state with small wrapping fraction is encountered during this unwrapping transition. The height of the energy barrier between the partially-wrapped and the completely-wrapped state, $\Delta\tilde{E}_{\mathrm{barrier}}$, can be characterized by barrier height for $w = w_2$, as indicated in Figs. 2.3 and 2.4. High energy barriers for ellipsoids with increased aspect ratio lead to an increased stability of the partially-wrapped state, compare section 2.4.3.

Special wrapping fractions are marked by points in Figs. 2.3 and 2.4, and are plotted in Fig. 2.5 as function of the surface tension for several aspect ratios. The wrapping fraction p_1 denotes the wrapping fraction for the stable partially-wrapped

4) Our numerical calculations and the fit function cannot capture a partially-wrapped at very high wrapping fraction, see Ref. [42]. Therefore the adhesion strength for that S_{21} occurs is obtained from the condition that the slope of the energy is zero at complete wrapping.

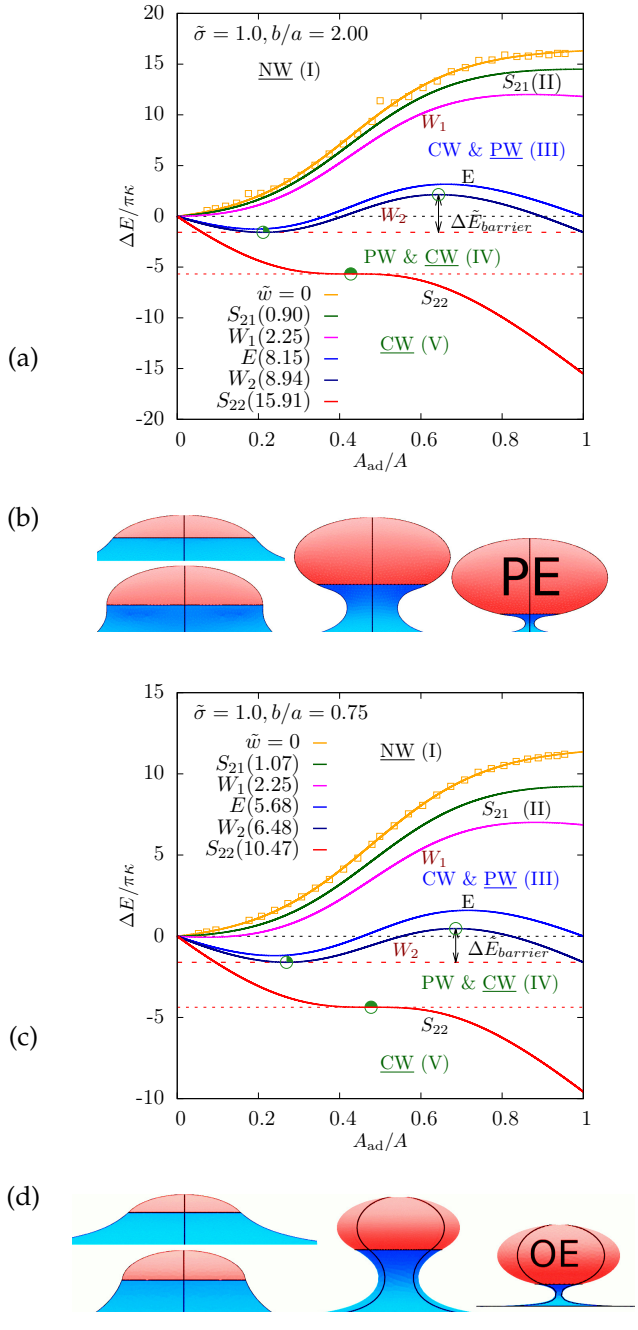

Figure 2.4: Wrapping energies for (a) a prolate ellipsoid (PE) with aspect ratio 2 and (c) an oblate ellipsoid (OE) with aspect ratio 0.75, analogous to Fig. 2.3 for a sphere. (b) and (d) Sketches for ellipsoids with wrapping fractions 0.30, 0.49, 0.84 and 0.95.

state, while p_2 is the wrapping fraction for the energy maximum, both for adhesion strength w_2. The saddle point of the energy, when the barrier between the

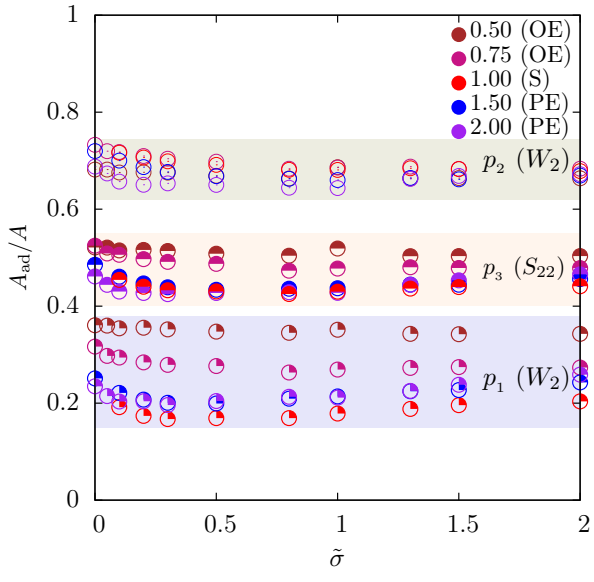

Figure 2.5: Wrapping fractions for special points marked on the wrapping-energy functions in Figs. 2.3 and 2.4 for several values of the reduced surface tension of the membrane and for several aspect ratios. At adhesion strength w_2, the partially-wrapped state is found at wrapping fraction p_1 and the energy maximum at wrapping fraction p_2; p_3 is the wrapping fraction for that the energy barrier between partially-wrapped and completely-wrapped state vanishes.

partially-wrapped and the completely-wrapped state vanishes on the spinodal S_{22}, occurs at wrapping fraction p_3. All wrapping fractions for special points depend only weakly on the surface tension, but decrease slightly with the increasing surface tension at small surface tensions.

When the partially-wrapped state has the same energy as the completely-wrapped state, the wrapping fractions for the partially-wrapped state are always well below 0.5. However, a strong dependence of the wrapping fraction on the particle shape is observed: whereas for prolate ellipsoids and spheres $p_1 \approx 0.2$, for oblate ellipsoids it increases strongly with decreasing aspect ratio. The maxima of the energy barriers are found for wrapping fractions between 0.6 and 0.7. For adhesion strengths $w > w_2$ the partially-wrapped state becomes metastable; in this regime, the wrapping fraction at which the metastable partially-wrapped state appears increases with increasing adhesion strength until it reaches the critical value p_3, which is found at approximately half wrapping.

2.4.2 Wrapping diagrams

For wrapping a spherical particle by a tension-less membrane, the only relevant energies that determine the uptake process are bending and adhesion energy for the adhered part. At every point of the sphere the bending energy is constant and the free membrane around the particle forms a catenoid-like deformation, i. e., a minimal surface with vanishing bending energy cost. Thus there exist only 2 pos-

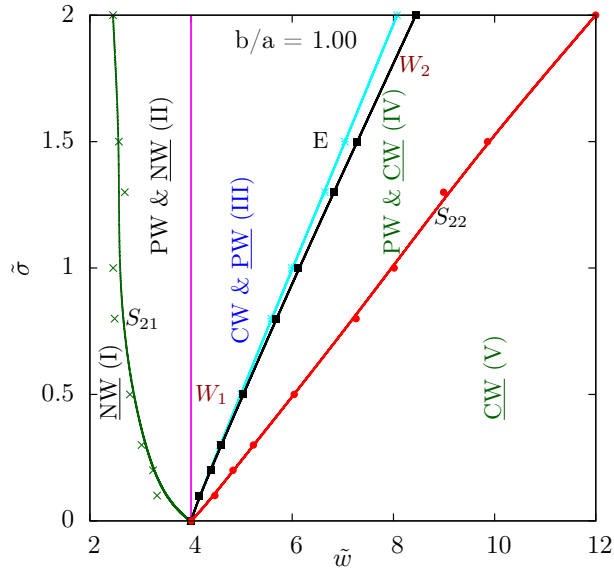

Figure 2.6: Wrapping states for spherical particles with reduced adhesion strength $\tilde{w}$ and reduced surface tension $\tilde{\sigma}$. Non-wrapped (NW), partially-wrapped (PW), and completely-wrapped (CW) states are found, stable and metastable states are indicated, stable states are underlined. The binodal W_1 separates a stable non-wrapped and a stable partially-wrapped state, the binodal W_2 separates a stable partially-wrapped and a stable completely-wrapped state. The two spinodals S_{21} and S_{22} belong to W_2. For all states on E, the unwrapped state has the same energy as the completely-wrapped state.

sible stable states, viz. a non-wrapped and a completely-wrapped state, that are separated by a continuous transition at $\tilde{w} = 4$. For a spherical particle and a finite membrane tension, also a stable partially-wrapped state is found, compare section 2.4.1. For ellipsoidal particles this partially-wrapped state exists both for finite and for vanishing surface tension.

In the wrapping diagrams for surface tension and adhesion strength in Figs. 2.6, 2.7, and 2.8, five regimes can be identified with different combinations of stable and metastable unwrapped, partially wrapped, and completely wrapped states. For small adhesion strengths, a stable non-wrapped state is found. In between the spinodal for the spontaneous transition between the completely-wrapped and the non-wrapped state S_{21}, and the binodal for the binding of the colloid to the membrane W_1, in addition to the stable non-wrapped state a metastable completely-wrapped state with high wrapping fraction appears [5]. The binding transition occurs at adhesion strength $\tilde{w}_1(PE) = \left[1 + (b/a)^{-2}\right]^2$ and $\tilde{w}_1(OE) = 4(b/a)^2$ for prolate and oblate ellipsoids respectively and is independent of the surface tension, see appendix 2.5 and Refs.[30,42,67]. Beyond the threshold adhesion strength for binding, a partially-wrapped state coexists with the metastable completely-wrapped state. For adhesion strengths beyond those for the binodal W_2, the completely-wrapped

5) It should be a partially-wrapped state at high wrapping fraction[42], but this cannot be described by the function in Eq. (2.4).

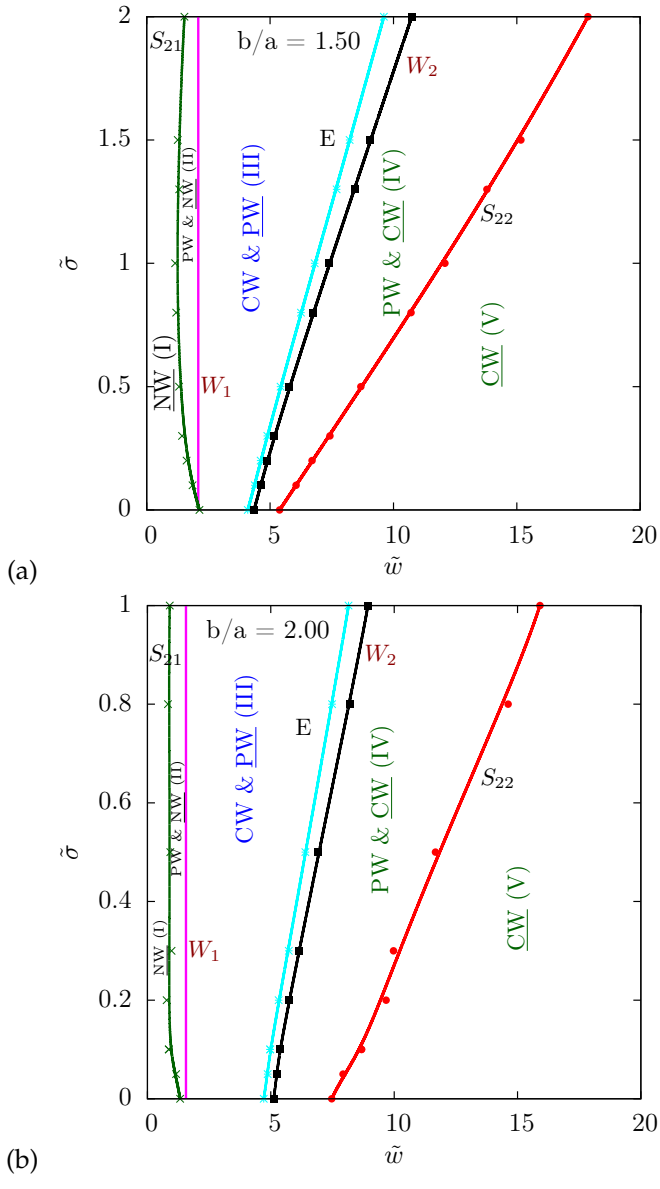

Figure 2.7: Wrapping states for prolate ellipsoidal particles with aspect ratios (a) 1.5 and (b) 2, plotted analogously to Fig. 2.6.

state becomes stable and the partially-wrapped state becomes metastable. Finally, beyond the spinodal S_{22}, the energy barrier between the completely-wrapped and the partially-wrapped state vanishes.

For spherical particles, all phase boundaries meet at a triple point for zero surface tension, see Fig. 2.6. However, as shown in Figs. 2.7 and 2.8 for ellipsoids, even for zero surface tension W_1 is shifted to smaller values of the adhesion strength compared with spherical particles, while the binodal W_2 is shifted to higher val-

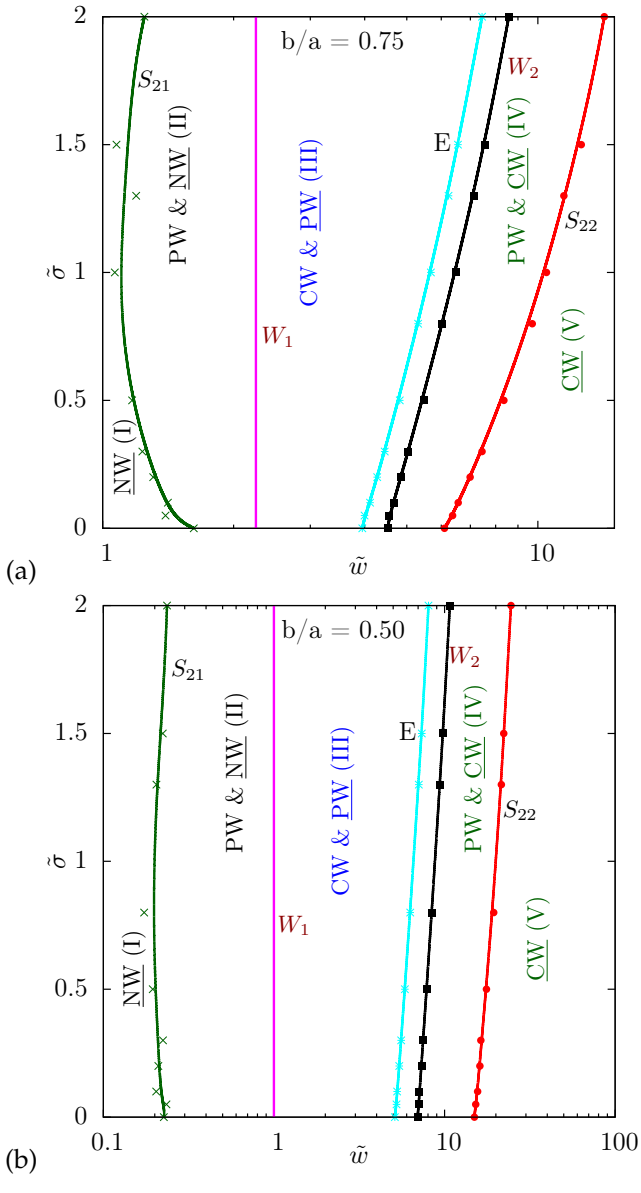

Figure 2.8: Wrapping states for oblate ellipsoidal particles with aspect ratios (a) 0.75 and (b) 0.5, plotted analogously to Fig. 2.6.

ues of the adhesion strength. For comparable aspect ratios, this effect is stronger for oblate ellipsoids than for prolate ellipsoids. This range of adhesion strengths, for which stable partially-wrapped states are found, increases both with the aspect ratio of the particle and the surface tension of the membrane. For increased aspect ratio it is easier to attach particles to the membrane, but at the same time it is more difficult to achieve completely-wrapped state. Binding occurs already for smaller adhesion strengths because of the reduced particle curvature at the point

of first contact, whereas complete wrapping requires higher energies because of the increased curvature of the particle at the tips. For high aspect ratios and rather 'flat' particles, the dependence of the binodal W_2 and both associated spinodals on the surface tension decreases.

2.4.3 Energy barrier

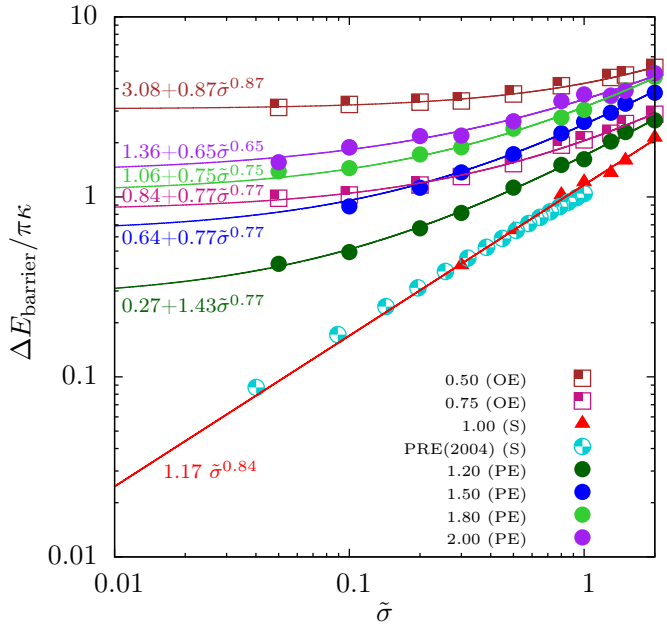

Figure 2.9: Energy barriers between partially-wrapped and completely wrapped state for the adhesion strength w_2 where partially and completely-wrapped state have equal energies. The barrier energies are plotted for several aspect ratios as function of the reduced surface tension $\tilde{\sigma}$ and fit by a function $\Delta\tilde{E}_{\mathrm{barrier}} = \tilde{E}_0 + \tilde{E}_1\tilde{\sigma}^{\nu}$. The values for the sphere are compared with those from Ref.[42].

In Figs. 2.3 and 2.4, the wrapping energy for adhesion strength w_2 shows a partially-wrapped state at a wrapping fraction p_1 that is separated by an energy barrier $\Delta\tilde{E}_{\mathrm{barrier}}$ from the completely-wrapped state. For $w > w_2$, the height of the barrier between a metastable partially-wrapped state and the completely-wrapped state determines the dynamics for the wrapping process. The activation energy that is needed for complete wrapping can be provided either by thermal kicks or by active forces from motor proteins. A comparison of the height of the energy barrier shown in Fig. 2.9 with the thermal energy $k_{\mathrm{B}}T$ therefore allows to estimate a characteristic time for the transition[13].

The energy barriers vary with the surface tension of the membrane and with particle shape. While for spherical particles the energy barrier vanishes for the tension-free case and can be fit by a power law[42], it levels off to finite values both for prolate and oblate ellipsoids. The energy barriers for ellipsoidal particles thus can be orders of magnitude higher than those for spherical particles. We fit the en-

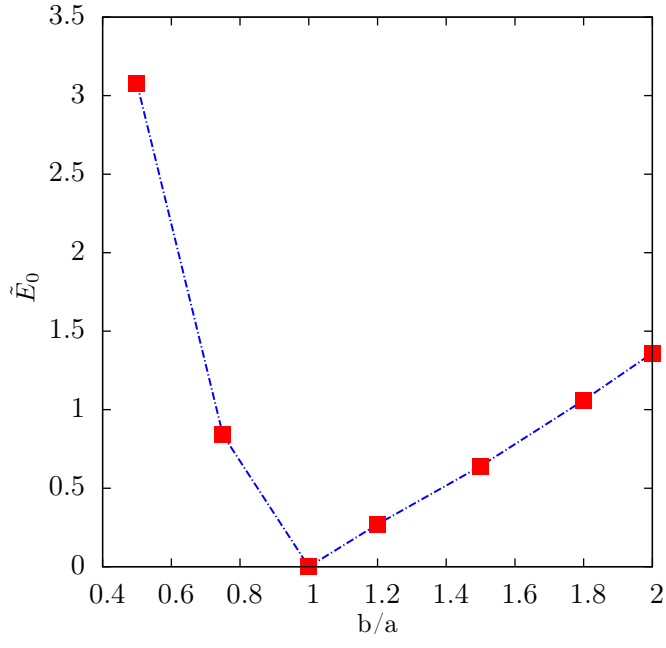

Figure 2.10: Energy barrier $\tilde{E}_0$ as a function of the aspect ratio b/a for vanishing surface tension. Oblate particles have b/a < 1 and prolate particles have b/a > 1.

ergy barriers as function of the wrapping fraction by $\Delta\tilde{E}_{\text{barrier}} = \tilde{E}_0 + \tilde{E}_1\tilde{\sigma}^{\nu}$. While the exponent ν is similar for all particles, the prefactors $\tilde{E}_0$ and $\tilde{E}_1$ strongly depend on the particle shape.

While in section 2.4.2 an extended parameter range for a partially-wrapped regime has been found for ellipsoidal particles compared with spherical particles, the energy barrier characterizes the stability of metastable partially-wrapped states. This can practically imply that partially-wrapped ellipsoidal particles are found in experiments even for adhesion strengths much higher than w_2, for that wrapping diagrams already predict a completely-wrapped particle. In Fig. 2.10, the energy barriers for vanishing surface tension are plotted as function of the aspect ratio of the particle. Only for $\tilde{E}_0 < k_{\text{B}}T/(\pi\kappa)$ the barrier height is comparable to thermal energy and complete wrapping is expected to occur at w_2. $\tilde{E}_0$ is of the order of 1 already for prolate ellipsoids with aspect ratio 1.5 thus corresponds to an energy barrier of about $\pi\kappa$. This implies that for particles whose shape considerably deviates from a sphere, adhesion strengths that are considerably higher than w_2 are required to wrap the particle and the partially-wrapped regime might extend almost up to the spinodal S_{22}.

2.4.4 Role of shape anisotropy

Stable non-wrapped, partially-wrapped and completely-wrapped regimes can be identified in Fig. 2.11, where the state of the system depends on membrane surface tension, particle aspect ratio, and adhesion strength. For spherical particles,

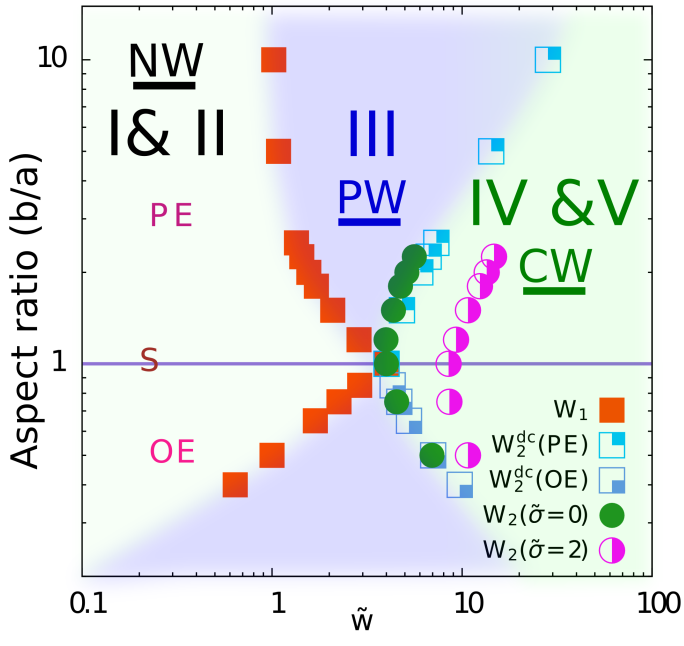

Figure 2.11: Stable wrapping states for different aspect ratios b/a, reduced adhesion strengths $\tilde{w}$, and for $\tilde{\sigma} = 0$ and for $\tilde{\sigma} = 2$. Prolate ellipsoids (PE) have aspect ratios $b/a > 1$, while for oblate ellipsoids (OE) have aspect ratios $b/a < 1$. Stable wrapping states are the non-wrapped state (NW), the partially-wrapped state (PW), and the completely-wrapped state (CW); the roman numbers correspond to those used in Figs. 2.6, 2.7, and 2.8. For blue open squares labeled with index dc, the deformed catenoid approximation has been used.

the transition from the non-wrapped to the completely-wrapped state occurs at the triple point for $\tilde{w} = 4$. For ellipsoids, the transition from the non-wrapped to the partially-wrapped state is found already for $w_1 < 4$, where $w_{1,\mathrm{PE}} \to 1$ for prolate ellipsoids with high aspect ratio and $w_{1,\mathrm{OE}} \to 0$ for disc-like oblate ellipsoids, compare Eqs. (2.12) and (2.13). The limiting cases for w_2 correspond to an infinite cylinder[40,48] and a flat disc[46,68] respectively. For the envelopment transition, we find an increased adhesion strength $\tilde{w}_2$ for the prolate and oblate ellipsoids with increasing asphericity; an additional shift towards higher adhesion strength is observed for finite surface tension.

Besides the numerical minimization technique to calculate w_2, we have used a deformed-catenoid approximation to estimate the wrapping energy that allows to estimate w_2 even for high aspect ratios such as 10. For a tensionless membrane, we numerically calculate the deformation energy for a wrapped ellipsoid by deforming a sphere with a catenoidal membrane patch, without any actual minimization. This method works well, because without surface tension the contribution of the deformation of the membrane patch around the particle is small. For oblate particles and bending-only, the membrane patch around the particle will assume a catenoid shape with vanishing bending energy and therefore does not have to be calculated.

As discussed in section 2.4.3, for $\tilde{w} > W_2$ the stable state is the completely-wrapped state (CW), but still the particles may be stuck in metastable partially-wrapped states unless there are sufficiently large fluctuations such that the energy barrier can be crossed, compare Fig. 2.9. Thus, for a given adhesion strength that is smaller than the one for the spinodal for spontaneous wrapping, we predict a considerably smaller amount of completely-wrapped particles the stronger the asphericity is.

2.5 Summary & conclusions

Complete wrapping a spherical particle using a tensionless free membrane occurs at reduced adhesion strength $\tilde{w} = 4$, directly from the unwrapped to the wrapped state without any energy barrier. For a membrane with surface tension the envelopment transition is shifted to higher adhesion strengths, while the binding transition remains at $\tilde{w} = 4$. The new partially-wrapped state is separated from the completely-wrapped state by an energy barrier. We find that a partially-wrapped state also exists for ellipsoidal particles, in a wider region of the phase diagram and with a higher energy barrier to the fully-wrapped state than for spherical particles. Therefore, the spherical shape facilitates complete wrapping for single particles; a biological example is the uptake and budding of almost spherical viruses[44,47].

In addition to a shift due to a membrane surface tension, for ellipsoidal particles the envelopment transition additionally shifts to higher adhesion strengths with increasing non-sphericity. The binding transition shifts to smaller adhesion strengths: for very long prolate ellipsoids $w_1 \to 1$ and for very flat oblate ellipsoids to $w_1 \to 0$. The partially-wrapped state is additionally stabilized by a higher energy barrier to the completely-wrapped state. Therefore, attachment of ellipsoidal particles to a membrane and partial wrapping is facilitated compared with spheres, while complete wrapping is hindered; typical wrapping fractions are $20 - 40\%$. Elongated viruses are found to form patterns on the membrane, see Ref.[25]. However, similar to curved inclusions the particles may bud cooperatively[9,12].

For typical lipid bilayer bending rigidities of $\kappa = 20\, k_B T$, the reduced energies $\tilde{E} \approx 1$ correspond to typical energies $E \approx 60\ k_B T$. Energy barriers at adhesion strengths where the energy of the partially-wrapped state equals the energy of the completely wrapped state can thus be of the order of $100\, k_B T$. Often the length scale for the particle in soft matter and biological system is of the order of hundred nanometer, therefore $\tilde{\sigma} = (a^2/\kappa)\sigma = 500\, \sigma\, \mathrm{nm}^2/k_B T$; a biologically relevant surface tension for the cell membrane, $\sigma = 0.003$ dyn/cm[69] corresponds to $\tilde{\sigma} \approx 1$ for a particle size $a = 100\,\mathrm{nm}$, to $\tilde{\sigma} \approx 0.25$ for a particle size $a = 50\,\mathrm{nm}$, and to $\tilde{\sigma} \approx 4$ for a particle size $a = 200\,\mathrm{nm}$. At a reduced tension $\tilde{\sigma} = 0.25$, the energy barrier to the completely wrapped state is an order of magnitude higher for prolate ellipsoids of aspect ratio 2 and oblate ellipsoids of aspect ratio 0.5 than for a spherical particle.

A typical adhesion strength can be estimated based on the binding strength of the HIV virus, $w \approx 0.1\, k_B T/\mathrm{nm}^2$[44]. The reduced adhesion strength is thus $\tilde{w} = 2(a^2/\kappa)w = 100$ for a particle with size $a = 100\,\mathrm{nm}$, $\tilde{w} \approx 25$ for $a = 50\,\mathrm{nm}$,

and to $\tilde{w} \approx 400$ for $a = 200\,\text{nm}$. All adhesion strengths are well in the region where wrapping occurs. However smaller adhesion strengths may occur for other viruses or smaller receptor densities in the membrane. An increased reduced tension hinders budding, but because $\tilde{\sigma}$ and $\tilde{w}$ both scale with the squared size of the particle, according to our calculations and previous wrapping calculations larger nano-particles are more likely to be wrapped completely. A lower limit for uptake is $\approx 20\,\text{nm}$, when the adhesion energy balances the bending energy[3,70–72]. However, there is also an upper limit given either by the length scale $\sqrt{\kappa/\sigma}$ where the wrapping becomes surface-tension dominated[42] or by receptor availability[70–72].

Our theoretical calculations predict an enhanced stability of partially-wrapped states for ellipsoidal particles. For cells, a lower uptake for ellipsoidal particles has been found experimentally[16,17,20], partially adhered ellipsoidal particles are also discussed in particular in Ref.[20], similarly disk-shaped particles show an increased adhesion to membrane and lower uptake[73,74]. Receptor-mediated wrapping of ellipsoidal particles has been studied in Ref.[75] with similar findings as in our work, but without surface tension of the membrane. The partially wrapped state can be of advantageous both from an application point of view as well as from a biological point of view: for example, elongated particles can be used as markers for imaging that stay in the cell membrane[27,28] and Ebola and Marburg viruses are not easily taken up by macrophages and may thus have a high virulence[3].

Appendix A: Triangulated membranes

Triangulated membranes are a powerful tool to study membranes and interfaces[5,8,60–65]. Using Surface Evolver[60], the membrane shape can be minimized with different schemes and the triangulation can be refined at any stage. In this appendix, we present the discretization that has been used to calculate the energy in Eq. (2.2). Surface tension and adhesion energies are proportional to the area of the membrane, they can be calculated basically as sum over all triangle areas. The bending energy is calculated, using the Surface Evolver method "star_perp_sq_mean_curvature", which assumes every vertex has incident triangles forming a star network around it, such that a_v is the average area associated locally with the vertex. The force acting on a vertex when the area changes thereby causing the vertex to move is given by the gradient of the area $(\boldsymbol{\nabla} a_v)$ associated with the vertex. For a smooth surface the gradient of the volume $(\boldsymbol{\nabla} \mathcal{V}_v)$ is equal to the magnitude of the area. But for a triangulated patch, the facets around the vertex tilt and thus the area is greater than the magnitude of the gradient of the volume. For a membrane patch, with a central vertex $\mathbf{v}$ and neighboring vertices $\mathbf{v}^1$, $\mathbf{v}^2$, $\mathbf{v}^3$, ... $\mathbf{v}^n$ a volume is given by

$$\mathcal{V}_v = \frac{1}{6}\mathbf{v} \cdot \left[\mathbf{v}^1 \times \mathbf{v}^2 + \mathbf{v}^2 \times \mathbf{v}^3 + ...\mathbf{v}^n \times \mathbf{v}^1\right] , \tag{2.6}$$

and the gradient of the volume is therefore

$$\boldsymbol{\nabla} \mathcal{V}_v = \frac{1}{6}\left[\mathbf{v}^1 \times \mathbf{v}^2 + \mathbf{v}^2 \times \mathbf{v}^3 + ...\mathbf{v}^n \times \mathbf{v}^1\right] . \tag{2.7}$$

The local mean curvature (h_v) at the vertex is

$$h_v = \frac{1}{2}\frac{\boldsymbol{\nabla} a_v \cdot \boldsymbol{\nabla} \mathcal{V}_v}{\boldsymbol{\nabla} \mathcal{V}_v \cdot \boldsymbol{\nabla} \mathcal{V}_v}\,. \tag{2.8}$$

Thus the discretized form of total squared mean curvature integral is given by,

$$\mathcal{E}_{\text{bend}} = 2\kappa \sum_{v=1}^{n} a_v h_v^2\,. \tag{2.9}$$

Once assembled, the surface can be minimized using different schemes, default being moving towards the direction of steepest descent of the energy linearly, while the mesh may be refined or smoothed at any stage. One may employ other minimization schemes like Hessian approach which calculates the energy of the surface configuration for a small perturbation and then uses the Hessian, a square matrix formed of the second derivatives of the energy which determines the best quadratic approximation of the energy to look for minimum energy states. Once converged to a minimum energy state, the surface may be analyzed for deformation profiles.

Appendix B: Binding transition (W_1)

The binding transition for particles to a membrane is determined by the mean curvature of the particle at the contact point and is independent of surface tension [42]. To calculate the binding transition for any particle shape, the Monge parametrization can be used, where the surface is described by a height field, $h(\boldsymbol{\rho})$, where $\boldsymbol{\rho} = (x, y)$ are the coordinates in the reference plane. For an almost planar membrane, a small-gradient approximation for the bending energy gives

$$\mathcal{E}_{\text{def}} = \int dA \frac{\kappa}{2} (\nabla^2 h(\boldsymbol{\rho}))^2\,, \tag{2.10}$$

with $\int dA$ the integral over the reference plane.

The critical adhesion strength at the binding transition marks the onset of adhesion, separating the unwrapped regime from the (partially) wrapped regime. Because it is completely determined by the competition between adhesion energy and bending energy, at the transition the mean curvature must equal the adhesion strength $\tilde{w}_1$,

$$\tilde{w}_1 = a^2 \left[\nabla^2 h(\boldsymbol{\rho} = 0)\right]^2\,, \tag{2.11}$$

for the contact point between membrane and particle at $\boldsymbol{\rho} = 0$. For spheres $\left[\nabla^2 h(\boldsymbol{\rho} = 0)\right]^2 = 4/a^2$, we find $\tilde{w}_1 = 4$, for prolate ellipsoids of aspect ratio b/a, such that the they are wrapped with their long axis parallel to the membrane,

$$\tilde{w}_1(\text{PE}) = \left[1 + \left(\frac{a}{b}\right)^2\right]^2\,, \tag{2.12}$$

and for oblate ellipsoids,

$$\tilde{w}_1(\text{OE}) = 4(b/a)^2\,. \tag{2.13}$$

Corrections: Chapter 2

The corrected eqn (5) is

$$\frac{\Delta E(A_{\mathrm{ad}}/A, \tilde{w})}{\pi\kappa} = f\left(\frac{A_{\mathrm{ad}}}{A}\right) - \frac{\tilde{w}A}{2\pi a^2}\frac{A_{\mathrm{ad}}}{A}\,. \tag{2.5}$$

In Fig. 4, 7, 8 and 11, the numerical values for the adhesion strengths of all phase boundaries except W_1 have to be multiplied by $4\pi a^2/A$. Corrected labels are $S_{21}(0.53)$, $E(4.76)$, $W_2(5.23)$ and $S_{22}(9.31)$ in Fig. 4 (a) and $S_{21}(1.28)$, $E(6.78)$, $W_2(7.73)$ and $S_{22}(12.49)$ in Fig. 4 (b). Corrected Figs. 7 , 8 and 11 are provided.

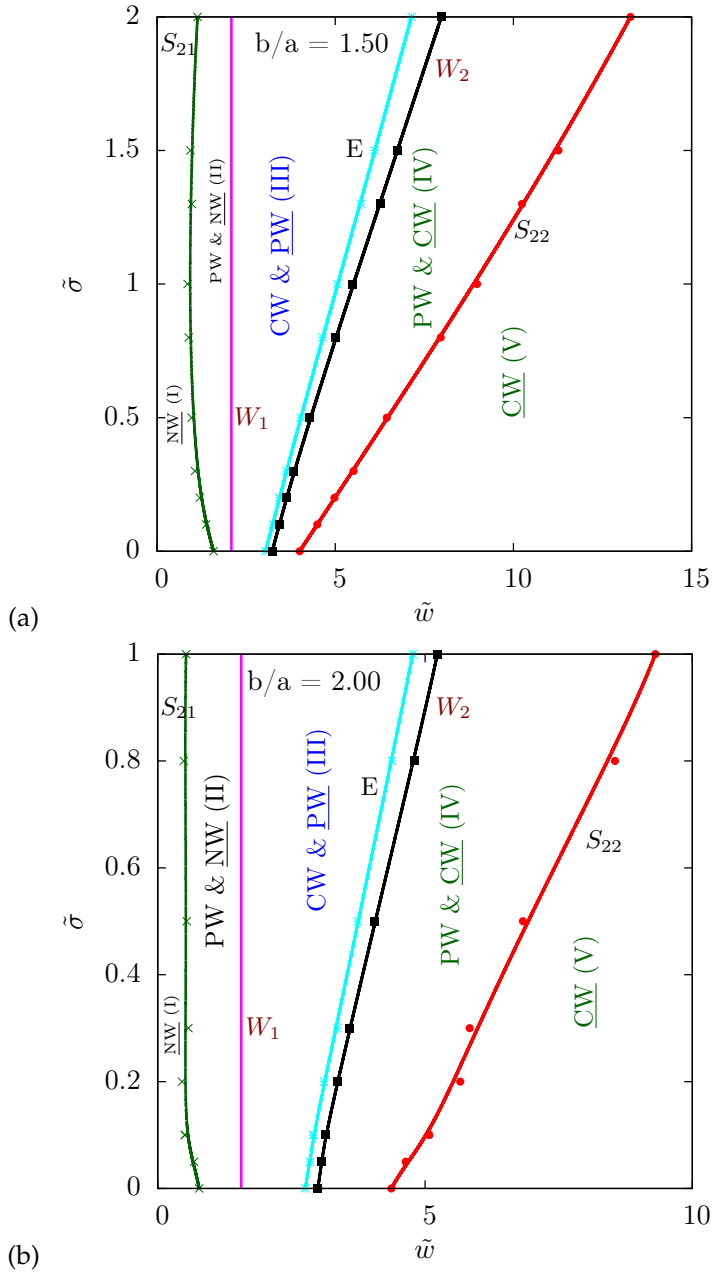

Figure 2.7: Wrapping states for prolate ellipsoidal particles with aspect ratios (a) 1.5 and (b) 2, plotted analogously to Fig. 6.

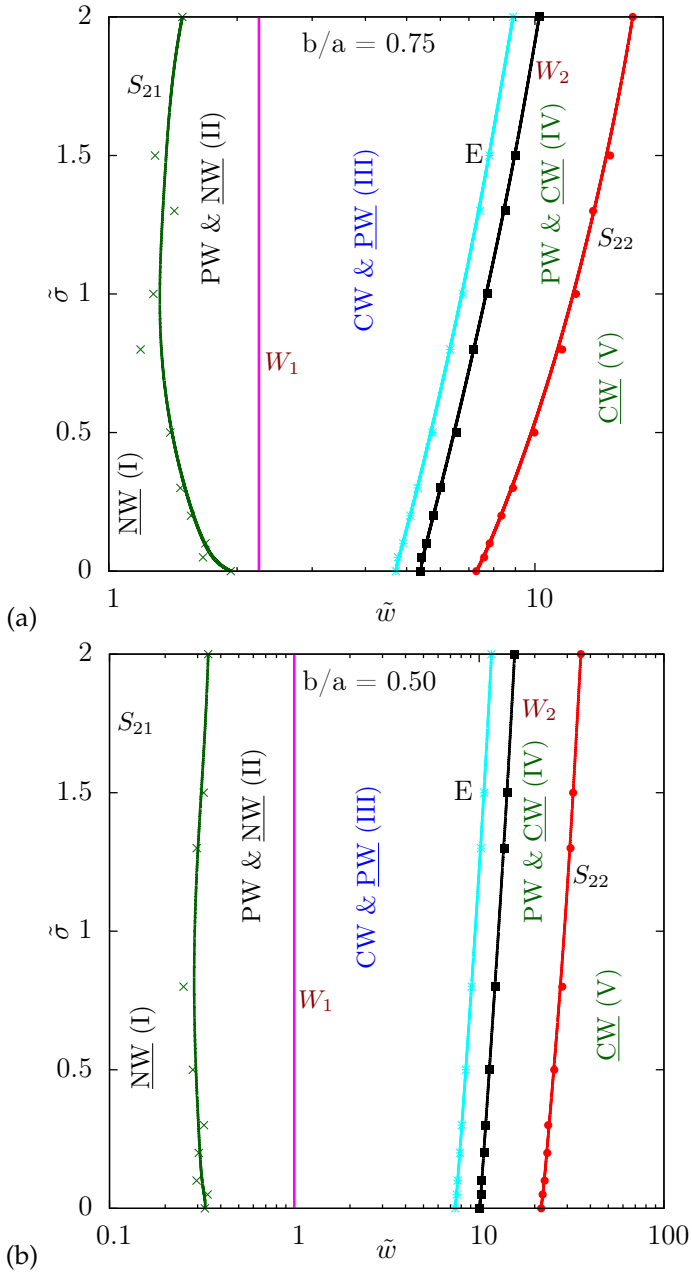

Figure 2.8: Wrapping states for oblate ellipsoidal particles with aspect ratios (a) 0.75 and (b) 0.5, plotted analogously to Fig. 6.

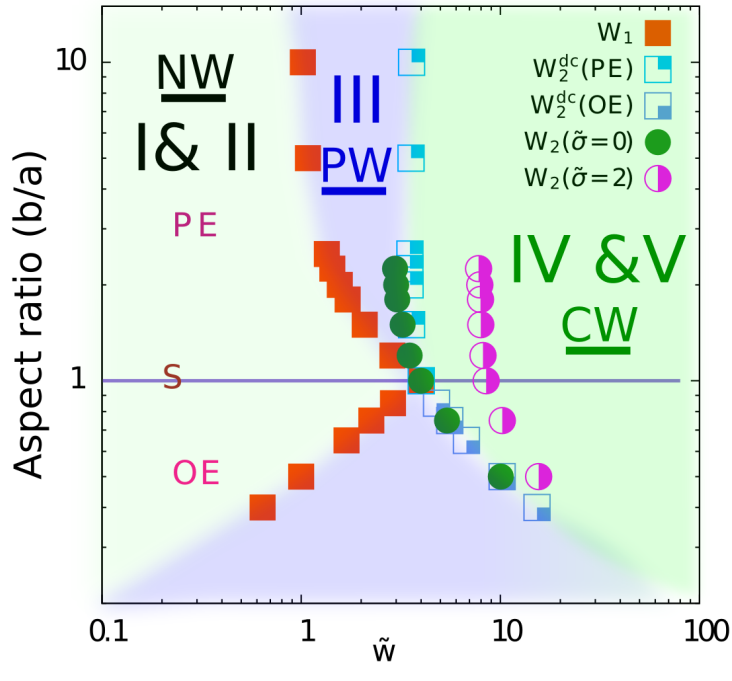

Figure 2.11: Stable wrapping states for different aspect ratios b/a, reduced adhesion strengths $\tilde{w}$, and for $\tilde{\sigma} = 0$ and for $\tilde{\sigma} = 2$. Prolate ellipsoids (PE) have aspect ratios $b/a > 1$, while for oblate ellipsoids (OE) have aspect ratios $b/a < 1$. Stable wrapping states are the non-wrapped state (NW), the partially-wrapped state (PW), and the completely-wrapped state (CW); the roman numbers correspond to those used in Figs. 6, 7, and 8. For blue open squares labeled with index dc, the deformed catenoid approximation has been used.

References: Chapter 2

1 H. T. McMahon and J. L. Gallop, *Nature*, 2005, **438**, 590–596.

2 J. H. Hurley, E. Boura, L.-A. Carlson and B. Różycki, *Cell*, 2010, **143**, 875–887.

3 I. Canton and G. Battaglia, *Chem. Soc. Rev.*, 2012, **41**, 2718–2739.

4 P. B. S. Kumar, G. Gompper and R. Lipowsky, *Phys. Rev. E*, 1999, **60**, 4610–4618.

5 P. B. Sunil Kumar, G. Gompper and R. Lipowsky, *Phys. Rev. Lett.*, 2001, **86**, 3911–3914.

6 T. Baumgart, S. T. Hess and W. W. Webb, *Nature*, 2003, **425**, 821–824.

7 S. Semrau, T. Idema, L. Holtzer, T. Schmidt and C. Storm, *Phys. Rev. Lett.*, 2008, **100**, 088101.

8 T. Kohyama, D. M. Kroll and G. Gompper, *Phys. Rev. E*, 2003, **68**, 061905.

9 B. J. Reynwar, G. Illya, V. A. Harmandaris, M. M. Mueller, K. Kremer and M. Deserno, *Nature*, 2007, **447**, 461–464.

10 W. Römer, L. Berland, V. Chambon, K. Gaus, B. Windschiegl, D. Tenza, M. R. E. Aly, V. Fraisier, J. C. Florent, D. Perrais and et al., *Nature*, 2007, **450**, 670–675.

11 P. Sens, L. Johannes and P. Bassereau, *Curr. Opin. Cell Biol.*, 2008, **20**, 476–482.

12 T. Auth and G. Gompper, *Phys. Rev. E.*, 2009, **80**, 031901.

13 R. Lipowsky, *J. Phys. II (France)*, 1992, **2**, 1825–1840.

14 R. Lipowsky, *Biophys. J.*, 1993, **64**, 1133–1138.

15 F. Jülicher and R. Lipowsky, *Phys. Rev. Lett.*, 1993, **70**, 2964–2967.

16 J. A. Champion and S. Mitragotri, *Proc. Natl. Acad. Sci. U.S.A.*, 2006, **103**, 4930–4934.

17 B. D. Chithrani, A. A. Ghazani and W. C. W. Chan, *Nano Lett.*, 2006, **6**, 662–668.

18 P. Decuzzi, R. Pasqualini, W. Arap and M. Ferrari, *Pharm. Res.*, 2009, **26**, 235–243.

19 J. P. Best, Y. Yan and F. Caruso, *Adv. Healthcare Mater.*, 2012, **1**, 35–47.

20 L. Florez, C. Herrmann, J. M. Cramer, C. P. Hauser, K. Koynov, K. Landfester, D. Crespy and V. Mailänder, *Small*, 2012, **8**, 2222–2230.

21 S. Tzlil, M. Deserno, W. M. Gelbart and A. Ben-Shaul, *Biophys. J.*, 2004, **86**, 2037–2048.

22 J. Mercer, M. Schelhaas and A. Helenius, *Annu. Rev. Biochem.*, 2010, **79**, 803–833.

23 S. E. A. Gratton, P. A. Ropp, P. D. Pohlhaus, J. C. Luft, V. J. Madden, M. E. Napier and J. M. DeSimone, *Proc. Natl. Acad. Sci. U.S.A.*, 2008, **105**, 11613–11618.

24 S. Barua, J.-W. Yoo, P. Kolhar, A. Wakankar, Y. R. Gokarn and S. Mitragotri, *Proc. Natl. Acad. Sci. U.S.A.*, 2013, **110**, 3270–3275.

25 K. Kubo, J. Freitas-Astúa, M. Machado and E. Kitajima, *J. Gen. Plant Pathol.*, 2009, **75**, 250–255.

26 Y. Liu, J. Tan, A. Thomas, D. Ou-Yang and V. Muzykantov, *Ther. Delivery*, 2012, **3**, 181–194.

27 D. Pissuwan, S. Valenzuela and M. B. Cortie, *Biotechnol. Genet. Eng. Rev.*, 2008, **25**, 93–112.

28 L. Xu, H. Kuang, L. Wang and C. Xu, *J. Mater. Chem.*, 2011, **21**, 16759.

29 C. Dietrich, M. Angelova and B. Pouligny, *J. Phys. II (France)*, 1997, **7**, 1651–1682.

30 R. Lipowsky and H. G. Döbereiner, *Europhys. Lett.*, 1998, **43**, 219–225.

31 S. Zhang, A. Nelson and P. A. Beales, *Langmuir*, 2012, **28**, 12831–7.

32 H. Noguchi and M. Takasu, *Biophys. J.*, 2002, **83**, 299–308.

33 Q. Zhang and Y. Ma, *J. Chem. Phys.*, 2006, **125**, 164710.

34 K. Yang and Y. Q. Ma, *Nat. Nanotechnol.*, 2010, **5**, 579–583.

35 S. Pogodin and V. A. Baulin, *ACS Nano*, 2010, **4**, 5293–5300.

36 J. Lin, H. Zhang, Z. Chen and Y. Zheng, *ACS Nano*, 2010, **4**, 5421–5429.

37 R. Vácha, F. J. Martinez Veracoechea and D. Frenkel, *Nano Lett.*, 2011, **11**, 5391–5.

38 J. U. Sommer, M. Werner and V. A. Baulin, *Europhys. Lett.*, 2012, **98**, 18003.

39 M. Deserno and W. Gelbart, *J. Phys. Chem. B*, 2002, **106**, 5543–5552.

40 T. R. Weikl, *Eur. Phys. J. E*, 2003, **12**, 9.

41 M. Deserno and T. Bickel, *Europhys. Lett.*, 2003, **62**, 767–774.

42 M. Deserno, *Phys. Rev. E.*, 2003, **69**, 031903.

43 M. Deserno, *J. Phys.: Condens. Matter*, 2004, **16**, S2061—-S2070.

44 S. X. Sun and D. Wirtz, *Biophys. J.*, 2006, **90**, L10–2.

45 J. Benoit and A. Saxena, *Phys. Rev. E*, 2007, **76**, 041912.

46 S. A. Nowak and T. Chou, *Phys. Rev. E.*, 2008, **78**, 021908.

47 R. Zhang and T. T. Nguyen, *Phys. Rev. E*, 2008, **78**, 051903.

48 S. Mkrtchyan, C. Ing and J. Z. Y. Chen, *Phys. Rev. E*, 2010, **81**, 1–9.

49 A. H. Bahrami, R. Lipowsky and T. R. Weikl, *Phys. Rev. Lett.*, 2012, **109**, 188102.

50 A. Šarić and A. Cacciuto, *Phys. Rev. Lett.*, 2012, **109**, 188101.

51 P. Canham, *J. Theor. Biol.*, 1970, **26**, 61 – 81.

52 W. Helfrich, *Z. Naturforsch. C*, 1973, **28**, 693–703.

53 M. I. Bloor and M. J. Wilson, *Phys. Rev. E*, 2000, **61**, 4218–4229.

54 O.-Y. Zhong-can and W. Helfrich, *Phys. Rev. A*, 1989, **39**, 5280–5288.

55 U. Seifert, K. Berndl and R. Lipowsky, *Phys. Rev. A*, 1991, **44**, 1182–1202.

56 F. Jülicher and R. Lipowsky, *Phys. Rev. E*, 1996, **53**, 2670–2683.

57 K. Khairy and J. Howard, *Soft Matter*, 2011, **7**, 2138.

58 W. Góźdź and G. Gompper, *Europhys. Lett.)*, 2001, **55**, 587.

59 W. T. Góźdź, *Langmuir*, 2007, **23**, 5665–5669.

60 K. A. Brakke, *Exp. Math.*, 1992, **1**, 141–165.

61 W. Wintz, H. G. Döbereiner and U. Seifert, *Europhys. Lett.*, 1996, **33**, 403–408.

62 *G. Gompper and D. M. Kroll: in Statistical Mechanics of Membranes and Surfaces, ed. D. R. Nelson, T. Piran, and S. Weinberg (World Scientific, Singapore, 2004) 2nd ed.*

63 D. M. Kroll and G. Gompper, *Science*, 1992, **255**, 968–971.

64 G. Gompper and D. M. Kroll, *J. Phys.: Condens. Matter*, 1997, **9**, 8795.

65 M. Fošnarič, A. Iglič, D. M. Kroll and S. May, *J. Chem. Phys.*, 2009, **131**, 105103.

66 H. Lehle, E. Noruzifar and M. Oettel, *Eur. Phys. J. E*, 2008, **26**, 151–160.

67 U. Seifert and R. Lipowsky, *Phys. Rev. A*, 1990, **42**, 4768.

68 X. Yi, X. Shi and H. Gao, *Phys. Rev. Lett.*, 2011, **107**, 1–5.

69 C. E. Morris and U. Homann, *J. Membr. Biol.*, 2001, **179**, 79–102.

70 S. Zhang, J. Li, G. Lykotrafitis, G. Bao and S. Suresh, *Adv. mater.*, 2009, **21**, 419–424.

71 H. Gao, W. Shi and L. B. Freund, *Proc. Natl. Acad. Sci. U.S.A.*, 2005, **102**, 9469–9474.

72 A. Chaudhuri, G. Battaglia and R. Golestanian, *Phys. Biol.*, 2011, **8**, 9.

73 G. Adriani, M. D. De Tullio, M. Ferrari, F. Hussain, G. Pascazio, X. Liu and P. Decuzzi, *Biomaterials*, 2012, **33**, 5504–13.

74 Y. Zhang, S. Tekobo, Y. Tu, Q. Zhou, X. Jin, S. A. Dergunov, E. Pinkhassik and B. Yan, *ACS Appl. Mater. Interfaces*, 2012, 4099–4105.

75 P. Decuzzi and M. Ferrari, *Biophys. J.*, 2008, **94**, 3790–3797.

3
Shape and Orientation Matter for the Cellular Uptake of Non-spherical Particles

3.1
Abstract

Recent advances in nanotechnology have made a whole zoo of particles of different shapes available for applications, but their interaction with biological cells and their toxicity is often not well understood. Experiments have shown that particle uptake by cells is determined by an intricate interplay between physicochemical particle properties like shape, size, and surface functionalization, but also by membrane properties and particle orientation. Our work provides systematic understanding, based on a mechanical description, for membrane wrapping of nanoparticles, viruses, and bacterial forms. For rod-like particles, we find stable endocytotic states with small and high wrapping fraction; an increased aspect ratio is unfavorable for complete wrapping. For high aspect ratios and round tips, the particles enter via a submarine-mode, side-first with their long edge parallel to the membrane. For small aspect ratios and flat tips, the particles enter tip-first via a rocket-mode.

3.2
Introduction

Transport within a biological cell and exchange of material across its membrane are basic processes that the cell uses to interact with its environment. Depending on size, shape, and surface properties, nanoparticles and micro-organisms can cross a cellular membrane either by penetration[1–3] or wrapping. For example, filo-viruses[4,5] and also brick-shaped intracellular mature virions[6] of the family Poxviridae (fowl-pox and pigeon-pox) get wrapped by the host plasma membrane. In particular, the Ebola[4,5] and the Marburg virus[5] are of much interest due to their enhanced virulence leading to high mortality rates. Their prolonged blood circulation time has inspired development of tubular filamentous vehicles[7] as potential drug-delivery agents for treating cancer. While wrapping of spherical particles has been studied in great detail[8–11], there is no systematic study and understanding for the wrapping of non-spherical particles[12–17].

Elongated viruses[4–6], such as Ebola, Marburg, and pox viruses, as well as the bullet-shaped Rhabdoviruses[18,19], exhibit competition between a submarine and

a rocket mode for cell entry via membrane wrapping. In submarine mode, the long axis of the particle is oriented parallel to the membrane and in rocket mode, it is oriented perpendicular to the membrane. Similar modes for uptake have been reported for rod-like nanoparticles[15–17,20] and multi-wall carbon nanotubes[21]. The aspect ratio is an important parameter to characterize the shape of elongated particles. Experimentally, a high aspect ratio has been found to suppress uptake compared to spherical particles of similar size[15,16]. More recently, uptake experiments with cube-like particles have been performed[17,22], but there is no systematic study for different sizes available so far. However, experiments and molecular dynamics simulations that show a role of shape[23–26], aspect ratio[15–17,20], and orientation[1,27–30] stress the importance of these geometric parameters for cellular uptake and toxicity studies.

Physically, nanoparticle attachment and wrapping is controlled by the competition between the adhesion-energy gain for contact between a nanoparticle and a membrane and the deformation-energy cost for the lipid bilayer. Attachment (binding) occurs when the adhesion strength is large enough to compensate the local bending-energy cost at the surface point of smallest curvature. This binding transition is predicted to be continuous (without an energy barrier)[11,31]. For higher values of the adhesion strength between particle and membrane, a discontinuous transition (with an energy barrier) occurs either between two frustrated endocytotic, partially-wrapped states or between a partially-wrapped and the completely-wrapped state. Only in the case of spherical particles and for a vanishing membrane tension the entire wrapping process is continuous. Special cases of wrapping of non-spherical nanoparticles have been addressed theoretically, such as the enhanced stability of partially-wrapped states for soft[32] and ellipsoidal[31] nanoparticles, the reorientation of ellipsoidal[33] and spherocylindrical[27,34] nanoparticles during uptake, and the perpendicular entry of cylindrical nanoparticles[27]. Many of these studies have been performed by molecular dynamics simulations.

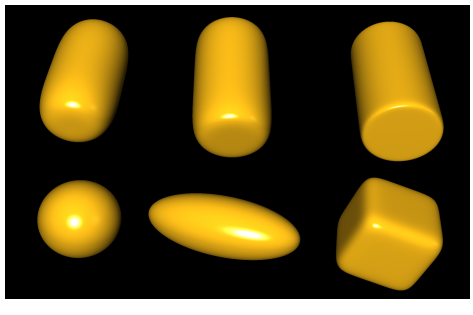

Figure 3.1: Shapes of non-spherical nanoparticles. Top row: rod-like particles of aspect ratio 2 with blunt tips and increasing edge curvature, defined by $[(x^2+y^2)/a^2]^{(n/2)}+(z/b)^n=1$ with $n=4$, $n=6$, and $n=20$. Bottom row: sphere, ellipsoid, Hauser's cube. We characterize the particles by their size a, which is the radius of the sphere, the half edge-length of the cube, and the short axis of the ellipsoidal and rod-like particles.

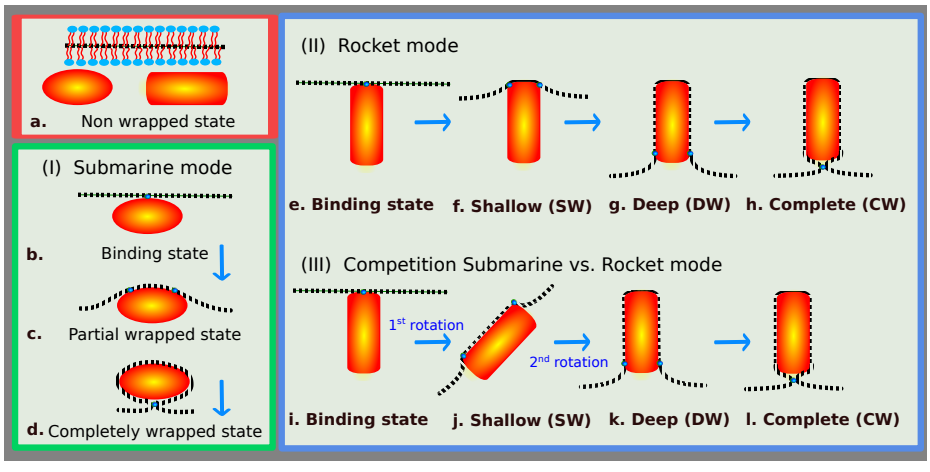

Figure 3.2: Modes of entry for nanoparticle uptake by membrane wrapping: (I) Submarine mode with the long axis of the particles oriented parallel to the membrane, (II) rocket mode with the long axis oriented perpendicular to the membrane, and (III) competition between submarine and rocket mode as observed for rod-like particles with high aspect ratios. The complete-wrapped particle is connected by an infinitely small catenoidal neck to the membrane, the particle orientation in this state is irrelevant.

In our work, we systematically investigate the role of nanoparticle shape (Fig. 3.1) and size, as well as membrane bending rigidity and tension, on membrane wrapping and cellular uptake. We predict phase diagrams for two classes of nanoparticles, nanorods and nanocubes, with varying aspect ratio and edge curvature. Possible modes of entry for elongated particles are shown in Fig. 3.2. Our phase diagrams for nanorods show a qualitatively different wrapping behavior compared to nanospheres and nanoellipsoids. In particular, we find two distinct partial-wrapped states, with shallow and deep wrapping. We show that global parameters like particle size and aspect ratio alone are by far not sufficient to determine particle endocytosis. Instead, local geometrical properties, such as the extrema of the local mean curvature, matter and change the wrapping behavior qualitatively.

All our calculations are based on the curvature energy[35] of lipid-bilayer membranes combined with a contact adhesion energy for the particle-membrane interaction. Thus, the total energy is

$$\mathcal{E}_{\text{tot}} = \int_S dS \left[H^2 + \sigma\right] - w \int_{S_{\text{ad}}} dS\,, \tag{3.1}$$

where S is the entire membrane area, S_{ad} the adhered membrane area, H the mean membrane curvature, κ the bending rigidity, σ the membrane tension, and w the adhesion strength for the interaction between membrane and nanoparticle. We use triangulated membranes and Surface Evolver to minimize the membrane deformation energies[36,37].

We model cube-like particles as Hauser's cube using $x^6 + y^6 + z^6 = a^6$, and rod-like particles using $[(x^2 + y^2)/a^2]^{(n/2)} + (z/b)^n = 1$ as regular ellipsoids with

$n = 2$ and as supereggs with $n \geq 4$. We consider nanorods with aspect ratios $1 \leq b/a \leq 3$, and $n = 4$ as well as $n = 6$; high values of n correspond to very flat tips, such that the shape becomes cylinder-like. We describe our system using a characteristic length scale, such as the particle size a (Fig. 3.1), typically $20 - 100\,\mathrm{nm}$ and a characteristic energy scale, such as the bilayer bending rigidity κ, typically $10 - 100\,\mathrm{k_BT}$. We then define dimensionless parameters, like the reduced deformation energy $\tilde{E} = \mathcal{E}_{\mathrm{tot}}/(\pi\kappa)$, the reduced membrane tension $\tilde{\sigma} = \sigma a^2/\kappa$, and the reduced adhesion strength $\tilde{w} = wA/2\pi\kappa$, where A is the particle surface area. Using these parameters for the axes of our phase diagrams, our predictions apply for arbitrary particle sizes.

All our calculations are based on the curvature energy[35] of lipid-bilayer membranes combined with a contact adhesion energy for the particle-membrane interaction. Thus, the total energy is

$$\mathcal{E}_{\mathrm{tot}} = \int_S dS \left[H^2 + \sigma\right] - w \int_{S_{\mathrm{ad}}} dS\,, \tag{3.2}$$

where S is the entire membrane area, S_{ad} the adhered membrane area, H the mean membrane curvature, κ the bending rigidity, σ the membrane tension, and w the adhesion strength for the interaction between membrane and nanoparticle. We use triangulated membranes and Surface Evolver to minimize the membrane deformation energies[36,37].

We model cube-like particles as Hauser's cube using $x^6 + y^6 + z^6 = a^6$, and rod-like particles using $[(x^2 + y^2)/a^2]^{(n/2)} + (z/b)^n = 1$ as regular ellipsoids with $n = 2$ and as supereggs with $n \geq 4$. We consider nanorods with aspect ratios $1 \leq b/a \leq 3$, and $n = 4$ as well as $n = 6$; high values of n correspond to very flat tips, such that the shape becomes cylinder-like. We describe our system using a characteristic length scale, such as the particle size a (Fig. 3.1), typically $20 - 100\,\mathrm{nm}$ and a characteristic energy scale, such as the bilayer bending rigidity κ, typically $10 - 100\,\mathrm{k_BT}$. We then define dimensionless parameters, like the reduced deformation energy $\tilde{E} = \mathcal{E}_{\mathrm{tot}}/(\pi\kappa)$, the reduced membrane tension $\tilde{\sigma} = \sigma a^2/\kappa$, and the reduced adhesion strength $\tilde{w} = wA/2\pi\kappa$, where A is the particle surface area. Using these parameters for the axes of our phase diagrams, our predictions apply for arbitrary particle sizes.

3.3 Ellipsoidal nanoparticles

We first consider uptake of ellipsoidal nanoparticles. Recent experimental[14,38] and theoretical[31] work shows enhanced binding, but lower uptake compared with spherical particles. For these particles, an extended region of the phase diagram exists with stable, frustrated endocytotic states at low wrapping fractions for which the long axis is oriented parallel to the membrane (Fig. 3.2(c)). A reorientation from parallel to perpendicular upon increased wrapping has been suggested recently[33]. We have determined phase diagrams for this system (see supplementary material), and confirm the presence of a perpendicular state at high wrapping fraction. In addition, we predict the complete-wrapping transition to be continuous. Surprisingly,

our results show that after reorientation from parallel to perpendicular, the adhesion strength required for complete wrapping is well above the adhesion strength required without reorientation. Reorientation thus leads to unfavorable, arrested endocytotic states (analogously to Fig. 3.2(g)), because wrapping the highly curved tip of the ellipsoid requires a high bending energy cost per area. Thus, a suppression of reorientation, as it might occur for fast wrapping, facilitates particle uptake.

3.4 Cube-like nanoparticles

The wrapping of cube-like and rod-like particles compared to the wrapping of spheres and ellipsoids is qualitatively different. For nanocubes, the binding occurs for almost vanishing adhesion strength with a 'flat' side oriented towards the membrane (Fig. 3.4(a)), because it requires hardly any membrane deformation. The bound state corresponds to the shallow-wrapped state (SW) in Fig. 3.4(b) that is separated by an energy barrier from the deep-wrapped state (DW). The transition from the deep-wrapped to the complete-wrapped state (CW) is also discontinuous, which further stabilizes the partially-wrapped states. The existence of shallow- and deep-wrapped states is a consequence of the inhomogeneous curvature distribution on the nanoparticle surface. The adhesion strength has to exceed a threshold for the adhesion energy of the lateral sides of the cube to compensate the deformation energy at the upper edges of the cube in Fig. 3.4(a). The deformation energy at the lower edges is even higher, because the membrane now has to nearly double back on itself, so that complete wrapping requires an even larger w. Note that a discontinuous transition between the DW and CW states does not exist for ellipsoids, because the curvature maxima are point-like (see supplementary material). The dependence of the phase boundaries on particle size a is taken into account by our dimensionless variables. The values of adhesion strength w and membrane tension σ for the phase transitions scale directly with the particle surface area A and inversely with the membrane bending modulus κ.

Figure 3.4(c) shows the phase diagram for wrapping of a nanocube. Because of the flat sides, the shallow-wrapped region starts for infinitesimal adhesion strength w. However, the translational and orientational entropy of the cube in the unbound state competes with the energy gain for adhesion. Adhesion therefore occurs only if $wa^2 \gtrsim k_B T$. In terms of the phase diagram, the unbound region due to entropy is a very small stripe for small adhesion strength of width $k_B T/\kappa$ (not shown). Deep wrapping occurs for an adhesion strength that is about twice the adhesion strength for complete wrapping of a sphere with equal surface area, $w_{sph} = 2\kappa/a^2$. Complete wrapping is found for an adhesion strength about three times higher than for a sphere. With increased membrane tension, both transitions from the shallow- to the deep-wrapped state (W_2) and from the deep-wrapped to the complete-wrapped state (W_3) shift to higher adhesion strengths.

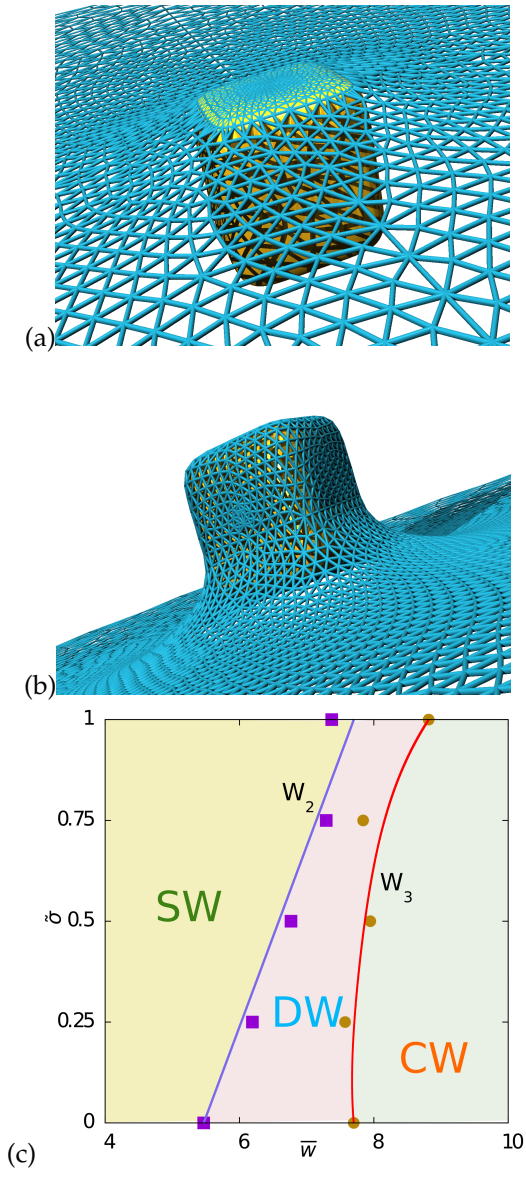

Figure 3.3: (a), (b): Membrane deformation for wrapping of Hauser's cube. The network of edges and triangles describes the membrane shape and is used for the numerical calculation of the curvature energy. Membrane conformations are shown at fixed tension $\tilde{\sigma} = 0.50$ for two corresponding states at the W_2 phase boundary: (a) a shallow-wrapped state with approximately 10% of particle wrapped, and (b) a deep-wrapped state with a wrapping fraction of approximately 80%. (c): Phase diagram for wrapping of Hauser's cube for membrane tension $\tilde{\sigma}$ and adhesion strength $\bar{w}$; the parameters are given in dimensionless form. We find a shallow-wrapped (SW), a deep-wrapped (DW), and a complete-wrapped (CW) state, separated by two discontinuous wrapping transitions, W_2 and W_3.

3.5 Rod-like nanoparticles

Next, we consider rod-like particles with blunt tips and different edge curvatures, characterized by the parameter n and the aspect ratio, see Fig. 3.1. Phase diagrams are shown in Fig. 2. At negligible membrane tension, the transition W_2 between shallow-wrapped and deep-wrapped states corresponds to adhesion strengths that are comparable with those required for complete wrapping of spherical particles; the transition shifts to higher adhesion strengths with increasing membrane tension. The envelopment transition W_3 is largely independent of the membrane tension, because the change in wrapped area between deep-wrapped and complete-wrapped state is small. Both increased aspect ratio and sharper edges suppress uptake, as can be seen in the phase diagrams of Fig. 2 by the shift of the W_3 transition to higher adhesion strengths, $\tilde{w}$. The parameter region for the deep-wrapped state widens with increasing aspect ratio, because the transition from the shallow-wrapped to the deep-wrapped state remains almost unaltered. This is due to the competition between the larger adhesion energy gain at the sides of the particles for higher aspect ratios and the increasing edge curvature (for fixed particle area).

Rod-like particles first bind with the long axis perpendicularly to the membrane (Fig. 3.2(e))[30], because adhesion at the blunt tips minimizes the deformation energy cost. For rounded edges ($n = 4$) or higher aspect ratios (Fig. 2(a), (b), and (d)), the particle switches to parallel orientation (Fig. 2(e)) after initial binding and back to perpendicular orientation for the deep-wrapped state (Fig. 2(f)). However, for the special case of sharper edges ($n = 6$) and aspect ratio 1.5 (Fig. 2(c)), the particle enters in rocket mode only (Fig. 2(g) and (h)). In virus and nanotube uptake experiments[4–6], both submarine and rocket modes have indeed been observed.

We have characterized the critical wrapping fractions for both stable states in Fig. 3(a) and (b). For the transition between shallow-wrapped and deep-wrapped states (W_2), and for both aspect ratios 1.5 and 2, the wrapping fraction jumps from about 10 % to about 80 %. For the envelopment transition (W_3), the wrapping fraction jumps from $80\,\% - 90\,\%$ to complete wrapping. For both discontinuous transitions, W_2 and W_3, we have also estimated spinodals (S_{22} and S_{32} in Fig. 2) for spontaneous wrapping and upper bounds for the energy barriers (Fig. 3(c) and (d)). The energy barriers, $\Delta E_{\mathrm{bar}}(W_2)$ and $\Delta E_{\mathrm{bar}}(W_3)$, are of the order of $\pi\kappa$. Both the energy barriers and the associated spinodals for the W_2 transitions (shallow- to deep-wrapped) are approximate values, because of the piecewise nature of the energy profile in our calculations (see supplementary material). By calculating the wrapping energies for all possible orientations, exact values for energy barriers and spinodals can be obtained, but the phase boundaries remain unaffected. The energy barriers and spinodals for the W_3 transition (deep- to complete-wrapped) are not connected with any orientation changes and are therefore exact; spontaneous complete wrapping occurs for adhesion strengths that are as much as $5 - 10$ times higher than for spherical nanoparticles.

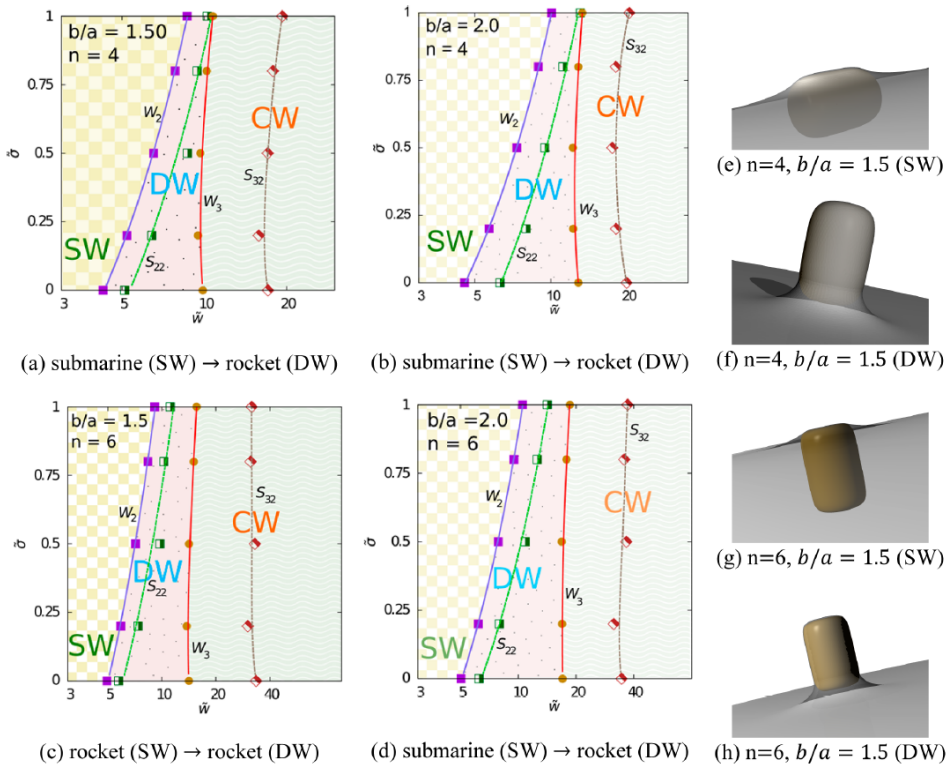

(a) submarine (SW) → rocket (DW)

(b) submarine (SW) → rocket (DW)

(e) n=4, $b/a = 1.5$ (SW)

(f) n=4, $b/a = 1.5$ (DW)

(c) rocket (SW) → rocket (DW)

(d) submarine (SW) → rocket (DW)

(g) n=6, $b/a = 1.5$ (SW)

(h) n=6, $b/a = 1.5$ (DW)

Figure 3.4: (a)-(d): Phase diagrams for wrapping of rod-like particles with equal surface areas and various aspect ratios, showing shallow-wrapped (SW), deep-wrapped (DW), and complete-wrapped (CW) states. A discussion for the cases of equal size a and equal volume (for a spherocylinder) is presented in the supplementary material. (e)-(f): Membrane and particle conformations for submarine and rocket states. As indicated below the phase diagrams, in most cases the transition from the SW to the DW state is associated with an re-orientation of the particle from submarine to rocket orientation. For the special case of aspect ratio 1.5 and $n = 6$, the particle is in rocket orientation both in the shallow-wrapped and the deep-wrapped state.

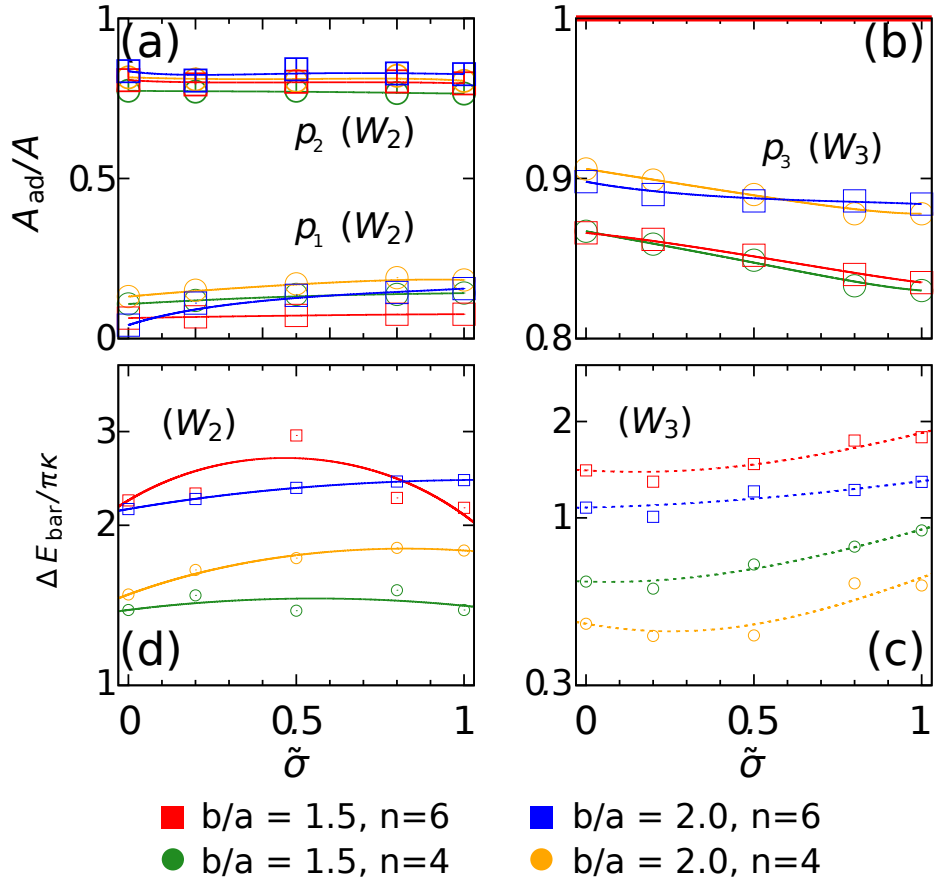

Figure 3.5: (a),(b): Wrapping fractions for stable states for the discontinuous wrapping transitions W_2 and W_3 for aspect ratios 1.5 and 2 and for $n = 4$ and 6. The shallow-wrapped states correspond to wrapping fractions of $10 - 20\%$, the deep-wrapped states to wrapping fractions of $80 - 90\%$. (c),(d): The energy barriers for both transitions, between the shallow-wrapped and the the deep-wrapped state and between the deep-wrapped and the complete-wrapped state, are of the order $\pi\kappa$ and increase with the sharpness of the edges.

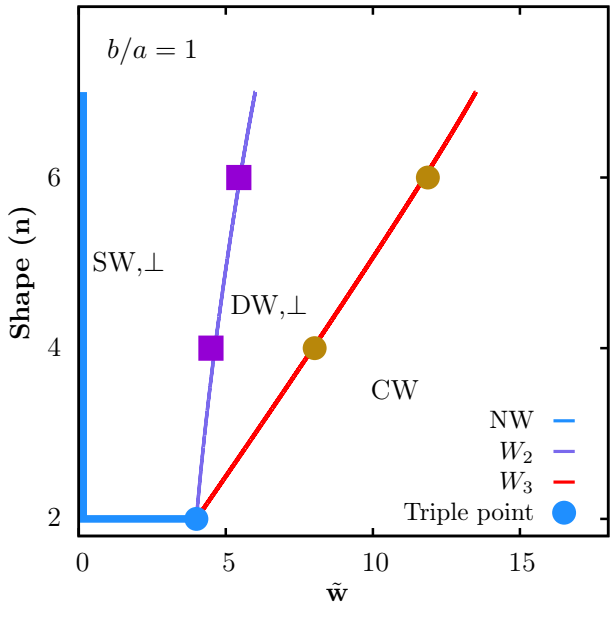

(a)

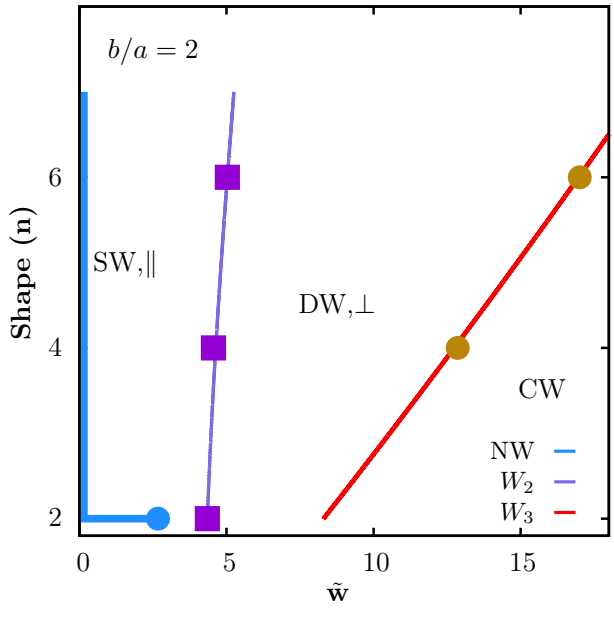

(b)

Figure 3.6: Role of edge curvature (characterized by n) on the wrapping behavior of a tensionless membrane for nanoparticles with fixed aspect ratio (a) $b/a = 1$ and (b) $b/a = 2$. The particle orientation in the shallow-wrapped (SW) and deep-wrapped (DW) states is indicated by the symbols $\perp$ and $\parallel$, corresponding to rocket and submarine orientation, respectively. Non-wrapped states are marked by light-blue lines.

particle shape	membrane	binding transition	shallow-wrapped state	deep-wrapping transition	deep-wrapped state	envelopment transition
spherical	κ	cont., for $w = 2\kappa/a^2$	-	-	-	$\equiv$ binding
spherical	κ and σ	cont., for $w = 2\kappa/a^2$	yes	-	-	discont.
ellipsoidal	κ, κ and σ	cont., indep. of σ	yes, submarine	discont., reorient.	yes, rocket	cont.
ellipsoidal (*)	κ, κ and σ	cont., indep. of σ	yes, submarine	-	-	discont.
cube-like	κ, κ and σ	at vanishing w	yes	discont.	yes	discont.
spherocylinder	κ, κ and σ	at vanishing w, rocket	yes, submarine	discont., reorient.	yes, rocket	discont.
rod-like	κ, κ and σ	at vanishing w, rocket	yes, submarine	discont., reorient.	yes, rocket	discont.
rod-like (*)	κ, κ and σ	at vanishing w, rocket	yes, submarine	-	-	discont.
rod-like (**)	κ, κ and σ	at vanishing w, rocket	yes, rocket	discont.	yes, rocket	discont.

Table 3.1: Shape dependence of particle wrapping, based on Refs.[11,31] and this work. The membrane can be characterized by bending rigidity only, 'κ', or by bending rigidity and membrane tension, 'κ and σ'; the binding transition can occur at finite or vanishing adhesion strength w; the particle can be in submarine or rocket orientation; transitions can be continuous (cont.) or discontinuous (discont.) and may involve reorientation (reorient.). The binding transition for ellipsoids is independent of the membrane tension and is given in Ref.[31]. (*) Fast wrapping at high adhesion strength, such that a bound ellipsoid cannot reorient to rocket orientation. (**) Rocket mode for supereggs with blunt tips and small aspect ratio (e. g. $n = 4$ and $b/a = 1.5$).

3.6 Role of shape and orientation

To elucidate the role of particle shape further, we show in Figs. 3.6 and 3.7 wrapping phase diagrams of nanorods as function of edge curvature and particle aspect ratio, respectively, both for fixed particle surface area. Figure 3.6 displays the wrapping states for varying edge sharpness in case of a tensionless membrane, at fixed aspect ratios $b/a = 1$ and $b/a = 2$. For spherical particles (Fig. 3.6(a), $n = 2$), the non-wrapped state directly transits to the completely-wrapped state, whereas for ellipsoidal particles (Fig. 3.6(b), $n = 2$), a partially-wrapped state can exist even for a tensionless membrane due to the high curvature at the tips. The sharp edges of rod-like particles with $n > 2$ imply two discontinuous transitions, W_2 and W_3, separating shallow-wrapped and deep-wrapped, and deep-wrapped and complete-wrapped states. The deep-wrapped regime extends strongly with increasing edge sharpness. Because of locally flat parts of their surface, rod-like nanoparticles adhere to the membrane already for very small adhesion strengths, in contrast to spheres and ellipsoids. For rod-like nanoparticles with $b/a = 1$, the rocket orientation is preferred for both partially-wrapped states independent of edge sharpness; for $b/a = 2$, nanoparticles reorient from submarine to rocket orientation when they cross the discontinuous transition W_2.

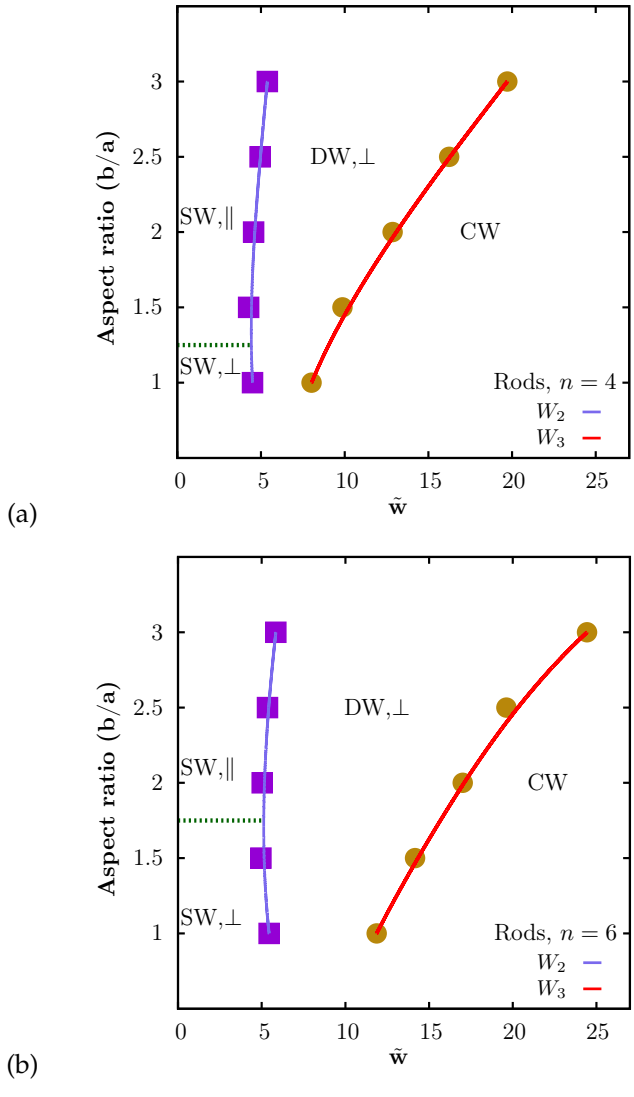

Figure 3.7: Role of aspect ratio on the wrapping behavior of a tensionless membrane for rod-like nanoparticles with (a) smoother edges ($n = 4$) and (b) sharper edges ($n = 6$). The particle orientation in the shallow-wrapped (SW) to deep-wrapped states (DW) is indicated by the symbols $\perp$ and $\parallel$, corresponding to rocket and submarine orientation, respectively.

Fig. 3.7 shows the wrapping states for rod-like nanoparticles with smoother ($n = 4$) and sharper edges ($n = 6$) as a function of the aspect ratio, with $1 \leq b/a \leq 3$. Increased edge sharpness increases the regime with rocket orientation in the shallow-wrapped state, but hardly affects the phase boundary between shallow-wrapped and deep-wrapped states. However, the phase boundary between deep-wrapped and completely-wrapped states shifts significantly to larger adhesion strengths for increased edge sharpness.

3.7 Conclusions

Interaction with cells and a successful passage through the plasma membrane is the primary step both for applications and the toxicity of nanoparticles. The versatile properties of nanoparticles predicted by our model of non-spherical nanoparticles provide interesting perspectives for their use as bio-sensors for optical imaging[39,40], as membrane-protein binding sensors[40], as drug delivery agents, and for use in photo-chemical treatment[22] using surface plasmon resonance techniques. Also, wrapping in systems containing many spherical colloidal particles can be rationalized by our model of elongated particles. Partially-attached spherical particles aggregate[41,42] and form necklace-like linear and tubular aggregates on the membrane[43,44] with increased adhesion strength. This is analogous to our frustrated endocytotic states with parallel and perpendicular orientation of rod-like colloids to the membrane. In Tab. S1, we summarize basic properties for wrapping of particles with different shapes as necessary prerequisites for predicting any desired or toxic effects.

Our results emphasize the importance for both, calculations using continuum membranes in equilibrium that provide a systematic understanding of wrapping energies[11,31,43–45], and dynamic molecular simulations[1,27,28,34] that add details for specific systems and further investigate dynamical aspects of the budding pathway.

Based on energy minimization, we find two different modes with parallel and perpendicular orientation for entry of elongated particles into cells. Particles with high aspect ratio bind in parallel orientation, but transit from deep to complete wrapping in perpendicular orientation. However, a major part of the wrapping process for spherocylinders studied in Ref.[27] seems to occur in parallel orientation. Parallel orientation favors complete wrapping, because a stable deep-wrapped state is avoided (see supplementary material). Calculations for specific particle sizes, which include dynamical, non-equilibrium aspects, show that the orientation also depends on the speed of internalization[21,34]; such dynamical calculations thus complement our systematic study of the influence of particle shape in equilibrium.

Our basic wrapping picture can be modified by additional parameters, such as surface functionalization or the more complex structure of the cell membrane. Surface functionalization[20,46] or coating of nanoparticles by corona proteins is captured by our model, as long as the particle's surface properties are homogeneous and can be expressed by an overall adhesion strength w. Inhomogeneous surface coatings require more detailed models and calculations. Also, a multicomponent membrane or the cell cytoskeleton may have to be taken into account for specific wrapping calculations, such as phagocytosis of *E. coli* with high aspect ratio. In this case, the cytoskeleton plays a significant role and contrary to our predictions, high aspect-ratio bacteria with rounded ends are wrapped starting at the tip in a "race to the pole"[30]. However, this does not invalidate our calculations based on membrane mechanics, but rather indicates that further energy or dynamic contributions may have to be taken into account.

Supporting material

Details about numerical calculations and additional images.

Acknowledgments

We thank K. Brakke (Selinsgrove, PA) for his advice on Surface Evolver and for helpful discussions on numerical techniques, and R. Korenstein (Tel Aviv) stimulating discussions on nanoparticles at membranes. Support from the EU FP7 NMP collaborative project PreNanoTox (309666) is gratefully acknowledged. SD acknowledges support from the International Helmholtz Research School of Biophysics and Soft Matter (IHRS BioSoft).

References: Chapter 3

1 K. Yang and Y. Q. Ma, *Nat. Nanotechnol.*, 2010, **5**, 579–583.

2 S. Pogodin, M. Werner, J.-U. Sommer and V. A. Baulin, *ACS Nano*, 2012, **6**, 10555–10561.

3 S. Pogodin and V. A. Baulin, *ACS Nano*, 2010, **4**, 5293–5300.

4 T. Noda, H. Ebihara, Y. Muramoto, K. Fujii, A. Takada, H. Sagara, J. H. Kim, H. Kida, H. Feldmann and Y. Kawaoka, *PLoS Pathog.*, 2006, **2**, 9.

5 S. Welsch, L. Kolesnikova, V. Krähling, J. D. Riches, S. Becker and J. A. G. Briggs, *PLoS Pathog.*, 2010, **6**, 9.

6 Y. Hatano, M. Yoshida, F. Uno, S. Yoshida, N. Osafune, K. Ono and M. Yamada, *J. Electron Microsc.*, 2001, **50**, 113–124.

7 Y. Geng, P. Dalhaimer, S. Cai, R. Tsai, M. Tewari, T. Minko and D. E. Discher, *Nat. Nanotechnol.*, 2007, **2**, 249–255.

8 S. Zhang, J. Li, G. Lykotrafitis, G. Bao and S. Suresh, *Adv. Mater.*, 2009, **21**, 419–424.

9 S. Zhang, A. Nelson and P. A. Beales, *Langmuir*, 2012, **28**, 12831–7.

10 H. Gao, W. Shi and L. B. Freund, *Proc. Natl. Acad. Sci. U. S. A.*, 2005, **102**, 9469–9474.

11 M. Deserno, *Phys. Rev. E.*, 2003, **69**, 031903.

12 W. Jiang, B. Y. S. Kim, J. T. Rutka and W. C. W. Chan, *Nat. Nanotechnol.*, 2008, **3**, 145–150.

13 G. Adriani, M. D. De Tullio, M. Ferrari, F. Hussain, G. Pascazio, X. Liu and P. Decuzzi, *Biomaterials*, 2012, **33**, 5504–13.

14 Y. Zhang, S. Tekobo, Y. Tu, Q. Zhou, X. Jin, S. A. Dergunov, E. Pinkhassik and B. Yan, *ACS Appl. Mater. Interfaces*, 2012, **4**, 4099–4105.

15 B. D. Chithrani, A. A. Ghazani and W. C. W. Chan, *Nano Lett.*, 2006, **6**, 662–668.

16 B. D. Chithrani and W. C. W. Chan, *Nano Lett.*, 2007, **7**, 1542–1550.

17 S. E. A. Gratton, P. A. Ropp, P. D. Pohlhaus, J. C. Luft, V. J. Madden, M. E. Napier and J. M. DeSimone, *Proc. Natl. Acad. Sci. U. S. A.*, 2008, **105**, 11613–11618.

18 D. K. Cureton, R. H. Massol, S. Saffarian, T. L. Kirchhausen and S. P. J. Whelan, *PLoS Pathog.*, 2009, **5**, e1000394.

19 P. Ge, J. Tsao, S. Schein, T. J. Green, M. Luo and Z. H. Zhou, *Science*, 2010, **327**, 689–693.

20 Y. Qiu, Y. Liu, L. Wang, L. Xu, R. Bai, Y. Ji, X. Wu, Y. Zhao, Y. Li and C. Chen, *Biomaterials*, 2010, **31**, 7606–7619.

21 X. Shi, A. von dem Bussche, R. H. Hurt, A. B. Kane and H. Gao, *Nat. Nanotechnol.*, 2011, **6**, 714–719.

22 Y. Wang, K. C. L. Black, H. Luehmann, W. Li, Y. Zhang, X. Cai, D. Wan, S.-Y. Liu, M. Li, P. Kim, Z.-Y. Li, L. V. Wang, Y. Liu and Y. Xia, *ACS Nano*, 2013, **7**, 2068–2077.

23 J. P. Best, Y. Yan and F. Caruso, *Adv. Healthcare Mater.*, 2012, **1**, 35–47.

24 P. Decuzzi, R. Pasqualini, W. Arap and M. Ferrari, *Pharm. Res.*, 2009, **26**, 235–243.

25 J. A. Champion and S. Mitragotri, *Proc. Natl. Acad. Sci. U. S. A.*, 2006, **103**, 4930–4934.

26 S. Mitragotri and J. Lahann, *Nat. Mater.*, 2009, **8**, 15–23.

27 R. Vácha, F. J. Martinez Veracoechea and D. Frenkel, *Nano Lett.*, 2011, **11**, 5391–5.

28 K. Yang, B. Yuan and Y. Q. Ma, *Nanoscale*, 2013, **5**, 7998–8006.

29 H. Herd, N. Daum, A. T. Jones, H. Huwer, H. Ghandehari and C.-M. Lehr, *ACS Nano*, 2013, **7**, 1961–1973.

30 J. Möller, T. Luehmann, H. Hall and V. Vogel, *Nano Lett.*, 2012, **12**, 2901–2905.

31 S. Dasgupta, T. Auth and G. Gompper, *Soft Matter*, 2013, **9**, 5473–5482.

32 X. Yi, X. Shi and H. Gao, *Phys. Rev. Lett.*, 2011, **107**, 1–5.

33 A. H. Bahrami, *Soft Matter*, 2013, **9**, 8642–8646.

34 C. Huang, Y. Zhang, H. Yuan, H. Gao and S. Zhang, *Nano Lett.*, 2013, **13**, 4546–4550.

35 W. Helfrich, *Z. Naturforsch. C*, 1973, **28**, 693–703.

36 G. Gompper and D. M. Kroll, Statistical Mechanics of Membranes and Surfaces, 2004.

37 K. A. Brakke, *Exp. Math.*, 1992, **1**, 141–165.

38 L. Florez, C. Herrmann, J. M. Cramer, C. P. Hauser, K. Koynov, K. Landfester, D. Crespy and V. Mailänder, *Small*, 2012, **8**, 2222–2230.

39 Y. Wang, Y. Liu, H. Luehmann, X. Xia, D. Wan, C. Cutler and Y. Xia, *Nano Lett.*, 2013, **13**, 581–585.

40 H.-J. Wu, J. Henzie, W.-C. Lin, C. Rhodes, Z. Li, E. Sartorel, J. Thorner, P. Yang and J. T. Groves, *Nat. Methods*, 2012, **9**, 1189–1191.

41 B. J. Reynwar, G. Illya, V. A. Harmandaris, M. M. Mueller, K. Kremer and M. Deserno, *Nature*, 2007, **447**, 461–464.

42 T. Auth and G. Gompper, *Phys. Rev. E.*, 2009, **80**, 031901.

43 A. Šarić and A. Cacciuto, *Phys. Rev. Lett.*, 2012, **109**, 188101.

44 A. H. Bahrami, R. Lipowsky and T. R. Weikl, *Phys. Rev. Lett.*, 2012, **109**, 188102.

45 T. R. Weikl, *Eur. Phys. J. E*, 2003, **12**, 9.

46 S. Barua, J.-W. Yoo, P. Kolhar, A. Wakankar, Y. R. Gokarn and S. Mitragotri, *Proc. Natl. Acad. Sci. U.S.A.*, 2013, **110**, 3270–3275.

3.8 Supplementary material

Supplementary material: Shape and Orientation Matter for the Cellular Uptake of Non-spherical Particles

We present here details about numerical methods and additional information about geometrical properties of the investigated nanoparticles, wrapping energies as a function of wrapping fraction that have been used to calculate the phase diagrams discussed in the main text, and provide further wrapping energies and phase diagrams for spheres[1], ellipsoids[2,3], rod-like particles[4–8], spherocylinders[9], and nanocubes[6,10]. Wrapping energies are shown in Figs. S1, S2, S3, and S4, phase diagrams are shown in Figs. S5 and S6.

Methods

Triangulated membranes are a powerful tool to numerically minimize the Helfrich curvature-elastic energy to obtain equilibrium membrane deformations with high accuracy[2,11]. Using Surface Evolver[12], we calculate the membrane deformation energy for cube-like and rod-like particles both with parallel and perpendicular orientation of the long axis of the particle to the membrane. Membrane tension and adhesion energies can be calculated as sum over all relevant triangle areas. For the discretization of the bending energy, we use the Surface Evolver algorithm "star_perp_sq_mean_curvature". The bending energy is given by

$$\mathcal{E}_{\text{bend}} = 2\kappa \sum_{v=1}^{n} a_v h_v^2 \tag{3.3}$$

with the local mean curvature at each vertex v,

$$h_v = \frac{1}{2} \frac{\boldsymbol{\nabla} a_v \cdot \boldsymbol{\nabla} \mathcal{V}_v}{\boldsymbol{\nabla} \mathcal{V}_v \cdot \boldsymbol{\nabla} \mathcal{V}_v} \,. \tag{3.4}$$

The area associated with each vertex is a_v and the volume is

$$\mathcal{V}_v = \frac{1}{6} \boldsymbol{v} \cdot \left[\boldsymbol{v}^1 \times \boldsymbol{v}^2 + \boldsymbol{v}^2 \times \boldsymbol{v}^3 + ... + \boldsymbol{v}^n \times \boldsymbol{v}^1 \right] , \tag{3.5}$$

such that

$$\boldsymbol{\nabla} \mathcal{V}_v = \frac{1}{6} \left[\boldsymbol{v}^1 \times \boldsymbol{v}^2 + \boldsymbol{v}^2 \times \boldsymbol{v}^3 + ... + \boldsymbol{v}^n \times \boldsymbol{v}^1 \right] , \tag{3.6}$$

where the postition vector for the vertex v is $\boldsymbol{v}$, while $\boldsymbol{v}^1$, $\boldsymbol{v}^2$, $\boldsymbol{v}^3$, ..., $\boldsymbol{v}^n$ are the position vectors for the neighboring vertices.

We calculate the deformation energies for membrane patches enclosed by circular wire frames with radius $20\,a$, where a is the radius of a sphere, the half edge-length of a cube, and the short axis of an ellipsoidal or rod-like particle. The slope of the membrane at the boundary and the height of the particle above the wire frame can adjust freely. Once the system is assembled, the energy is minimized by moving the vertices towards the direction of steepest descent of the energy landscape, while the mesh is adaptively refined several times in-between the energy minimization steps. During the initial steps of the energy minimization, the contact line, where the membrane detaches from the particle, can vary its shape freely. For the final minimization steps, we fix the shape of the contact line to improve numerical stability and use the Hessian algorithm for minimization, which is the best quadratic approximation of the energy and helps to converge quickly to the minimum energy state. Although we allow the contact line to optimize its shape, we do not observe a significant contact line undulation for our systems. A significant undulation of the contact line has been observed for ellipsoids attached to small vesicles[3], the energy gain for deforming the contact line therefore appears to be much bigger for these systems than for the planar membranes in our calculations.

The deformation energies for non-spherical particles that can change orientation are constructed as piecewise functions of the wrapping fraction by always choosing the minimum energy for both particle orientations. We calculate deformation energies up to almost complete wrapping and are therefore able to evaluate the transition from the shallow-wrapped to the deep-wrapped and—for cube-like and rod-like particles—the transition from the deep-wrapped to the complete-wrapped state, which has not been possible for the ellipsoids that are wrapped by small vesicles in Ref.[3].

In our study, we do not account for the process where the particle pinches off from the membrane patch that would be connected with a change of membrane topology, but rather calculate the membrane deformation energy costs until the particle is (almost) completely wrapped. In the highest wrapping state, the membrane has a very small catenoid-like connection to membrane patch that does not contribute significantly to the deformation energy. The wrapping energy curves for both orientations connect smoothly to the energy for the completely-wrapped state with $A_{ad}/A = 1$ that has been calculated for an isolated particle, see Figs. S1 and S4.

Geometric properties of investigated nanoparticles

For all investigated nanoparticles, we provide in Tab. S1 the aspect ratio (b/a), the surface area A, and the integral of the squared mean curvature of the particles, H^2, over the entire particle surface area, which is proportional to the total bending energy for wrapping. The particle shapes are defined by $x^6 + y^6 + z^6 = a^6$ for cube-like particles and $[(x^2 + y^2)/a^2]^{(n/2)} + (z/b)^n = 1$ for rod-like particles (regular ellipsoids have $n = 2$ and super-eggs $n \geq 4$).

particle shape	b/a	A	$\int \mathbf{H^2 dS}$
nanocube	1.0	19.61	26.43
prolate ellipsoid, $n = 2$	1.25	14.71	12.88
oblate ellipsoid, $n = 2$	0.80	10.93	12.93
nanorod, $n = 4$ ($n = 6$)	1.0	15.46 (16.56)	15.94 (20.10)
nanorod, $n = 4$ ($n = 6$)	1.5	20.84 (22.26)	16.09 (19.52)
nanorod, $n = 4$ ($n = 6$)	2.0	26.34 (28.05)	17.11 (20.12)
nanorod, $n = 4$ ($n = 6$)	2.5	31.92 (33.91)	18.44 (21.17)
nanorod, $n = 4$ ($n = 6$)	3.0	37.55 (39.79)	19.93 (22.43)

Table S1: Geometric properties of studied nanoparticles with aspect ratio b/a and area A.

Wrapping energies of spherocylinder and rod-like nanoparticles

In Fig. S1, membrane deformation energies as function of the wrapping fraction of the particle are shown for ellipsoidal and rod-like particles at fixed membrane tension $\tilde{\sigma} = 0.8$. The energies are plotted both for submarine (parallel) and rocket (perpendicular) orientation. Physically relevant is the lower branch of the energy profiles at each wrapping fraction, see also Fig. S4. These energy functions, together with a double-tangent construction, are the basis for calculating wrapping phase diagrams for $\tilde{w}$ and $\tilde{\sigma}$. Fig. S1 demonstrates, for example, that the dip for a rod-like particle with perpendicular orientation at $A_{ad}/A_{total} \simeq 0.8$ becomes much more pronounced with increasing n from $n = 2$ to $n = 6$, which signals the increased stability of a deep-wrapped rocket state.

3.8.1 Spherocylinders

In Fig. S2, membrane deformation energies for spherocylindrical particles are compared with those of spherical particles. All energy profiles for spherocylinders show a partially-wrapped state in parallel orientation at small wrapping fraction, due to the weakly concave shape of the wrapping energy functions at small wrapping fraction, and a partially-wrapped state in perpendicular orientation at high wrapping fraction. The energy cost per wrapped area for the spherical caps is twice as high as for the cylindrical parts; the energy profiles for inclined states between parallel and perpendicular wrapping fall in-between these two limiting energy profiles[13]. Inclined states therefore change the energy barrier, but the do not change the minimal energy states that are used to calculate the phase boundaries. The sharply bent membrane, where it detaches from the nanoparticle on one side for small inclination angles, will further increase the bending energy costs for inclined orientations compared with rocket and submarine orientation.

Figure S2 demonstrates that the comparison of spherical and spherocylindrical particles is not unique, but also depends on whether radius, surface area, or volume are the same in both cases. For a spherocylinder with the same radius a as the sphere, the transition from the deep-wrapped to the complete-wrapped state occurs

for the same adhesion strength as wrapping of the sphere. This explains why the uptake limit for the binding strength determined in Ref.[9] has been found to be almost the same for a sphere and for two different spherocylinders, all with the same radius. For spherocylinders with equal surface area and equal volume, the transition between the deep-wrapped state and the complete-wrapped state occurs at higher adhesion strength than for wrapping of a corresponding sphere. In these cases the increased particle aspect ratio hinders complete wrapping, which might be the reason why many viruses have an almost spherical, icosahedral shapes.

The binding in rocket orientation that is predicted by our calculations has been observed for both dynamical calculations in Ref.[9] and in Ref.[13]. In Ref.[9]—with a high receptor density and therefore for fast wrapping—the transition to complete wrapping orientation occurs in submarine orientation. For slower wrapping, deep-wrapped cylinders have rocket orientation[13], as suggested by our wrapping energy calculations.

3.8.2 Rod-like particles

In Fig. S3, membrane deformation energies for rod-like particles with blunt tips and rounded edges ($n = 4$) and aspect ratio $b/a = 2.0$ are plotted as function of the wrapping fraction analogously to Fig. S1, but for various membrane tensions σ. With increased membrane tension, the energy difference between the complete-wrapped state with and without membrane tension increases proportionally to $\sigma A_{\text{particle}}$. As shown in the phase diagrams for particles with equal surface areas in Fig. 4 of the main text, we find a membrane-tension dependence mainly for the value of the adhesion strength for the W_2 transition between the shallow-wrapped and the deep-wrapped state. Wrapping phase diagrams for particles with equal radii a are given in Fig. S6. Figure S3 demonstrates that for rod-like particles the membrane tension is important for the adhesion strengths that characterise the wrapping process (i. e., for the slope of the deformation energy as function of the wrapping fraction), but does not qualitatively change the deformation energy functions.

In Fig. S4, membrane deformation energies and wrapping energies for a rod-like particle with $n = 4$, $b/a = 1.5$ and $\tilde{\sigma} = 0.8$ are plotted as function of the wrapping fraction. The figure demonstrates how the boundaries in the wrapping phase diagrams are calculated. The phase diagrams in this work are obtained from the piecewise deformation energy function given by the minimum energy for parallel and perpendicular particle orientation, as shown in Fig. S4(a). While the binding transition occurs for vanishing adhesion strength, the wrapping energies for phase boundaries between the shallow-wrapped and the deep-wrapped state and between the deep-wrapped and the complete-wrapped state correspond to finite values of the adhesion strength, see Fig. S4(b).

Wrapping Phase Diagrams

3.8.3 Ellipsoids

In Fig. S5, wrapping phase diagrams are compared for 'fast' wrapping of ellipsoids in submarine orientation and for 'slow' wrapping that allows for reorientation from parallel to perpendicular. The 'fast-wrapping' scenario applies when wrapping is fast compared with particle reorientation[2]. In this case, the particle achieves a complete-wrapped state directly from the shallow-wrapped states (and may detach from the membrane into the cell before it enters the deep-wrapped state with high wrapping fraction). This transition occurs for similar adhesion strengths as the transition from the shallow-wrapped to the deep-wrapped state for wrapping with reorientation.

Reorientation of ellipsoids has been suggested previously for wrapping of nanoparticles by vesicles with sizes comparable to the ellipsoid size[3], whereas our calculations apply for interaction of nanoparticles with giant unilamellar vesicles and cells. Our calculations show that reorientation to the rocket-like orientation does not help to achieve the complete-wrapped state, because of the very steep increase of the bending energy just before complete wrapping. Complete wrapping with reorientation (not shown) thus requires significantly higher adhesion strengths than wrapping without reorientation, see Fig. S2. Figure S5 demonstrates that 'fast' wrapping that suppresses particle reorientation facilitates complete wrapping in this case; similar observations apply to rod-like particles.

3.8.4 Wrapping diagrams for particles with same size

In Fig. S6, wrapping phase diagrams for several particles with fixed size a are shown, where the radius of the sphere in Fig. S6(a) equals half the length of the cube in Fig. S6(b), and the length of the short axes of the rod-like particles in Fig. S6(c)-(f). Our phase diagram for spherical particles agrees with the phase diagram shown in Ref.[1]. For cube-like and rod-like particles, wrapping is qualitatively different than for spherical particles and depends not only on particle size and aspect ratio, but also on the sharpness at the edges. Comparison with the phase diagrams in Fig. 4 of the main text shows that for equal surface areas of rod-like particles the W_3 transition from the deep-wrapped to the complete-wrapped state that is relevant for complete uptake is shifted to higher adhesion strengths for higher aspect ratios, but remains unchanged for particles with equal sizes. The comparison of Fig. S6 with Fig. 4 in the main text shows the importance of both, the particle shape *and* the characteristic particle size, see also Fig. S2.

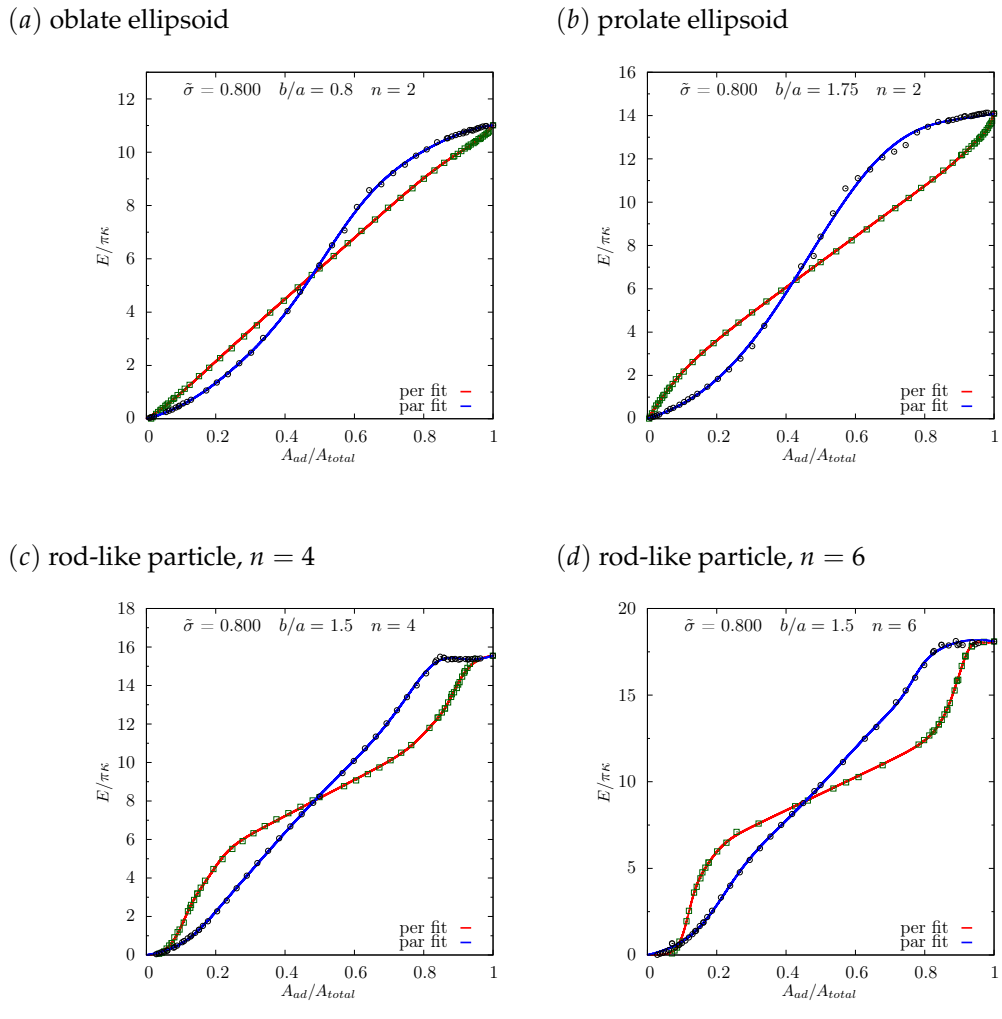

Figure S1: Membrane deformation energies for various particles at fixed membrane tension $\tilde{\sigma} = 0.8$ as function of the wrapping fraction: (a) oblate ellipsoid, (b) prolate ellipsoid, (c) rod-like particle with $n = 4$, and (d) rod-like particle with $n = 6$. All figures show data for perpendicular (per) and parallel (par) orientation of the symmetry axis of the particle to the membrane. Numerical data (points) and fit functions (lines) are plotted. The fit functions are constructed for ellipsoids by one sigmoidal function, and for rod-like particles by a sum of two sigmoidal functions and a product of a linear function, a monotonously increasing Fermi function, and a monotonously decreasing Fermi function.

(a) $b/a = 1.5$, equal size $a_{\mathrm{cyl}} = a_{\mathrm{sph}}$

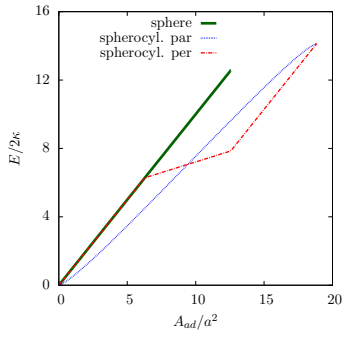

(d) $b/a = 2.0$, equal size $a_{\mathrm{cyl}} = a_{\mathrm{sph}}$

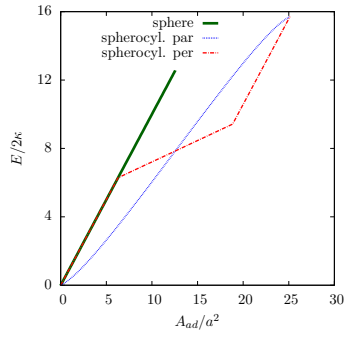

(b) $b/a = 1.5$, equal area A, $a_{\mathrm{cyl}} = 0.82 a_{\mathrm{sph}}$

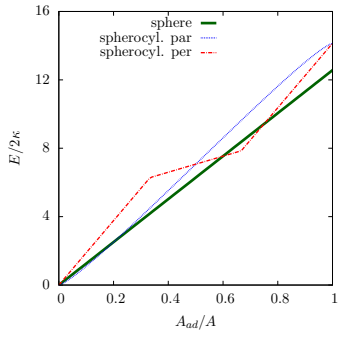

(e) $b/a = 2.0$, equal area A, $a_{\mathrm{cyl}} = 0.71 a_{\mathrm{sph}}$

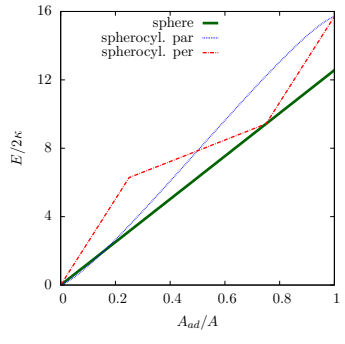

(c) $b/a = 1.5$, equal volume V, $a_{\mathrm{cyl}} = 0.83 a_{\mathrm{sph}}$

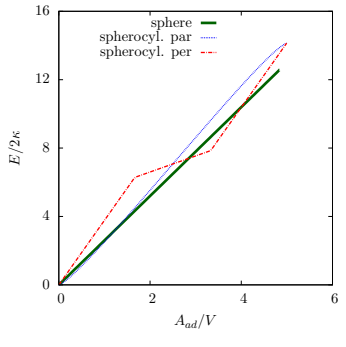

(f) $b/a = 2.0$, equal volume V, $a_{\mathrm{cyl}} = 0.74 a_{\mathrm{sph}}$

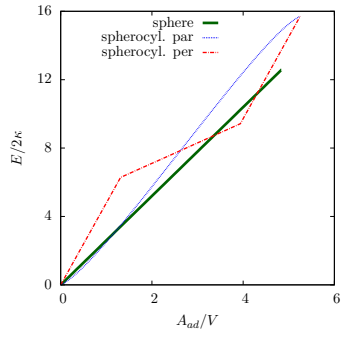

Figure S2: Membrane deformation energies for a sphere with radius a (see Fig. 1 of the main text) and spherocylinders with aspect ratios $b/a = 1.5$ and $b/a = 2$ for vanishing membrane tension. The deformation energy cost for the free membrane around the adhered particle is not taken into account. All figures show data for perpendicular (per) and parallel (par) orientation of the spherocylinders to the membrane. For a sphere and a spherocylinder with $b/a = 1.5$, the wrapping energies are plotted for (a) equal particle radii a, (b) equal surface areas A and (c) equal volumes V of the nanoparticles. The subfigures (d), (e), and (f) are analogous plots for spherocylinders with aspect ratio $b/a = 2.0$.

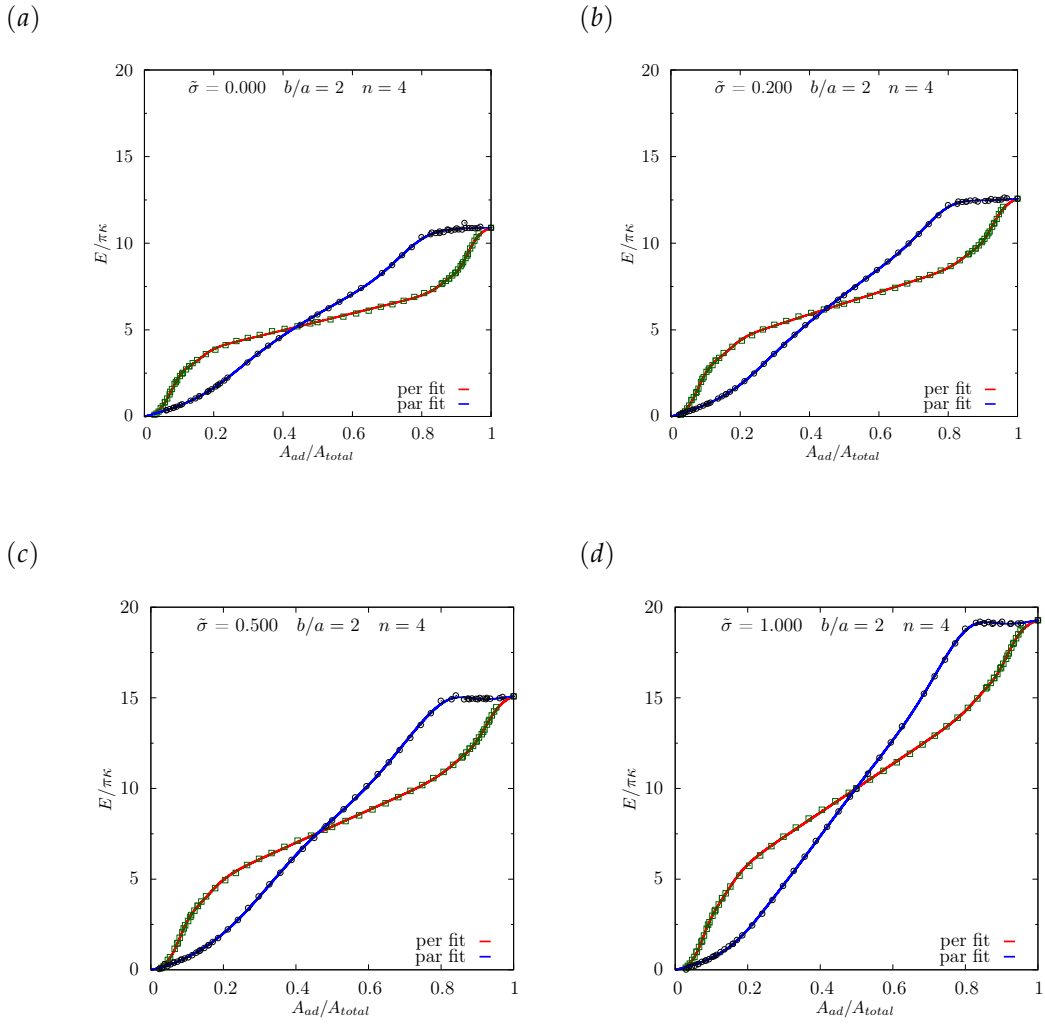

Figure S3: Membrane deformation energies as function of the wrapping fraction for rod-like particles with $n = 4$ and for reduced membrane tensions $0 \leq \tilde{\sigma} \leq 1$.

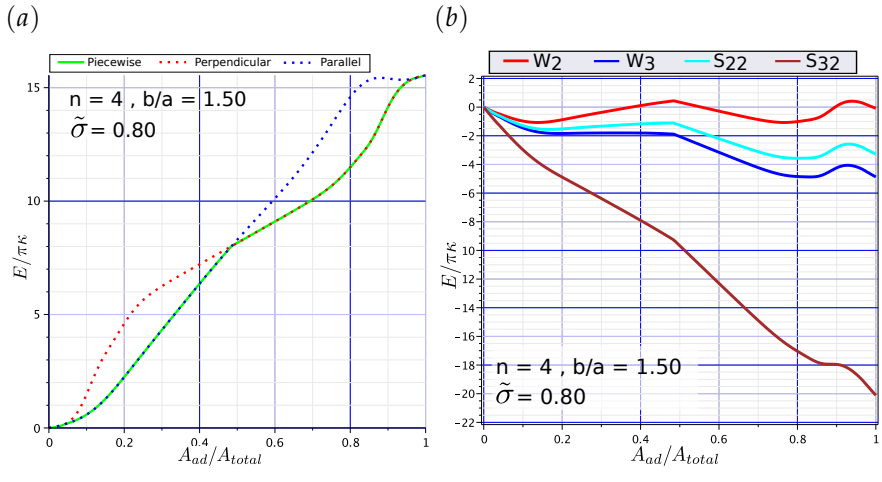

Figure S4: Membrane deformation energies and wrapping energies as function of the wrapping fraction for rod-like particles with blunt tips and rounded edges ($n = 4$), aspect ratio 1.5, and reduced membrane tension $\tilde{\sigma} = 0.8$. (a) Membrane deformation energy. Exploiting energy minimization, the physically relevant membrane deformation energy is the minimum energy with a given wrapping fraction for all potential orientations of the particle relative to the membrane. We have approximated the energy deformation profile obtained from all possible particle orientations by piecewise functions obtained by considering only parallel and perpendicular orientation. (b) Wrapping energy, given by the sum of deformation and adhesion energy. At the phase boundary W_2 the shallow-wrapped and the deep-wrapped state have equal energy; these two energy minima are separated by the energy barrier $\Delta E_{\mathrm{bar}}(W_2)$. At the phase boundary W_3 the energy for the deep-wrapped state is equal to the energy of the complete-wrapped state, both states are separated by the energy barrier $\Delta E_{\mathrm{bar}}(W_3)$. The spinodal S_{22} is approximated by the wrapping energy profile where the slope of the energy for parallel orientation at the point where parallel and perpendicular orientation have equal energy vanishes. For the spinodal S_{32} the transition from the deep-wrapped to the complete-wrapped state occurs spontaneously (and the energy barrier between both states vanishes).

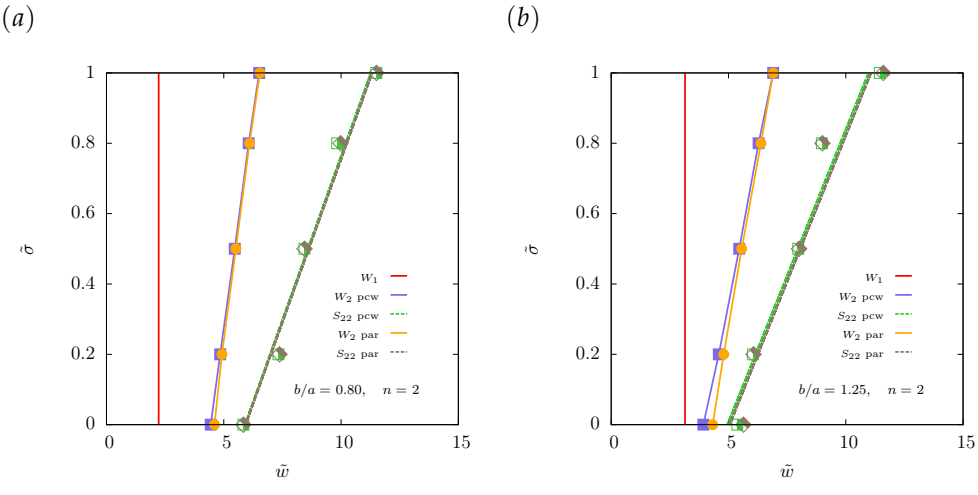

Figure S5: Wrapping phase diagrams of (a) an oblate and (b) a prolate ellipsoidal particle for membrane tension and adhesion strength. Phase boundaries are plotted for fast wrapping (parallel orientation only, par) and for slow wrapping (reorientation parallel to perpendicular, pcw). Binding occurs for the ellipsoid oriented parallel to the membrane and is independent of membrane tension (W_1). The phase boundary W_2 is the transition between the shallow-wrapped and the complete-wrapped state if there is no reorientation, and between the shallow-wrapped and the deep-wrapped state if the particle reorients from parallel to perpendicular. The spinodals for the spontaneous transition to the complete-wrapped or deep-wrapped state are given by S_{22}.

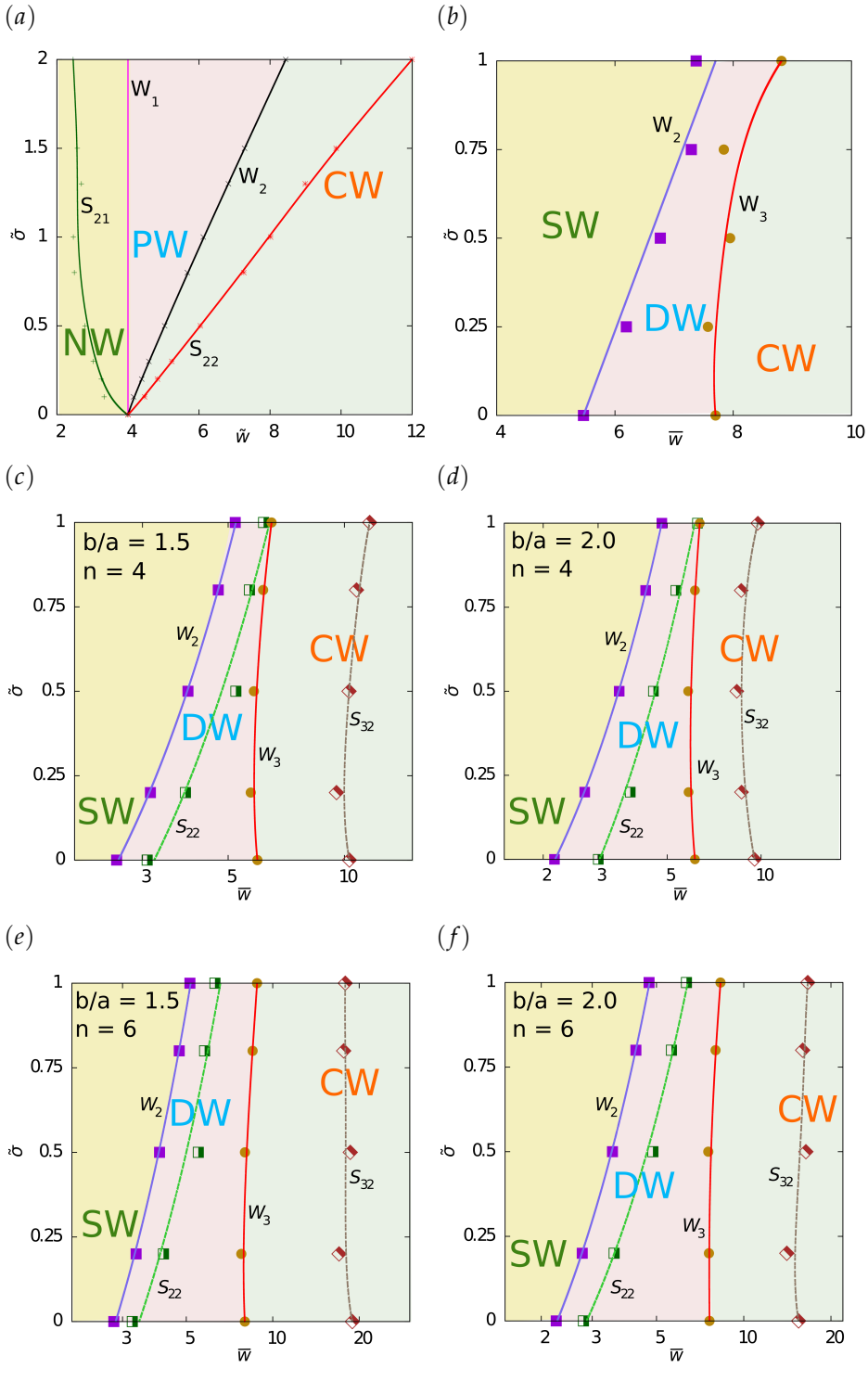

Figure S6: Wrapping phase diagrams for a spherical particle of radius a, (b) a nano-cube with edge-length $2a$ and (c-f) nano-rods of varying shapes with short axes of length a. For the spherical particle we find non-wrapped (NW), partially-wrapped (PW) and complete-wrapped (CW) states; for cube-like and rod-like particles we find shallow wrapped (SW), deep-wrapped (DW), and complete-wrapped (CW) states. To facilitate the comparison for particles with the same size a, the phase diagrams are plotted for $\bar{w} = 2wa^2/\kappa$, where $\tilde{w}/\bar{w} = A/4\pi a^2$.

References: Chapter 2 (Supplementary material)

1 M. Deserno, *Phys. Rev. E.*, 2003, **69**, 031903.

2 S. Dasgupta, T. Auth and G. Gompper, *Soft Matter*, 2013, **9**, 5473–5482.

3 A. H. Bahrami, *Soft Matter*, 2013, **9**, 8642–8646.

4 B. D. Chithrani, A. A. Ghazani and W. C. W. Chan, *Nano Lett.*, 2006, **6**, 662–668.

5 B. D. Chithrani and W. C. W. Chan, *Nano Lett.*, 2007, **7**, 1542–1550.

6 S. E. A. Gratton, P. A. Ropp, P. D. Pohlhaus, J. C. Luft, V. J. Madden, M. E. Napier and J. M. DeSimone, *Proc. Natl. Acad. Sci.*, 2008, **105**, 11613–11618.

7 Y. Qiu, Y. Liu, L. Wang, L. Xu, R. Bai, Y. Ji, X. Wu, Y. Zhao, Y. Li and C. Chen, *Biomaterials*, 2010, **31**, 7606–7619.

8 A. G. Cherstvy and E. Petrov, *Phys. Chem. Chem. Phys.*, 2013, Advance online publication, doi:10.1039/C3CP53433B.

9 R. Vácha, F. J. Martinez Veracoechea and D. Frenkel, *Nano Lett.*, 2011, **11**, 5391–5.

10 Y. Wang, K. C. L. Black, H. Luehmann, W. Li, Y. Zhang, X. Cai, D. Wan, S.-Y. Liu, M. Li, P. Kim, Z.-Y. Li, L. V. Wang, Y. Liu and Y. Xia, *ACS Nano*, 2013, **7**, 2068–2077.

11 G. Gompper and D. M. Kroll, Statistical Mechanics of Membranes and Surfaces, 2004.

12 K. A. Brakke, *Exp. Math.*, 1992, **1**, 141–165.

13 C. Huang, Y. Zhang, H. Yuan, H. Gao and S. Zhang, *Nano Lett.*, 2013, **13**, 4546–4550.

4
Membrane-wrapping contributions to malaria parasite invasion of the human erythrocyte

4.1
Abstract

The blood stage malaria parasite, the merozoite, has a small window of opportunity during which it must successfully target and invade a human erythrocyte. The process of invasion is nonetheless remarkably rapid. To date, mechanistic models of invasion have focused predominantly on the parasite actomyosin motor contribution to the energetics of entry. Here, we have conducted a numerical analysis using dimensions for an archetypal merozoite to predict the respective contributions of the host-parasite interactions to invasion, in particular the role of membrane wrapping. Our theoretical modeling demonstrates that erythrocyte membrane wrapping alone, as a function of merozoite adhesive and shape properties, is sufficient to entirely account for the first key step of the invasion process, that of merozoite reorientation to its apex and tight adhesive linkage between the two cells. Next, parasite-induced reorganization of the erythrocyte cytoskeleton and release of parasite-derived membrane can also account for a considerable energetic portion of actual invasion itself, through membrane wrapping. Thus, contrary to the prevailing dogma, wrapping by the erythrocyte combined with parasite-derived membrane release can markedly reduce the expected contributions of the merozoite actomyosin motor to invasion.Wetherefore propose that invasion is a balance between parasite and host cell contributions, evolved toward maximal efficient use of biophysical forces between the two cells.

4.2
Introduction

The asexual cycles of infection, through replication, rupture, and reinfection of human erythrocytes by *Plasmodium* parasites are responsible for all malaria disease pathology. Extensive effort has focused on understanding the cellular and molecular basis for each stage of the process, invasion in particular, with a view to designing novel chemotherapeutics or vaccines to prevent or treat the disease [1]. Invasion of the erythrocyte itself is mediated by the blood stage parasite, called the merozoite, which is thought to use an internal molecular motor based on actin and myosin to drive itself into the red cell [2]. Conceptually, the process can be

divided into discrete steps, defined by a range of imaging studies using electron [3–5], tomographic [6], fluorescence [7–10], and video microscopy [11,12] as shown schematically in Fig. 1. Invasion commences with low affinity, long-range (12 to 40 *nm*), and nondirectional binding of the erythrocyte by the merozoite, which then reorients such that the merozoite apex directly contacts the target cell.

Formation of a close-range interaction follows (4 *nm* or less), leading to the establishment of an erythrocyte-merozoite tight junction [3,4]. This critical structure, seen as an electron dense zone between erythrocyte and merozoite by electron microscopy, is the organizing nexus around which invasion events appear to be orchestrated. It acts as the aperture through which the merozoite passes during invasion and segregates erythrocyte membrane from an emerging vacuolar membran (likely parasite membrane-derived in part), which fuses to form the parasitophorous vacuole into which the parasite moves and develops postinvasion (see [3,14], and references therein). Each of these steps is facilitated by an array of merozoite surface proteins (MSPs), which permanently pattern the parasite surface, and apically secreted parasite antigens, released at egress from the infected cell before reentry. Many of the latter group are lead candidates for inclusion in developmental blood stage vaccines, including the apical membrane antigen (AMA)-1, erythrocyte binding antigens, and reticulocyte binding antigen homolog (Rh) proteins, which interact to varying degrees, and at varying distances, with erythrocyte membrane componen [1].

Several studies have attempted to map out a broad model of invasion, incorporating the breadth of molecular and cellular events (e.g., [7,9,10]). However, few studies have taken into consideration the biophysical interactions between host and parasite cells, in particular the contribution that the erythrocyte membrane and underlying cytoskeleton might play [15]. This has largely been influenced by longstanding evidence that activity of the parasite actomyosin motor alone defines successful host-cell entry [16,17]. Surprisingly, such a parasite-centric model is quite unique among human intracellular pathogens, which almost universally employ a degree of host involvement in invasion [18]. Instead, its broad acceptance relies heavily on the general perceived inactivity of the mature erythrocyte [19] and studies using the related apicomplexan parasite, *Toxoplasma gondii*, which, until recently, was believed to invade independently of host-cell remodeling processes [20]. Recently, this view has started to be challenged by studies showing that host cell cytoskeletal rearrangements do occur during *Toxoplasma* and nonerythroid *Plasmodium* invasion [21] and the recent demonstration of a residual level of invasion in the absence of myosin and actin in *Toxoplasma* [22]. These studies clearly suggest that a role of processes other than motor-driven force production in facilitating apicomplexan invasion deserves focused attention.

Certainly, there is a body of evidence that the erythrocyte responds, at least minimally, to invasion both physically, with the membrane oscillating or flexing [11–13], and biochemically (reviewed in [19]). The physical response, with visible folds on parasite binding, is expected for a membrane that has a shear modulus [23,24], which is caused by the regular spectrin network that supports the erythrocyte membrane [25,26]. Biochemical contributions have also been widely studied, and hint at a potential membrane contribution to the parasitophorous vacuole [14].

To date, however, no strong evidence exists to suggest an energetic contribution to invasion from the erythrocyte.

Here, we have sought to assess the energetic contributions of the *Plasmodium* parasite and wrapping by the erythrocyte and parasite-derived membranes to invasion. In contrast to previous membrane wrapping calculations that have explored models involving spherical, ellipsoidal, or rod-like particles [27–34], we have uniquely incorporated the asymmetrical egg-like shape of the merozoite, which influences differentially wrapped states. Using numerical calculations of membrane interactions and membrane wrapping processes between an experimentally determined archetypal egg shaped merozoite and the erythrocyte, we present evidence that membrane wrapping of the erythrocyte can account for merozoite reorientation to its apex in an entirely parasite energy independent manner. Furthermore, a considerable portion of the energy requirements for subsequent stages of full parasite invasion (i.e., for complete membrane wrapping) can also be achieved through parasite-induced modifications to the erythrocyte membrane and by parasite-injected membrane material that may alter surface tension and spontaneous curvature of the wrapping membrane. Wrapping under these conditions requires only a small energetic input from the parasite actomyosin motor for entry, i.e., overcoming energy barriers between stable membrane-wrapped states. Seen in this light, we propose that erythrocyte invasion should be considered as evolved toward a state of maximal energetic efficiency, exploiting both innate host cell properties and parasite motor force to facilitate complete entry.

Our article is organized as follows.We first use cryo-x-ray tomography to construct an idealized merozoite that approximates the experimentally observed merozoite shape. We then calculate the energetic contributions of membrane wrapping to merozoite reorientation and subsequent invasion into the erythrocyte, using a model with bending-rigidity and membrane tension contributions for the curvature elastic energy of the erythrocyte membrane, an adhesive interaction between the merozoite and the erythrocyte, and a line tension for the tight junction. For several parameter values in our theoretical model, we quantify the required motor force for invasion. Finally, we summarize our complete biophysical model for merozoite invasion assessing likely contributions of the actomyosin motor of the merozoite and wrapping energy contributions of the erythrocyte membrane.

4.3
Materials and methods

4.3.1
Experimental derivation of merozoite dimensions

The culture of *Plasmodium falciparum* parasites using donated blood from the Australian Red Cross Society has been approved by The Walter and Eliza Hall Institute Human Ethics (HEC 86/17) Committee. *P. falciparum* parasites (from a D10 parental strain [35]) were maintained using standard culturing procedures in human O+ erythrocytes at 4% hematocrit with 0.5 % wt/vol Albumax II (Life Technologies,

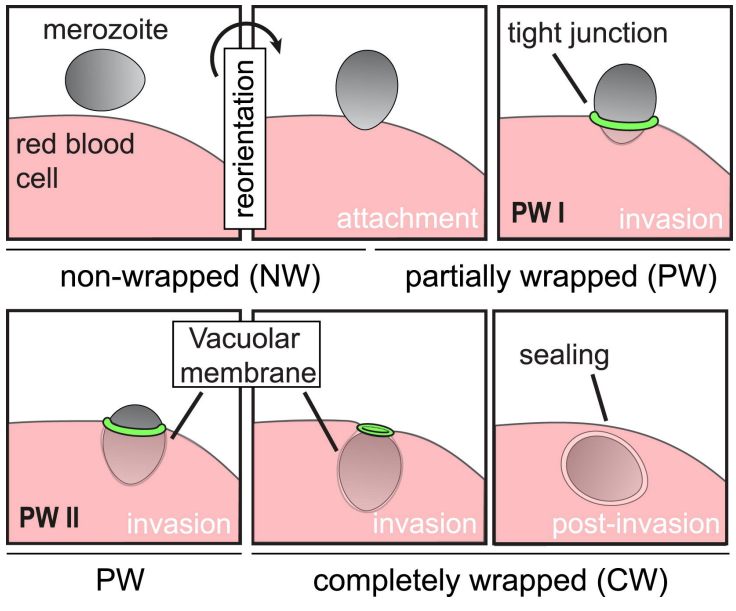

Figure 1: The stages of merozoite invasion. Schematic representation depicting different wrapping phases of the merozoite from reorientation through to invasion and postinvasion (see below for definitions of wrapped states).

Grand Island, NY). Cultures were maintained in synchrony using 5 % Sorbitol treatment or via treatment with 30 infectious units ($\sim 230 \mu g/mL$) heparin (Pfizer) [35] and cultured through to schizogony for merozoite isolation. Free merozoites were filtered through a 1.2 μm, 32 mm syringe filter (Sartorius Stedim Biotech, Epsom, UK) as described [35], and then cryo-preserved for X-ray analysis and imaged as detailed previously [6]. Merozoite dimensions, volume, and surface area were calculated on rendered tomographic images following segmentation and alignment with IMOD with rendering via Blender (www.blender.org).

4.3.2 Deformation energy calculations and dimensionless parameters for erythrocyte-membrane wrapping

Toward calculating the energetic costs required to deform the erythrocyte membrane sufficiently to facilitate complete invasion, we decoupled the invasion process into two critical energetic steps (see Fig. 1): i), reorientation of the merozoite toward its apex (the site at which adhesive proteins are released and the required direction for successful invasion [11]); and ii), invasion itself (movement through the tight junction into the erythrocyte [3]). The physics of wrapping that characterizes the adhesion contribution to both reorientation and invasion is governed by bending energy and tension of the erythrocyte membrane, the contact energy between merozoite surface and erythrocyte membrane, and the line tension at the

position of the tight junction where the merozoite squeezes through. Thus, the total energy required is

$$\mathcal{E} = \mathcal{E}_{\text{bending}} + \mathcal{E}_{\text{membrane tension}} + \mathcal{E}_{\text{adhesion}} + \mathcal{E}_{\text{line tension}} \ . \tag{4.1}$$

To calculate the total energy for the erythrocyte with the adhered merozoite, bending rigidity and membrane tension, adhesion strength, and line tension contributions are integrated over the entire membrane area, $\mathcal{S}_{\text{erythrocyte}}$, the adhered membrane area, $\mathcal{S}_{\text{adhered}}$, and the length of the contact line where the erythrocyte membrane detaches from the merozoite, respectively, so that

$$\mathcal{E} = 2\kappa \int_{\mathcal{S}_{\text{erythrocyte}}} dS(H - c_0)^2 + \sigma \int_{\mathcal{S}_{\text{erythrocyte}}} dS - w \int_{\mathcal{S}_{\text{adhered}}} dSH + \gamma \oint_{\text{contact line}} dl \ . \tag{4.2}$$

The various contributions to Eq. 2 are explained in more detail below. We calculate the energy on the parasite surface only assuming the outer membrane to be flat, i.e., we employ a cap-like model analogous to the model used in [36]. We do not account for a direct contribution of the shear modulus of the red blood cell membrane, because we assume that successful invasion requires a destruction of the cytoskeleton on the membrane that wraps the merozoite. However, in our model the cytoskeleton around the merozoite remains intact and contributes to the line tension γ. Details of the numerical calculations are described in the Supporting Material.

Membrane wrapping of the merozoite can be understood as a competition between two energetic contributions: the elastic deformation energy of the membrane adhered to the merozoite and the specific contact interaction between merozoite and membrane. Note that the vacuolar membrane enveloping the merozoite after successful invasion is likely composed of both erythrocyte membrane and parasite-derived vacuolar membrane (added differentially during the stages of invasion stage). A key determinant for the membrane model is the curvature elasticity of the erythrocyte membrane, with bending rigidity κ, where the energy required for bending the membrane is determined by the squared mean curvature H^2 of the membrane at every point [37]. The mean curvature is $H = (c_1 + c_2)/2$, with c_1 and c_2 being the principal curvatures corresponding to the maximum and minimum curvatures at each point of the membrane (38). The preferred average shape of the membrane is characterized by its spontaneous curvature c_0. A finite value for c_0 indicates that either the membrane or its surrounding is asymmetric and that consequently the preferred shape of the membrane is not flat, a feature clearly applicable to the erythrocyte [39,40]. The bending energy is complemented by an energetic cost for the excess membrane area characterized by the membrane tension σ. This excess area can either be attributed to flattening out part of the intrinsic membrane fluctuations [41,42] or to other mechanisms. The tension term contains a contribution from the spectrin network that is adsorbed to the membrane [26,43].

For the merozoite to successfully enter the erythrocyte, the energy gain due to the contact of merozoite surface and the enveloping membrane must be sufficiently large, such that the completely wrapped state corresponds to the lowest energy.

Furthermore, wrapping alone also requires a downhill pathway in the energy landscape, but–as discussed later–the actomyosin motors of the parasite may help to overcome energy barriers. A measure for both nonspecific adhesion and receptor binding is given by the adhesion strength w. Individual protein-mediated adhesion may couple to the membrane shape via membrane proteins that prefer curved regions [44–47], and we therefore assume in our model that the adhesion strength is dependent on the mean local membrane curvature H (if not stated otherwise). This also allows us to implement higher adhesion strengths at the tip-shaped apex of the merozoite, which accounts for the secretion of adhesion molecules from this region of the parasite (see description below). However, other distributions of receptors and thus adhesion strength are also possible including a homogeneous receptor distribution on the parasite surface, but will not change our general conclusions.

To complete the energetic contributions during invasion, we associate a line tension γ with the tight junction [3,4], where the parasite squeezes through the erythrocyte membrane into the nascent parasitophorous vacuole [14]. The line tension may arise either from proteins within the tight junction itself, from lipid segregation next to the entering cell [48–50], from stretching of the cortical spectrin cytoskeleton underlying the erythrocyte membrane, from sharp bending of the membrane next to the tight junction, or a combination of these contributions. Either way it acts as a natural demarcation line between regions with different biophysical properties: the membrane at the site of invasion within the boundaries of the line tension and the membrane beyond (i.e., outside of the boundary of the line tension), where the spectrin cytoskeleton is expected to remain intact.

The parameters κ, c_0, σ, w, and γ together with the shape of the merozoite thus determine the energetic cost for the erythrocyte membrane deformation required for entry. These parameters are illustrated in Fig. S1 (see the Supporting Material). Electron microscopy images in Fig. S2 A show close contact of the merozoite and the erythrocyte membrane that motivates the adhesion energy contribution.

The absolute values for the model parameters can be translated into dimensionless parameters using the radius of a sphere with the same surface area as the parasite a , as the basic length scale of the system, and the membrane bending rigidity κ as the energy scale. These dimensionless parameters indicated by a tilde, $\tilde{c}_0 = c_0 a^2 H_0$, $\tilde{\sigma} = \sigma a^2/2\kappa$, $\tilde{w} = (wH_0 4\pi a^2)/2\kappa$, and $\tilde{\gamma} = \gamma a/2\kappa$. The average mean curvature of the merozoite can be calculated as surface integral using the archetypal merozoite defined in the next section, $H_0 = \int_{\text{merozite}} dSH / \int_{\text{merozite}} dS = 2.5/a$.The spontaneous curvature can be used to construct an effective adhesion strength, $\tilde{w}_{eff} = \tilde{w} + \tilde{c}_0$, and and effective surface tension, $\tilde{\sigma}_{eff} = \tilde{\sigma} + \tilde{c}_0^2/(aH_0)^2$, such that the phases for different values of the spontaneous curvature can be extracted using the effective parameter values.

4.4
Results and discussions

4.4.1
An archytepal merozoite

To calculate the contribution of erythrocyte membrane wrapping to malaria parasite invasion, we first had to develop a standardized model of a blood stage parasite. Deriving figures for such a cell from any imaging approach is not trivial, because each naturally produces errors as a result of cryopreservation or fixation with wide associated variances [6]. We have recently shown that cryo-x-ray tomography preserves physical parameters of the blood stage merozoite most accurately [6]. Using this approach, we derived experimental measurements from 11 reconstructions of cryopreserved merozoites for length and width as well as estimates for mean volume and surface area. This enabled us to mathematically define an archetypal merozoite(Fig. 2, A–B).

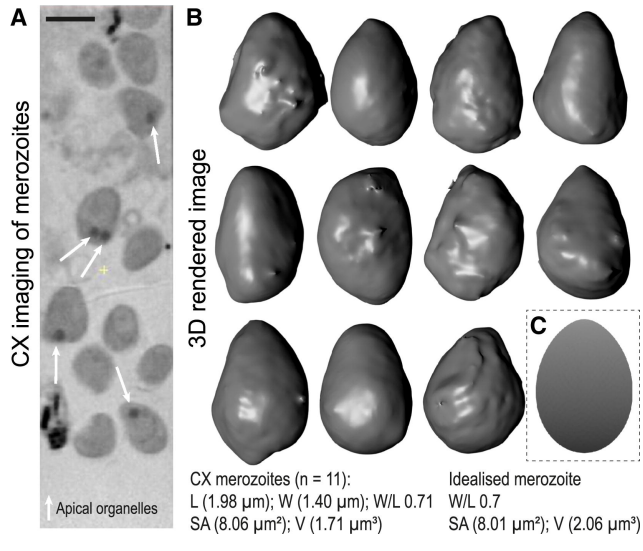

Figure 2: Defining an idealized archetypal merozoite. (A) A section through cryo-x-ray imaged free *P. falciparum* merozoites cryopreserved in a capillary. Apical secretory organelles (specifically rhoptries) are visible as dense spots indicated by arrows. (B) Isosurface rendered merozoites from (A). (C) The idealized archetypal merozoite simulated as an asymmetrical egg-shaped rigid particle.

Mean physical measurements were $L = (1.98 \pm 0.08)\,\mu m$ length, $W = (1.40 \pm 0.06)\,\mu m$ width, with volume and surface area averaging $V_{actual} = (1.71 \pm 0.15)\,\mu m^3$ and $A_{actual} = (8.06 \pm 0.72)\,\mu m^2$, respectively, where the errors are given by the standard deviations of the measurements. These dimensions give a width/length ratio of the egg-shaped merozoite as 0.71. These measurements led to a model particle that allows a mathematical description of merozoite shape with a pointed apex and rounded base (as shown in Fig. 2 C). This was used throughout subsequent ener-

getic calculations. It is currently unclear whether surface convolutions observed at the macroscopic level are indicative of a native ruffled organization at the merozoite surface or an artifact of imaging. For modeling purposes, we therefore assume (conservatively) that the merozoite has a smooth surface. Conceptually, incorporation of ruffling or rippling would provide additional contact area and thus adhesion energy, but would also increase the bending-energy costs.

The egg shape of the merozoite is defined by $(x^2+y^2+z^2)^2 = R_a x^3 + (R_a - R_b)x(y^2+z^2)$ with $R_a = 1\,\mu m$ and $R_b = 0.7\,\mu m$, which also describes the shape of a chicken egg [51]. We find good agreement for surface area ($A_{idealized}$) and volume ($V_{idealized}$) of this idealized merozoite with the values measured experimentally. We use two constants, k_1 and k_2, where $A_{idealised} = k_1 L^2$ and $V_{idealised} = k_2 L^3$ to characterize the shape. For the idealized merozoite, $k_1 = 2.04$, giving $A_{idealised} = k_1 L^2 = 8.01\,\mu m^2$. The surface area derived from rendered X-ray images of the merozoite solves k_1 as $A_{actual}/L^2 = 2.06$. For the idealized merozoite, we find $k_2 = 0.27$, giving $V_{idealised} = k_2 L^3 = 2.08\,\mu m^2$. The volume measured from the rendered x-ray images above solves k_2 as $V_{actual}/L^3 = 0.22$. Comparison of the surface area of the idealized merozoite with the surface area of a sphere, $4\pi a^2 = 8.01\,\mu m^2$, defines a characteristic length scale $a = 0.8\,\mu m$ for the wrapping model described below.

4.5 Merozoite attachment and reorientation via erythrocyte membrane wrapping

Merozoites, at egress from the infected erythrocyte, are released into the blood stream with an array of surfacebound membrane proteins (MSPs) [1]. Concurrent with release, apical organelles (specifically the micronemes) commence secretion of additional classes of high-affinity binding ligands onto the surface, which diffuse toward the merozoite base [7,10,52,53]. This defines a two-stage adhesive surface potential ranging from low affinity and evenly distributed at egress to high affinity, with an apical bias, before or at commencement of the invasion process beginning with reorientation.

Traditionally, merozoite reorientation has been viewed as occurring either via random rolling of the parasite or being entirely parasite driven [13] with few studies considering host-cell membrane dynamics [15,39]. In the absence of directional motility(which has not been described for the free merozoite), we expect the merozoite to hit a target erythrocyte in random orientation. This primary, loosely attached state (governed by surface MSPs) involves very shallow wrapping and is clearly reversible[11,12]. To reach a state of stable attachment, the energy gain due to the adhesion strength has to exceed the bending-energy cost for wrapping the erythrocyte membrane around the merozoite. Because the tight junction has not yet formed at reorientation and the membrane is not yet stretched, Eq. 2 reduces to its first and third term only [28], i.e., reorientation in our model is determined by the membrane bending rigidity and the adhesion strength only.

By comparing the bending energy and the adhesion energy at the point of contact, we find the critical adhesion strength w^* (or the dimensionless value $\tilde{w}^* = w^* a^2/2\kappa$). The bending-energy cost is proportional to the squared local mean cur-

vature of the merozoite and, for a homogeneous adhesion strength on the merozoite surface, binding with the least curved point at the side of the merozoite is thus energetically favorable. The distribution of local adhesion strength, which is required to induce merozoite adhesion in all orientations with equal probability, is plotted in Fig. 3. From the minimal reduced adhesion strength $\tilde{w}^* = w^* a^2/2\kappa = 5$, we can estimate a minimal adhesion strength for this stable attached binding as $w^* = 10^{-4}\, k_B T/nm^2$ for an archetypal merozoite with $a = 0.8\,\mu m$ and bending rigidity $\kappa = 50\, k_B T$. This value is below those of conventional receptor-ligand bonds (e.g., involved in viral invasion [54]), which could be expected for the invasion proteins known to be present on the merozoite's surface during entry. Thus, at reasonable levels of surface-protein binding to the erythrocyte membrane a minimal adhesion strength readily leads to stable attachment of the nonorientated merozoite.

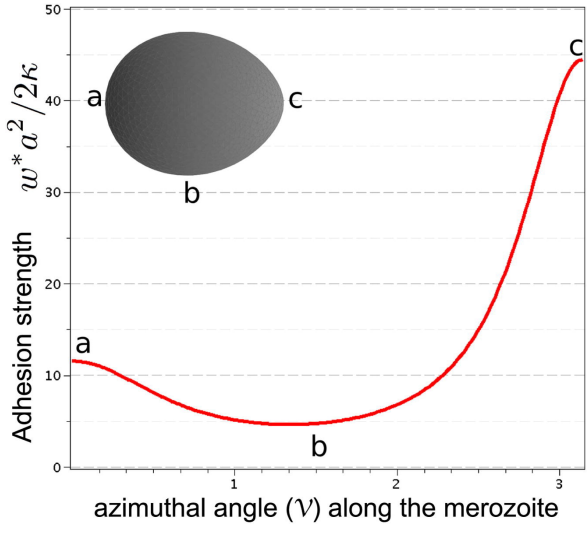

Figure 3: Modeling adhesive interactions between the merozoite and erythrocyte. Calculated threshold adhesion strength (using Eq. 1 with bending and adhesion terms only) $w^* a^2/2\kappa$ for attachment of the merozoite as a function of the azimuthal angle in a polar representation of the merozoite shape: (a) $v = 0$, (b) $0 > v > \pi$, and (c) $v = \pi$ correspond to the flat basal end, the side, and the apex adhered to the membrane, respectively (see Materials and Methods).

To achieve a tip-first orientation of the merozoite, a gradient of the adhesion strength that favors attachment of the tip over other orientations is required. As discussed previously, such a gradient of adhesion strength from apex to base is entirely reasonable. Apical membrane antigen 1 (AMA-1), is translocated onto the merozoite surface at parasite egress [53], existing in a clear apical-basal gradient, which then freely diffuses around the merozoite periphery [52]. To achieve reorientation each newly formed adhesion toward one end will require detachment at the side opposing the rolling direction. As long as the difference of the sum of adhesion and bending energy between newly formed and lost adhesion sites is negative, an

energy funnel will drive merozoite rolling and reorientation. The adhesion strength at the tip has to be about nine times higher than at the side of the merozoite for it to reorient to the apex.

Evidence that inhibition of AMA-1 function disrupts merozoite reorientation directly supports its involvement in apical realignment by a natural apical-basal adhesive gradient [55]. Wrapping forces and their change down an energy gradient during reorientation alone could therefore entirely explain apical reorientation without a need for parasite motor force or for host membrane buckling. Entrapment in metastable states that correspond to local minima in the energy landscape for reorientation may be overcome by additional input of energy from motor forces. Evidence for the low rates of invasion efficiency of free merozoites, however, could suggest that arrest in such energetic dead ends is a major cause for failed invasion [35].

4.6 Merozoite invasion via erythrocyte membrane wrapping

We next sought to determine the contribution of membrane wrapping for the actual process of invasion. True invasion, involving formation of a junction and a nascent parasitophorous vacuole, is only initiated once apical reorientation has occurred [11]. At this point in time, three key cellular and molecular events occur: 1), secretion of a complex of proteins across the erythrocyte membrane that likely define two sides of the merozoite erythrocyte tight junction; 2), secretion of membrane material from parasite apical stores (namely the rhoptries); and 3), activation of a parasite actomyosin motor. Toward assessing how the contributions of membrane-wrapping might facilitate invasion, post attachment and reorientation, we calculated numerically phase diagrams of the wrapping states of the system based on the native tip-first orientation and the global minimum in the energy landscape for a given adhesion strength (Fig. 4).

In Fig. 4 A, the state of the system is characterized by adhesion strength w, membrane tension σ, and for a fixed line tension γ, i.e., a fixed energy cost per length for the tight junction between parasite and red cell. The value that we used for the line tension, $\sim 0.1\ k_{\mathrm{B}}T/nm$ is comparable to the line tension at lipid domain boundaries [56], and might mimic a line tension due to protein aggregation. However, our model does not rely on this specific value and can be used for any value of the line tension that might be generated by one of the other mechanisms described in the Materials and Methods section. In Fig. 4 B, we show a phase diagram for vanishing membrane tension and the phases are plotted for various values of adhesion strength and line tension. In both phase diagrams, we find parameter regimes where the merozoite is free (non wrapped, NW), where it is partially wrapped by the erythrocyte membrane (PW I and PW II), and where it is completely wrapped (CW) (see also Fig. 1). A more detailed discussion of the phase diagrams can be found in the Supporting Material.

For small adhesion strengths, the merozoite does not attach to the erythrocyte (NW). For higher adhesion strengths, PW I, PW II, and CW states are found. From

a physical point of view, adhesion strengths $5 \geq \tilde{w} \leq 15$, where partially wrapped states are found, are likely of most significance with regard to invasion energetics. The values of w for the transition to wrapped states are given by the phase boundaries between the NW regime to PW regimes (W_0 and the part of W_1 for small surface and line tensions) and the boundary between NW and CW regimes (E). For low surface tensions ($\tilde{\sigma} < 7.5$) there is an energy barrier between PW states with a small and high wrapping fractions, whereas for a large enough surface tension ($\tilde{\sigma} \geq 7.5$), the energy barrier between PW I and PW II disappears and the wrapping fraction increases continuously with the adhesion strength. Large adhesion strengths allow immediate complete wrapping and erythrocyte entry, but might also be associated with unspecific binding to other membranes and problems associated with membrane surface-coat shedding. Thus, lower affinity interactions seem to be favorable. Fig. 4 shows that a minimal value $\tilde{w} = 5 - 7$ is large enough to generate a stable, PW state. Successful invasion requires an end state in the CW region of the phase diagram. However, if the energy barrier of the transition to the CW state is high but invasion is assisted by additional forces, such as motor forces (see below), successful invasion might occur already for smaller adhesion strengths.

Fig. 5 shows the critical wrapping fractions of the merozoite surface area between which the W_1 and W_2 transitions (shown in Fig. 4 A) occur as a function of the reduced adhesion strength for a reduced line tension $\tilde{\gamma} \approx 0.20$. In the PW region I, tip-wrapped states (as experimentally observed in early stages of invasion) occur with 20 % of the merozoite surface area in contact with the erythrocyte. States with a higher wrapping fraction of the merozoite up to 90 % are found in the PW region II. In Fig. 5 the hatched regions correspond to unstable states that form the energy barriers associated with the discontinuous phase transitions. The unstable region between the PW states vanishes for adhesion strengths larger than $\tilde{w} = 12$, which corresponds to the critical point in Fig. 4 A.

The line tension, at which the erythrocyte membrane detaches from the merozoite, is a key determinant for the stability of PWstates, both hindering the entry of the parasite for early stages and favoring wrapping at later stages (Fig. 4 B, *arrow d*). This contact line, seen as an electron-dense zone in electron micrographs [3,6], must be stretched at the onset of entry and will contract after the point of maximal diameter of the merozoite has passed. In the phase diagram in Fig. 4 B, invasion is considered with respect to wrapping states across values of line tension and adhesion strength, while keeping the adhesion strength fixed. For small values of the line tension, PW states with high wrapping fraction are found, whereas for large values of the line tension (larger than $\tilde{\gamma} \approx 0.35$) the transition occurs directly from the free, NW state to the CW, invaded state. In this way, a robust line tension helps to facilitate complete invasion and avoid PW states with high wrapping fraction. Thus, from a biological point of view, there are clear adaptive advantages associated with formation of a demarking tension between the parasite and host cell. This may in part explain the origin of the tight junction as a strategy for differentiating between membrane regions and contributing to reducing the energetic requirements for reaching an invaded state rather than, necessarily, only as a point of motor traction [16].

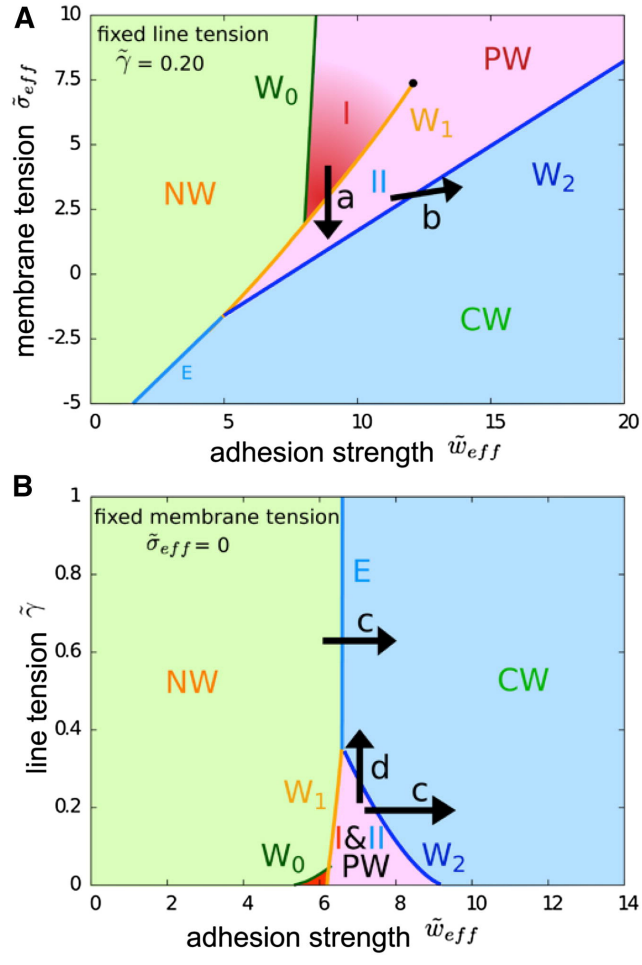

Figure 4: Wrapping phase diagram for fixed line tension or membrane tension. (A) Wrapping states of the system of a tip-first-oriented merozoite for fixed reduced line tension $\tilde{\gamma} = 0.20$ and several values of effective adhesion strength and effective membrane tension: non wrapped merozoite (NW), partially wrapped merozoite with small (PW I) and high wrapping fractions (PW II), and completely wrapped/fully invaded merozoite (CW), see Fig. 1. The transition W0 is a continuous transition, whereas the transitions W_1, W_2, and E are associated with energy barriers. The transition W_1 ends at a critical point where the difference between PW I and PW II vanishes. The terms in Eq. 2 can be rearranged, such that the spontaneous curvature c_0 can be combined with the membrane tension and the adhesion strength to an effective membrane tension, $\sigma_{eff} = \tilde{\sigma} + \tilde{c}_0^2/(aH_0)^2$, and an effective adhesion strength, $\tilde{w}_{eff} = \tilde{w} + \tilde{c}_0$, respectively. The critical point is indicated by a black point (•). (B) Wrapping states of the system of a tip-first-oriented merozoite for vanishing effective membrane tension, $\tilde{\sigma}_{eff} = 0$, and several values of effective adhesion strength and line tension. The notation is analogous to A. Both phase diagrams with additional wrapping spinodals that indicate the values of the adhesion strength beyond which the energy barrier vanishes and spontaneous wrapping occurs, are shown in Fig. S3. However, the energy barriers may also be crossed by other mechanisms: arrow a indicates the effect of unstructured membrane secreted by the merozoite (Fig. S2B), arrow b shows the effect of favorable spontaneous curvature, arrow c the effect of increased adhesion strength, and arrow d the effect of increased line tension.

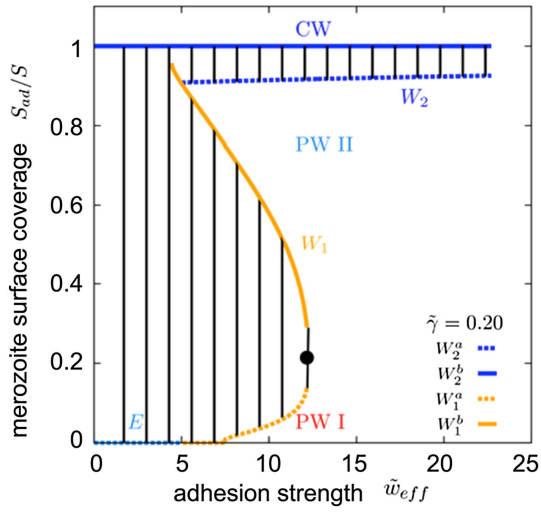

Figure 5: Merozoite surface coverage for different adhesion strengths. Merozoite surface coverage for different adhesion strengths and reduced line tension $\tilde{\gamma} = 0.20$. W_1, W_2, and E, are the phase boundaries and lines demarking equal energy of free and CW states, see Fig. 4 A. The critical point is indicated by a black point (•). The wrapping fractions where the system jumps between discontinuous transitions are indicated using the dotted or the solid lines, corresponding states are connected by tie-lines. W_1^a and W_2^a indicate lower, whereas W_1^b and W_2^b higher wrapped fractions of the merozoite surface area for the W_1 and W_2 transitions, the two phase regions in the phase diagram indicated by the black tie-lines are unstable and correspond to the energy barriers.

During the invasion process, experimental evidence clearly shows both secretion of unstructured membrane by the merozoite (discharged from the rhoptry organelles) and gross changes in the membrane curvature of the erythrocyte [6,7,13,57] (Fig. S2 B). The effect of such events on the status of invasion can be directly interpreted in light of the phase diagram in Fig. 4. When the lipid bilayer area of the erythrocyte is increased by additional unstructured membrane from the parasite, the tension of the membrane that wraps the merozoite is lowered considerably. This corresponds to a move in the wrapping diagram from a PW to a CW state (Fig. 4 A, *arrow a*). In addition to extra membrane area being provided, the unstructured nature of this membrane as well as any detachment or reorganization of the spectrin cytoskeleton from the bilayer [19,39] can change the spontaneous curvature of the membrane to a value that is more favorable for wrapping (Fig. 4 A, *arrow b*). Mathematically, the spontaneous curvature can be taken into account using the effective adhesion strength and the effective surface tension, otherwise leaving the wrapping phase diagrams unchanged (see Materials and Methods). These results point to specific benefits that would arise from local disruption of the spectrin network, either directly or indirectly, by the merozoite, something that has been observed empirically by electron microscopy of invading parasites [58].

4.6.1 Merozoite invasion supported by motor activity

Having explored the role of adhesive forces (from parasite invasion adhesins), bending rigidity, membrane tension, line tension, and spontaneous curvature of the erythrocyte membrane to membrane wrapping states, we next sought to estimate the degree of active forces required from the parasite to overcome energy barriers and facilitate transitions to completed invasion. The current model for the source of parasite active motor force posits that an anchored myosin motor inside the parasite cell (directly tethered to a cytoskeletal compartment within the cell pellicle) transmits force directly through a short polymerized actin filament, which itself is linked to the surface-bound adhesin. The binding of this surface adhesin to a red cell receptor and their combined passage towards the base of the merozoite length (through the fluid plasma membrane) is then thought to generate a rearward force driving the parasite forward (Fig. 6, A and B) [59].

Two energetic events could be envisaged to require the force generated by this actomyosin motor: breaking or moving aside of the erythrocyte cytoskeleton at the site of invasion (to allow entry) and overcoming wrapping energy barriers.

At the specific site of entry, we assume that the cytoskeleton of the erythrocyte gets disassembled, which is experimentally supported by evidence that there is an erythrocytic ATP requirement for invasion [60,61] and the dependency of cytoskeletal reorganization on ATP [43,62]. This implies that, at the onset of true invasion (postattachment), the merozoite is wrapped by a membrane without an explicit contribution of the shear modulus. For local disassembly of the cytoskeleton, a stretching force would be required that may be contributed by motor activity. A rough estimate shows that for the cross-sectional area of the merozoite ($\sim 1\,\mu m^2$ [6]), a few hundred spectrin bonds would have to be broken/segregated to accommodate an entering merozoite (for a spectrin bond length of $\sim 60 - 100\ nm$, the average length between the protein complexes that bind the ends of the spectrin filaments to the lipid bilayer membrane [25]).

The second, and more obvious energetic barrier requiring parasite motor force in our model is clear from the stable states depicted in Fig. 4. For intermediate adhesion strengths, energy barriers (see the Supporting Material) separate the PW states internally (W_1) and the completely invaded state from the PW states (W_2). The energy barriers between NW and CW states decrease with increasing adhesion strength [32] but increase with increasing line tension. Spontaneous invasion from adhesion alone could only occur with unreasonably large adhesion strengths combined with a small line and surface tensions. Therefore, it is far more likely that application of force by the merozoite itself facilitates the transitions between NW, PW, and CW states. Estimates of the required motor activity to wrap the merozoite can be derived from the force calculated for merozoite invasion without adhesion energy (Fig. 6 C). The maximal force F_z (besides a very small wrapping fraction below 5 %) is of the order of $20\ \kappa/a = 1\,k_BT/nm$, or $\sim 5pN$. Typical estimates of the force related to a single, motility-dependent adhesion site for a *Plasmodium* preerythrocytic parasite on a glass substrate (though not necessarily a single motor) are $\sim 6.5\ pN$ [63]. Therefore, a small number of adhesion sites in the context

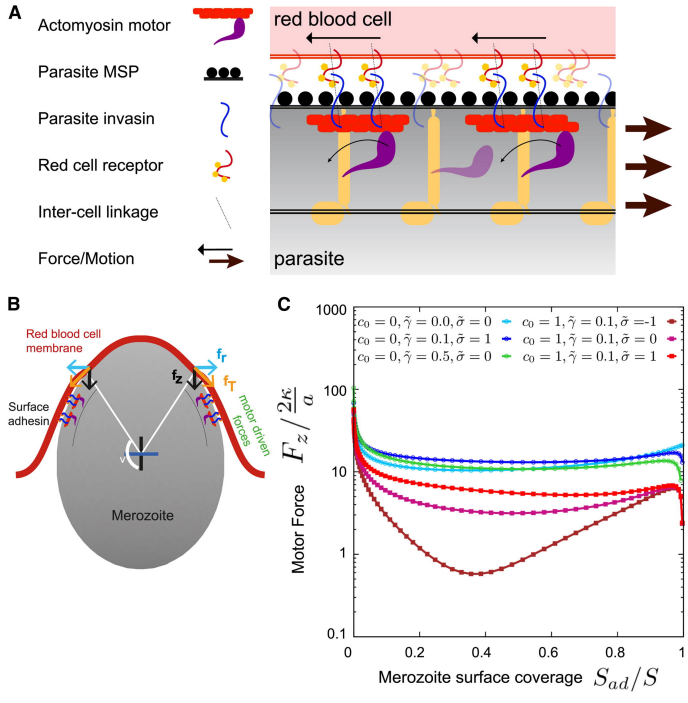

Figure 6: The contribution of motor driving forces in merozoite invasion. (A) The current model for the topology of the parasite actomyosin motor and its linkage with the red blood cell surface through secreted invasins. (B) Actomyosin force supports merozoite invasion. f_t is the force acting tangentially along the membrane-cortex surface as it wraps along the particle, whereas the f_z is the component of this tangential force along the z axis whose role is to inject the particle into the membrane while the component f_r is balanced by an equal magnitude force acting along the other side of the membrane. (C) Estimate for the motor driven forces required to push a nonadhesive merozoite into the erythrocyte membrane to achieve complete invasion. $F_z = 2\pi r f_z$, is the estimate for the total invasive force acting along the symmetry axis required to inject the merozoite as a function of the fraction of the merozoite surface covered by erythrocyte membrane; r is the radius of the rim where the merozoite detaches from the membrane.

of an invasion event could be easily sufficient to overcome the energy barriers required for entry. *T. gondii* myosin A, considered the direct ortholog of that involved in merozoite invasion [64], has a step size of 5.2 nm [65]. Although its stall force is not known, most myosin types generate forces in the order of 0.5 to 5 pN per motor molecule [66,67]. Given that myosin A is only single headed and cannot be processive, and assuming a small duty ratio of 5 % (approximately that for muscle myosin [68]), at each instant between 2 and 10 motors should be bound. Using a stochastic attachment model and assuming 5 motors are bound, invasion would require $\sim 5/0.05 = 100$ motors (lower and upper limits being 40 to 200 motors) to perform without failure under these conditions.

As shown in Fig. 6 C, the required force for invasion can be reduced by orders of magnitude if factors such as favorable spontaneous curvature of the erythrocyte membrane or expulsion of unstructured membrane accompany invasion. There is

strong evidence for both (see above), which suggests that the energetic contribution of the motor estimated previously could be much lower. Irrespective of the alternative contributions of parasite adhesion or membrane remodeling, the need for an active directional motor force, such as that generated by the parasite actomyosin machinery, cannot be eliminated: due to energy barriers between stable membrane-wrapped states (see the Supporting Material), the motor likely plays an essential role for achieving robust invasion. In this way, our modeling is consistent with experimental evidence suggesting that actomyosin motor activity is essential for merozoite invasion [16,17,64]. Residual invasion following complete motor inactivity in the related apicomplexan *T. gondii* might suggest alternative host-cell processes that are not possible in the erythrocyte (such as phagocytosis) or redundant invasion machinery in the parasite that is currently unaccounted for [22]. What is clear, however, is that at its most energy efficient, theoretical predictions for erythrocyte invasion envision a balance between passive host cell-dependent processes (nonetheless stimulated and controlled by the parasite) and those that are parasite-energy dependent. This rejects the perceived dogma wherein merozoite invasion is entirely parasite driven.

4.7
A complete biophysical model for invasion incorporating membrane wrapping

By integrating basic parasitological observations of merozoite maturation and surface protein biology with biophysical consideration of membrane wrapping, we can now propose a complete mechanistic model of invasion (Fig. 7).

At the outset, it is clear that the early stages of invasion are setup at merozoite egress from the infected erythrocyte [10,53,69]. Daughter merozoites are liberated into the blood stream (Fig. 7 A) with a surface studded evenly with MSPs, which provide low-strength reversible (and nonorientated) attachment to a target erythrocyte [1] (Fig. 7 B). At egress, a second, variable population of adhesive proteins (which we term adhesins [8]) are released apically from secretory micronemes (Fig. 7 B). Their diffusion through the merozoite plasma membrane sets up a transient adhesive gradient from apex to base on its surface (Fig. 7 B). This gradient is biologically dependent on many factors, not least the timing of release [53], and may compensate the increased bending energy cost at the apex required for merozoite reorientation. The initial apical gradient transitions the merozoite from a reversible (MSP determined) to an irreversible (adhesin determined) attached state on the target erythrocyte surface that can be sufcient alone to reorientate the merozoite without parasite energy-dependent forces (Fig. 7 C). Of note, mature merozoites with complete surface release of adhesins (and homogeneity through the plasma membrane at times tending toward $\sim$ 10 min, Fig. 7 B) will be unable to reorientate by wrapping forces alone, possibly explaining their short invasion half-life [35]. Once reorientation has occurred, the merozoite typically exists in a stable, tip-wrapped/PW state with $<$ 10 % of the parasite wrapped (Fig. 7 C and Fig. 4 and Fig. 5, PW I).

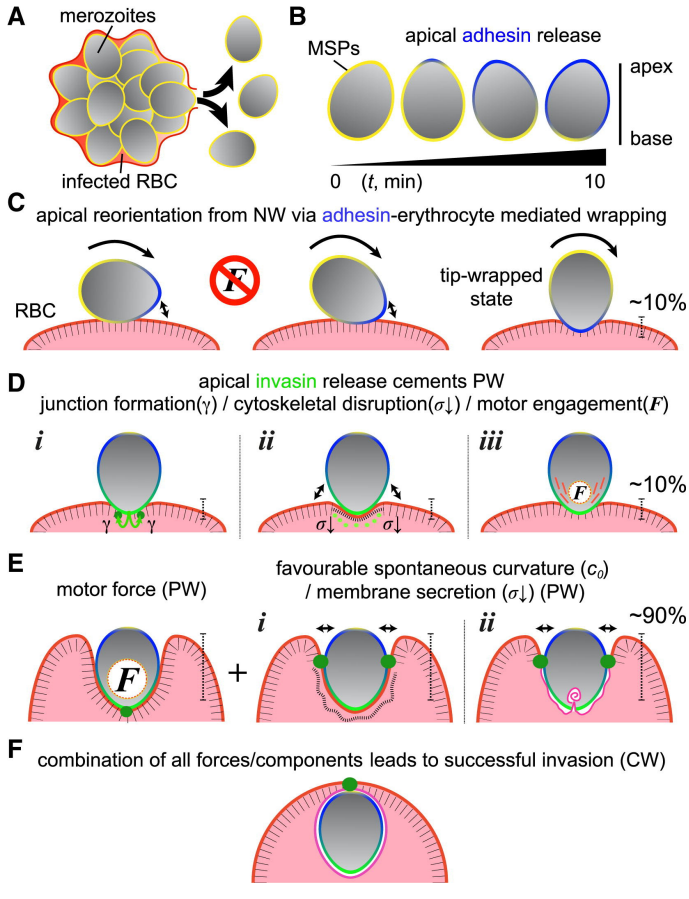

Figure 7: Schematic for biophysical interactions between the *Plasmodium* merozoite and the human erythrocyte. A complete biophysical model for merozoite invasion of the erythrocyte from release (A and B), to attachment and reorientation facilitating a stable, tip-wrapped state (C), to PW states (D and E), and full invasion/CW states (F). See main text for details.

A $\sim$ 10 % PW state (Fig. 7 C, *right panel*) is also found in our wrapping energy calculations (Fig. 4 and Fig. 5, PW I) and in the biological system likely coincides with (or is directly preceded by) apical release of a third population of invasion-specic adhesive proteins, which we term invasins [8] (*green*) to distinguish them from adhesins. These are associated with either a second population of micronemes or the rhoptry organelles [8,70] (Fig. 7 D). Some of these are secreted inside the target erythrocyte [7], with others staying with the merozoite surface [8]. Combined, the rhoptries and the proteins released facilitate four key processes (Fig. 7 D and Fig. 4, *arrows*): i), establishment of the merozoite-erythrocyte tight junction (*dark green*), which in our model acts as line tension (γ); ii), a (still to be determined) class of proteins, predicted to be secreted inside the erythrocyte, which may facilitate disruption of the underlying erythrocyte cytoskeleton (*thick to thin dashed line*) [19,71] leading to a more favorable spontaneous curvature (c_0); iii), secretion of membrane

from the merozoite's apical stores [7,57] lowering the tension of the erythrocyte membrane (σ) facilitating further wrapping (Fig. 7 E, *right panel*, and Fig. 4, *arrow a*), which has a favorable spontaneous curvature and reduces surface tension; and iv) a nal class of proteins, released onto the surface of the merozoite, which engage with the actomyosin motor inside the merozoite permitting force generation (**F**) [72]. We suggest that each of these factors helps the merozoite to overcome energy barriers associated with transitions between low and high PW states (Fig. 4, Fig. 5, and Fig. 7, D and E). Motor force allows the merozoite to then cross the remaining energy barriers and to achieve invasion up to $\sim$ 90 % wrapping. At this critical juncture in invasion (Fig. 7 E, Fig.S3, and Fig. S5, PW II), the merozoite will either jump to a CW/invaded state (Fig. 7 F) or invasion will fail. In reality, these scenarios likely coexist and are continuations of the previous stages of invasion. They are also entirely reasonable given known experimental observations (e.g., [57,71], Fig. S2 B). The successfully invaded parasite now lies within a vacuole inside the target erythrocyte [14]. At this stage, the vacuole will need to be sealed and erythrocyte cytoskeleton reformed.

Two core conclusions can be drawn from this model. First, that reorientation to irreversible attachment can be simply viewed as a parasite energy-independent, shape/adhesin-dependent wrapping process. Second, that membrane wrapping during merozoite invasion combined with other biophysical considerations can account for the major energetic requirements of invasion. Successful invasion requires traversal across energy barriers (associated with the discontinuous transitions), which are likely achieved via actomyosin motor contributions. However, what is striking is that our calculations for membrane wrapping together with biological evidence suggest mechanisms that make parasite entry into the erythrocyte energetically more favorable compared to a model that is parasite motor-driven alone. Nonmotor contributions such as cytoskeletal remodeling and the line tension from the junction thus contribute to invasion energetics in ways that have perhaps not been appreciated. It is worth stressing that, irrespective of wrapping models, motor force does still appear to be a constant requirement [17,64]. Our work demonstrates that even when membrane-wrapped states are stable, the essential role of the motor likely lies in overcoming energy barriers between the PW and CW states.

Clearly, it is now paramount to actually measure the forces experienced by the merozoite, and assess the contributions from membrane-wrapping and myosin motors. In addition, direct assessment of the membrane contributions from the parasite apex to the nascent vacuole [14] and the search for factors that modulate the erythrocyte cytoskeleton either directly or indirectly to facilitate invasion [19] also become important. This latter point is particularly worth highlighting. A parasite-induced role for the host cell is clearly documented if one looks beyond *Toxoplasma* and *Plasmodium spp.* to other apicomplexan parasites [73–75]. Could the erythrocyte be stimulated to contribute in a similar fashion to invasion? The erythrocyte membrane and cytoskeleton play a particularly active role during erythroblast enucleation, which involves extensive cytoskeletal remodeling that helps expel the nuclear compartment [76,77]. Given the presence of such a machinery combined with evidence that the mature erythrocyte cytoskeleton and membrane exist in a dy-

namic cycling state [43,78] it is certainly conceivable that the parasite might stimulate innate active processes within the erythrocyte to further reduce the energy cost for entry.

In summary, our results point to an evolutionarily balanced consideration of merozoite invasion, strongly favoring a model by which passive processes, such as adhesion-driven wrapping, and active parasite-induced processes, such as erythrocyte cytoskeleton remodeling and membrane injection (and of course motor contribution), combine to maximize invasion efciency. Strategies targeting either of these facets of invasion, or a combination of the two, may therefore be important as we strive for more effective antimalarial therapeutics.

Supporting material

Four figures, supporting data, some details of the theoretical analysis, a discussion of discontinuous transitions in the phase diagram, and reference (79) are available.

Acknowlegments

This work was the result of a "Meeting of Minds" symposium held at the Institut Pasteur, Paris and we are grateful to the Mairie de Paris, OzEMalaR (the Australia/Europe Malaria Research Cooperative) and the Institut Pasteur, Paris for facilitating the meeting. The authors thank Robert Menard for critical input into the study and Carolyn Larabell, Mark A. Le Gros (University of California, San Francisco) and Christian Knoechel (Lawrence Berkeley National Laboratory) for assistance and advice with X-ray tomography undertaken at the National Center for X-ray Tomography, Lawrence Berkeley National Laboratory. X-ray tomography work was supported by grants from the National Center for Research Resources (5P41RR019664-08) and the National Institute of General Medical Sciences (8 P41 GM103445-08) from the National Institutes of Health. Direct funding to support parasitological work was from the NHMRC (Project Grant APP1047085, JB) and, for theoretical work, from the EU FP7 NMP collaborative project PreNanoTox (Project Grant 309666, GG). SD acknowledges support by the International Helmholtz Research School of Biophysics and Soft Matter (IHRS BioSoft). ESZ is supported by an Australian Postgraduate Award (APA); NG wishes to thank the Mayent-Rothschild Visiting Professor Grant at the Institut Curie for funding; TJS is supported by a Wellcome Trust project grant (No. 094277). AMT is supported by an NHSBT RD grant and the Wellcome Trust; TB acknowledges support from the Agence Nationale de Recherche (JCJC SVSE 5-2011); JB was supported by a Future Fellowship from the Australian Research Council, ARC (FT100100112) and is currently supported by a New Investigator Award from the Wellcome Trust (100993/Z/13/Z).

References: Chapter 4

1. Cowman A. F., Berry D. and Baum J. 2012. The cellular and molecular basis for malaria parasite invasion of the human red blood cell. J Cell Biol. 198: 961-971.

2. Baum J., Gilberger T.-W., Frischknecht F. and Meissner M. 2008. Host-cell invasion by malaria parasites: insights from Plasmodium and Toxoplasma. Trends Parasitol. 24: 557-563.

3. Aikawa M., Miller L. H., Johnson J. and Rabbege J. 1978. Erythrocyte entry by malarial parasites. A moving junction between erythrocyte and parasite. J Cell Biol. 77: 72-82.

4. Bannister L. H., Butcher G. A., Dennis E. D. and Mitchell G. H. 1975. Structure and invasive behaviour of Plasmodium knowlesi merozoites in vitro. Parasitology. 71: 483-491.

5. Ladda R., Aikawa M. and Sprinz H. 1969. Penetration of erythrocytes by merozoites of mammalian and avian malarial parasites. J Parasitol. 55: 633-644.

6. Hanssen E., Dekiwadia C., Riglar D. T., Rug M., Lemgruber L., Cowman A. F., Cyrklaff M., Kudryashev M., Frischknecht F., Baum J. and Ralph S. A. 2013. Electron tomography of Plasmodium falciparum merozoites reveals core cellular events that underpin erythrocyte invasion. Cell Microbiol. 15: 1457-1472.

7. Riglar D. T., Richard D., Wilson D. W., Boyle M. J., Dekiwadia C., Turnbull L., Angrisano F., Marapana D. S., Rogers K. L., Whitchurch C. B., Beeson J. G., Cowman A. F., Ralph S. A. and Baum J. 2011. Super-Resolution Dissection of Coordinated Events during Malaria Parasite Invasion of the Human Erythrocyte. Cell Host Microbe. 9: 9-20.

8. Zuccala E. S., Gout A. M., Dekiwadia C., Marapana D. S., Angrisano F., Turnbull L., Riglar D. T., Rogers K. L., Whitchurch C. B., Ralph S. A., Speed T. P. and Baum J. 2012. Subcompartmentalisation of proteins in the rhoptries correlates with ordered events of erythrocyte invasion by the blood stage malaria parasite. PLoS One. 7: e46160.

9. Srinivasan P., Beatty W. L., Diouf A., Herrera R., Ambroggio X., Moch J. K., Tyler J. S., Narum D. L., Pierce S. K., Boothroyd J. C., Haynes J. D. and Miller L. H. 2011. Binding of Plasmodium merozoite proteins RON2 and AMA1 triggers commitment to invasion. Proc Natl Acad Sci U S A. 108: 13275-13280.

10. Singh S., Alam M. M., Pal-Bhowmick I., Brzostowski J. A. and Chitnis C. E. 2010. Distinct external signals trigger sequential release of apical organelles during erythrocyte invasion by malaria parasites. PLoS Pathog. 6: e1000746.

11. Dvorak J. A., Miller L. H., Whitehouse W. C. and Shiroishi T. 1975. Invasion of erythrocytes by malaria merozoites. Science. 187: 748-750.

12. Gilson P. R. and Crabb B. S. 2009. Morphology and kinetics of the three distinct phases of red blood cell invasion by Plasmodium falciparum merozoites. Int J Parasitol. 39: 91-96.

13. Mitchell G. H. and Bannister L. H. 1988. Malaria parasite invasion: interactions with the red cell membrane. Crit Rev Oncol Hematol. 8: 255-310.

14. Lingelbach K. and Joiner K. A. 1998. The parasitophorous vacuole membrane surrounding Plasmodium and Toxoplasma: an unusual compartment in infected cells. J Cell Sci. 111: 1467-1475.

15. Lew V. L. and Tiffert T. 2007. Is invasion efficiency in malaria controlled by pre-invasion events? Trends Parasitol. 23: 481-484.

16. Angrisano F., Riglar D. T., Sturm A., Volz J. C., Delves M. J., Zuccala E. S., Turnbull L., Dekiwadia C., Olshina M. A., Marapana D. S., Wong W., Mollard V., Bradin C. H., Tonkin C. J., Gunning P. W., Ralph S. A., Whitchurch C. B., Sinden R. E., Cowman A. F., McFadden G. I. and Baum J. 2012. Spatial localisation of actin filaments across developmental stages of the malaria parasite. PLoS One. 7: e32188.

17. Miller L. H., Aikawa M., Johnson J. G. and Shiroishi T. 1979. Interaction between cytochalasin B-treated malarial parasites and erythrocytes. Attachment and junction formation. J Exp Med. 149: 172-184.

18. Sibley L. D. 2004. Intracellular parasite invasion strategies. Science. 304: 248-253.

19. Zuccala E. S. and Baum J. 2011. Cytoskeletal and membrane remodelling during malaria parasite invasion of the human erythrocyte. Br J Haematol. 154: 680-689.

20. Dobrowolski J. M. and Sibley L. D. 1996. Toxoplasma invasion of mammalian cells is powered by the actin cytoskeleton of the parasite. Cell. 84: 933-939.

21. Gonzalez V., Combe A., David V., Malmquist N. A., Delorme V., Leroy C., Blazquez S., Menard R. and Tardieux I. 2009. Host cell entry by apicomplexa parasites requires actin polymerization in the host cell. Cell Host Microbe. 5: 259-272.

22. Andenmatten N., Egarter S., Jackson A. J., Jullien N., Herman J. P. and Meissner M. 2013. Conditional genome engineering in Toxoplasma gondii uncovers alternative invasion mechanisms. Nat Methods. 10: 125-127.

23. Huang J., Juszkiewicz M., de Jeu W. H., Cerda E., Emrick T., Menon N. and Russell T. P. 2007. Capillary wrinkling of floating thin polymer films. Science. 317: 650-653.

24. Vliegenthart G. A. and Gompper G. 2006. Forced crumpling of self-avoiding elastic sheets. Nat Mater. 5: 216-221.

25. Ursitti J. A. and Pumplin D. W. 1991. Ultrastructure of the human erythrocyte cytoskeleton and its attachment to the membrane. Cell Motil Cytoskeleton. 19: 227-243.

26. Auth T., Safran S. A. and Gov N. S. 2007. Fluctuations of coupled fluid and solid membranes with application to red blood cells. Phys Rev E Stat Nonlin Soft Matter Phys. 76: 051910.

27. Lipowsky, R., and H. G. D′obereiner. 1998. Vesicles in contact with nanoparticles and colloids. Europhys. Lett. 43:219–225.

28. Deserno M. 2004. Elastic deformation of a fluid membrane upon colloid binding. Phys Rev E Stat Nonlin Soft Matter Phys. 69: 031903.

29. Tollis, Sylvain and Dart, Anna E and Tzircotis, George and Endres, Robert G. 2010. The zipper mechanism in phagocytosis: energetic requirements and variability in phagocytic cup shape. BMC Syst. Biol. 4:149.

30. Bahrami, A. H., R. Lipowsky, and T. R. Weikl. 2012. Tubulation and aggregation of spherical nanoparticles adsorbed on vesicles. Phys. Rev. Lett. 109:188102.

31. Sarić, A., and A. Cacciuto. 2012. Fluid membranes can drive linear aggregation of adsorbed spherical nanoparticles. Phys. Rev. Lett. 108:118101.

32. Dasgupta S., Auth T. and Gompper G. 2013. Wrapping of ellipsoidal nanoparticles by fluid membranes. Soft Matter. 9: 5473-5482.

33. Bahrami, A. H. 2013. Orientational changes and impaired internalization of ellipsoidal nanoparticles by vesicle membranes. Soft Matter. 9:8642–8646.

34. Dasgupta, S., T. Auth, and G. Gompper. 2014. Shape and orientation matter for the cellular uptake of nonspherical particles. Nano Lett. 14:687–693.

35. Boyle M. J., Wilson D. W., Richards J. S., Riglar D. T., Tetteh K. K., Conway D. J., Ralph S. A., Baum J. and Beeson J. G. 2010. Isolation of viable Plasmodium falciparum merozoites to define erythrocyte invasion events and advance vaccine and drug development. Proc Natl Acad Sci USA. 107: 14378-14383.

36. Lipowsky R. 1992. Budding of Membranes Induced by Intramembrane Domains. Journal De Physique Ii. 2: 1825-1840.

37. Helfrich W. 1973. Elastic properties of lipid bilayers: theory and possible experiments. Z Naturforsch C. 28: 693-703.

38. Gray A. and Abbena E. 2006. Modern Differential Geometry of Curves And Surfaces With Mathematica. CRC Press.

39. Kabaso D., Shlomovitz R., Auth T., Lew V. L. and Gov N. S. 2010. Curling and local shape changes of red blood cell membranes driven by cytoskeletal reorganization. Biophys J. 99: 808-816.

40. Auth T., Safran S. A. and Gov N. S. 2007. Filament networks attached to membranes: cytoskeletal pressure and local bilayer deformation. New Journal of Physics. 9:

41. Seifert U. 1995. The concept of effective tension for fluctuating vesicles. Zeitschrift für Physik B Condensed Matter. 97: 299-309.

42. Farago, O., and P. Pincus. 2004. Statistical mechanics of bilayer membrane with a xed projected area. J. Chem. Phys. 120:2934–2950.

43. Gov N. S. and Safran S. A. 2005. Red blood cell membrane fluctuations and shape controlled by ATP-induced cytoskeletal defects. Biophys J. 88: 1859-1874.

44. Tian A. and Baumgart T. 2009. Sorting of lipids and proteins in membrane curvature gradients. Biophys J. 96: 2676-2688.

45. Veksler A. and Gov N. S. 2007. Phase transitions of the coupled membrane-cytoskeleton modify cellular shape. Biophys J. 93: 3798-3810.

46. Auth T. and Gompper G. 2009. Budding and vesiculation induced by conical membrane inclusions. Phys Rev E. 80: 031901.

47. Sorre B., Callan-Jones A., Manneville J. B., Nassoy P., Joanny J.-F., Prost J., Goud B. and Bassereau P. 2009. Curvature-driven lipid sorting needs proximity to a demixing point and is aided by proteins. Proc Natl Acad Sci U S A. 106: 5622-5626.

48. Heberle F. A., Wu J., Goh S. L., Petruzielo R. S., Feigenson G. W. 2010. Comparison of three ternary lipid bilayer mixtures: FRET and ESR reveal nanodomains. Biophys. J. 99:3309–3318.

49. Schäfer, L. V., and S. J. Marrink. 2010. Partitioning of lipids at domain boundaries in model membranes. Biophys. J. 99:L91–L93.

50. Hutchison, J. B., R. M. Weis, and A. D. Dinsmore. 2012. Change of line tension in phase-separated vesicles upon protein binding. Langmuir. 28:5176–5181.

51. Yamamoto N. (2007) We Find an Equation of Egg Shaped Curves. www16.ocn.ne.jp/∼akiko-y/Egg/index_egg_E.html.

52. Treeck M., Zacherl S., Herrmann S., Cabrera A., Kono M., Struck N. S., Engelberg K., Haase S., Frischknecht F., Miura K., Spielmann T. and Gilberger T. W. 2009. Functional analysis of the leading malaria vaccine candidate AMA-1 reveals an essential role for the cytoplasmic domain in the invasion process. PLoS Pathog. 5: e1000322.

53. Collins C. R., Hackett F., Strath M., Penzo M., Withers-Martinez C., Baker D. A. and Blackman M. J. 2013. Malaria parasite cGMP-dependent protein kinase regulates blood stage merozoite secretory organelle discharge and egress. PLoS Pathog. 9: e1003344.

54. Sun S. X. and Wirtz D. 2006. Mechanics of HIV-1 Virus Entry into Host Cells. Biophys J. 90: L10-12.

55. Mitchell G. H., Thomas A. W., Margos G., Dluzewski A. R. and Bannister L. H. 2004. Apical membrane antigen 1, a major malaria vaccine candidate, mediates the close attachment of invasive merozoites to host red blood cells. Infect Immun. 72: 154-158.

56. García-Sáez A. J., Chiantia S. and Schwille P. 2007. Effect of line tension on the lateral organization of lipid membranes. J Biol Chem. 282: 33537-33544.

57. Bannister L. H., Mitchell G. H., Butcher G. A. and Dennis E. D. 1986. Lamellar membranes associated with rhoptries in erythrocytic merozoites of Plasmodium knowlesi: a clue to the mechanism of invasion. Parasitology. 92: 291-303.

58. Aikawa M., Miller L. H., Rabbege J. R. and Epstein N. 1981. Freeze-fracture study on the erythrocyte membrane during malarial parasite invasion. J Cell Biol. 91: 55-62.

59. Baum J., Papenfuss A. T., Baum B., Speed T. P. and Cowman A. F. 2006. Regulation of apicomplexan actin-based motility. Nat Rev Microbiol. 4: 621-628.

60. Ayi K., Liles W. C., Gros P. and Kain K. C. 2009. Adenosine triphosphate depletion of erythrocytes simulates the phenotype associated with pyruvate kinase deficiency and confers protection against Plasmodium falciparum in vitro. J Infect Dis. 200: 1289-1299.

61. Olson J. A. and Kilejian A. 1982. Involvement of spectrin and ATP in infection of resealed erythrocyte ghosts by the human malarial parasite, Plasmodium

falciparum. J Cell Biol. 95: 757-762.

62. Park Y., Best C. A., Auth T., Gov N. S., Safran S. A., Popescu G., Suresh S. and Feld M. S. 2010. Metabolic remodeling of the human red blood cell membrane. Proc Natl Acad Sci U S A. 107: 1289-1294.

63. Hegge S., Uhrig K., Streichfuss M., Kynast-Wolf G., Matuschewski K., Spatz J. P. and Frischknecht F. 2012. Direct manipulation of malaria parasites with optical tweezers reveals distinct functions of Plasmodium surface proteins. ACS Nano. 6: 4648-4662.

64. Pinder J. C., Fowler R. E., Dluzewski A. R., Bannister L. H., Lavin F. M., Mitchell G. H., Wilson R. J. and Gratzer W. B. 1998. Actomyosin motor in the merozoite of the malaria parasite, Plasmodium falciparum: implications for red cell invasion. J Cell Sci. 111: 1831-1839.

65. Herm-Goetz A., Weiss S., Stratmann R., Fujita-Becker S., Ruff C., Meyhofer E., Soldati T., Manstein D. J., Geeves M. A. and Soldati D. 2002. Toxoplasma gondii myosin A and its light chain: a fast, single-headed, plus-end-directed motor. Embo J. 21: 2149-2158.

66. Finer J. T., Simmons R. M. and Spudich J. A. 1994. Single myosin molecule mechanics: piconewton forces and nanometre steps. Nature. 368: 113-119.

67. Tyska M. J., Dupuis D. E., Guilford W. H., Patlak J. B., Waller G. S., Trybus K. M., Warshaw D. M. and Lowey S. 1999. Two heads of myosin are better than one for generating force and motion. Proc Natl Acad Sci U S A. 96: 4402-4407.

68. Harris D. E. and Warshaw D. M. 1993. Smooth and skeletal muscle myosin both exhibit low duty cycles at zero load in vitro. J Biol Chem. 268: 14764-14768.

69. Abkarian M., Massiera G., Berry L., Roques M. and Braun-Breton C. 2011. A novel mechanism for egress of malarial parasites from red blood cells. Blood. 117: 4118-4124.

70. Kremer K., Kamin D., Rittweger E., Wilkes J., Flammer H., Mahler S., Heng J., Tonkin C. J., Langsley G., Hell S. W., Carruthers V. B., Ferguson D. J. and Meissner M. 2013. An overexpression screen of Toxoplasma gondii Rab-GTPases reveals distinct transport routes to the micronemes. PLoS Pathog. 9: e1003213.

71. Rangachari K., Dluzewski A., Wilson R. J. and Gratzer W. B. 1986. Control of malarial invasion by phosphorylation of the host cell membrane cytoskeleton. Nature. 324: 364-365.

72. Baum J., Richard D., Healer J., Rug M., Krnajski Z., Gilberger T.-W., Green J. L., Holder A. A. and Cowman A. F. 2006. A conserved molecular motor drives

cell invasion and gliding motility across malaria life cycle stages and other apicomplexan parasites. J Biol Chem. 281: 5197-5208.

73. Elliott D. A., Coleman D. J., Lane M. A., May R. C., Machesky L. M. and Clark D. P. 2001. Cryptosporidium parvum infection requires host cell actin polymerization. Infect Immun. 69: 5940-5942.

74. Lumb R., Smith K., O'Donoghue P. J. and Lanser J. A. 1988. Ultrastructure of the attachment of Cryptosporidium sporozoites to tissue culture cells. Parasitol Res. 74: 531-536.

75. Shaw M. K. 2003. Cell invasion by Theileria sporozoites. Trends Parasitol. 19: 2-6.

76. Lee J. C., Gimm J. A., Lo A. J., Koury M. J., Krauss S. W., Mohandas N. and Chasis J. A. 2004. Mechanism of protein sorting during erythroblast enucleation: role of cytoskeletal connectivity. Blood. 103: 1912-1919.

77. Konstantinidis G., Moustakas A. and Stournaras C. 2011. Regulation of myosin light chain function by BMP signaling controls actin cytoskeleton remodeling. Cell Physiol Biochem. 28: 1031-1044.

78. Betz T., Lenz M., Joanny J.-F. and Sykes C. 2009. ATP-dependent mechanics of red blood cells. Proc Natl Acad Sci USA. 106: 15320-15325.

79. Elsa, A., S. Salamon, and A. Gray. 2006. Modern Differential Geometry of Curves and Surfaces with Mathematica. CRC Press, Boca Raton, FL.

4.8
Supplementary material

Supplementary material: Membrane-wrapping contributions to malaria parasite invasion of the human erythrocyte

Description Of Erythrocyte-Membrane Wrapping

Towards calculating membrane-wrapping contributions to invasion we sought to identify core parameters associated with parasite entry. Four key parameters were selected, adhesive forces, bending energy, target membrane tension and a line tension (Fig. S1).

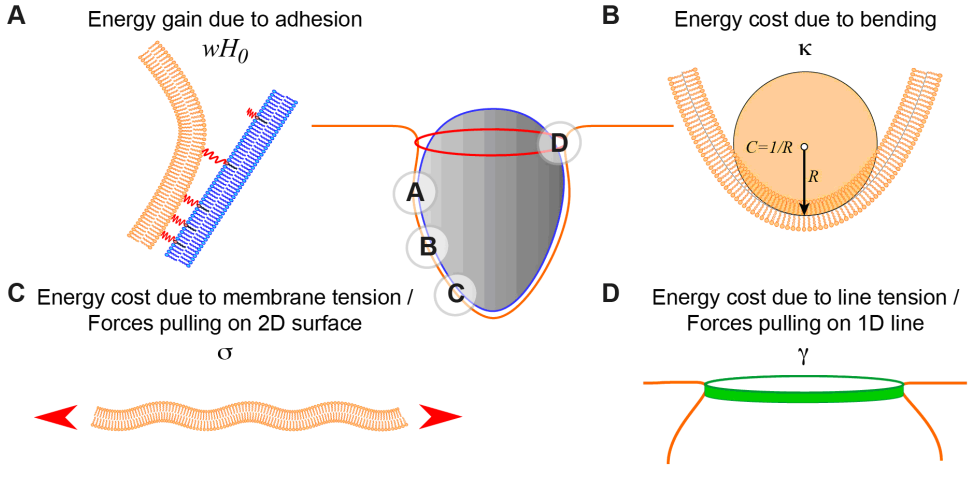

Figure S1: Schematic explanation of the different energetic contributions used to model the role of the host membrane in merozoite invasion. **A.** adhesion strength, **B.** bending energy, **C.** membrane tension and **D.** line tension (see main text for details).

When the host membrane (Fig. S1, orange) comes close to the parasite membrane (Fig. S1 A, blue), adhesion molecules form an attractive interaction between the two membranes (illustrated with red springs). The adhesion strength, wH_0, which quantifies the adhesion energy, depends on the local concentration of the adhesion molecules. In experiments, close contact between the merozoite and the erythrocyte membrane is observed [1] that supports a close adhesive interaction between the two cells (Fig. S2 A).

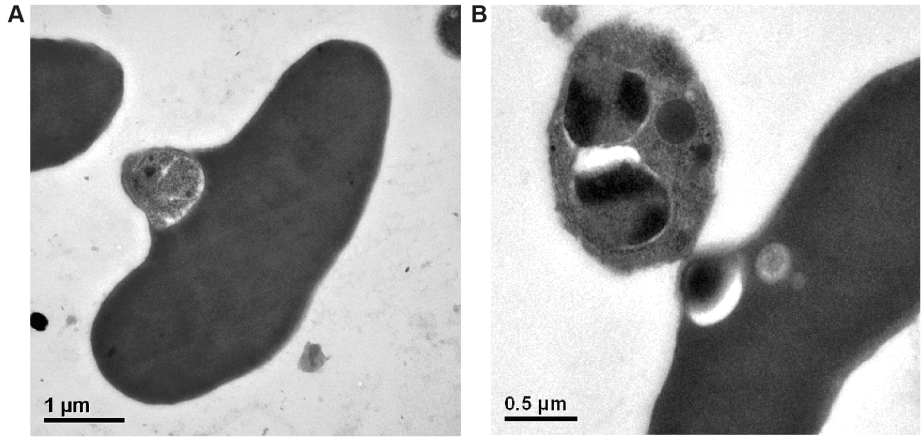

Figure S2: Electron micrographs of merozoites from *Plasmodium falciparum* in the process of invading an erythrocyte. **A.** Demonstration of the close proximity between plasma membrane of the merozoite and the plasma membrane of the erythrocyte during invasion as revealed by high pressure freezing and freeze substitution (as compared with other approaches which can give rise to a substantial slack space between parasite and host cell in nascent parasitophorous vacuole). Imaging conditions as described in [1]. **B.** Release of membrane from apex of parasite during the invasion process. Here merozoite invasion is arrested with cytochalasin D (an inhibitor of invasion), which prevents completion of invasion but does not prevent release of membrane whorls from rhoptry bulb. Imaging conditions as described in [1].

Bending a membrane also requires energy that is determined by two contributions; the bending modulus κ, which reflects the rigidity of the membrane against a forced bending, and the actual degree of bending which is quantified by the curvature C (Fig. S1 B). The curvature ! can be simply visualized by fitting a circle along the curve and then taking the inverse radius of this circle: $C = 1/R$. Hence, high curvature corresponds to a small circle radius, while a flat membrane has no curvature, which corresponds to an infinite radius. Since the membrane is a two-dimensional ($2D$)) surface, curvature can exist at any point in the two directions. The relevant curvature is the mean curvature, $H = (1/R_x + 1/R_y)/2$.

Two tension forces play key roles in the invasion process. Host membrane tension relates to an energetic cost that is related to a lateral pulling on the membrane (Fig. S1 **C**). Typically, biological membranes are soft enough to fluctuate because of thermal movement, which is analogous to the Brownian diffusion of a small particle. This movement means that the apparent membrane area measured when looking on the membrane is smaller than the real area that includes the area "hidden" in the fluctuations. Physically, it means that when a pulling force is applied (red arrows), the apparent membrane area increases. The membrane tension can also be reduced by release of membrane from the apex of the parasite (Fig. S2 **B**). The membrane tension is then defined by the force required to increase the membrane area. Hence high tension (represented by the term σ) means that high forces are required to increase the apparent area.

A final energetic contribution comes from the spring-like behaviour of the cytoskeleton along the furrow at the membrane inclusion, referred to here as a line tension (Fig. S1 **D**). This spring-like behaviour can be modelled by an elastic rubber band that lies around the furrow, and hence wants to constrict the furrow. The spring stiffness of this rubber band is modelled by the line tension (represented by the term γ). Physically, in the first phase on invasion (PW I) the merozoite has to stretch this rubber band, which costs energy. However, once over the point of maximal diameter (PW II), the line tension actually helps pushing the merozoite inside the host cell.

Calculation of the merozoite wrapping energy

The key ingredients for calculating the energy for wrapping a merozoite are the shape of our archetypal merozoite and our model for the deformation energy defined by Eq. 2 of the main text. The egg shape of the archetypal merozoite is $(x^2+y^2+z^2)^2 = R_a x^3 + (R_a - R_b)x(y^2+z^2)$ with $R_a = 1\,\mu m$ and $R_b = 0.7\,\mu m$. For the calculation of the deformation energy, the shape is parametrized in spherical coordinates using the polar angle u and the azimuthal angle v,

$$\begin{aligned} x(u,v) &= \big[\frac{(2R_a - R_b)\sin(v)}{4} + \frac{R_b \sin(2v)}{8}\big]\cos(u) \\ y(u,v) &= \big[\frac{(2R_a - R_b)\sin(v)}{4} + \frac{R_b \sin(2v)}{8}\big]\sin(u) \\ z(u,v) &= \big[\frac{2R_a + R_b\cos(v)}{4}\big]\cos(v)\,, \end{aligned}$$

where $0 \le u < 2\pi$ and $0 \le v < 2\pi$. The distance from the symmetry axis as function of the azimuthal angle is

$$\rho(v) = \sqrt{x^2+y^2} = \big[\frac{(2R_a - R_b)\sin(v)}{4} + \frac{R_b \sin(2v)}{8}\big]\,,$$

and the radial coordinate of the merozoite surface,

$$r(v) = \sqrt{x^2+y^2+z^2} = \sqrt{\big[\frac{(2R_a - R_b)\sin(v)}{4} + \frac{R_b \sin(2v)}{8}\big]^2 + \big[\frac{2R_a + R_b\cos(v)}{4}\big]^2\cos(v)^2}\,.$$

In spherical coordinates, Eq. 2 in the main text becomes

$$E = 2\pi \int_0^{v_{wrap}} dv\, g_{\rho v}\, \rho(v)\,[2\,\kappa(H(v))^2 + \sigma - wH(v)] + 2\pi\rho(v)\gamma\,,$$

where $g_{\rho v} = \sqrt{d\rho^2 + dv^2} = (2R_a - R_b)\sin(v)/4 + R_b \sin(2v)/8$, and v_{wrap} determines the degree of wrapping. Note that in our model the membrane deformation energy is only calculated for the membrane that is attached to the merozoite. The integrals are evaluated numerically using the computer algebra program *Maple*.

Both the bending energy and the adhesion energy contributions in our model require the calculation of the mean curvature. The mean curvature can be expressed by the fundamental forms of the merozoite surface [2],

$$H = \frac{eG - 2fF - gE}{EG - F^2}$$

where E, F, and G are the first fundamental forms and e, f, and g are the second fundamental forms.

Discontinuous phase transitions with energy barriers

The phase boundary W_0 between the NW and the PW states in Fig. S3 and Fig. 4 in main text is the binding transition that we use to discuss reorientation based on the local adhesion strength and bending energy. With a small membrane and line tension, PW and even CW regions may extend to smaller adhesion strengths than those associated with the threshold adhesion strength for W_0. This might at first appear to be surprising, since for very shallow wrapping the value of the membrane tension would not be expected to alter the transition [3,4]. However, the nature of the W_0 transition and the W_1, W_2, and E transitions in the phase diagram are different: while the W_0 transition is a continuous transition, the transitions W_1, W_2 and E are associated with an energy barrier (E also indicates when the unwrapped and the completely-wrapped state have equal energy). These latter transitions correspond to a jump in the fraction of the merozoite surface that is in contact with the enveloping membrane as the transition is passed (Fig. 4). For adhesion strengths very close to those phase boundaries, transitions cannot occur spontaneously.

For the phase boundaries W_1 and W_2, the spinodals S_{12} and S_{22} indicate the parameter regime where the transition occurs spontaneously and beyond that the energy barrier vanishes with increasing $\tilde{w} + \tilde{c}_0$. Only for values of adhesion strength that are larger than those of the spinodals does the energy barrier vanish and further wrapping occur spontaneously. In Fig. 5 in main text, we indicate the wrapping fractions of the stable states between which the discontinuous transitions occur; the tie lines mark the parameter region that corresponds to states on the energy barrier. In Fig. S4 we show the energy profile for a state on the discontinuous transition W_1 when the system traverses from a low wrapping fraction (PW I) to a higher wrapping fraction (PW II). The profile shows explicitly the energy barrier that needs to be overcome for further wrapping at the adhesion strength $\tilde{w} = 10.066$ for reduced membrane tension $\tilde{\sigma} = 4.5$. The low wrapping fraction state is found at $S_{ad}/S = 0.045$ and the high wrapping fraction state at $S_{ad}/S = 0.575$. The maximum of the energy barrier with height $\Delta E/2\kappa = 0.228$ is located at $S_{ad}/S \approx 0.25$. In order to jump from the PW I state to a PW II state, there is thus a need for an "activation energy" that facilitates invasion. The energy barrier for the W_2 transition that separates the partially-wrapped state with high wrapping fraction from the completely-wrapped state is typically much smaller than the energy barrier for

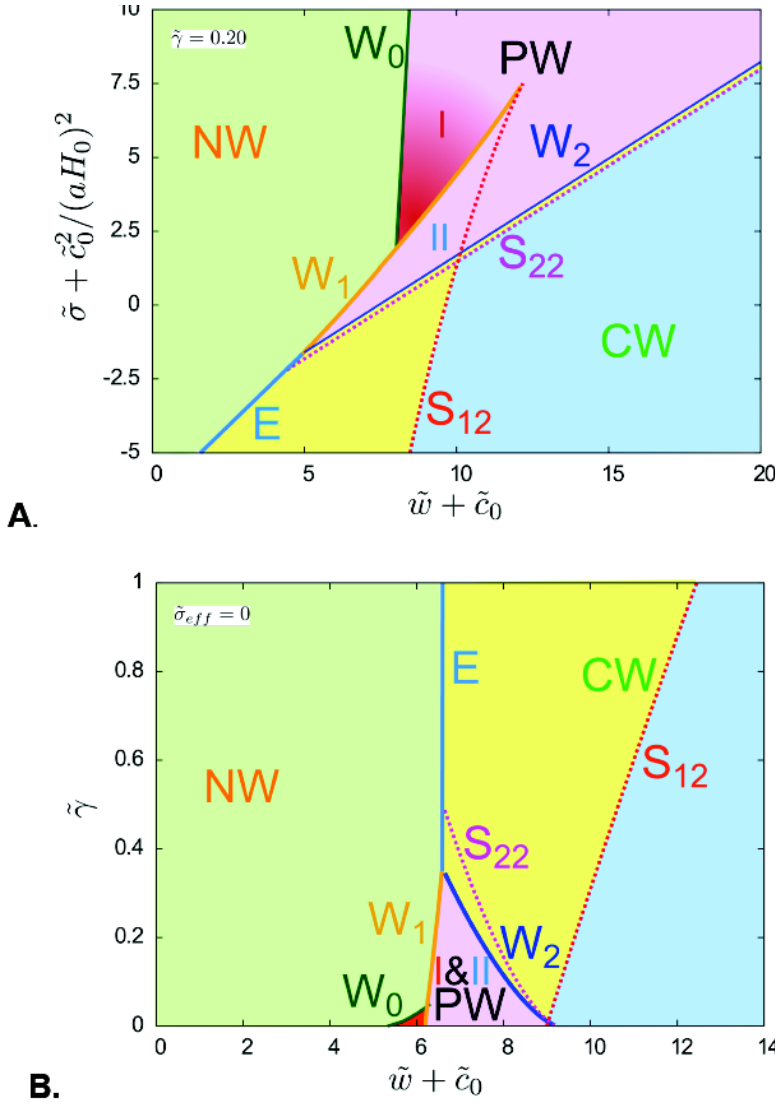

Figure S3: Phase diagrams Fig. 4 in the main text including the upper spinodals. S_{12} indicates the adhesion strengths at which the transition associated with the phase boundary W_1/E occurs spontaneously, while the spinodal S_{22} belongs to the phase boundary W_2. Spontaneous wrapping therefore occurs in the blue part of the CW region, while in the yellow part an energy barrier has to be overcome. **A.** Wrapping states for fixed reduced line tension $\tilde{\gamma} = 0.20$ and several values of adhesion strength and membrane tension. **B.** Wrapping states of the system of a tip-first oriented merozoite for vanishing effective membrane tension and several values of adhesion strength and line tension.

the W_1 transition. Hence, the spinodal is found for adhesion strengths close to values where the W2 transition occurs. Actomyosin motor activity may be a key determinant to overcome wrapping energy barriers and the barriers can be used

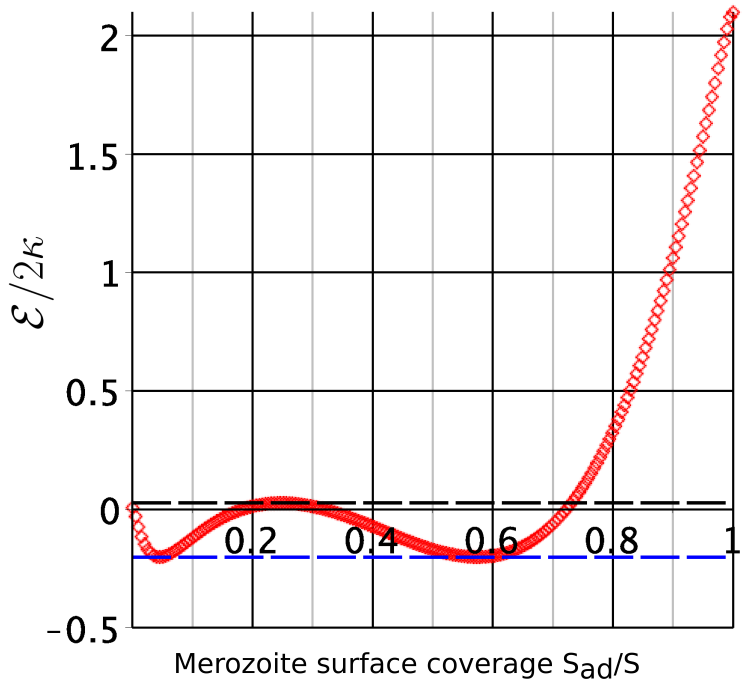

Figure S4: Energy profile for a state on the W_1 phase boundary. Energy profile at reduced effective adhesion strength $\tilde{w} = 10.066$ and reduced membrane tension $\tilde{\sigma} = 4.5$, see Figs. 4 and 5 in main text. The transition between the PW I state for $S_{ad}/S = 0.045$ and the PW II state for $S_{ad}/S = 0.575$ is associated with an energy barrier $\Delta E/2\kappa = 0.228$ whose maximum is found at $S_{ad}/S \approx 0.25$.

to estimate the required motor activity. However, activity alone is not sufficient to study invasion. When the motor stops to act (e.g. once invasion is almost complete) the merozoite will only remain wrapped in cases where its final state lies within the CW region of the phase diagram (Fig. S3 and Fig. 4 in main text).

References: Chapter 4 (Supplementary material)

1. Hanssen E., Dekiwadia C., Riglar D. T., Rug M., Lemgruber L., Cowman A. F., Cyrklaff M., Kudryashev M., Frischknecht F., Baum J. and Ralph S. A. 2013. Electron tomography of Plasmodium falciparum merozoites reveals core cellular events that underpin erythrocyte invasion. Cell Microbiol. 15: 1457-1472.

2. Elsa, A., S. Salamon, and A. Gray. 2006. Modern Differential Geometry of Curves and Surfaces with Mathematica. CRC Press, Boca Raton, FL.

3. Lipowsky, R., and H. G. Doebereiner. 1998. Vesicles in contact with nanoparticles and colloids. Europhys. Lett. 43:219–225.

4. Farago, O., and P. Pincus. 2004. Statistical mechanics of bilayer membrane with a xed projected area. J. Chem. Phys. 120:2934–2950.

5
Interfacing Electrogenic Cells with 3D Nanoelectrodes: Position, Shape, and Size Matter

5.1
Abstract

An in-depth understanding of the interface between cells and nanostructures is one of the key challenges for coupling electrically excitable cells and electronic devices. Recently, various 3D nanostructures have been introduced to stimulate and record electrical signals emanating from inside of the cell. Even though such approaches are highly sensitive and scalable, it remains an open question how cells couple to 3D structures, in particular how the engulfment-like processes of nanostructures work. Here, we present a profound study of the cell interface with two widely used nanostructure types, cylindrical pillars with and without a cap. While basic functionality was shown for these approaches before, a systematic investigation linking experimental data with membrane properties was not presented so far. The combination of electron microscopy investigations with a theoretical membrane deformation model allows us to predict the optimal shape and dimensions of 3D nanostructures for cell-chip coupling.

5.2
Introduction

Several techniques for interfacing excitable cells with electrical devices have been developed to study ion channel functionality over the long-term [1], restore lost sensing capabilities [2], control motor disorders [3], and control heartbeat [4]. The success of the numerous extracellular interface concepts proposed in basic science is limited by problems ranging from improper cell adhesion to inadequate device stability [5]. To overcome such limitations, the design of engineered interfaces [6,7] is mainly based on successful application of emerging technologies, such as nanotechnology [8-11]. The interface between cells and nanostructures has been studied extensively [12-16]. In particular, the morphology of cells interfacing 3D nanoelectrodes has been investigated in detail [17-27], as these are prominent candidates to solve the aforementioned problems. Potential mechanisms for coupling between electrogenic cells and multiple 3D nano- and microstructures are proposed and used for extracellular applications [6,9,10,26,28-32]. Most of these 3D nano and microstructures can be classified under twomain types: cylindrical pillars with and

without a cap. Here, the cell response depends on the cytoskeletal contribution driven by an actin ring, which forms around the 3D nanostructures [33], enabling the engulfment-like event [34-36]. Former studies lack information about how a cell interfaces a single 3D nanostructure, which is the basic investigation needed for understanding the cell interaction with multiple 3D nanostructures. Moreover, several important and fundamental questions were not addressed yet. Which of the two most-used structures leads to a better engulfment-like event by the cell? How does the position of the engulfment-like event affect the cell response and the coupling to the 3D nanostructure ? Here, we present a methodical investigation of the cell-3D nanostructure interface using focused ion beam (FIB) and scanning electron microscopy (SEM). We characterize the position of the engulfment-like event of 3D nanopillars by cardiomyocyte-like HL-1 cells [37] and the deformation of the extracellular membrane. Finally, we investigate which 3D nanoelectrodes are optimal for engulfment by cardiomyocyte-like cells to find the best design in terms of dimension and shape, and explain the biological driving forces that favor one structure over the other. This work will facilitate a prediction of the optimal parameter combination for the best coupling of electrogenic cells with 3D nanoelectrodes for *in vitro* and *in vivo* applications.

5.3
HL-1 Cells on 3D Nanostructures: Position of the Engulfment like Event

First, we analyzed the location of the engulfment-like event as schematically shown in Fig. 1 a. It is known that during a typical endocytic event, the cell membrane wraps around the particle that is then internalized by a cell [38,39]. We investigated the relative position of an engulfment-like event by an electrogenic cell type (HL-1 cells) on cylindrical nanopillars with and without mushroom-shaped caps. We fabricated nanostructure arrays with a pitch of 25 μm, to ensure that in most cases a cell adheres only to a single 3D nanostructure. We tested nanopillars with stalk height, H, from 300 up to 1000 nm and radius, R_sS, from 150 to 400 nm (examples are given in Fig. 1 b, i-vi), with aspect ratio, γ ($H/2R_s$), of the stalk in the range of 0.4-3.3 (see Supporting Information S1). For cylinders with caps, we considered a cap radius, R_c, that varied in the range of 300-1000 nm. HL-1 cells [37] were cultured on 3D nanostructures for 3 days *invitro* (DIV) and then chemically fixed. The membrane and the nucleus were fluorescently stained. The cells were observed with fluorescent microscopy (Fig. 1 c, i-iv) and SEM after critical point drying. To quantify the relative position of a single 3D nanostructure, the cell shape was fit with three equidistant and concentric elliptical regions of interest (ROIs) with respect to the ellipse axes (Fig. 1 d-f). The blue ROI determines the edge of cell, the red ROI defines the middle of the cell and the black ROI represents the center of the cell, where the nucleus was located in most cases. We found 23 % of engulfment-like events in the center, 37 % in the middle and 40 % at the edge of the cell. When normalizing the rate to the effective area, we find double the occurrence of structures in the center of the compared to the middle and at the edge of the cell (Fig. 1 (g)).

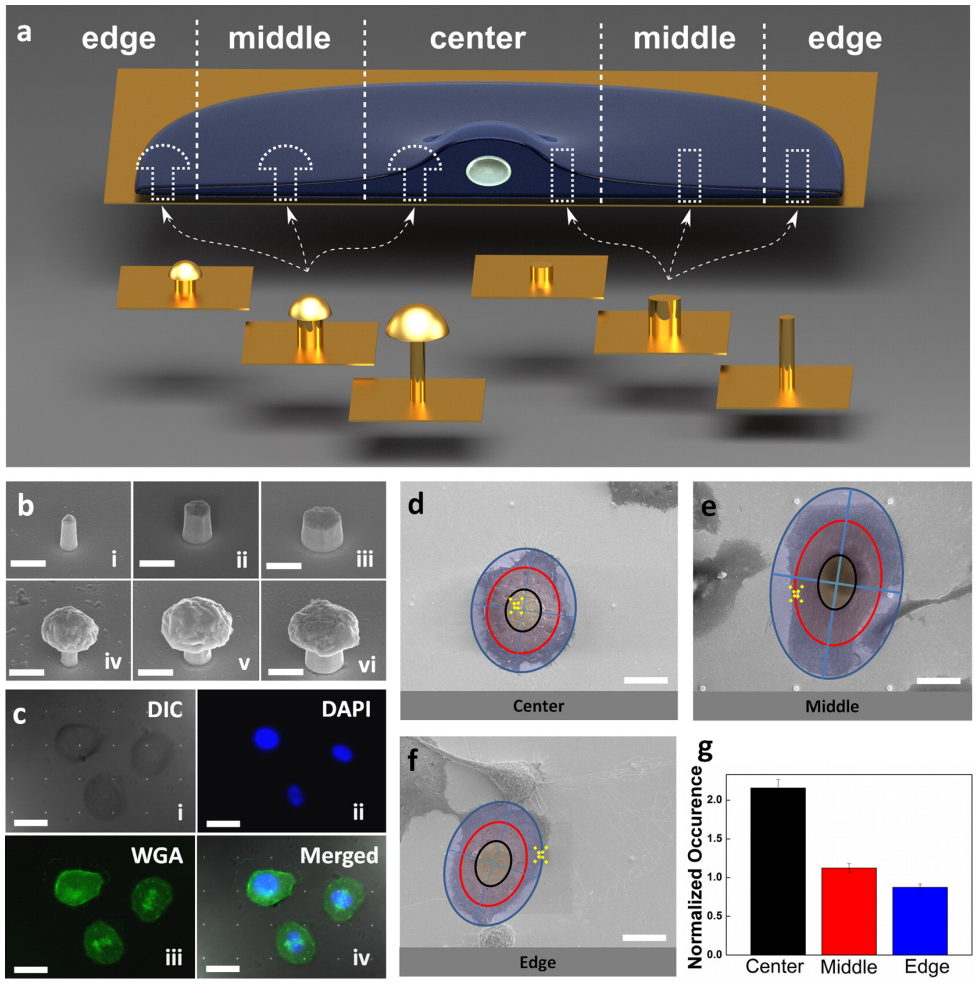

Figure 1: Investigation of engulfment-like events of HL-1 cells on 3D nanostructures. (a) schematic for the position of the engulfment-like event in the cell on cylinders with and without caps (different stalk aspect ratios); (b) example of nanostructured gold cylinders without caps (i-iii) and cylinders with caps (iv-vi) on planar gold (scale bar 0.8 μm, tilt 52°); (c) DIC image of HL-1 cells on an array of 3D nanostructures (i) HL-1 nuclei stained with DAPI in blue (ii), wheat germ agglutinin (WGA) staining of the cell membrane in green (iii) and merged DIC, DAPI, and WGA image (iv) (scale bar 25 μm); (d) scanning electron micrograph (SEM) of an HL-1 cell engulfing a 3D nanostructure in the center; (e) in the middle; (f) at edge of the cell (yellow cross indicates the position of the pillar, scale bars 15 μm); (g) normalized occurrence of engulfment events in the center, middle, and edge of the cell.

5.4
Nanostructures Engulfed at the Edge of the Cell Favor Engulfment and Free Membrane Deformation.

Next, we studied engulfment-like events at the edge of the cell in more detail. From our SEM investigation, we observed cells deforming their cell membrane according to the shape of the nanopillar (Fig. 2 a, Fig. 3a). To further characterize the interface between the cell membrane and the 3D nanopillars, we performed sequential cross sectioning (see Supporting Information S2) of cells ($N = 110$) with FIB and acquired images with SEM. The junctional membrane detaches from the planar substrate revealing the rough planar gold, which was further analyzed by atomic force microscopy (AFM) measurements (see Supporting Information S5). We refer to the extracellular membrane domain facing the substrate as "junctional" membrane, and the domain facing the culture medium as "free" membrane as previously established in literature [40]. Analyzing the cross sections through the center of the nanopillar, we trace the shape of the free membrane (solid line) as in Fig. 2 b, Fig. 3 b. At the cell edge, we found that the junctional membrane adheres around the nanopillar for all shapes and dimensions and also remains attached to the surrounding flat gold substrate while the free membrane develops different shapes. For a detailed study of the free membrane response to nanopillars with different dimensions and shapes, we plot the membrane shapes for different H and R_s, as shown in Fig. 2 c,d and Fig. 3 c,d. Cylinders without caps favor a "tent-like" deformation of the free membrane (Fig. 2 c,d) independent of the actual cylinder dimensions. Independent of R_s, tent-like deformations were observed only around cylinders with caps only in the case of small H (and thus low γ), as shown in Fig. 2 d. High pillars with caps promote an hourglass shape, in particular for the smallest R_s ($150\ nm$) as shown in Fig. 3 c with $\gamma = 3.3$. From our experimental investigation, we could distinguish two elementary scenarios: hourglass-like membrane shapes, as induced by taller capped cylinders (Fig. 3 e), and tent-like shapes, as induced by cylinders without caps (Fig. 2 e) or small capped cylinders. These two scenarios can be better understood by analyzing the FIB/SEM micrographs in Fig. 2 b and Fig. 3 b, where we observe that the intracellular region is very thin because of the nearly 2D structure of the cytoskeleton [41] at the edge of the cell. Motivated by the experimental observations described above, we construct a theoretical model to investigate the role of capped pillar height by neglecting the cytoskeletal contribution, and estimating the deformation energy by a continuum curvature-elasticity Helfrich description of the membrane [42]. We considered a semispherical cap of radius R_c placed at height H above the planar substrate. The free membrane wraps around the cap and flattens onto the planar substrate at detachment length, $R_{d,F}$, closely paralleling the junctional membrane, with only a thin layer of intracellular material. To investigate how the pillar height influences the free membrane response, we define the ratio H/R_c as a fundamental parameter. We assume that the membrane has a bending rigidity, κ, which expresses the resistance of the membrane to bending deformations. A final parameter is $R_{d,F}/R_c$, which indicates the cell's response to the planar substrate vs the width of the cap. We use $\kappa = 50\, k_B T$ (resulting in a Young's modulus $E \sim 10^6 - 10^7\ Pa$ for a thin membrane sheet), as previously shown for red blood cells [43]. We evaluate the free membrane's shape

at equilibrium by calculating the deformation energy for several values of H/R_c as a function of the detachment length, *i.e.*, as a function of $R_{d,F}/R_c$. Hourglass membrane shapes occur only at intermediate H/R_c (*i.e.*, 2 and 2.5) and only when $R_{d,F}/R_c$ is small. In these cases, the deformation energy is smaller than that for low or high H/R_c with small $R_{d,F}/R_c$ (Fig. 4 (a)). However, the hourglass membrane profiles (states (i) and (ii) in Fig. 4) for small $R_{d,F}/R_c$ require higher deformation energy costs $\mathcal{E}_{\text{bend}}$ than tent-like shapes with large $R_{d,F}/R_c$ (states (iii) and (iv) in Fig. 4 (see also Supporting Information S8). An effective contact interaction of the free membrane can be characterized by the adhesion strength w which can be extracted from the local mean curvature of the free membrane at the detachment point (see Supporting Information S8). In our experiments, we utilized caps with an average radius of 400 nm, and $H/R_c = 1.25$ or $H/R_c = 2.5$ that correspond to stalk heights of 0.5 μm and 1 μm, respectively. We calculate the membrane deformation profiles for structures of these two heights for different detachment lengths (see Supporting Information S8). As expected from the deformation energy calculations, hourglass deformations are found for these favorable nanopillar heights (Fig. 3 c), while the shorter pillars, as in Fig. 3 d are wrapped less. Fig. 3 c and d illustrate that the membrane deformation scales with stalk radius, R_s, for cylindrical pillars, as expected for systems dominated by bending rigidity. However, the higher bending-energy costs for the hourglass states compared to the tent-like states need to be compensated; we believe that this is achieved by the actin of the free membrane joining toward the junctionalmembrane (Fig. 3 b) thereby providing higher effective contact interaction.

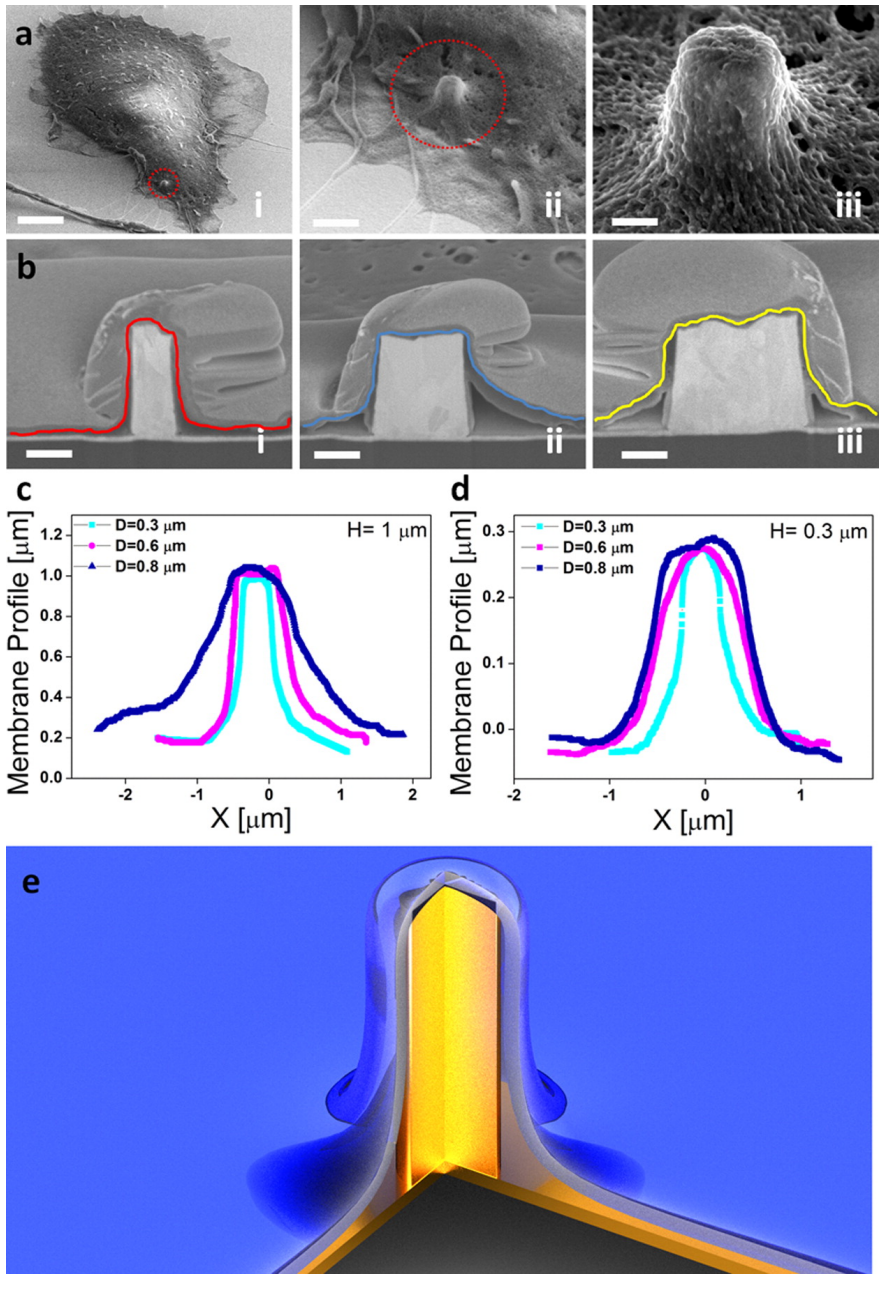

Figure 2: Free membrane deformation at the edge of the cell as response to 3D cylindrical nanostructures without caps. (a) SEM micrographs of individual fixed HL-1 cells, each engulfing a cylinder without a cap ((i) scale bar 10 μm, (ii) scale bar 1 μm, (iii) scale bar 0.2 μm); (b) FIB cross sections of fixed HL-1 on cylinders without caps (scale bars 0.3 μm); (c) membrane profiles for different diameter pillars with cylinder height of 1 μm; (d) membrane profiles for different diameter pillars with cylinder height of 0.3 μm; (e) schematic of a cell promoting an engulfment-like event of a cylindrical nanopillar without cap at the edge of the cell.

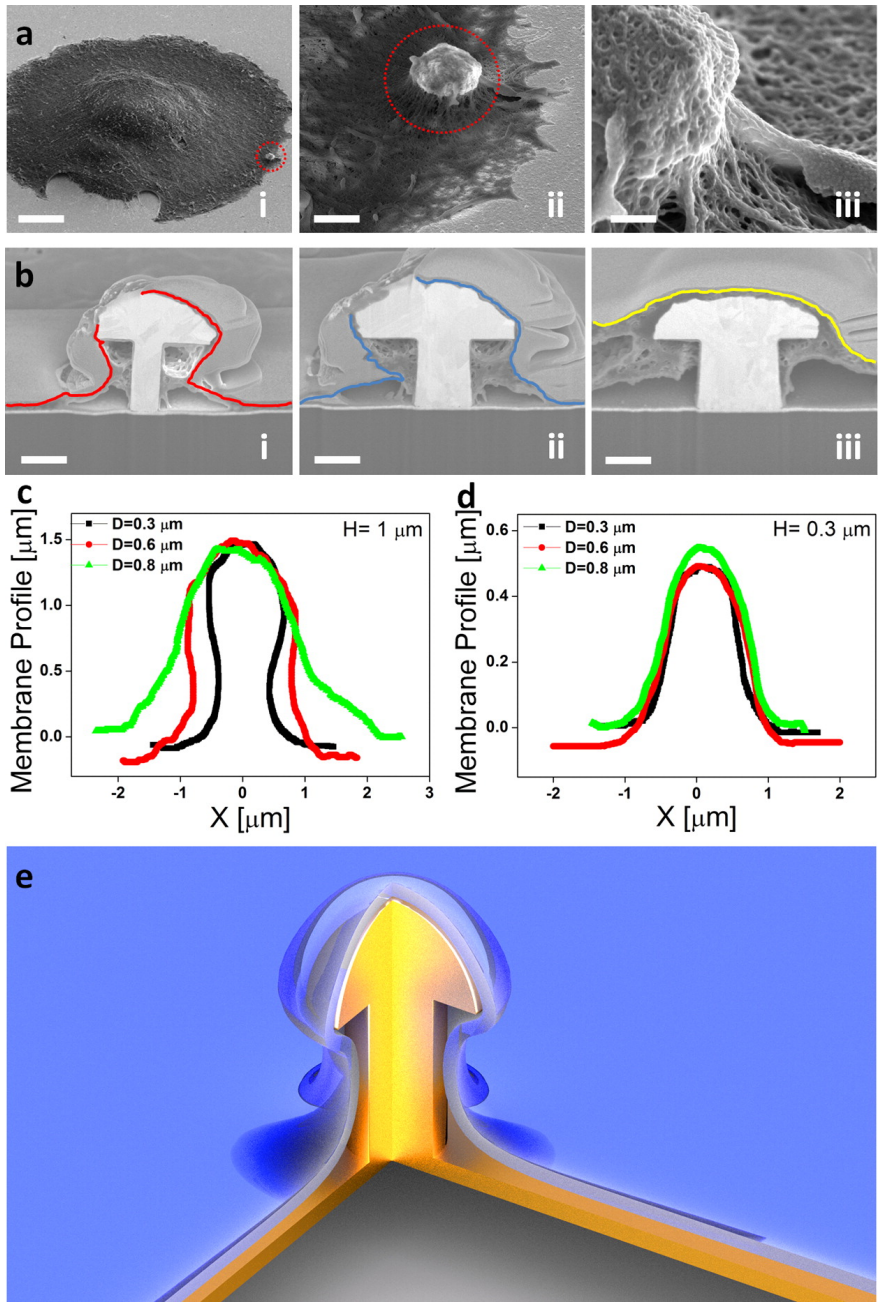

Figure 3: Free membrane deformation at the edge of the cell as response to 3D cylindrical nanostructures with caps. (a) SEM micrographs of individual fixed HL-1 cells engulfing a cylinder with a cap ((i) scale bar 5 μm, (ii) scale bar 1.5 μm, (iii) scale bar 250 nm); (b) FIB cross sections of fixed HL-1 on cylinders with caps (scale bars 0.3 μm); (c) membrane profiles for different stalk diameters with stalk height 1 μm; (d) membrane profiles for different stalk diameter pillars with cylinder height of 0.3 μm; (e) schematic of a cell promoting an engulfment-like event of a cylindrical nanopillar with cap at the edge of the cell.

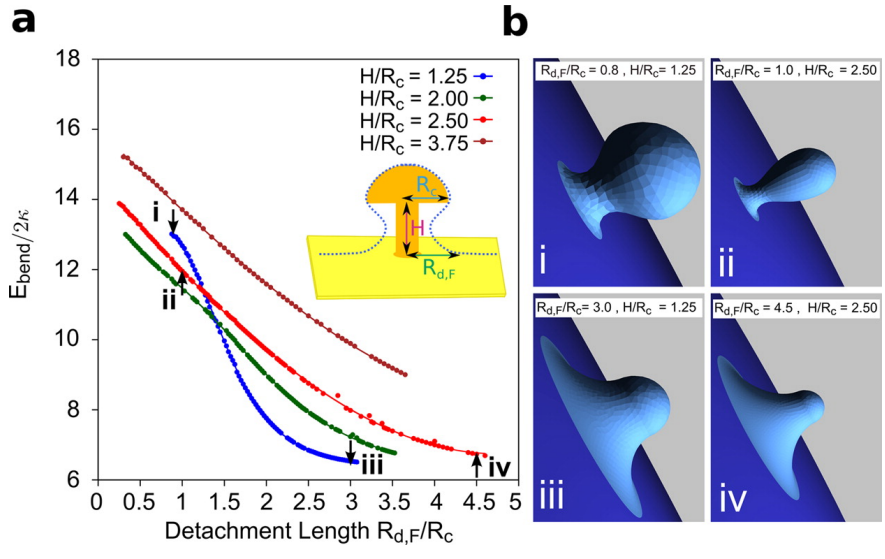

Figure 4: Theoretical analysis of the membrane deformation profiles at the edge of the cell. (a) Bending energy for different stalk heights,H, and cap radii, R_c, as a function of the detachment length, $R_{d,F}/R_c$. Because of the scale invariance, the bending energy depends only on the ratios H/R_c and $R_{d,F}/R_c$ and not on the absolute values of the dimensions. (b) Membrane shapes for the parameter values indicated by the arrows in the inset of (a).

5.5
Nanopillar Shape and Dimension Induce Differences in Junctional Membrane Deformation at the Cell Center.

Finally, we investigated the interface of HL-1 cells on 3D nanostructures when an engulfment-like event occurs at the center of the cell. We observed that the free membrane does not sense the structure underneath, which allows us to focus on the interaction of the 3D nanostructure with the junctional membrane. During the endocytosis of a nanoparticle, the actin filaments provide key active forces during membrane wrapping [34-36]. In the case of 3D nanostructures fixed on a substrate, the membrane does not form a complete bud encapsulating the structure, but the junctional membrane deforms and establishes a ring-like assembly around the 3D structure [33] In the center of the cell, the central junctional membrane only partially attaches to the pillar, and detaches from the flat gold surface of the substrate (Fig. 5 a,b). These phenomena were previously observed for Neuro-2a [18] and primary neurons, [44] where the membrane engulfing a mushroom-like nanostructure in the center of the cell detached from the planar substrate. We investigated the junctional membrane responses to the 3D nanostructures by analyzing FIB cross sections through the center of the pillar (Fig. 5 a,b). The junctional membrane was characterized with regard to four independent parameters as shown in Fig. 5 c,d (see also Supporting Information S2). $R_{d,J}$), the cross-sectional area of the detaching membrane (A), the engulfment length (d_e), and the attachment angle (α. $R_{d,J}$ is the

horizontal distance from the membrane attachment point on the planar substrate to the central z-axis of the pillar. d_e is evaluated as the vertical projection from the top of the pillar to the membrane attaching point on the pillar stalk, as shown in Fig. 5 c. α is the angle between the curving membrane and the vertical of the pillar, at the point where the membrane is not attached to the stalk under the cap (see Supporting Information S3). On the one hand, for stalk aspect ratios between 0.4 and 0.75, $R_{d,J}$ for the nanopillars with and without cap are comparable (0.75 μm in average) as shown in Fig. 5 (e). On the other hand, when the aspect ratio is highest (3.3), we observed an average $R_{d,J}$ of 0.25 μm on for a nanopillar without a cap, while $R_{d,J}$ was more than 10 times higher (2.6 μm) for a nanopillar with a cap. The difference in $R_{d,J}$ causes the resulting difference in A of 0.42 μm^2 and 0.04 μm^2 for a cylinder with a cap and without a cap, respectively (Fig. 5 (f)). We calculate the engulfment percentage, f, as the ratio between d_e and the total height of the pillar (Fig. 5 (g)). For both shapes, the highest engulfment percentage was achieved at the highest aspect ratio ($\gamma = 3.3$). In this case, the cells engulf 75 % of the volume of nanopillars without cap and up to 95 % of the volume of nanopillars with cap. To analyze α, the tangent of the junctional membrane was extended to the vertical axis of the pillar (see Supporting Information S3). We define a threshold engulfment angle when the membrane forms an angle less than 90° with the vertical axis of the pillar, as shown in Fig. 5 h and described in details in the Supporting Information S3. According to our data, all nanopillars with caps promote an engulfment-like event, except for structures of the lowest aspect ratio, $\gamma = 0.4$. We assume that the curvature of the junctional membrane is influenced mostly by the cytoskeletal forces pulling the junctional membrane toward the free membrane while the actin ring around the nanopillar is mostly generating forces pulling the junctional membrane toward the substrate.36 Moreover, we assume that the actin filaments influence the membrane attachment point on the stalk (Fig. 5 i). At highest aspect ratio (*i.e.*, 3.3), we found the biggest detachment length (and thus the area), the highest engulfment percentage and the smallest attachment angle. The angle, in particular, is a very important parameter since angles lower than 90° indicate that the membrane highly deforms around the 3D nanostructure. In fact, such a high wrapping state is comparable to what happens for complete phagocytosis events where the membrane deforms around the particle until the complete encapsulation. This means that for typical phagocytosis events, the membrane pulls toward the particle to form an invagination. Here, the membrane "tries" to invaginate the 3D nanostructures and deforms accordingly. Since the 3D nanostructure is fixed on the planar substrate, the cell is not able to internalize it but the cell membrane stays in the invaginating deforming status. For angles greater than 90° the membrane has a tent-like deformation, which is clearly a sign for a nonencapsulating-like membrane. On the basis of the calculated parameters, we approximated effective seal resistances in the vicinity of the nanoelectrodes with an assumed constant gap between adhered junctional membrane and the nanoelectrode (see Supporting Information S6).

We analyzed the central membrane deformation profiles theoretically (see Supporting Information S7) by the same model used for the description of the engulfment-like event at the edge of the cell. In addition, we consider the contribution of the cytoskeleton stress, which we quantify by an effective pressure, p, normal to the

planar substrate. For fixed engulfment percentage and detachment length, we find a transition from a tent-like deformation without cytoskeletal stress, to more curved shape of the junctional membrane at high cytoskeletal stress (Fig. 6 a, i-iv). The theoretical model is applicable for fitting every experimental data set with good agreement, here we show few examples in Fig. 6 d-g. This agreement justifies the choice of an effective pressure for the cytoskeleton stress in our model, as schematically shown in Fig. 6 b. As done previously for the edge of the cell, we assumed a bending rigidity of $\kappa = 50\,k_{\mathrm{B}}T$ for the junctional membrane. The cytoskeletal stress and adhesion strength of the cell to the substrate are extracted from the averaged experimental data (Fig. 6 c and inset). The cytoskeletal stress for cylinders without caps is $p < 440\,Pa$, which is comparable to cytoskeletal stress reported for fibroblasts [45] (range from 10 Pa to several kPa). Up to $\gamma = 1.6$, the cytoskeletal stress increases with the pillar's aspect ratio. Then it appears to have decreased again at $\gamma = 3.3$. However, the uncertainty for the calculated high cytoskeletal stress is large, as discussed in the Supporting Information S7. Surprisingly, in the case of cylinders with caps, the cytoskeletal stress is 1 order ofmagnitude smaller than for cylinders without caps for that the cytoskeletal stress is $p < 30\,Pa$. This shows that the cell is actively responding to the presence of the nanopillars and that the cytoskeleton adapts to the substrate underneath. This distinguishes our model from the model of Xie et al. [27] where the membrane deformation is influenced mostly by gravitational forces. For capped nanopillars with $\gamma = 1.6$ and $\gamma = 3.3$, we find cytoskeletal stresses of only $p = 2\,Pa$. This indicates that capped nanopillars with high aspect ratio more easily promote an engulfment-like event by HL-1 cells than all other nanopillars that we have studied. Points of attachment with enriched adhesion molecules have been reported previously on 3D nanostructures [46]. We find for cylinders with and without cap that these regions of presumably higher adhesion strength correspond to areas requiring strong cytoskeletal pulling forces to achieve the membrane deformations observed (inset Fig. 6 6c). We found adhesion strengths between the cell and the substrate of up to $w = 5\mu J/m^2$ for cylinders without cap and down to $w = 500nJ/m^2$ for cylinders with cap. The values of the adhesion strengths are similar to those that have been measured for adhered vesicles47 but smaller than those quoted by Xie et al [27].

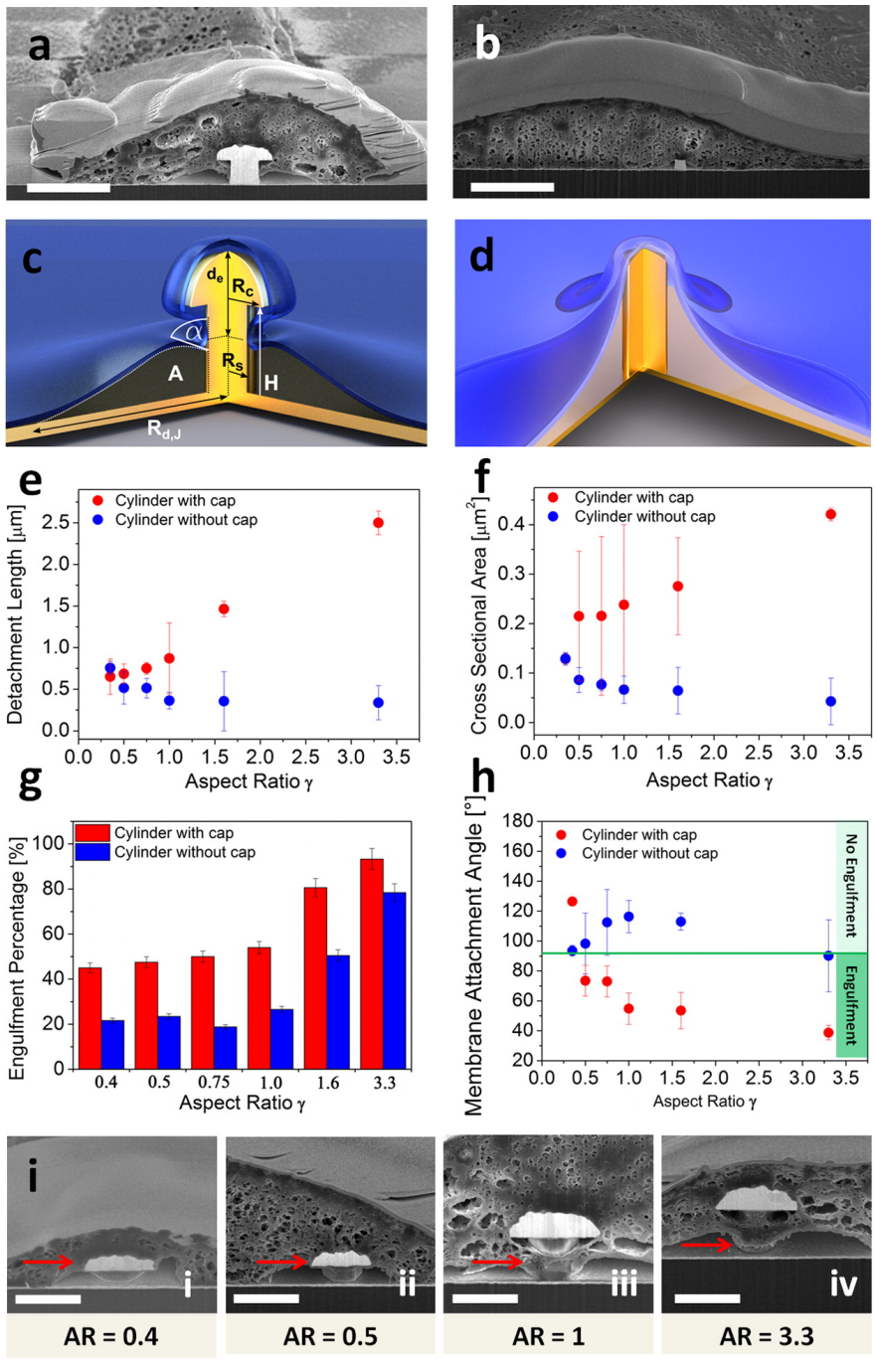

Figure 5: Junctional membrane deformation investigation in the center of the cell. (a) FIB cross section of HL-1 engulfing a cylinder with a cap in the center of the cell (scale bar 1 μm); (b) FIB cross section of HL-1 engulfing a cylinder without a cap in the center of the cell (scale bar 1 μm); (c) schematic of experimental parameters calculated for cylinders with caps and (d) schematic of junctional membrane attaching a cylinder without cap; (e) junctional membrane detachment length, $R_{d,J}$, plotted as a function of the stalk aspect ratio, γ; (f) area, A, plotted as a function of γ; (g) engulfment percentage, f, plotted as a function of γ; (h) angle, R, plotted as a function of γ, with the engulfment threshold at 90°; (i) ring like structure on the stalk at different values of γ (I and ii scale bar, 1 μm; iii and iv scale bar, 1.5 μm).

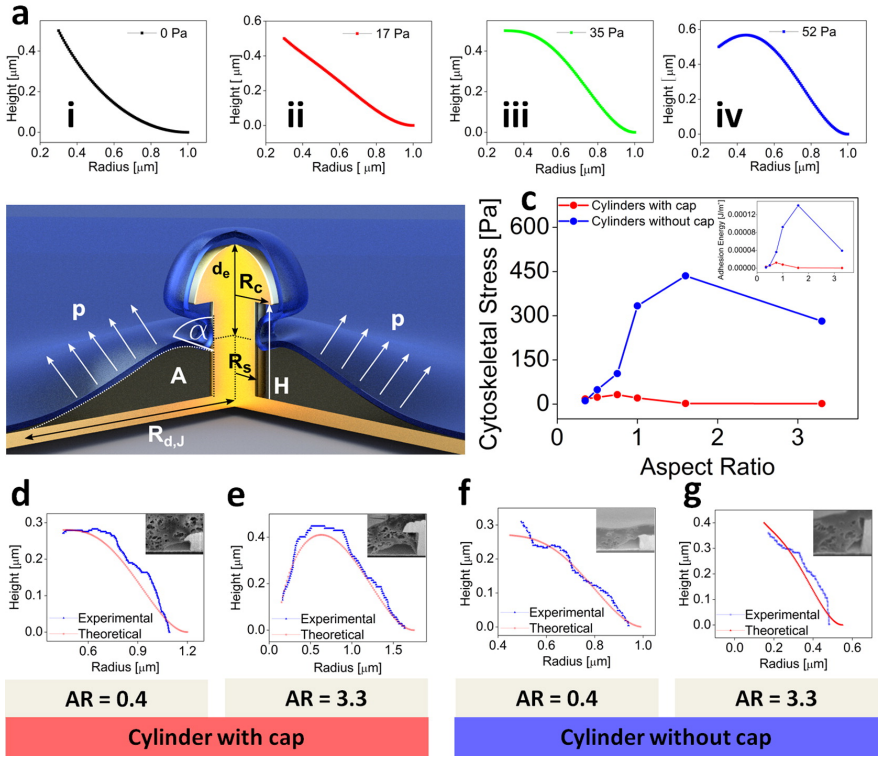

Figure 6: Theoretical analysis of the membrane deformation profiles in the center of the cell. (a) Membrane deformation for fixed pillar radius, R_s, membrane height at the stalk height, H, and detachment length, $R_{d,F}$, and several values of cytoskeletal stress, p. (b) Schematic describing the theoretical model. (c) Cytoskeletal stress and strength of adhesion to the substrate for several aspect ratios, extracted from the experimental data given in Figure 5d-g), comparison of experimental and theoretical deformation profiles.

5.6 Conclusion

Previous works regarding in-cell recordings considered the possibility to have a 3D nano- or microelectrode in the very proximity of the cell junctional membrane. This very close contact, confirmed also by TEM studies, improved the electrical seal resistance and, thus, the quality of the recorded action potentials from electrogenic cells. In this work, we have studied the effect of shape and dimensions of 3D nanopillars/nanoelectrodes using a systematic approach for analyzing the cell- nanoelectrode interface. First, we found that HL-1 cells prefer to engulf 3D nanostructures in the center of the cell compared to the periphery. Cells deform their membranes in different ways depending on the position of the engulfment-like event. It is very likely that the engulfed nanopillar is stabilized by an actin network in the center of the cell, while this network is in a much more dynamic state at the edge of the cell, driving the filopodia on the planar substrate. Then, we performed combined experimental and theoretical studies at the periphery of the cell, which allow the prediction of free membrane deformations by considering simple lipid-bilayer deformations. For the center of the cell, we need to additionally account for the contribution of the cytoskeletal stress. Consequently, we can estimate the junctional membrane deformation depending on nanopillar shape and dimensions, assuming that the free membrane cannot sense the 3D nanostructure underneath due to the intervening contents of the cell. We conclude that in both scenarios;edge and center-higher membrane coverage of the 3D electrode is observed for the cylinder with cap. We estimated the effective seal resistance in the vicinity of our nanoelectrode from the SEM images according to the method described by Fendyur et al. [20], assuming a cleft between the adhered cellmembrane and nanoelectrode of 25 nm (see Supporting Information S6). In the center of the cell, we obtained seal resistances of about 6 and 54 MΩ for γ, respectively, for capped cylinders. These values are similar to those reported before by modeling [20,24]. Beside the shape of the 3D nanostructures, the dependency of the seal resistance on the engulfment-like position suggests that for in-cell recording the position of the cell on the active electrode plays a key role for the quality of the signal. In summary, capped cylinders with $\gamma = 3.3$ energetically and biomechanically favor hourglass-like adhesion compared to nanopillars with smaller γ. We can conclude that for interfacing electrogenic cells with 3D nanoelectrodes positioned within the cell, the shape and size of the 3D nanoelectrodematter. Future studies shall focus on recordings of electrogenic cells with nanopillars whose caps have been designed on the basis of the results presented here. Furthermore, we will investigate whether neuronal cell membranes respond differently to the HL-1 cells considering that neuronal cells are definitely less stiff than cardiomyocytes-like cells, which are typically as stiff as fibroblasts.

5.7
Methods

Chemicals

Unless otherwise noted, all the chemicals were provided by Sigma Aldrich, St. Louis, USA

5.7.1
Fabrication of gold spines

Gold micro spines were fabricated similarly as previously shown [21]. In summary, a layer of evaporated gold of 40 nm was deposited on a 10×10 mm^2 silicon substrate.To fabricate the micro spines with different stalk heights, three different e-beam resists have been spin-coated on to the substrates: AR-P 669.04, 679.04 and 669.07 (Allresist GmBH, Berlin, Germany) at 3000 rpm, which resulted in a resist thickness of about 300, 500,and about 1000 nm, respectively. The arrays of circular apertures (300, 500, 800 nm of diameter) were created by means of e-beam lithography with a pitch of 25 μm. Next, the samples were baked at high temperature in order to form round shaped aperture edges. Subsequently, these apertures were filled with gold by electrodeposition. In the case of the mushroom shaped pillar the electrodepostion was performed in order to have caps of 300-2000 nm in diameter. As final step of spine preparation, the resist was removed in acetone releasing the free standing gold micro spines. The samples were then cleaned in 2-propanol and flowing distilled water for 4 h, sterilized with UV and coated with fibronectine and of 0.02 % Bacto Gelatin (Fisher Scientific) for 1h.

5.7.2
HL-1 culture

Confluent HL-1 cells [48] in a T-25 flask were treated with 0.05 % 4 Trypsin/EDTA (Life Technologies), suspended in 5 ml of Claycomb medium and centrifuged for 5 minutes at 1700 rpm. The cell pellet was resuspended in 5 ml of medium; 15 μl of the suspension was then plated on every substrate, after 1h the medium volume was filled up to 3 ml for every sample.

5.7.3
Membrane stain and fixation of cells

After 2DIV, the cells were washed with in Phosphate Buffer Saline (PBS) solution (137 mM NaCl, 2.7 mM KCl, 8 mM Na_2HPO_4, 1.8 mM KH_2PO_4), chemically fixed with 3.2% glutaraldehyde in PBS. Cell membranes and nuclei were stained with 1:1000 dilution in PBS of Wheat Germ Agglutinin Alexa Fluor 488 (Life Technologies) and 1:500 in PBS of DAPI. The cells were observed in a fluorescence microscope (AxioImager Z.1, Carl Zeiss AG) and then, prepared for the scanning electron microscope. For the actin stain, themembrane was permeablized with 0.1%

TritonX in milk blocking solution, Phalloidin-Biotin-XX (Life Technologies) compound was diluted in a 1:500 concentration in the total volume, and, finally, Streptavidin Nanogold-AlexaFluor 488 (Life Technologies) was used in a dilution of 1:50 in milk blocking solution. In addition, the samples were stained with 0.5% osmium tetroxide and washed with water. The water was replaced with ethanol in different concentrations (10%-100% v/v), and finally, the cells on the substrates were dried by critical point drying (see Supporting Information S4). Before the SEM, a thin layer of platinum was sputtered on the samples.

5.7.4
Scanning Electron Microscopy and Focused Ion Beam

The focused ion beam cross-sectioning was performed with a Helios Nanolab Dualbeam (FEI Company). First, a 0.4 μm layer of platinum was deposited via electron beam induced deposition (EBID). The sample was then tilted by 52° and an additional 0.4 μm thick platinum layer was deposited by ion beam induced deposition (IBID) with a current of 0.43 nA at 30 kV. The milling and the polishing of the cross sections have been performed using a voltage of 30 kV and a current of 80 pA [49]. The images were then acquired in scanning electron mode fixing a voltage at 3 kV.

5.7.5
Image processing and analysis

Images were processed and analyzed with ImageJ. The contrast and the brightness were not varied from the original SEM pictures. All the parameters evaluated and discussed in the paper were manually analyzed, except for the membrane profile, in the case of the pillar positioned at the edge of the cell. In this case, an automatic macro utility was used for the outline recognition (courtesy of Zhanna Santybayeva, ICS-7, Forschungszentrum Juelich, Germany). For data analysis and plotting, we used Origin 8.2

5.7.6
Theoretical model

The deformation energy cost due to bending energy for a fluid membrane is given by ,

$$\mathcal{E}_{\text{bend}} = 2\kappa \int_A dS H^2 \ , \tag{5.1}$$

where κ is the bending rigidity of the membrane, $H = (c_1 + c_2)/2$ the mean curvature, and S the entire membrane area. The curvatures c_1 and c_2 are the principal curvatures, *i. e.*, the smallest and the largest curvature at each point of the membrane. We show that the experimentally measured membrane deformation profiles can be described well even with a vanishing surface tension contribution. The adhesion energy gain is given by the contact energy between the pillar and the nanostructure,

$$\mathcal{E}_{\text{ad}} = -w \int_{S_{ad}} dS \ , \tag{5.2}$$

where w is the adhesion strength and S_{ad} the membrane area adhered to the structured substrate. For calculating the deformation profile of the lower membrane, we use in addition a homogeneous pressure term, $-ph(x,y)$, where the membrane is described by a height field $h(x,y)$ and the pressure mimics the contractile forces of the cytoskeleton. Assuming a perfect wetting condition, i.e., a contact angle of π at the detachment point of the tensionless membrane with either the substrate (for the junctional membrane deformation at centre of the cell) or on the junctional membrane (for the free membrane deformation at the edge of the cell) , we estimate an effective strength of the adhesion w using the local curvature c at the detachment point such that, $c = \sqrt{2w/\kappa}$.

Supporting material

Details about numerical calculations and additional images.

Acknowlegments

F.S. and S.D. acknowledge the International Helmholtz Research School of Biophysics and Soft Matter (IHRS BioSoft) for the financial support. Direct funding to support theoretical work from the EU FP7 NMP collaborative project PreNanoTox (Project Grant 309666, GG) is acknowledged. S.D. thanks Ken Brakke (Selinsgrove, PA) for his assistance and helpful discussions in numerical techniques about Surface Evolver. The authors thank Rudolf Merkel (Jülich), Zhanna Santybayeva (Juelich) and Markus Deserno (Pittsburg, PA) for stimulating discussions and advice. F.S. thanks Vanessa Maybeck (Jülich) for helpful discussions and language advice.

References: Chapter 5

1. Bakkum, D. J. et al. Tracking axonal action potential propagation on a high-density microelectrode array across hundreds of sites. Nat. Commun. 4, (2013).

2. Dagnelie, G. Retinal implants: emergence of a multidisciplinary field. Curr. Opin. Neurol. 25, 67–75 (2012).

3. Volkmann, J. et al. Selecting deep brain stimulation or infusion therapies in advanced Parkinson's disease: an evidence-based review. J. Neurol. 260, 2701–2714.(2013).

4. Fisher, J. D., Kim, S. G. Mercando, A. D. Electrical devices for treatment of arrhythmias. Am. J. Cardiol. 61, A45–A57 (1988).

5. Spira, M. E. Hai, A. Multi-electrode array technologies for neuroscience and cardiology. Nat. Nanotechnol. 8, 83–94 (2013).

6. Hai, A., Shappir, J. Spira, M. E. In-cell recordings by extracellular microelectrodes. Nat. Methods 7, 200–202 (2010).

7. Silva, G. A. Neuroscience nanotechnology: progress, opportunities and challenges. Nat. Rev. Neurosci. 7, 65–74 (2006).

8. Almquist, B. D. Melosh, N. A. Fusion of biomimetic stealth probes into lipid bilayer cores. Proc. Natl. Acad. Sci. U. S. A. 107, 5815–5820 (2010).

9. Robinson, J. T. et al. Vertical nanowire electrode arrays as a scalable platform for intracellular interfacing to neuronal circuits. Nat. Nanotechnol. 7, 180–184 (2012).

10. Xie, C., Lin, Z., Hanson, L., Cui, Y. Cui, B. Intracellular recording of action potentials by nanopillar electroporation. Nat. Nanotechnol. 7, 185–190 (2012).

11. Duan, X. et al. Intracellular recordings of action potentials by an extracellular nanoscale field-effect transistor. Nat. Nanotechnol. 7, 174–179 (2012).

12. Ross, A. M., Jiang, Z., Bastmeyer, M. Lahann, J. Physical Aspects of Cell Culture Substrates: Topography, Roughness, and Elasticity. Small 8, 336–355 (2012).

13. Sniadecki, N. J., Desai, R. A., Ruiz, S. A. Chen, C. S. Nanotechnology for Cell–Substrate Interactions. Ann. Biomed. Eng. 34, 59–74 (2006).

14. Andersson, A.-S. et al. Nanoscale features influence epithelial cell morphology and cytokine production. Biomaterials 24, 3427–3436 (2003).

15. Pogodin, S.; Hasan, J.; Baulin, V. A.; Webb, H. K.; Truong, V. K.; Phong Nguyen, T. H.; Boshkovikj, V.; Fluke, C. J.; Watson, G. S.; Watson, J. A.; et al. Biophysical Model of Bacterial Cell Interactions with Nanopatterned Cicada Wing Surfaces. Biophys. J. 2013, 104, 835–840.

16. Pierre-Louis, O. Adhesion of Membranes and Filaments on Rippled Surfaces. Phys. Rev. E: Stat., Nonlinear, Soft Matter Phys. 2008, 78, 021603.

17. Hai, A. et al. Changing gears from chemical adhesion of cells to flat substrata toward engulfment of micro-protrusions by active mechanisms. J. Neural Eng. 6, 066009 (2009).

18. Van Meerbergen, B. et al. in 2008 30th Annu. Int. Conf. IEEE Eng. Med. Biol. Soc. Vols 1-8 1833–1836 (Ieee, 2008).

19. Xie, C. et al. Noninvasive Neuron Pinning with Nanopillar Arrays. Nano Lett. 10, 4020–4024 (2010).

20. Fendyur, A., Mazurski, N., Shappir, J. Spira, M. E. Formation of Essential Ultrastructural Interface between Cultured Hippocampal Cells and Gold Mushroom-Shaped MEA- Toward 'IN-CELL' Recordings from Vertebrate Neurons. Front. Neuroengineering 4, (2011).

21. Panaitov, G., Thiery, S., Hofmann, B. Offenhäusser, A. Fabrication of gold micro-spine structures for improvement of cell/device adhesion. Microelectron. Eng. 88, 1840–1844 (2011).

22. Martiradonna, L. et al. Beam induced deposition of 3D electrodes to improve coupling to cells. Microelectron. Eng. 97, 365–368 (2012).

23. VanDersarl, J. J., Xu, A. M. Melosh, N. A. Nanostraws for Direct Fluidic Intracellular Access. Nano Lett. 12, 3881–3886 (2012).

24. Hanson, L., Lin, Z. C., Xie, C., Cui, Y. Cui, B. Characterization of the cell-nanopillar interface by transmission electron microscopy. Nano Lett. 12, 5815–5820. (2012).

25. Wierzbicki, R. et al. Mapping the Complex Morphology of Cell Interactions with Nanowire Substrates Using FIB-SEM. PLoS ONE 8, e53307 (2013).

26. Santoro, F., Schnitker, J., Panaitov, G. Offenhäusser, A. On Chip Guidance and Recording of Cardiomyocytes with 3D Mushroom-Shaped Electrodes. Nano Lett. (2013). doi:10.1021/nl402901y

27. Xie, X. et al. Mechanical Model of Vertical Nanowire Cell Penetration. Nano Lett. (2013). doi:10.1021/nl403201a

28. Hai, A., Shappir, J. Spira, M. E. Long-Term, Multisite, Parallel, In-Cell Recording and Stimulation by an Array of Extracellular Microelectrodes. J. Neurophysiol. 104, 559–568 (2010).

29. Hai, A. Spira, M. E. On-chip electroporation, membrane repair dynamics and transient in-cell recordings by arrays of gold mushroom-shaped microelectrodes. Lab. Chip 12, 2865–2873 (2012).

30. Verma, P. Melosh, N. A. Gigaohm resistance membrane seals with stealth probe electrodes. Appl. Phys. Lett. 97, 033704–033704–3 (2010).

31. Fendyur, A. Spira, M. E. Toward on-chip, in-cell recordings from cultured cardiomyocytes by arrays of gold mushroom-shaped microelectrodes. Front. Neuroengineering 5, (2012).

32. Braeken, D. et al. in World Congr. Med. Phys. Biomed. Eng. Sept. 7 - 12 2009 Munich Ger. (Dössel, O. Schlegel, W. C.) 212–215 (Springer Berlin Heidelberg, 2010).

33. Spira, M. E. et al. Improved Neuronal Adhesion to the Surface of Electronic Device by Engulfment of Protruding Micro-Nails Fabricated on the Chip Surface. in Solid-State Sens. Actuators Microsyst. Conf. 2007 TRANSDUCERS 2007 Int. 1247–1250 (2007). doi:10.1109/SENSOR.2007.4300363

34. Kaksonen, M., Toret, C. P. Drubin, D. G. Harnessing actin dynamics for clathrin-mediated endocytosis. Nat. Rev. Mol. Cell Biol. 7, 404–414 (2006).

35. Lamaze, C., Fujimoto, L. M., Yin, H. L. Schmid, S. L. The Actin Cytoskeleton Is Required for Receptor-mediated Endocytosis in Mammalian Cells. J. Biol. Chem. 272, 20332–20335 (1997).

36. Jeng, R. L. Welch, M. D. Cytoskeleton: Actin and endocytosis — no longer the weakest link. Curr. Biol. 11, R691–R694 (2001).

37. Claycomb, W. C. et al. HL-1 cells: A cardiac muscle cell line that contracts and retains phenotypic characteristics of the adult cardiomyocyte. Proc. Natl. Acad. Sci. 95, 2979–2984 (1998).

38. Dasgupta, S., Auth, T. Gompper, G. Wrapping of ellipsoidal nano-particles by fluid membranes. Soft Matter 9, 5473–5482 (2013).

39. Dasgupta, S., Auth, T. Gompper, G. Shape and Orientation Matter for the Cellular Uptake of Nonspherical Particles. Nano Lett. (2014). doi:10.1021/nl403949h

40. Fromherz, P., Offenhäusser, A., Vetter, T. Weis, J. A neuron-silicon junction: a Retzius cell of the leech on an insulated-gate field-effect transistor. Science 252, 1290–1293 (1991).

41. Vinzenz, M. et al. Actin branching in the initiation and maintenance of lamellipodia. J. Cell Sci. 125, 2775–2785 (2012).

42. Helfrich, W. Elastic properties of lipid bilayers: theory and possible experiments. Z. Für Naturforschung Teil C Biochem. Biophys. Biol. Virol. 28, 693–703 (1973).

43. Noguchi, H. Gompper, G. Shape transitions of fluid vesicles and red blood cells in capillary flows. Proc. Natl. Acad. Sci. U. S. A. 102, 14159–14164 (2005).

44. Sileo, L. et al. Electrical coupling of mammalian neurons to microelectrodes with 3D nanoprotrusions. Microelectron. Eng. 111, 384–390 (2013).

45. Ananthakrishnan, R. Ehrlicher, A. The Forces Behind Cell Movement. Int. J. Biol. Sci. 3, 303–317 (2007).

46. Thomas, W. E., Vogel, V. Sokurenko, E. Biophysics of Catch Bonds. Annu. Rev. Biophys. 37, 399–416 (2008).

47. Smith, A.-S. Seifert, U. Effective adhesion strength of specifically bound vesicles. Phys. Rev. E 71, 061902 (2005).

48. Hai, A. et al. Spine-shaped gold protrusions improve the adherence and electrical coupling of neurons with the surface of micro-electronic devices. J. R. Soc. Interface 6, 1153–1165 (2009).

49. Claycomb, W. C. et al. HL-1 cells: A cardiac muscle cell line that contracts and retains phenotypic characteristics of the adult cardiomyocyte. Proc. Natl. Acad. Sci. 95, 2979–2984 (1998).

50. Santoro, F.; Neumann, E.; Panaitov, G.; Offenhäusser, A. FIB Section of Cell-Electrode Interface: An Approach for Reducing Curtaining Effects. Microelectron. Eng. 2014, 124, 17–21.

5.8
Supplementary material

Supplementary material: Interfacing Electrogenic Cells with 3D Nanoelectrodes: Position, Shape, and Size Matter

S1 : Base aspect ratio

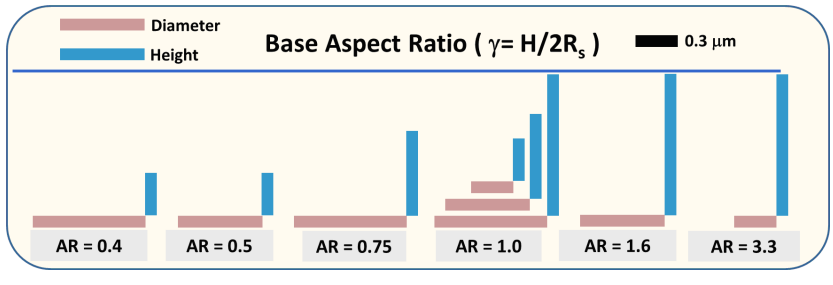

Figure S1: Scheme of all stalk aspect ratios considered in the image analysis.

The fabricated nanopillars (cylindrical and mushroom shaped), were of 3 different stalk heights H: 300 nm, 600 nm, 1000 nm. For the radii R_s, we had: 150 nm, 300 nm, 400 nm. As aspect ratio we considered $H/2R_s$, so the final aspect ratios were 0.4 (0.3 μm/0.8 μm), 0.5 (0.3 μm/ 0.6 μm), 0.75 (0.6 μm/ 0.8 μm), 1 (0.3 μm/0.3 μm, 0.6 μm/0.6 μm, 1 μm/ 0.8 μm was also approximated to 1), 1.6 (1 μm/ 0.6 μm), 3.3 (1 μm/ 0.3 μm). The aspect ratio 2 (0.6 μm/ 0.3 μm) was not considered for the statistics due to the small number of measurements. For cylinders with caps, we considered a cap radius, R_c, in the range of 0.15-1 μm. Depending on the parameters of the cylinder: typically the cap radius increased linearly with the stalk radius.

S2: FIB image analysis for pillars engulfed in the center of the cell

Sequential cross sections were obtained with FIB [1], considering a sequence thickness of 100-200 nm depending on the dimensions of the pillars (Fig. S2-I). The image processing and analysis were performed with ImageJ. Fig. S2-II (a) shows an example of the analyzed parameters in the case of the pillar with a mushroom shape, Fig. S2-II (b) shows an example of the attachment angle α measurements in case of cylindrical pillars. For the angle measurements, we used the plug-in "ThreePointsCircularROI" (freeware provided by G.Landini).

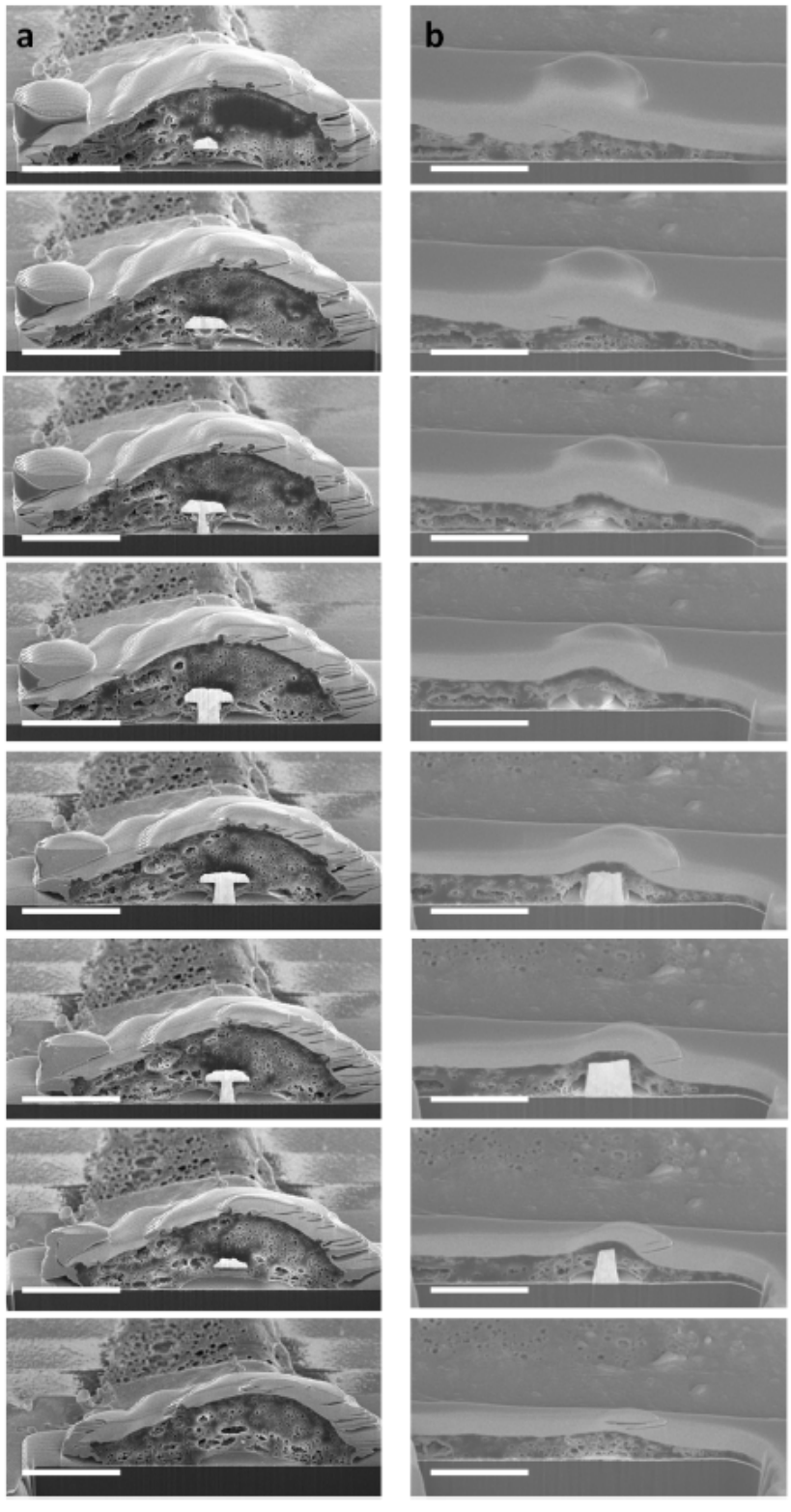

Figure S2: -I: a) Sequential cross sections of an HL-1 engulfing a cylinder with cap in the center (scale bar 2 μm) ; b) sequential cross sections of HL-1 engulfing a cylinder without cap in the center (scale bar 2 μm).

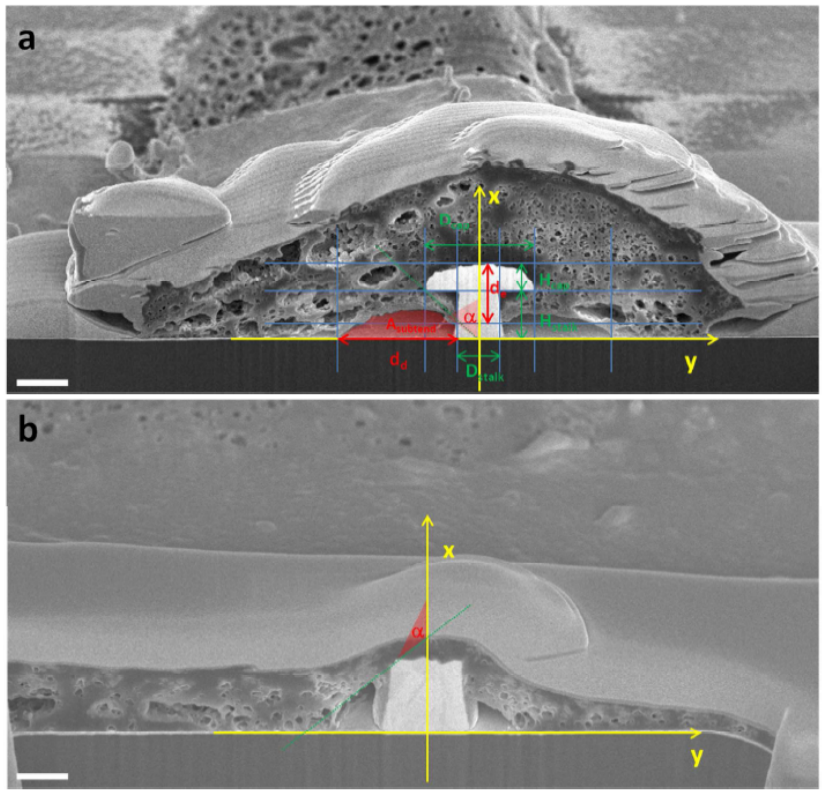

Figure S2: -II: a) example of cross section for cylinder with cap engulfed in the center (scale bar 0.5 μm); b) indication of membrane contact angle analyzed for HL-1 engulfing a cylinder without cap in the center (scale bar 0.4 μm).

S3: Attachment angle analysis

The angle α is determined as the angle between the attaching membrane and the vertical axis of the pillar. We distinguished three attachment scenarios: $\alpha < 90°$, $\alpha = 90°$, $\alpha > 90°$ as shown in the schematic of Fig. S3.

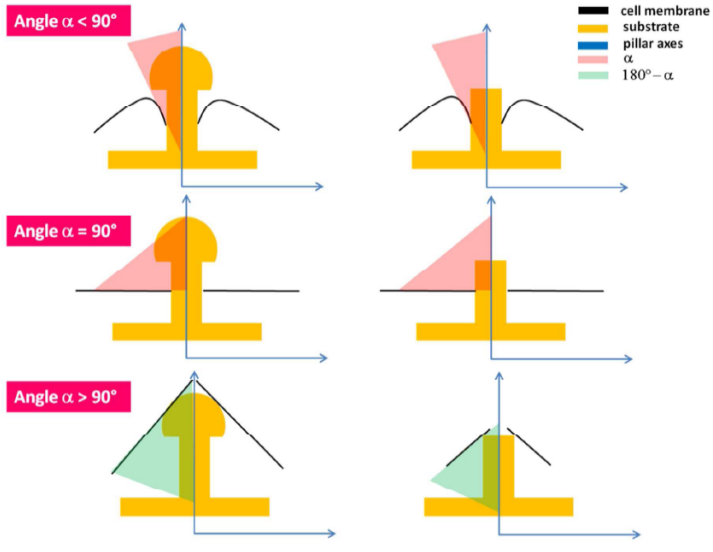

Figure S3: Attachment angle analysis

S4: Immuno-gold-stain of actin filaments

HL-1 cells were washed with PBS solution and fixed after 2 DIV with 3.2 % glutaraldehyde for 15 min at room temperature. After washing with PBS, the samples were in milk blocking solution (BS) for 1 hour and then the membrane was permeabilized for 15 min with 0.1 % TritonX at room temperature. After washing, the actin was stained first with 1:500 dilution of Phalloidin-XX- Biotin (Life Technologies) and then with 1:50 dilution of Streptavidin- Nanogold- Alexa 488 (Life Technologies) in BS for 1 h each. Afterwards, the samples were carefully washed and treated with 0.02 M sodium citrate for 10 min. In addition, the samples were stained with 0.5 % osmium tetroxide for 1h. Finally, the samples were washed with distilled water, dehydrated with ethanol ranging in concentration from 10 % up to 100 % (5 minutes each) and dried using critical point drying (the ethanol was exchange 10 times with liquid CO_2. Fig. S4 (a) shows a FIB cross section of a HL-1 cell engulfing the pillar in the middle. In order to visualize the gold nanoparticles on the actin filaments the contrast was enhanced (Fig. S4 b) and colored for analysis of the nanoparticles distribution. The gold nanoparticles stain allowed us to visualize the actin filaments and bundles morphology.

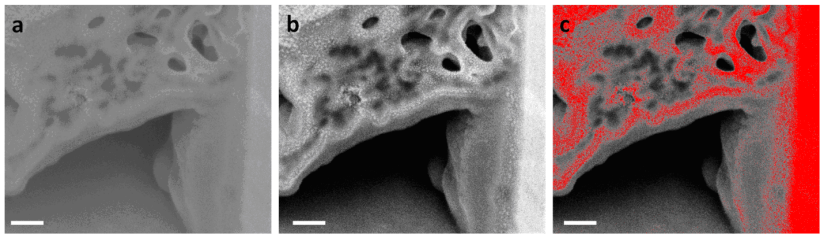

Figure S4: a) SEM image of immuno-gold stain of actin in case of HL-1 engulfing a cylindrical pillar in the middle; b) contrast enhancement of SEM image with actin immuno-gold staining; c) red colored gold nanoparticles on actin (scale bars 100 nm).

S5: Analysis of membrane detachment

Our investigation was focused on FIB sectioning and SEM image acquisition. We minimized artifacts due to sample preparation and performed a step-by-step protocol, [1] considering an optimal current of 80 pA for platinum IBID, sectioning and polishing of the cross sections. Fig.S5 (a-b) show two examples of FIB cuts when a pillar was engulfed in the center and at the edge of the cell, respectively. We ensured that the material underneath the cell, visible from the detached cell membrane, is the gold substrate. Moreover, we compared the gold morphology from Fig.S5 (a) with a flat gold area without cells on the same substrate. In order to estimate the roughness of the flat gold, we observed first a mushroom shaped pillar at an 85° tilt(Fig.S5 c-d) and then acquired images of the planar gold without any

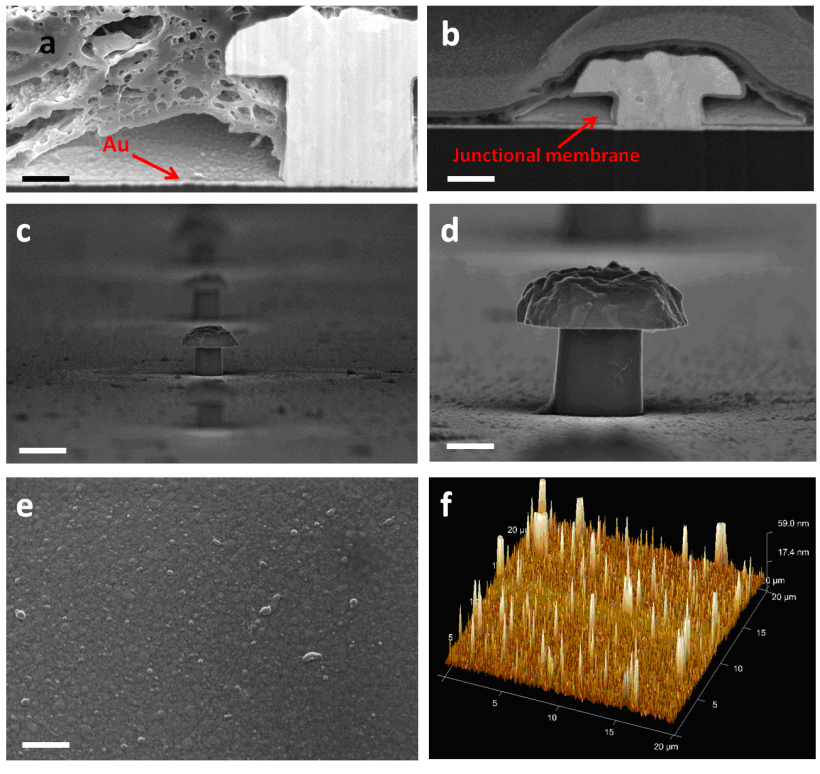

Figure S5: a) Cross section of HL-1 engulfing a cylinder with cap in the center showing the junctional membrane detaching from the planar substrate (scale bar 0.4 μm); b) cross section of cell engulfing a cylinder with cap at the edge with junctional membrane completely attached to the planar substrate (scale bar 0.25 μm); c) SEM image of a cylinder with row of caps (scale bar 1.5 μm, tilt 85°); d) SEM image of a single cylinder with cap (scale bar 0.5 μm) tilt 85°); e) SEM image of planar gold (scale bar 250 nm); f) AFM measurement of planar gold substrates.

pillar. In Fig.S5 (e), it is visible that the planar gold substrate is not planar on the nanoscale but rather showing some nanograins. In order to verify that SEM observations, we performed AFM measurements on the planar gold allowing us to measure a mean roughness of about 10 nm. We therefore conclude that this morphology on the nanoscale is not originating from organic materials but just from the rather rough gold substrates. If we compare Fig.S5 (a) with Fig.S5 (b): fixing the contrast, brightness, we observe that the junctional membrane in Fig.S5 (b) is showing a darker color value than the values of the gold pillars. In SEM investigations, dark regions often indicate not highly conductive materials, such as biological materials, which consist mainly of carbon.

S6: Calculating effective seal resistances

We estimated the effective seal resistance in the vicinity of our nanoelectrode according to Fendyur et al. [2] by assuming in series connected resistive elements of an equivalent circuit. Consequently, we estimate for a capped cylinder the effective seal resistance $R_{seal,c}$:

$$R_{seal,c} = R_{stalk} + R_{rim} + R_{cap} \ . \tag{5.3}$$

Accordingly we describe for a non-capped cylinder the seal resistance $R_{seal,nc}$:

$$R_{seal,c} = R_{stalk} + R_{rim} \ , \tag{5.4}$$

The stalk contribution R_{stalk} is determined by:

$$R_{stalk} = \rho h_{stalk} / (2\pi d_j r_{stalk}) \ . \tag{5.5}$$

with the rim contribution R_{rim} is given by:

$$R_{rim} = \rho / (2\pi d_j) \ln(\frac{r_{cap}}{r_{stalk}}) \ . \tag{5.6}$$

Furthermore, we approximate the resistance contributions R_{cap} and R_{top} by approximating this as a special case of R_{rim} for a r'_{cap} considering the curvature of the spherical cap and a very small effective r'_{stalk} value. The stalk heights are given by h_{stalk}, r_{cap} equals the cap radius and r_{stalk} the stalk radius. The conductivity (ρ) within the cleft is assumed to be 100 Ω cm, the cleft thickness for cardiomyocytes is approximated with $d_j = 25\,nm$ [3]. The seal resistance (Fig.S6 is then obtained by considering the engulfment percentage in the center of the cell (Fig. 5 g). The absolute seal resistances $R_{seal,c}$ and $R_{seal,nc}$ in this elementary approximation are highly dominated by the stalk contribution for aspect ratios greater than 1.0 and can reach 54 $M\Omega$ for a capped cylinder with an aspect ratio of 3.3.

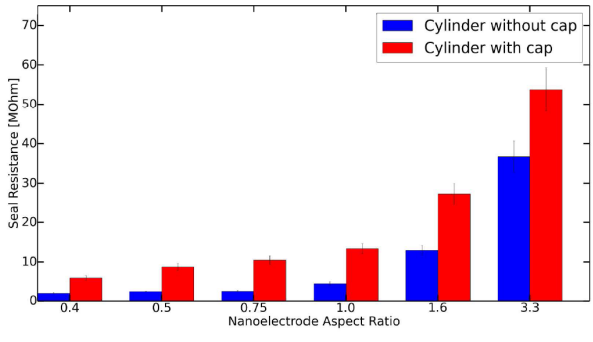

Figure S6: Effective seal resistance in the vicinity of a nanoelectrode as a function of the structural aspect ratio (H/D) in the center of the cell (engulfment $< 100\%$).

Theoretical analysis for pillars engulfed in the center of the cell

In the center of the cell, the junctional membrane detaches from the substrate around the pillar due to the pulling forces of the cytoskeleton. The membrane can be described in Monge gauge by a height field $h(x,y)$ above a reference plane. For almost planar membranes, the mean curvature can be expressed by the Laplacian, $H = \nabla^2 h(x,y)/2$, and the membrane deformation energy is

$$\mathcal{E} = \int_A dA \left[\frac{\kappa}{2}(\nabla^2 h(\boldsymbol{\rho}))^2 - p h(\boldsymbol{\rho})\right] . \tag{5.7}$$

where $\rho = (x,y)$ is the vector in the reference plane and the center of the pillar is located at $\rho_p = (0,0)$; A is the membrane area projected to the reference plane. The membrane bending energy is characterized by the bending rigidity κ ; the cytoskeletal stress is modeled by the pressure p. The optimal membrane profile is found by energy minimization and satisfies the Euler-Lagrange equation [4],

$$\nabla^4 h(\boldsymbol{\rho}) = p/\kappa . \tag{5.8}$$

The deformation profile that solves the equation is,

$$\boldsymbol{\rho} = \frac{\rho^2}{4}(2c_2 - c_3) + c_4 + (c_1 + \frac{\rho^2}{2}c_3)\ln(\rho) + \frac{\rho^4}{64}\frac{p}{\kappa} , \tag{5.9}$$

where the integration constants are determined by the boundary conditions for the detachment from pillar and substrate. Two boundary conditions are given by the detachment height at the pillar, $h(r_d) = 0$ and $h(r_s) = h_s$, with stalk radius $r_s = R_s$ and the detachment radius of the membrane from the substrate, $r_d = R_{d,J}$. The membrane detaches smoothly from the substrate, such that the third boundary condition is $dh(\rho)/d\rho|_{\rho=r_d} = 0$. The detachment angle at the pillar is unknown, which implies that the corresponding natural boundary condition at the stalk, $\nabla^2 h(\boldsymbol{\rho})^2|_{\rho=r_s} = 0$, has to be fulfilled.

We therefore find the integration constants:

$$c_1 = \frac{64h_s\kappa r_d^2\left[2(\ln r_d - \ln r_s) - 1\right] + p r_d^2\left[5r_s^4 - 8r_s^2 r_d^2 + 3r_d^2 + 2(3r_s^4 - 2r_d^4)(\ln r_d - \ln r_s)\right]}{64\kappa\left[(r_s^2 - r_d^2) + 2r_d^2(\ln r_d - \ln r_s)(1 + \ln r_s - \ln r_d)\right]}$$

$$\begin{aligned} c_2 \;=\; & \Big[64\kappa(h_s + 2h_s\ln r_s) + p(r_d^4 + 4r_d^2 r_s^2 - 5r_s^2 + 2\ln r_s(3r_s^4 + 3r_d^4 + 4r_d^4\ln r_s)) \\ & -4r_d^2(2r_s^2 + r_d^2)(1 + 2\ln r_s)\ln r_d + 16r_s^2 r_d^2(\ln r_d)^2) \\ & / \Big[64((r_s^2 - r_d^2) - 2r_d^2(\ln r_s - \ln r_d)(1 + \ln r_s - \ln r_d))\Big] \end{aligned}$$

$$c_3 = \frac{-64h_s\kappa + p\left[3r_s^4 - 4r_s^2 r_d^2 + r_d^4 + 4r_d^2(r_d^2 - 2r_s^2)(\ln r_s - \ln r_d)\right]}{32\kappa\left[(r_s^2 - r_d^2) - 2r_d^2(\ln r_s - \ln r_d)(1 + \ln r_s - \ln r_d)\right]}$$

$$
\begin{aligned}
c_4 \;=\; & \Big[64h_s r_d^2(2(1+\ln r_s)\ln r_d - 1 - \ln r_s - 2\ln r_d^2) - pr_d^2(2r_d^4(\ln r_s)^2 \\
& +(3r_s^4 - 4r_s^2 r_d^2 + 3r_d^4 - 2(3r_s^4 + r_d^4)\ln r_d)\ln r_s \\
& -r_s^2(r_s^2 - r_d^2 - 2(r_s^2 - 2r_d^2)\ln r_d^2 + 6r_s^4 \ln r_d^2))\Big] \\
& / \left[64\kappa((r_s^2 - r_d^2) - 2r_d^2(\ln r_s - \ln r_d)(1 + \ln r_s - \ln r_d))\right]
\end{aligned}
$$

The detachment angle of the stalk is :

$$
\begin{aligned}
\alpha \;=\; & \pi/2 - \tan^{-1}\Big[64(h_s(r_s^2 - r_d^2 + 2r_d^2(\ln r_d - \ln r_s)) + p((r_d^2 - r_s^2)(r_s^4 - 4r_s^2 r_d^2 + 3r_d^2)) \\
& + 2r_d^2(r_d^4 + 2r_s^2 r_d^2 - 3r_s^4 + 4r_s^4(\ln r_s - \ln r_d))(\ln r_s - \ln r_d)))\Big] \\
& / \left[(64r_s(r_s^2 - r_d^2 - 2r_d^2(\ln r_s - \ln r_d)(1 + \ln r_s - \ln r_d)))\right]
\end{aligned}
$$

In Fig. S7 (a), we plot α as function of the pressure p for stalk radius R_s = 0.3 μm , detachment height $h_s = 0.2\,\mu m$, and detachment length $R_{d,J} = 0.9\,\mu m$, and for $\kappa = 50\,k_B T$. We find a large angle for small p and a small angle for high p . Furthermore, for very high pressure the angle changes only weakly with the cytoskeletal stress. Therefore a small error in the experimental measurement of the parameters in this regime can lead to a large error for the cytoskeletal strength that we determine from the experimental deformation profiles. Using the standard deviation from the experimental values, we find that the error bar for the maximal cytoskeletal strength in Fig. 6 of the main manuscript, $p = 435\ Pa$, ranges from 135 $Pa < p <$ 1,850 Pa.

In Fig. S7 (b), we plot the total energy for the junctional membrane around a pillar as function of the detachment length for $R_s = 0.3\,\mu m$, $h_s = 0.2\,\mu m$, $\kappa = 50\,k_B T$, $w = 12.5\,\mu J/m^2$, and several pressure values $p = 0$, $p = 52Pa$, and $p = 104Pa$. The minimum of the energy corresponds to the optimal detachment length, for high pressure the membrane detaches from the substrate. The bending energy has a minimum value at a specific detachment length; while a finite pressure decreases the total energy of the system for increasing detachment length, the lack of adhesion energy increases the total energy for increasing detachment length (Fig. S7 (c)). The optimal detachment length therefore increases with increasing pressure (Fig. S7 (d)). The membrane deformation profiles change from catenoid-like for vanishing pressure to cone-like for $p = 57Pa$, and to a strongly detached membrane for $p = 114Pa$ (Fig.S7 (a)).

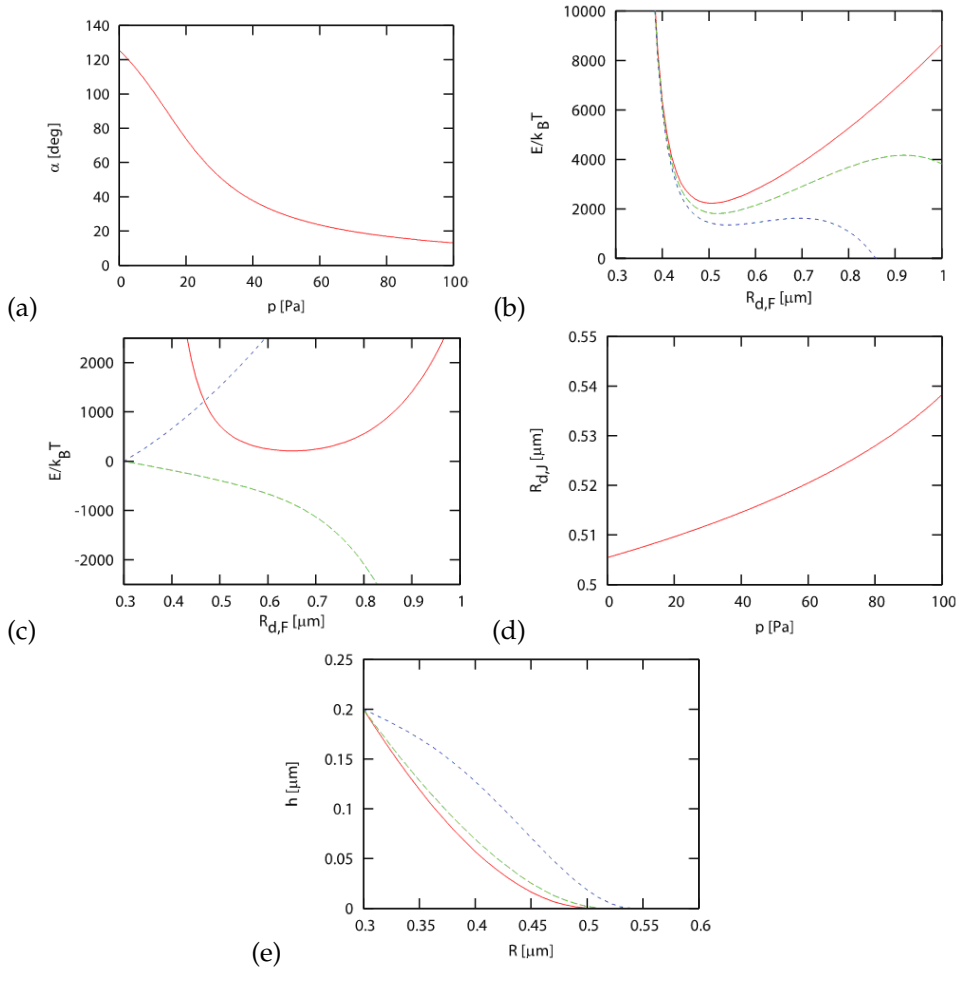

Figure S7: a) Angle α for the detachment of the junctional membrane for a pillar with stalk radius $R_s = 0.3\,\mu m$, detachment height $h_s = 0.2\,\mu m$, detachment length $R_{d,J} = 0.9\,\mu m$ and for $\kappa = 50\,k_\mathrm{B}T$. b) Total energy of the junctional membrane as function of the detachment length $R_{d,J}$ for a pillar with stalk radius $R_s = 0.3\,\mu m$, detachment height $h_s = 0.2\,\mu m$, membrane bending $\kappa = 50\,k_\mathrm{B}T$, adhesion strength $w = 12.5\,\mu J/m^2$, and $p = 0$ (red, solid), $p = 52Pa$ (green, long dashed), and $p = 104Pa$ (blue, short dashed). c) Bending contribution (red, solid), adhesion contribution (blue, short dashed), and pressure contribution (green, long dashed) to the total energy of the junctional membrane as function of the detachment length $R_{d,J}$ for a pillar with stalk radius $R_s = 0.3\,\mu m$ and detachment height $h_s = 0.2\,\mu m$, membrane bending rigidity $\kappa = 50\,k_\mathrm{B}T$, adhesion strength $w = 12.5\,\mu J/m^2$, and $p = 52Pa$. d) Membrane detachment length $R_{d,J}$ as function of the pressure p for a pillar with stalk radius $R_s = 0.3\,\mu m$ and detachment height $h_s = 0.2\,\mu m$, membrane bending rigidity $\kappa = 50\,k_\mathrm{B}T$ and adhesion strength $w = 12.5\,\mu J/m^2$. e) Membrane deformation profiles for a pillar with stalk radius $R_s = 0.3\,\mu m$, detachment height $h_s = 0.2\,\mu m$, membrane bending rigidity $\kappa = 50\,k_\mathrm{B}T$, adhesion strength $w = 12.5\,\mu J/m^2$, and $p = 0$ (red, solid), $p = 52Pa$ (green, long dashed), and $p = 104Pa$ (blue, short dashed).

S8: Theoretical analysis for pillars engulfed at the edge of the cell

To investigate the deformation of a membrane adhering to a substrate we employ triangulated [5] membranes using the finite element package Surface Evolver [6]. Fig. S8 (a) shows a membrane deforming around the hemispherical cap of radius R_c at a height H from the substrate and detaching at a distance $R_{d,F}$. This model elegantly captures the experimental situation of the free membrane deforming at the edge of the cell in response to pillar geometry and detachment distance, $R_{d,F}$.

We next calculate the bending energy for a tensionless membrane of bending rigidity κ that detaches tangentially at the cap and connects smoothly to the substrate and detachment length $R_{d,F}$. The integral of the squared mean curvature, H^2, over the entire membrane area A is given by $\mathcal{E}_{\text{bend}} = 2\kappa \int_A dA H^2$ and comprises the deformation cost due to bending. This quantity is calculated numerically by discretization on triangulated network.

We find the membrane deformation profile by minimizing the discretized squared mean curvature energy over the triangulated network, using the Surface Evolver method "star_perp_sq_mean_curvature", as described in our previous work [7,8]. To search for the global minima in the energy landscape, the default method in Surface Evolver is to estimate the negative gradient of the energy and move linearly along the direction of steepest descent of the energy landscape. In addition to the minimization steps, the network is refined and smoothened to achieve numerical consistency with the estimated bending energy during energy minimization. To avoid meta-stable states and ensure convergence with high precision for the estimated value of bending energy, we also use the Hessian for minimization. This approach uses the Hessian matrix formed by the second derivatives of the energy to determine the best quadratic approximation of the energy to seek for equilibrium profiles.

The choice of a tensionless membrane allows us to interpret the local curvature c given by the inverse radius of a circle approximating the deformation profile at the detachment point as an adhesion strength w between the membrane and the substrate [9], since $c = \sqrt{2w/\kappa}$. Such an adhesion strength is difficult to estimate in experiments and therefore the continuum membrane model is an efficient tool to extract such information from the deformation profiles of the membrane. Another advantage of choosing vanishing membrane tension is that the deformation costs due to bending are scale invariant, therefore the predictions from the model are universally valid, independent of the chosen characteristic length scale of the system given by the radius R_c of the cap.

A typical value for the cap radius used in our experiments is 0.4 μm. In Fig. S8 (b), we show the theoretical membrane deformation profiles for a small and high stalk height, H=0.5 μm and H=1.0 μm. For each stalk height, varying the detachment length $R_{d,F}$ significantly affects the membrane profile around the cap each equilibrium deformation profile corresponds to a particular deformation cost, see Fig. 5 in the main text. Deep-wrapped states occur for small $R_{d,F}$ with a higher curvature c near detachment point of the membrane from the substrate than for shallow-wrapped states with higher $R_{d,F}$ values. This clearly indicates that deep-

wrapped states require higher adhesion strengths to compensate the higher deformation costs due to bending, as shown in Fig. 5 of main text.

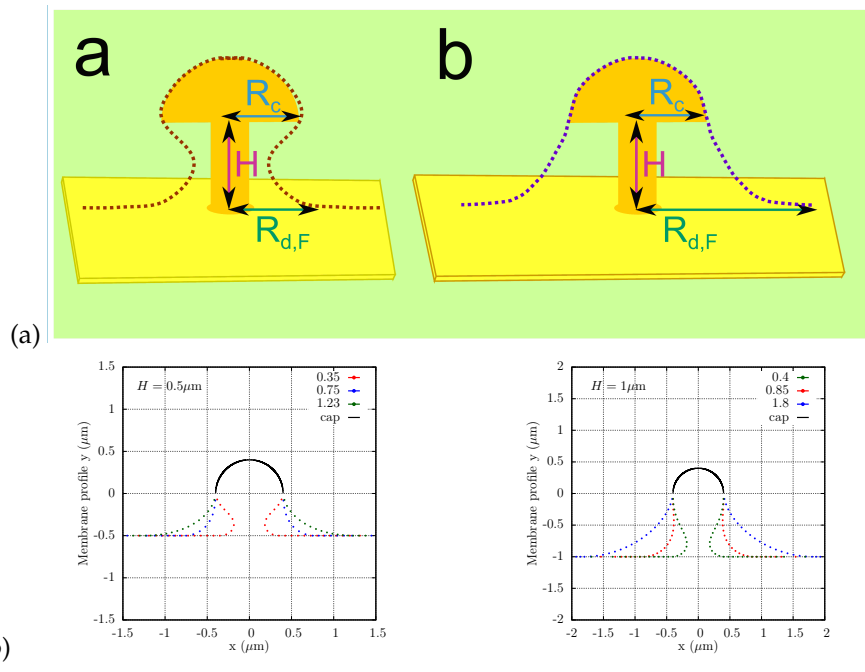

Figure S8: a) Membrane deformation profile (shown with dashed line) around a hemispherical cap of radius R at a height H from the substrate. The membrane detaches from the substrate at a distance $R_{d,F}$ from the center of the pillar. For small $R_{d,F}$, a deep wrapped state (left) is found with high curvature near the detachment point on the substrate compared with the shallow state (right) where the membrane only weakly wraps the pillar in response to the pillar geometry. b) Membrane deformation profiles for pillars with stalk heights $H = 0.5\ \ \mu m$ and $H = 1\ \mu m$, cap radius $R_c = 0.4$ μm and several values of the detachment length given in the figure legend.

References: Chapter 5 (Supplementary material)

1. Santoro, F.; Neumann, E.; Panaitov, G.; Offenhäusser, A. FIB Section of Cell–electrode Interface: An Approach for Reducing Curtaining Effects. Microelectron. Eng. 2014, 124, 17–21.

2. Fendyur, A.; Mazurski, N.; Shappir, J.; Spira, M. E. Formation of Essential Ultrastructural Interface between Cultured Hippocampal Cells and Gold Mushroom-Shaped MEA- Toward "IN-CELL" Recordings from Vertebrate Neurons. Front. Neuroengineering 2011, 4.

3. Hai, A.; Dormann, A.; Shappir, J.; Yitzchaik, S.; Bartic, C.; Borghs, G.; Langedijk, J. P. M.; Spira, M. E. Spine-Shaped Gold Protrusions Improve the Adherence and Electrical Coupling of Neurons with the Surface of Micro-Electronic Devices. J. R. Soc. Interface 2009, 6, 1153–1165.

4. Dan, N.; Berman, A.; Pincus, P.; Safran, S. A. Membrane-Induced Interactions between Inclusions. J. Phys. II 1994, 4, 1713–1725.

5. G. Gompper; D. M. Kroll. Triangulated-Surface Models of Fluctuating Membranes. In Statistical Mechanics of Membranes and Surfaces; World Scientific, 2004; pp. 359–426.

6. Brakke, K. A. The Surface Evolver. Exp. Math. 1992, 1, 141–165.

7. Dasgupta, S.; Auth, T.; Gompper, G. Wrapping of Ellipsoidal Nano-Particles by Fluid Membranes. Soft Matter 2013, 9, 5473–5482.

8. Dasgupta, S.; Auth, T.; Gompper, G. Shape and Orientation Matter for the Cellular Uptake of Nonspherical Particles. Nano Lett. 2014, 14, 687–693.

9. Seifert, U.; Lipowsky, R. Adhesion of Vesicles. Phys. Rev. A 1990, 42, 4768–4771.

II Capillary interactions at interfaces

6
Capillary Assembly of Microscale Ellipsoidal, Cuboidal, and Spherical Particles at Interfaces

6.1
Abstract

Micron-sized anisotropic particles with homogeneous surface properties at a fluid interface can deform the interface due to their shape. The particles thereby create excess interfacial area and interact in order to minimize this area, which lowers the total interfacial energy. We present a systematic investigation of the interface deformations around single ellipsoidal particles and cuboidal particles with rounded edges in the near field for various contact angles and particle aspect ratios. The correlation of these deformations with capillary bond energies—the interaction energies of two particles at contact—quantifies the relation between the interactions and the near-field deformations. We characterize the interactions using effective power laws and investigate how anisotropic particles self-assemble by capillary forces. Interface deformations and particle interactions for cuboidal particles are weaker compared with those for ellipsoidal particles with the same aspect ratios. For both particle shapes, the bound state in side-by-side orientation is most stable, while the interaction in tip-to-side orientation is repulsive. Furthermore, we find capillary attraction between spherical and ellipsoidal particles. Our calculations therefore suggest cluster formation of spherical and ellipsoidal particles, which elucidates the role of spherical particles as stoppers for the growth of worm-like chains of ellipsoidal particles. The interaction between spherical and ellipsoidal particles might also explain the suppression of the "coffee-ring effect" that has been observed for evaporating droplets with mixtures of spherical and ellipsoidal particles. In general, our calculations of the near-field interactions complement previous calculations in the far field and help to predict colloidal assembly and rheological properties of particle-laden interfaces.

6.2
Introduction

For a system with more than one phase, an energetic cost is associated with the interface where two phases are in contact. The presence of particles reduces the area of direct contact between the phases, but nonspherical particles can lead to interface deformations and therefore locally create excess interface area. Mini-

mization of this excess area induces anisotropic, long-range interactions between the particles[1–3]. These capillary interactions at fluid interfaces determine the assembly of both mesoscopic and macroscopic particles[4–6]. An illustrative example at the macroscopic scale is insects that exploit their capillary interaction with walls to “climb up" the meniscus[7]. For micron-sized colloidal systems, capillary interactions lead to self-assembled two-dimensional aggregates in various forms, such as capillary arrows[8], rod-like assemblies[9], worm-like chains[10,11], and networks[12,13].

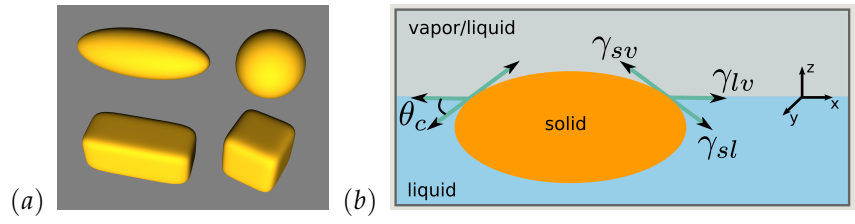

Figure 1: (a)Shapes of anisotropic particles: ellipsoidal particle with aspect ratio 3, spherical particle, and cuboidal particles with aspect ratios 2.25 and 1. We characterize the particle size a by half the minor axis of the ellipsoid, by the radius of a sphere, and by half the short edge of a cuboid. (b) Schematic representation of an ellipsoidal particle trapped at a fluid interface. The interfacial tensions between the different phases are γ_{sv}, γ_{sl}, and γ_{lv}, where s indicates the solid, l the liquid, and v the vapor (or another liquid) phase. The contact angle θ_c is determined by the Young-Dupré equation.

Colloids at interfaces can be used to fabricate colloidosomes, capsules with adjustable size and mechanical properties that can be applied for encapsulation and controlled release of drugs[14]. Another example for colloidosomes is fat globules in homogenized milk with mean diameter of less than 1 ¯m that are stabilized by casein micelles with diameters between 50 and 600 nm[15]. Colloids can also lead to the formation of surfactant-free Ramsden-Pickering emulsions[12,16,17] and bijels[18]. However, particles at interfaces can also have a destabilizing effect. For example, crushed mineral crystals like galena or hematite when immersed in thin films destabilize foams used for froth floatation[19]. In general, capillary interaction energies are proportional to the interfacial tension and increase with the amount of excess area that is generated due to distortion of the interface around particles. Stronger interface deformations result in stronger capillary interactions. For typical particle sizes of several micrometers, capillary interaction energies are much larger than the thermal energy k_BT.

Technological advancement in fabrication techniques has facilitated experimental studies of colloidal assembly for anisotropic particles of various shapes, such as ellipsoidal, cube-like, and peanut-like shapes[10,17]. nonspherical particles can cause interface deformations solely due to their shape anisotropy. For example, for ellipsoidal particles at an air-water interface, the interface is pushed down at the tips and pulled up at the sides for contact angles $\theta_c < 90°$[11,20]. This creates a quadrupolar distortion of the interface height. In the far field, the interface distortions for various particle shapes can be described using a multipole expansion. The dominant multipole contribution for ellipsoidal particles is the quadrupole[21,22].

However, for more complex particle shapes and for the calculation of particle-particle interactions in the near field, a quadrupolar approximation is not sufficient. Using numerical calculations employing triangulated surfaces, we calculate interface deformations and interaction potentials for ellipsoidal and cuboidal particles, see Fig. 1 (a).

For micron-sized spherical particles with homogeneous surface properties, a planar interface remains undeformed around the particle. Therefore two spherical particles at a planar interface do not experience lateral capillary forces. Additional forces are required to deform the interface and induce particle-particle interactions, such as floatation forces due to the balance of buoyancy and gravity for large particles[23] and immersion forces due to partial wetting of particles confined in thin films[24,25]. In addition, curved interfaces induce capillary interactions between spherical particles (and modify interactions between nonspherical particles)[2,26]. We will show that a spherical particle interacts with a nonspherical particle at a planar interface via interface deformation.

We first introduce the model and describe the numerical method employed. Next, we present our numerical results for interface deformations around single ellipsoidal and cuboidal particles and compare our results with experimental data from the literature. Finally, we calculate interactions between two ellipsoidal particles, two cuboidal particles, and a spherical and an ellipsoidal particle.

6.3 Model

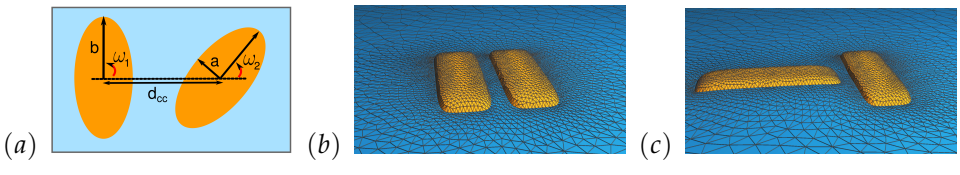

Figure 2: (a) Angles ω_1 and ω_2 indicate the orientation of the particle 1 or 2, respectively, with respect to the vector joining the centers of the two particles. The center-to-center distance is given by d_{cc} for a particle of aspect ratio b/a. Triangulated interface around two cuboidal particles with aspect ratios $b/a = 3$ for contact angle $\theta_c = 60°$ in (b) side-by-side, (c) tip-to-side orientation.

The energy cost per area of the interface is characterized by the interface tensions. Typical adsorption energies of mesoscopic particles are several orders of magnitude larger than the thermal energy k_BT and lead to an almost irreversible entrapment of the particle at the interface[27,28]. However, interface deformations around the particles require much smaller energies than the detachment of a particle from the interface and can arise due to imposed electromagnetic or gravitational fields[21,23,29,30], inhomogeneous chemical surface properties of the particles[10,31], surface roughness[32,33], and particle shape[11,22,34–36].

The energy of smooth homogeneous particles at interfaces is given by

$$E = \gamma_{lv} S_{lv} + \gamma_{sv} S_{sv} + \gamma_{sl} S_{sl} \,, \tag{6.0}$$

where γ_{lv}, γ_{sv}, and γ_{sl} are the interface tensions. Here, s indicates the solid particle, l the liquid phase, and v the vapor phase (or another liquid phase). S_{lv} is the interfacial area between liquid and vapor, S_{sv} is the area of the particle that is exposed to the vapor, and S_{sl} the area of the particle that is in contact with the liquid. The contact angle θ_c is determined by the force balance at the contact line, see Fig. 1 (b). Using the Young-Dupré equation, $\gamma_{sv} = \gamma_{lv} \cos\theta_c + \gamma_{sl}$, we rewrite Eq. (6.3) as

$$E = \gamma_{lv}(S_{lv} - S_{sl}\cos\theta_c) + \gamma_{sv}(S_{sl} + S_{sv})\,. \tag{6.0}$$

The second term in Eq. (6.3) is constant, because $S_{sl} + S_{sv}$ is the the total surface area of the particle. For fixed contact angle, the energy of the system therefore depends only on the first term, which is proportional to the liquid-vapor interfacial tension γ_{lv} that we will refer to as γ henceforth. Typical values for interface tensions are 70 mN/m for the air-water interface and 20 mN/m for an ethanol/air or a methanol/air interface.

To satisfy the Young-Dupré equation locally at every point on the three-phase contact line, the interface around an ellipsoidal particle or a cuboidal particle with rounded edges cannot be planar. Only in mirror-symmetric situations with $\theta_c = 90\,^\circ$, a planar interface around these particles remains flat. The system's tendency is to reduce its total energy and therefore to reduce the total interface area. The overlap of the interfacial deformations around the particles leads to long-range interface-mediated interactions between the particles, also called (lateral) capillary forces. The capillary forces determine the interaction of particles at interfaces together with direct interactions, such as electrostatic, magnetic, and elastic interactions[21,29,30].

The importance of gravitational forces can be characterized by the Bond number, also known as Eötvös number Eo, which is the ratio of gravitational and interfacial forces, $\mathrm{Bo} = \Delta\rho g a^2/\gamma$. $\Delta\rho$ is the density difference between particle and fluid, g is the gravitational constant, and a the size of the particle. Gravitational forces can be neglected if the Bond number is much smaller than 1. For a typical density difference between silica and water and for particle sizes in the micrometer range[26], $\mathrm{Bo} \approx 10^{-8}$. Hydrodynamic forces can be neglected if the capillary number, $\mathrm{Ca} = \eta v/\gamma$, is much smaller than 1. The capillary number is the ratio of viscous forces and capillary forces, where η is the viscosity of the fluid and v is the velocity of the particle. For typical velocities of $100\,^-\mathrm{m/s}$ for particles with sizes of few micrometers in water[22], $\mathrm{Ca} < 10^{-5}$. Therefore, both direct hydrodynamic interactions and a distortion of the interface due to particle motion do not have to be taken into account for micron and submicron-sized particles.

Interaction energies between two particles are expressed with respect to the undisturbed flat interface in absence of the particles, such that the energy of two non-interacting particles (at large distances) vanishes. Lengths are usually given in units of the particle size a, energies as $\Delta E/\gamma a^2$. For a typical particle size $a \approx 1\,\mu m$ (Fig. 1 (a)) and a typical interfacial tension $\gamma \approx 20\,\mathrm{k_B T/nm^2}$, $\gamma a^2 \approx 2 \times 10^7\, k_B T$.

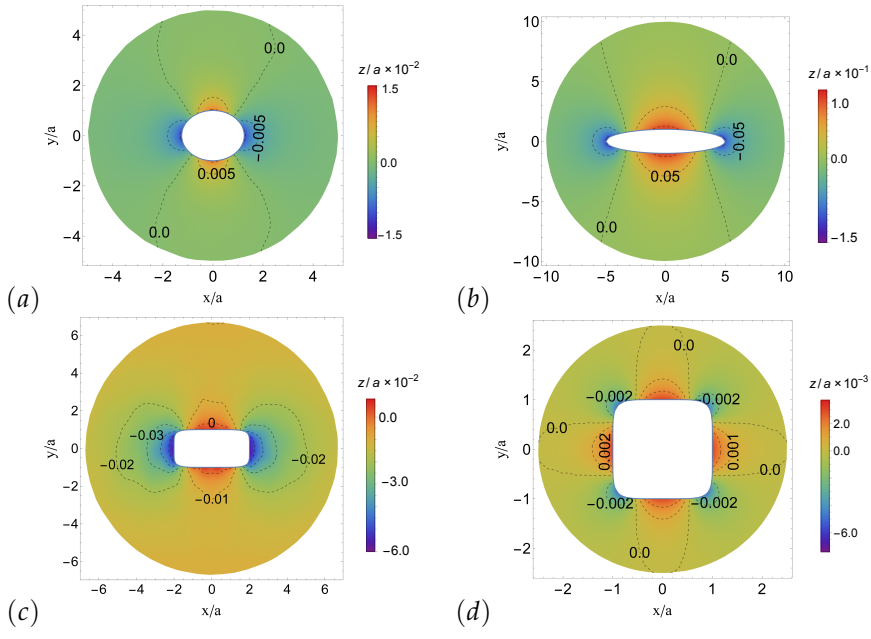

Figure 3: Deformation profiles of an interface around (a) an ellipsoidal particle with aspect ratio 1.25 at $\theta_c = 53.84^\circ$, (b) an ellipsoidal particle with aspect ratio 5.0 at $\theta_c = 48.47^\circ$, (c) a box-like particle with aspect ratio 2.0 at $\theta_c = 62.93^\circ$, and (d) a particle with Hauser's cube shape at $\theta_c = 56.28^\circ$. For all particles, we have used the contact angle θ_c that corresponds to maximum particle-induced interface distortion; see Fig. 4.

6.4 Method

We describe cuboidal particles by the shape equation $(x/b)^6 + (y^6 + z^6)/a^6 = 1$ and ellipsoidal particles by $(x/b)^2 + (y^2 + z^2)/a^2 = 1$. We vary the aspect ratios in the range $1 \leq b/a \leq 10$, where for $b/a = 1$ we obtain Hauser's cube and a sphere, respectively. The interface patches to which the particles are bound are delimited by circular wire frames with radii between $20a$ and $50a$. We investigate both ellipsoidal and cuboidal particles with their long axes parallel to the interface. This is the stable orientation for prolate ellipsoidal particles and a stable or metastable orientation for cuboids[37,38]. We assume that this orientation of the particles remains unchanged when the particles approach each other. For particles attached to membranes, the orientation changes considerably when the inter-particle distance changes and a tilt angle with respect to their azimuthal axis has to be taken into account[39].

In order to calculate the capillary interaction, we have to obtain an accurate interface deformation for the boundary conditions given by the Young-Dupré equation and the particle shape. With the assumption of small deformations of the interface, approximative approaches have been used, such as the superposition of axisymmetric interfacial deformations due to single particles obtained from solution of the linearized Young-Dupré equation[20,36,40], superposition of capillary multipoles[1,22,33,41,42], an inclined-flat plate approximation[43], and a functional expansion of the interfacial energy for displacements of the contact line position[44].

However, these approaches are limited in their applicability and generally hold for large distances between the particles, i. e., in the far field. An analytical description of the interface deformation for arbitrary particle shape remains elusive, because it requires solving a fully non-linear second-order partial differential equation. Therefore, there has been much interest in accurate numerical approaches using finite-element methods[2,9,22,26,34,35,45,46] and boundary-element methods[3,8,47,48], which are more flexible in terms of their applicability.

We use the finite-element program Surface Evolver[49] version 2.60 to minimize the energy and to obtain deformation profiles, see Figs. 2 and 3. An interface is initially set up using a triangulated network of first-order Lagrange elements, where edges are defined by straight lines and triangles by planar patches. The contact line at the particle is optimized in regular steps to attain its equilibrium profile. During the energy minimization we optimize the vertical position of the particle with respect to the fluid interface boundary allowing it to attain its equilibrium position. For single particles, this approach is equivalent to fixing the vertical position of the particle and letting the interface at the far field free, such that it can adjust to its optimal height. The global minimum is approached using an algorithm that uses both non-linear Hessian and steepest-descent energy minimization steps[49]. We refine the mesh adaptively to obtain accurate values for the energy. For the final minimization steps, the triangulation is switched to a network formed by second-order Lagrange elements. In addition to the end-point vertices, each edge is endowed by a midpoint vertex thereby describing it as a quadratic curve. This allows calculation of surface energies with an extremely high precision.

6.5 Interface Deformations

For a nonspherical particle with homogeneous surface composition, a constant contact angle is usually not achieved for a planar interface and for $\theta_c \neq 90\,^\circ$. Figure 3 shows calculated interface deformations $h(x,y)$ around ellipsoidal and cuboidal particles; the deformation is also experimentally accessible using phase-shift interferometry[3,8,11,20,50]. Quadrupolar symmetry for the interface deformation is found for elongated particles, which is in good agreement with theoretical predictions and experiments for polystyrene ellipsoidal particles at the air-water interface[3,20]. Therefore the deformation profile around elongated particles is often characterized by the amplitude of an elliptical quadrupole[22], which can be extracted from the interface deformation profiles along the long and short axes (shown in the Supporting Information).

While we expect cubes with sharp edges not to deform the interface, we observe a considerable interface deformation for our cuboidal particles. The finite edge curvature therefore plays a crucial role for the qualitative behavior of the particle at the interface. For a cuboidal particle defined by $(x/b)^n + (y^n + z^n)/a^n = 1$ with $n > 4$ and even, the edge curvature is $c_{\mathrm{edge}} = 2^{(2-n)/2n}(n-1)/a$. Our elongated cuboidal particles with $n = 6$ and a face on the interface show interface deformations that are dominated by the quadrupolar contribution, as observed for ellipsoids. Hauser's

cubes with $n = 6$ and aspect ratio $b/a = 1$ induce a qualitatively different interface deformation with a leading octupolar contribution to the interface deformation around the particle; see Fig. 3.

While the quadrupolar approximation for the interface deformation around single ellipsoidal particles works very well in the far field, we will focus in the subsequent part of the manuscript on numerical calculations for near-field interface deformations that cannot easily be calculated analytically. We characterize the deformation by the difference of the maximal and minimal height along the contact line at the particle, Δu.

6.5.1
Near-Field Interface Deformations around Single Ellipsoidal and Cuboidal particles

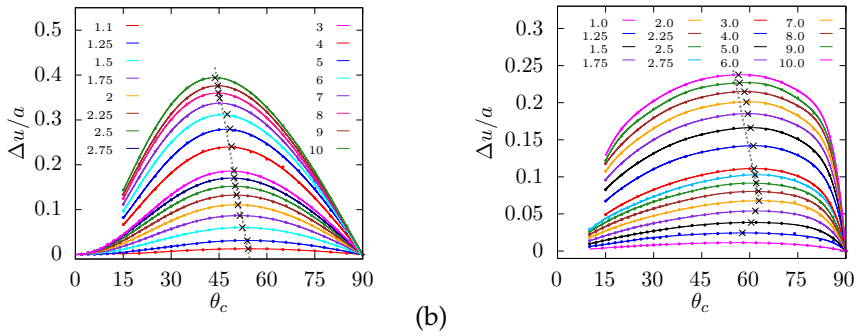

(a) (b)

Figure 4: Maximal height difference Δu of the contact line for (a) ellipsoidal particles and (b) cuboidal particles with several aspect ratios $1 \leq b/a \leq 10$. Our numerical data are normalized by half the length of the minor axis a and plotted as function of the contact angle θ_c. The maximum value of Δu, depicted by $\times$, shifts to smaller contact angles with increasing particle aspect ratio, as indicated by the gray lines that serve as guides to the eye.

Figure 4 shows the variation of $\Delta u/a$ with the contact angle for single ellipsoids and cuboids with various aspect ratios, where a is the half the minor axis of an ellipsoid and half the short edge of a cuboidal particle. In Ref. 3, the length chosen to normalize Δu is the radius R of the spherical particles that has been stretched to obtain the ellipsoids. In order to compare these results with our reported $\Delta u/a$ values, our data have to be rescaled by $a/R = \sqrt[3]{a/b}$. With increasing contact angle, $\Delta u/a$ grows nonlinearly from zero, attains a peak value $\Delta u_{\max}/a$, and finally decreases to zero for $\theta_c = 90°$. For ellipsoids, our numerically calculated values are in excellent agreement with those from previous calculations using boundary element methods[3] and multipole expansions[44], see Supporting Information.

For ellipsoids with aspect ratios $1.1 \leq b/a \leq 10$, the position of the peak is found for contact angles $43° < \theta_c < 54°$, see Fig. 4 (a). The peak shifts from larger to smaller contact angles with increasing aspect ratio of the particle[3], while the height of the peak increases from $\Delta u_{max}/a \approx 0.013$ for $b/a = 1.1$ to $\Delta u_{max}/a \approx 0.4$ for $b/a = 10$; tabulated data are provided in the Supporting Information. We have calculated $\Delta u/a$ for aspect ratios up to $b/a = 13$ (see Supporting Information) and

find that the peak height increases monotonically with increasing aspect ratio for fixed length of the small axis of the particle. Because larger interface deformations correspond to stronger interactions between particles, the 40-fold increase of $\Delta u_{\max}/a$ in our calculations predicts much more robust capillary interactions for increased particle aspect ratios.

In Fig. 4 (b), $\Delta u/a$ is plotted for cuboidal particles with aspect ratios $1 \leq b/a \leq 10$. Contrary to a spherical particle, Hauser's cube (that is obtained for $b/a = 1$) leads to a finite contact line undulation. Our elongated cuboidal particles induce contact line undulations that are about a factor of $1/2$ weaker than for ellipsoidal particles with the same aspect ratio. For aspect ratios $b/a > 2$, the position of the peak in $\Delta u/a$ decreases from $\theta_c \approx 63^\circ$ for $b/a = 2$ to $\theta_c \approx 55^\circ$ for $b/a = 10$. However, the weak dependence of $\Delta u/a$ on θ_c makes it difficult to evaluate the peak position accurately. As for ellipsoids, the maximal interfacial deformation increases with increasing aspect ratio from $\Delta u_{max}/a \approx 0.07$ for $b/a = 2$ to $\Delta u_{max}/a \approx 0.24$ for $b/a = 10$. We therefore also expect for cuboidal particles an increase of the strength of the capillary interaction between particles with increased aspect ratio.

6.5.2 Comparison with Experimental Measurements

An experimentally measured $\Delta u/a$ value can correspond to two contact angles, because of the nonmonotonic dependence of $\Delta u/a$ on the contact angle θ_c. This results in a "contact angle mystery", if one aims at extracting the contact angle and therefore the surface properties of a particle from measurements of the interface deformation.

In Fig. 5 (a), the contact angle solutions are plotted together with corresponding experimental measurements of $\Delta u_c/a$ taken from Ref. 20. Note that this experimental value $\Delta u_c/a$ is the height difference around the contour of the particle, which is smaller than $\Delta u/a$ that is measured along the contact line[20]. The lower branch for smaller θ_c has already been reported in Ref. 20, the upper branch more recently in Ref. 3. We find good agreement with this data in the literature. Because all ellipsoids for the experimental measurements have been fabricated from polystyrene spheres, the expectation is that the chemical properties of their surfaces are identical and θ_c does not vary with the aspect ratio. The variation of θ_c with b/a in Fig. 5 (a) has therefore been attributed to the change of the surface properties upon stretching the particle in the experiments[3,11].

In Fig. 5 (b), the branches of the contact angle are plotted for a fixed value of $\Delta u/a$ independent of the aspect ratio. The contact angles on the upper branch increase and the contact angles on the lower branch decrease monotonically with increasing aspect ratio. For $\Delta u/a = 0.043$, two branches are found already for small aspect ratios, but they change only marginally with the aspect ratio for large aspect ratios. For $\Delta u/a = 0.23$, corresponding contact angles can only be found for $b/a \gtrsim 4$; therefore, there is a significant variation with the aspect ratio for $4 < b/a < 13$. In Fig. 6 (a), the branches are calculated for cuboidal particles at fixed $\Delta u/a = 0.045$ and for $1.75 \leq b/a \leq 6$. Contrary to ellipsoids, where the variation of the contact angles with the aspect ratio is of similar magnitude for both branches, for cuboids

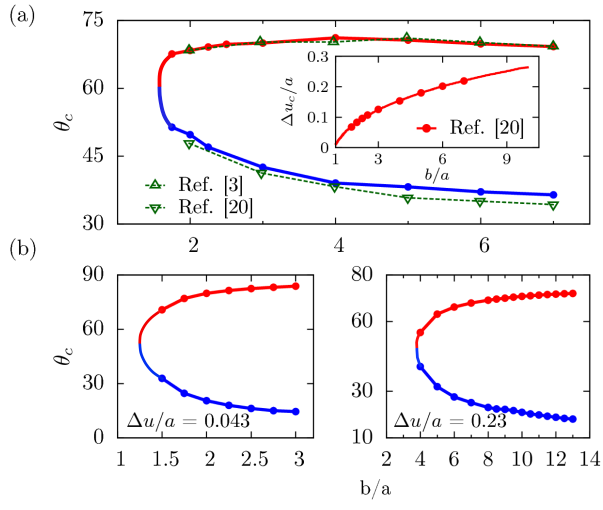

Figure 5: Ellipsoidal particles. (a) Contact angles that correspond to experimentally measured values[20] for Δu_c (shown in the inset) for several aspect ratios b/a; see Fig. 4 (a). The upper branch (red) is the solution for large θ_c, while the lower branch (blue) is the solution for small θ_c. Both contact angle branches evaluated are in good agreement with previously reported data.[3,20] (b) Contact angle branches as a function of the aspect ratio for $\Delta u/a = 0.043$ (left) and $\Delta u/a = 0.23$ (right).

the upper branch varies over a much smaller range of the contact angle, $79° < \theta_c < 89°$, than the lower branch, $7° < \theta_c < 39°$.

Due to the double-valued relation between the aspect ratio and the contact angle, it is not sufficient to measure $\Delta u/a$ only to determine the surface properties of the ellipsoids. In addition, the projected area S enclosed by the undulating contact line can be determined by reflection illumination (as for interferometry). The ratio of this projected area to the projected area for $\theta_c = 90°$, S/S_0, is a monotonically increasing function of θ_c. Because $S(\theta_c)/S_0$ is single-valued for all θ_c, it can be used to "solve" the contact angle mystery and choose the correct branch. S/S_0 for ellipsoids has already been calculated in Ref. 3; our calculations agree well with the data from the literature, as shown in Fig. S3 in the Supporting Information. In Fig. 6 (b), we plot S/S_0 for cuboidal particles. Our numerical results can therefore be used to evaluate experimentally measured particle-induced interface distortions around cuboidal particles.

6.6 Two-Particle Interactions

The total interface area and thus the total energy of a system of several particles can be lowered or increased by the interference of the interface deformations around particles. We have calculated the pair interactions between two ellipsoidal particles and two cuboidal particles that approach each other in various relative orientations, see Figs. 7 and 2. We have also calculated the capillary interaction between a spherical and an ellipsoidal particle, see Fig. 10.

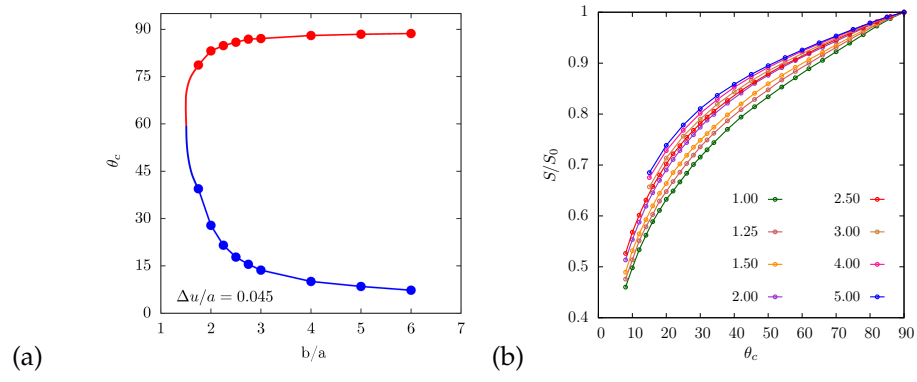

Figure 6: Cuboidal particles. (a) Contact angles θ_c as function of aspect ratio $1.75 \leq b/a \leq 6$ at $\Delta u/a = 0.045$, see Fig. 4 (b). The upper branch (red) is the solution for small θ_c, while the lower branch (blue) is the solutions for small θ_c. (b) Ratio of projected area enclosed by the contact line for the contact angle θ_c to the projected area enclosed by the contact line for $\theta_c = 90°$, S/S_0 is plotted for varying aspect ratio $1.00 \leq b/a \leq 5$.

6.6.1
Capillary Interaction between Ellipsoidal Particles

The interaction potential for particles at large distances between their centers of mass, d_{cc}, assuming a quadrupolar interface deformation due to each particle is[44]

$$\Delta E_{cap}^{quad}/\gamma a^2 = -3\pi \cos(2\omega_1 + 2\omega_2)(\Delta u/a)^2 (d_{cc}/a)^{-4}\,. \tag{6.0}$$

The angles ω_1 and ω_2 describe the particle orientation with respect to the line that joins the centers of the particles for particle 1 and particle 2, respectively; see Fig. 2. The equation is valid in the far field and assumes quadrupolar interface deformations around the particles. For $\omega_1 = \omega_2 = 90°$ the particles are oriented side-by-side (S-S) and for $\omega_1 = \omega_2 = 0°$ tip-to-tip (T-T), see Figs. 7 (a) and (b). Equation (6.6.1) predicts attraction for S-S and T-T, but repulsion for tip-to-side (T-S) orientation with $\omega_1 = 0°$ and $\omega_2 = 90°$, see Fig. 7 (c). The interaction potential decays as $(d_{cc}/a)^{-4}$; interestingly, the magnitude of the predicted interaction energies are equal in S-S, T-T, and T-S orientation for equal center-of-mass distances.

In Fig. 7, the pair interaction potentials for ellipsoidal particles are plotted for θ_c = 50° and 80° for distances $d_{cc}/a \lesssim 15$. The interactions are attractive in S-S and T-T orientations and repulsive in T-S orientation. We fit the numerical data by effective power laws, $\Delta E/\gamma a^2 = k(d_{cc}/a)^{-m}$, where the exponent $-m$ characterizes the decay of the interaction. In S-S and T-T orientations the interaction potential decays more slowly ($m < 4$) and more rapidly ($m > 4$) than in the far field, respectively. Consequently we expect the values of the interaction energies at small distances to differ from that predicted by Eq. (6.6.1). For the T-S orientation, $m \approx 4$ is only slightly smaller than in the far field, and the interaction potential is of the same order of magnitude as the interaction potential predicted by Eq. (6.6.1). Therefore, in general, the quadrupolar approximation does not describe the capillary interaction quantitatively in the near field; the exponents obtained from the power-law fits and the energies of the ellipsoids at contact are tabulated in the Supporting Information.

The capillary forces are $F_{cap} = \partial \Delta E / \partial d_{cc}$ and fit by the power law $F_{cap} \sim (d_{cc}/a)^{-(m+1)}$. Using Eq. (6.6.1), we find $F_{cap}^{quad} \sim (d_{cc}/a)^{-5}$. Experimental measurements of the interaction force in Ref. 11 give $m = 4 \pm 0.3$ and $m = 3.1 \pm 0.2$ for particles with aspect ratios in the range $3 < b/a < 4.3$ in T-T and S-S orientation, respectively. Analogously to the evaluation of the experimental data, we fit our numerical results to an effective power-law decay of the interaction potential in the near field[11], where the power-law exponent $m(b/a, \theta_c, \omega_1, \omega_2)$ depends strongly on the contact angle, the aspect ratios, and the relative orientations of the particles. With increasing aspect ratio, m decreases for S-S orientation and increases for T-T orientation.

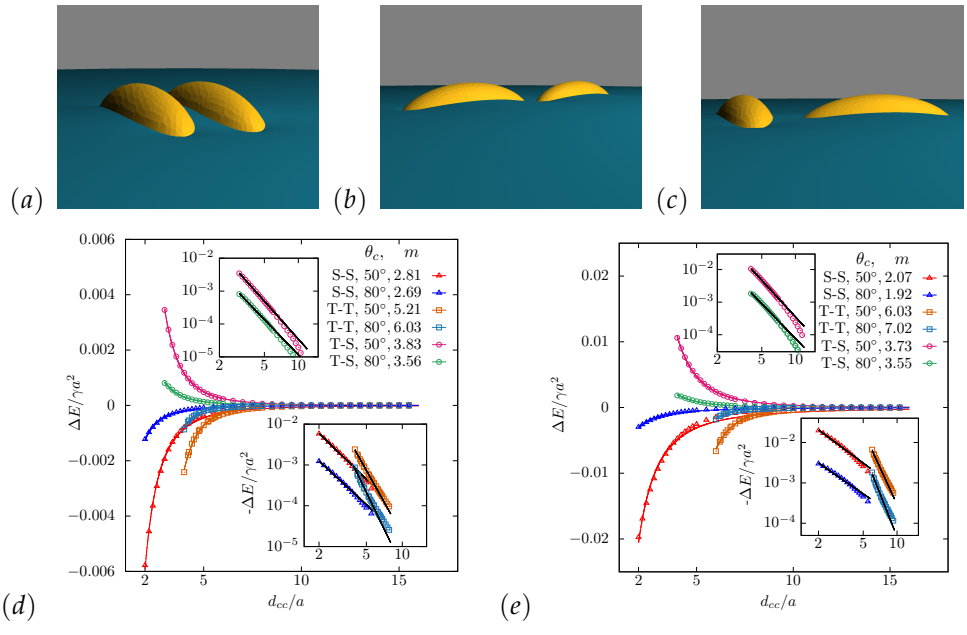

Figure 7: Two ellipsoidal particles with aspect ratios $b/a = 3$ for contact angle $\theta_c = 50°$ in (a) side-by-side, (b) tip-to-tip and (c) tip-to-side orientation. The particles attract each other in side-by-side and tip-to-tip orientation and repel each other in tip-to-side orientation. The side-by-side orientation is energetically most stable. Interaction energies $\Delta E/\gamma a^2$ for two identical ellipsoidal particles with aspect ratios (d) $b/a = 2$ and (e) $b/a = 3$ and contact angles θ_c = 50° and $\theta_c = 80°$. The energies are plotted as a function of d_{cc}/a for side-by-side (S-S), tip-to-tip (T-T), and tip-to-side (T-S) orientation. The interaction is attractive in S-S and T-T orientation and repulsive in T-S orientation. Inset: fit of the numerical data using $\Delta E/\gamma a^2 = k(d_{cc}/a)^{-m}$; the fit parameters are given in the figure and tabulated in the Supporting Information.

The far-field description of the interaction potential in Eq. 6.6.1 predicts $\Delta E_{cap}^{quad} \sim (\Delta u/a)^2$, which connects the interface deformation around single particles calculated in Fig. 4 with the interaction potentials between two particles calculated here. Based on the data of Fig. 4 (a), we expect to find maximal capillary interaction for $40° < \theta_c < 50°$. Indeed, Fig. 7 shows the expected qualitative dependence of the interaction potential on the aspect ratio. Furthermore, the interaction potential between two ellipsoids with $b/a = 3$ is stronger than the interaction potential between two ellipsoids with $b/a = 2$, which agrees with our calculations for Δu. The

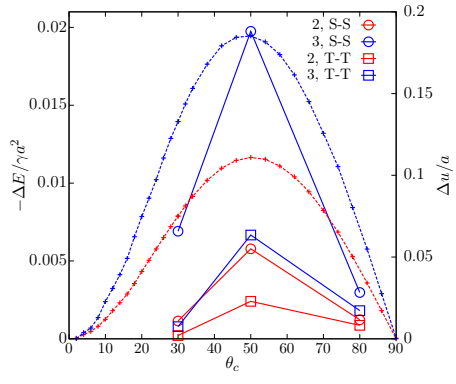

Figure 8: Energies of capillary bonds between two identical ellipsoidal particles at contact in side-by-side (S-S) and tip-to-tip (T-T) orientation (filled circles and squares) and maximal contact line height difference $\Delta u/a$ (crosses connected by dashed lines, see Fig. 4 (a)). The numerical data are plotted for contact angles θ_c = 30°, $\theta_c = 50°$, and $\theta_c = 80°$ and for aspect ratios $b/a = 2$ (shown in red) and $b/a = 3$ (shown in blue). For both aspect ratios, the side-by-side bond energy is larger than the tip-to-tip bond energy.

energies of the "capillary bonds", when the particles touch each other, are shown in Fig. 8 together with $\Delta u/a$ for $b/a = 2$ and $b/a = 3$, and for several contact angles. The bond energies for S-S orientation are higher than for T-T orientation. For S-S orientation, the bond energies roughly follow the predictions of Eq. (6.6.1), but the bond energies in T-T orientation are one order of magnitude larger than those obtained from Eq. (6.6.1).

6.6.2 Capillary interaction between cuboidal particles

The interaction potentials for a pair of cuboidal particles with rounded edges are plotted in Fig. 9 for aspect ratios $b/a = 3$ and contact angles $\theta_c = 40°$ and $\theta_c = 60°$. The interaction is attractive for S-S and T-T orientation and repulsive for T-S orientation. As for ellipsoidal particles, the interaction in S-S orientation is stronger than the interaction in T-T orientation. The logarithmic plots in the insets of Fig. 9 show that the near-field interaction potentials can again be fitted using effective power-law functions. For both S-S and T-T orientation, the interaction potentials differ considerably from the prediction for the far field by Eq. (6.6.1). Furthermore, the interaction potential for T-T orientation decays faster than for S-S orientation, which is analogous to our results for ellipsoids with $b/a = 3$, see Fig. 7.

As expected, larger interaction energies are found for contact angles θ_c that correspond to larger undulations Δu of the contact line, see Fig. 4 (b). The strength of the capillary interaction also increases with increasing aspect ratio (not shown). However, the interface deformations around our cuboidal particles are smaller compared with ellipsoidal particles. The capillary interaction in S-S orientation for our cuboidal particle with aspect ratio $b/a = 3$ is about $1/2$ of the capillary interaction for an ellipsoidal particle with $b/a = 3$, while the capillary interaction for the T-T orientation is similar for ellipsoid and cuboid. The bond energies for S-S orientation

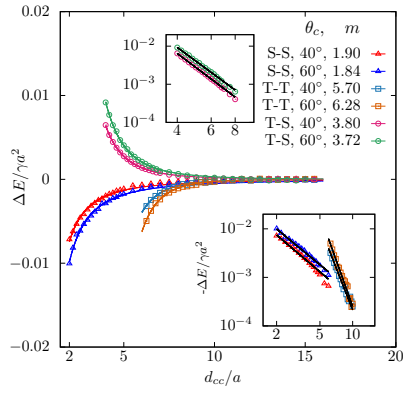

Figure 9: Interaction energies $\Delta E/\gamma a^2$ for two identical cuboidal particles with aspect ratios $b/a = 3$ and contact angles $\theta_c = 40°$ and $\theta_c = 60°$. The energies are plotted as function of d_{cc}/a for side-by-side (S-S), tip-to-tip (T-T), and tip-to-side (T-S) orientation. The interaction is attractive in S-S and T-T orientations and repulsive in T-S orientation. Inset: fit of the numerical data using $\Delta E/\gamma a^2 = k(d_{cc}/a)^{-m}$; the fit parameters are given in the figure and tabulated in the Supporting Information.

are still considerably larger than for T-T orientation, such that we expect the formation of chain-like aggregates of our cuboidal particles in the same way as observed for ellipsoids[10,11].

6.6.3 Capillary Interaction between a Spherical and an Ellipsoidal Particle

In Fig. 10, the interaction potential between an ellipsoidal particle with $b/a = 5$ and a spherical particle is plotted. For both particles, the contact angle is $\theta_c = 48.73°$, which corresponds to the maximal interface deformation around the ellipsoidal particle. In our calculations, spherical particles with radii $r = 3a$ and $r = 4a$ approach the ellipsoidal particle either at its tip or at its side. The spherical particles are found to preferably attach at the side of the ellipsoidal particle. For a sphere with radius $r = 3a$, the bond energy at contact at the side is about twice the bond energy at contact at the tip. For a spherical particle with radius $r = 4a$, the bond energy at the tip is almost unchanged compared with the smaller particle, but the bond energy at the side is about three times larger than the bond energy at the tip.

The capillary attraction of a spherical and an ellipsoidal particle may appear surprising; spherical particles do not deform a planar interface and therefore do not experience mutual capillary interaction. However, the origin of the capillary attraction with ellipsoids can be motivated by the deformation of curved interfaces around spherical particles, which leads to a mutual capillary interaction of spherical particles[26,51,52]. For a system with a spherical and an ellipsoidal particle, a "curved interface" is locally generated by the ellipsoidal particle. Therefore, the sphere interacts with the interface deformation around the ellipsoid, as shown by deformed contact lines on the sphere, see Fig. S4 of the Supporting Information.

The energy gain if an ellipsoidal particle attaches to a spherical particle is smaller than if the ellipsoidal particle attaches to another ellipsoidal particle. Therefore, a spherical particle in the middle of a chain of ellipsoidal particles is in a kinetically-trapped, metastable state. However, our results have interesting implications for mixtures of spherical and ellipsoidal particles. For example, the range of the interaction between an ellipsoidal particle and a chain of ellipsoids that ends with a spherical particle is shorter than between an ellipsoidal particle and a chain of ellipsoids that ends with an ellipsoidal particle, see Fig. 7 (b) and (c) and Fig. 10. Therefore spherical particles that are attached to the ends of chains acts as a "stoppers" that do not inhibit, but that hinder the further growth of the chains.

"Coffee rings" are observed after evaporation of droplets that contain spherical particles[53,54], but the addition of ellipsoidal particles suppresses the coffee-ring formation[55,56]. The suppression depends on the size of the particles[56]: small spheres with diameter $1.3\,\mu m$ form a coffee ring despite the presence of ellipsoids with aspect ratio $b/a = 3.5$ that have been fabricated by stretching $1.3\,\mu m$-diameter polystyrene spheres. However, systems that contain spheres with diameter $5\,\mu m$ mixed with the same ellipsoids at the same volume fractions exhibit coffee-ring formation only for small volume fractions of ellipsoids; complete suppression of the coffee ring is observed for sufficiently high volume fraction of ellipsoids. This size dependence may be explained by our calculations for the interaction energies, which indicate that the capillary attraction between an ellipsoidal particle and a spherical particle is larger for a spherical particle with diameter $5\,\mu m$ than for a spherical particle with diameter $1.3\,\mu m$.

6.7 Summary and Conclusions

We have numerically calculated the deformation of a planar interface around ellipsoidal and cuboidal particles in the near field. For the contact angle that corresponds to the maximal height difference of the contact line, the long-range interaction between two identical particles is expected to be strongest. We have calculated the interaction energies between particles and we have approximated the numerical data by power-law functions of the interparticle distance to characterize the interaction in the near field. Bonds between particles that touch each other in side-by-side orientation are most stable. For cuboidal particles, a finite edge curvature is crucial to induce an interface deformation.

Capillary interactions are the dominant interactions for a wide range of length scales, e. g. for colloids in the micrometer range[10], for mosquito eggs in the millimeter range[3], and for copper plates in the centimeter range[7]. Typical interaction energies for micrometer-sized ellipsoidal and cuboidal particles are on the order of $10^8\,k_BT$. Our calculations for the near-field interface deformations explain the formation of chain-like and rod-like aggregates of elongated particles[9,10,17,48]. Cuboidal particles with aspect ratio $b/a = 1$, which assemble in tile-like aggregates[9,17,48], experience only a weak mutual interaction.

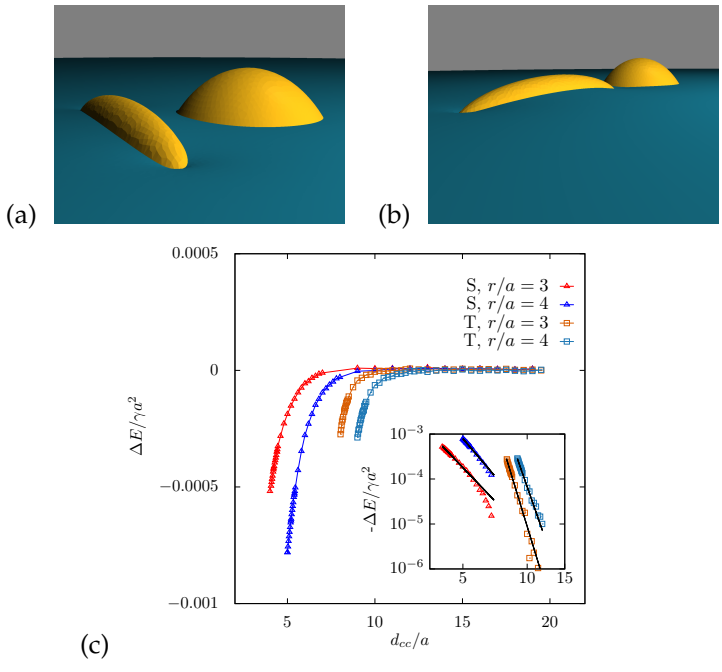

Figure 10: Interaction of a spherical particle with an ellipsoidal particle of aspect ratio $b/a = 5$. The contact angle $\theta_c = 48.47°$ has been used for both particles. The energies are plotted for spherical particles with radii $r = 3a$ and $r = 4a$ that approach the ellipsoidal particle (a) at the side and (b) at the tip, here shown for a spherical particle with $r = 3a$. (c) Interaction energies $\Delta E/\gamma a^2$ as function of d_{cc}/a between the centers of mass of the particles. Inset: double-logarithmic plot and the fit of the numerical data to a power-law decay.

Although spherical particles do not deform a planar interface, we find a finite attractive force between a spherical and an ellipsoidal particle. The spherical particles preferably attach to the side of the ellipsoids. The interaction strongly depends on the size of the spherical particles compared with the size of the ellipsoidal particles and is weaker than the interaction between two ellipsoidal particles. Our calculated interaction energies may explain recent experiments where addition of ellipsoidal particles with aspect ratio $b/a = 3.5$ to droplets that contain spherical particles has been found to suppress the formation of a "coffee ring" and to result in a more uniform deposition of particles when the droplet evaporates[55]. Consistent with our calculations, suppression of the coffee ring for mixtures of spherical and ellipsoidal particles is observed only for sufficiently large spherical particles. For droplets that contain ellipsoidal particles only, a strong suppression of the coffee ring is already observed for very moderate aspect ratios $b/a \approx 1.5$ of the ellipsoids[55].

Quantitative knowledge about the interaction potentials between particle interfaces in the near field is fundamental for understanding rheological properties of particle monolayers[1,28,42], which comprise beautiful soft matter model systems with promising applications. Our results for ellipsoidal and cuboidal particles at planar interfaces help to understand and predict experimental observations sys-

tematically. However, other contributions than an anisotropic particle shape can also induce colloidal interactions. In a pioneering work on capillary interactions for small particles, where particle weight has no effect, Lucassen predicted that box-like particles with pinned sinusoidal contact lines induce interface deformations that lead to attractive interactions in the far field and to repulsive interactions if the undulations do not match exactly in the near field [36]. This has recently been experimentally demonstrated [35].

The deformation of interfaces and capillary interactions can be viewed as limiting "tension only" case for biological membranes, whose conformations are governed by both curvature elasticity and membrane tension. Although in lipid bilayer membranes the interaction between inclusions and attached particles is often successfully studied using models with bending rigidity only [39,57], some quantities such as the membrane deformation around attached particles may also depend significantly on membrane tension [58–60]. For example, the "capillary interaction" of proteins immersed in biomembranes has been studied numerically in Ref. 24.

Triangulated surfaces are a versatile method for further investigations, such as of the role of interface curvature, of line tension at the contact line for small particles [25], and of particles with chemically structured surfaces such as Janus particles.

ACKNOWLEDGMENTS

We thank K. A. Brakke (Selinsgrove, PA) for his advice on Surface Evolver and for helpful discussions on numerical techniques, S. Othman (Ramallah) for assisting us with the preparation of the manuscript, and M. P. Lettinga (Jülich) and J. Vermant (Leuven) for stimulating discussions about nanoparticles at interfaces. SD and MK acknowledge support by the International Helmholtz Research School of Biophysics and Soft Matter (IHRS BioSoft). MF was supported by the NRW Scholarship Program. Support from the EU FP7 NMP collaborative project PreNanoTox (309666) is gratefully acknowledged.

Supporting material

Further numerical data to characterize the single particle induced interface deformation and the capillary interaction between ellipsoidal and cuboidal particles.

References: Chapter 6

1 J.-B. Fournier and P. Galatola, *Phys. Rev. E*, 2002, **65**, 031601.

2 M. Cavallaro, L. Botto, E. P. Lewandowski, M. Wang and K. J. Stebe, *Proc. Natl. Acad. Sci. U. S. A.*, 2011, **108**, 20923–20928.

3 J. Loudet and B. Pouligny, *Eur. Phys. J. E*, 2011, **34(8)**, 1–17.

4 N. Bowden, A. Terfort, J. Carbeck and G. M. Whitesides, *Science*, 1997, **276**, 233–235.

5 K. J. Stebe, E. Lewandowski and M. Ghosh, *Science*, 2009, **325**, 159–160.

6 M. Grzelczak, J. Vermant, E. M. Furst and L. M. Liz-Marzán, *ACS Nano*, 2010, **4**, 3591–3605.

7 Y. Yu, M. Guo, X. Li and Q.-S. Zheng, *Langmuir*, 2007, **23**, 10546–10550.

8 J. C. Loudet and B. Pouligny, *Europhys. Lett.*, 2009, **85**, 28003.

9 E. P. Lewandowski, J. A. Bernate, A. Tseng, P. C. Searson and K. J. Stebe, *Soft Matter*, 2009, **5**, 886–890.

10 Z. Zhang, P. Pfleiderer, A. B. Schofield, C. Clasen and J. Vermant, *J. Am. Chem. Soc.*, 2011, **133**, 392–395.

11 J. C. Loudet, A. M. Alsayed, J. Zhang and A. G. Yodh, *Phys. Rev. Lett.*, 2005, **94**, 018301.

12 B. Madivala, S. Vandebril, J. Fransaer and J. Vermant, *Soft Matter*, 2009, **5**, 1717–1727.

13 A. B. D. Brown, C. G. Smith and A. R. Rennie, *Phys. Rev. E*, 2000, **62**, 951–960.

14 A. Dinsmore, M. F. Hsu, M. Nikolaides, M. Marquez, A. Bausch and D. Weitz, *Science*, 2002, **298**, 1006–1009.

15 M. Glantz, A. Hakansson, H. Lindmark Månsson, M. Paulsson and L. Nilsson, *Langmuir*, 2010, **26**, 12585–12591.

16 R. Aveyard, B. P. Binks and J. H. Clint, *Adv. Colloid Interface Sci.*, 2003, **100**, 503–546.

17 J. W. J. de Folter, E. M. Hutter, S. I. R. Castillo, K. E. Klop, A. P. Philipse and W. K. Kegel, *Langmuir*, 2014, **30**, 955–964.

18 K. Stratford, R. Adhikari, I. Pagonabarraga, J.-C. Desplat and M. E. Cates, *Science*, 2005, **309**, 2198–2201.

19 A. Dippenaar, *Int. J. Miner. Process.*, 1982, **9**, 1 – 14.

20 J. C. Loudet, A. G. Yodh and B. Pouligny, *Phys. Rev. Lett.*, 2006, **97**, 018304.

21 M. Oettel and S. Dietrich, *Langmuir*, 2008, **24**, 1425–1441.

22 E. P. Lewandowski, M. Cavallaro, L. Botto, J. C. Bernate, V. Garbin and K. J. Stebe, *Langmuir*, 2010, **26**, 15142–15154.

23 M. M. Nicolson, *Math. Proc. Cambridge Philos. Soc.*, 1949, **45**, 288–295.

24 P. A. Kralchevsky and K. Nagayama, *Adv. Colloid Interface Sci.*, 2000, **85**, 145 – 192.

25 F. Bresme and M. Oettel, *J. Phys.: Condens. Matter*, 2007, **19**, 413101.

26 D. Ershov, J. Sprakel, J. Appel, M. A. C. Stuart and J. van der Gucht, *Proc. Natl. Acad. Sci. U. S. A.*, 2013, **110**, 9220–9224.

27 P. Pieranski, *Phys. Rev. Lett.*, 1980, **45**, 569–572.

28 B. Madivala, J. Fransaer and J. Vermant, *Langmuir*, 2009, **25**, 2718–2728.

29 M. Oettel, A. Dominguez and S. Dietrich, *Phys. Rev. E*, 2005, **71**, 051401.

30 M. Nikolaides, A. Bausch, M. Hsu, A. Dinsmore, M. P. Brenner, C. Gay and D. A. Weitz, *Nature*, 2002, **420**, 299–301.

31 B. J. Park, T. Brugarolas and D. Lee, *Soft Matter*, 2011, **7**, 6413–6417.

32 R. Van Hooghten, L. Imperiali, V. Boeckx, R. Sharma and J. Vermant, *Soft Matter*, 2013, **9**, 10791–10798.

33 D. Stamou, C. Duschl and D. Johannsmann, *Phys. Rev. E*, 2000, **62**, 5263–5272.

34 L. Botto, E. P. Lewandowski, M. Cavallaro and K. J. Stebe, *Soft Matter*, 2012, **8**, 9957–9971.

35 L. Yao, L. Botto, M. Cavallaro, Jr, B. J. Bleier, V. Garbin and K. J. Stebe, *Soft Matter*, 2013, **9**, 779–786.

36 J. Lucassen, *Colloids Surf.*, 1992, **65**, 131 – 137.

37 A. R. Morgan, N. Ballard, L. A. Rochford, G. Nurumbetov, T. S. Skelhon and S. A. Bon, *Soft Matter*, 2013, **9**, 487–491.

38 G. Morris, S. Neethling and J. Cilliers, *J. Colloid Interface Sci.*, 2011, **361**, 370–380.

39 B. J. Reynwar and M. Deserno, *Soft Matter*, 2011, **7**, 8567–8575.

40 D. Vella and L. Mahadevan, *Am. J. Phys.*, 2005, **73**, 817–825.

41 K. D. Danov, P. A. Kralchevsky, B. N. Naydenov and G. Brenn, *J. Colloid Interface Sci.*, 2005, **287**, 121 – 134.

42 E. Van Nierop, M. Stijnman and S. Hilgenfeldt, *Europhys. Lett.*, 2005, **72**, 671.

43 C. Pozrikidis, *J. Colloid Interface Sci.*, 2011, **364**, 248–256.

44 H. Lehle, E. Noruzifar and M. Oettel, *Eur. Phys. J. E*, 2008, **26**, 151–160.

45 L. Botto, L. Yao, R. L. Leheny and K. J. Stebe, *Soft Matter*, 2012, **8**, 4971–4979.

46 H. Rezvantalab and S. Shojaei-Zadeh, *Langmuir*, 2013, **29**, 14962–14970.

47 C. Pozrikidis, *Engineering Analysis with Boundary Elements*, 2012, **36**, 836 – 844.

48 A. He, K. Nguyen and S. Mandre, *Europhys. Lett.*, 2013, **102**, 38001.

49 K. A. Brakke, *Exp. Math.*, 1992, **1**, 141–165.

50 C. Blanc, D. Fedorenko, M. Gross, M. In, M. Abkarian, M. A. Gharbi, J.-B. Fournier, P. Galatola and M. Nobili, *Phys. Rev. Lett.*, 2013, **111**, 058302.

51 A. Würger, *Phys. Rev. E*, 2006, **74**, 041402.

52 C. Zeng, F. Brau, B. Davidovitch and A. D. Dinsmore, *Soft Matter*, 2012, **8**, 8582–8594.

53 R. D. Deegan, O. Bakajin, T. F. Dupont, G. Huber, S. R. Nagel and T. A. Witten, *Nature*, 1997, **389**, 827–829.

54 R. D. Deegan, O. Bakajin, T. F. Dupont, G. Huber, S. R. Nagel and T. A. Witten, *Phys. Rev. E*, 2000, **62**, 756–765.

55 P. J. Yunker, T. Still, M. A. Lohr and A. Yodh, *Nature*, 2011, **476**, 308–311.

56 P. Yunker, A. Yodh and T. Still, *Physics of Complex Colloids*, 2013, **184**, 447.

57 T. Auth and G. Gompper, *Phys. Rev. E.*, 2009, **80**, 031901.

58 M. Deserno, *Phys. Rev. E.*, 2003, **69**, 031903.

59 S. Dasgupta, T. Auth and G. Gompper, *Soft Matter*, 2013, **9**, 5473–5482.

60 S. Dasgupta, T. Auth and G. Gompper, *Nano Letters*, 2014, **14**, 687–693.

6.8 Supplementary material

Supplementary material: Capillary Assembly of Microscale Ellipsoidal, Cuboidal, and Spherical Particles at Interfaces

In this supplementary material, we present numerical data to further characterize the interface deformation around and the capillary interaction between ellipsoidal and cuboidal particles. For a contact angle $\theta_c \neq 90\,^\circ$, a constant contact angle cannot be achieved for a planar interface around an ellipsoidal particle and around a cuboidal particle with rounded edges. For $\theta_c < 90\,^\circ$, the interface is pulled down at the tips and pulled up at the sides of the ellipsoids, thereby creating excess interface area. Fig. S1 shows the deformation of the interface around an ellipsoidal particle in the directions of the long and the short axis. The deformation profiles are plotted for contact angles $\theta_c^{\max}$ that correspond to maximal interfacial distortions for the given aspect ratios of the particles. It is obvious that the interface deformation increases with increasing aspect ratio, which implies that the capillary interaction between two particles will also increase. The difference of the highest and lowest points along the contact line normalized by the minor axis of a particle, $\Delta u/a$, characterizes the interface deformation in the near field. Fig. S2 shows a non-monotonic variation of $\Delta u/a$ with θ_c together with data from the literature[1,2]. Our numerical results show good agreement with the published data.

The maximal height difference $\Delta u/a$ along the undulating contact line vanishes for mirror-symmetric conditions at $\theta_c = 0^\circ$ and 90°, and varies non-monotonically for intermediate angles attaining a peak value $\Delta u_{\max}/a$ at particular contact angle $\theta_c^{\max}$. For ellipsoidal particles, the calculated peak value monotonically increases from $\Delta u_{\max}/a = 0.0128$ for $b/a = 1.1$ to $\Delta u_{\max}/a = 0.4307$ for $b/a = 13$. Another experimentally measurable quantity is the projected area enclosed by the undulating contact line, S, which is obtained by calculating the area enclosed by the polygon formed by the vertices of the contact line projected to the x-y plane. In Fig. S3, we plot S/S_0, where S_0 is the area enclosed by the contact line for $\theta_c = 90^\circ$. The monotonically increasing function S/S_0 allows to single out the correct contact angle solution where Δu is ambiguous.[1]

The peak values of $\Delta u_{\max}/a$ for all aspect ratios that we have calculated and the corresponding contact angles that vary in the range $43^\circ < \theta_c^{\max} < 55^\circ$ are reported in Tab. S1. In Tab. S2, we report the peak values for the contact line deformation for cuboidal particles. Because of the very small variation of $\Delta u/a$ with θ_c, it is difficult to calculate the contact angles that correspond to the peak values at small aspect ratios accurately. In Tab. S3, we report the parameters obtained by fitting the numerically calculated interaction potentials in the near field to $\Delta E/\gamma a^2 = k(d_{cc}/a)^{-m}$, as well as the bond angles at contact.

Fig. S4 shows the deformation of the contact line on a spherical particle that is next to an ellipsoidal particle. The contact line at the spherical particle is pulled up if the spherical particle is located next to the side of the ellipsoid and is pulled down if the spherical particle is located next to the tip of the ellipsoid. Part of the excess area generated by the ellipsoidal particle is therefore reduced due to the presence of the spherical particle, which leads to an attractive interaction between both particles.

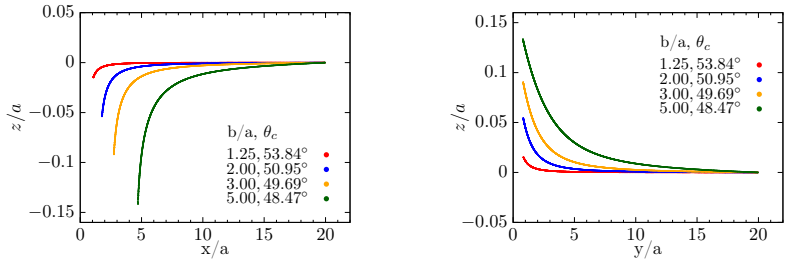

(a) (b)

Figure S1: Interface deformation around ellipsoidal particles with aspect ratios $b/a = 1.25$, $b/a = 2$, $b/a = 3$, and $b/a = 5$ in the direction of (a) their long axis along the x axis and (b) their short axis along the y axis. The contact angles have been chosen such that the difference between the highest and the lowest point of the contact line is maximal.

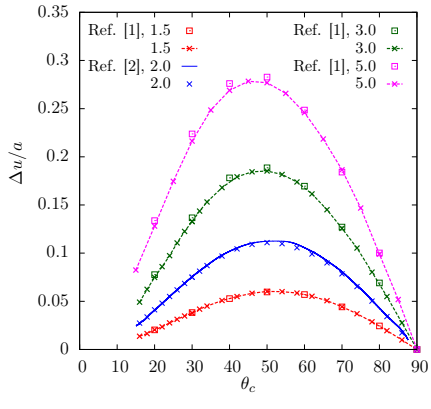

Figure S2: Maximal height difference along the contact line, Δu, as function of the contact angle θ_c for ellipsoidal particles. Our numerical data for aspect ratios $b/a = 1.5$, $b/a = 2$, $b/a = 3$, and $b/a = 5$ are plotted together with data taken from Ref. [1] and Ref. [2].

b/a	$\Delta u_{max}/a$	θ_c^{max}
1.10	0.01284	54.12°
1.25	0.0310	53.84°
1.50	0.0600	52.34°
1.75	0.0867	51.55°
2.00	0.1110	50.95°
2.25	0.1331	50.55°
2.50	0.1530	50.10°
2.75	0.1714	49.73°
3.00	0.1872	49.67°
4.00	0.2410	48.94°
5.00	0.2803	48.47°
6.00	0.3126	47.56°
7.00	0.3483	45.20°
8.00	0.3600	44.82°
9.00	0.3762	44.61°
10.00	0.3940	43.73°
11.00	0.4091	43.31°
12.00	0.4203	43.22°
13.00	0.4307	43.21°

Table S1: Peak values $\Delta u_{\max}$ of the maximal height differences Δu along the contact line and corresponding contact angles $\theta_c^{\max}$ for ellipsoidal particles with aspect ratios in the range $1.1 \leq b/a \leq 13$.

b/a	$\Delta u_{max}/a$	θ_c^{max}
2.00	0.0678	62.93°
2.25	0.0806	62.73°
2.50	0.0918	61.98°
2.75	0.1030	61.63°
3.00	0.1110	61.31°
4.00	0.1417	61.11°
5.00	0.1660	60.27°
6.00	0.1850	59.38°
7.00	0.2007	58.96°
8.00	0.2147	58.36°
9.00	0.2266	56.83°
10.00	0.2375	56.47°

Table S2: Peak values $\Delta u_{\max}$ of the maximal height differences Δu along the contact line and corresponding contact angles $\theta_c^{\max}$ for cuboidal particles with aspect ratios in the range $2 \leq b/a \leq 10$.

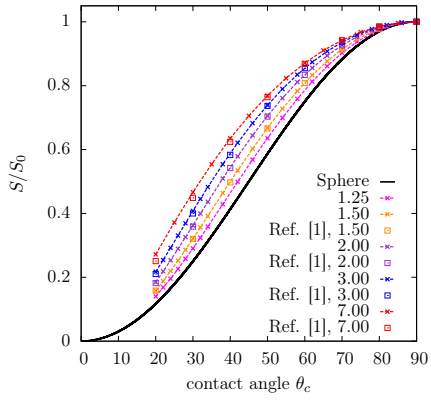

Figure S3: Ratio of projected area S enclosed by the contact line for the to the projected area enclosed by the contact line for $\theta_c = 90°$, S_0, as function of the contact angle θ_c for ellipsoidal particles with aspect ratios in the range $1.25 \leq b/a \leq 7$. Our data are plotted together with numerical data taken from Ref. [1]. For a spherical particle, S/S_0 varies as $\sin^2\theta_c$, as shown by the solid line. For all contact angles between $0°$ and $90°$, S/S_0 attains higher values for ellipsoidal particles in comparison to the analytical result for a spherical particle.

particle shape	**aspect ratio**	**orientation**	θ_c	**k**	**m**	**bond energy** $\Delta E/\gamma a^2$
Ellipsoidal	2	S-S	50°	-0.0415	2.81	-0.00578
			80°	-0.0080	2.69	-0.00122
		T-T	50°	-3.2039	5.21	-0.00241
			80°	-3.4804	6.03	-0.00087
		T-S	50°	0.2342	3.83	0.00349
			80°	0.0421	3.56	0.00084
	3	S-S	50°	-0.0863	2.07	-0.01975
			80°	-0.0117	1.92	-0.00298
		T-T	50°	-310.682	6.03	-0.00667
			80°	-489.442	7.02	-0.00181
		T-S	50°	1.89	3.73	0.01081
			80°	0.2694	3.55	0.00196
Cuboidal	3	S-S	40°	-0.0278	1.90	-0.00744
			60°	-0.0355	1.84	-0.00989
		T-T	40°	-107.6	5.70	-0.00395
			60°	-478.773	6.28	-0.00626
		T-S	40°	1.2484	3.80	0.00643
			60°	1.5979	3.72	0.00925

Table S3: Fit parameters k and m and bond energies for particles at contact obtained from the fit functions. Data for ellipsoidal and cuboidal particles in side-by-side (S-S), tip-to-tip (T-T), and tip-to-side (T-S) orientation is provided. The fit parameters correspond to the fits to the power law $\Delta E/\gamma a^2 = k(d_{cc}/a)^{-m}$ (where d_{cc} is the distance between the centers of mass of the particles) shown in the insets of Figs. 7 and 9 in the main manuscript; some of the bond energies are plotted in Fig. 8 of the main manuscript. For the repulsive tip-to-side orientation, the largest repulsive energy for direct contact of the particles is provided instead of a bond energy.

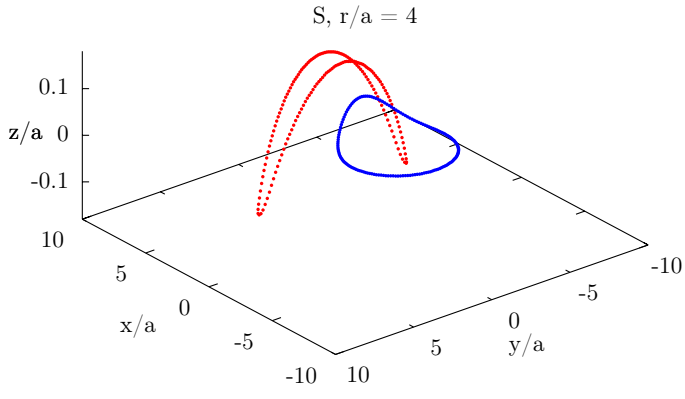

(a)

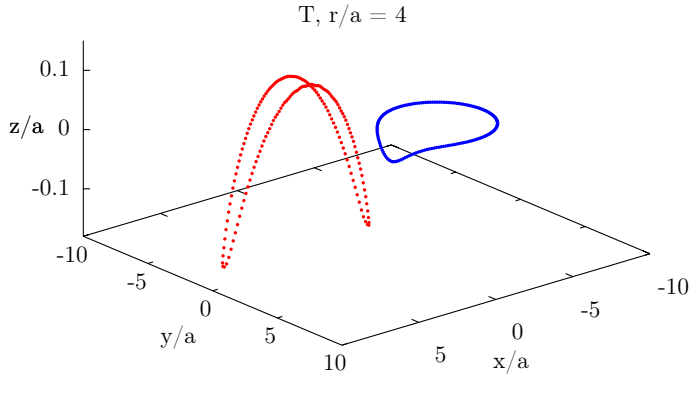

(b)

Figure S4: Contact line deformations for a spherical particle of radius $r = 4a$ and an ellipsoidal particle of aspect ratio $b/a = 5$ at a fluid interface with contact angle $\theta_c = 48.47°$ for both particles. The spherical particle approaches the ellipsoidal particle (a) at the side and (b) at the tip.

References: Chapter 6 (Supplementary material)

1 J. Loudet and B. Pouligny, *Eur. Phys. J. E*, 2011, **34(8)**, 1–17.

2 H. Lehle, E. Noruzifar and M. Oettel, *Eur. Phys. J. E*, 2008, **26**, 151–160.

7
Summary & outlook

7.1
Conclusion

Membrane budding initiates intracellular vesicle transport and has been studied for a variety of soft matter systems. Cellular uptake of nanoparticles depending upon particle size can occur via two possible pathways. For small nanoparticles, the preferred "entry pathway" is via penetration[1] of cell membrane, which has been studied extensively both via computer simulations[2–6] and experiments[7]. However for larger nanoparticles, the preferred pathway for uptake is via membrane wrapping[1,8,9]. Due to a striking development in nanotechnology[10,11], a large variety of shapes[12–14] and sizes have been synthesized, and the need for their technological use for various purposes requires a thorough understanding of the role of shape in cellular interaction and uptake. However, there remains a major gap in the physical understanding to how non-spherical particles enter into cells.

Towards this goal, a holistic understanding of the mechanistic aspects of cellular entry via membrane wrapping for various particle geometry is presented in Chapters 2 and 3. A numerical analysis of the wrapping behavior for non-spherical particles like rods, ellipsoids, and cubes is conducted, based on competing energetic contributions from membrane deformation due to curvature elasticity and surface tension, and contact interaction between the nanoparticle and membrane. As wrapping occurs over long length and time-scales[15,16], its numerical calculation poses a computational challenge for a systematic study of such systems using dynamical simulations. Therefore, using a mesoscopic approach the wrapping behavior is investigated, that not only allow us to characterize the role of individual parameters, but also provide a generic prediction of the wrapping characteristics over a wide range of parameters.

For both prolate and oblate ellipsoidal particles having the same length along the short axis as the particle radius of a spherical particle, the binding transition occurs at smaller adhesion strengths when they approach the membrane with their lowest curvature end first. Partially-wrapped states exist only for finite surface tensions for spherical particles. However, partially-wrapped states for ellipsoids occur already for tensionless membranes. Partially-wrapped states for ellipsoidal particles are long-lived, due to higher energy cost for wrapping of the highly-curved tips. An energy barrier separating the partially wrapped states from completely wrapped states suggest a lower uptake rate of ellipsoidal particles by cells com-

pared to spherical particles as seen in recent experiments[17,18]. For rod-like, ellipsoidal, and spherocylindrical nanoparticles, particle reorientation from parallel to perpendicular impedes complete endocytosis, as the particle remains stuck in a frustrated endocytic state. On comparing wrapping energies for both a submarine- and rocket-like mode predict that the submarine-like mechanism is a more efficient wrapping strategy. For non-spherical particles like nanocubes and nanorods, there are stable endocytic states at both low and high wrapping fractions which allow the technological use of these particles a bio-markers[19,20], for development of biosensors[21,22] and for photo-thermal treatment[23,24]. For nanorods, it is not only the aspect ratio as the major geometric parameter that governs the membrane wrapping – as proposed by current experimental/theoretical investigations – but also the curvature of the tips. Depending on the local curvature at their tips, the nanorods can exhibit competing modes (submarine-like or rocket-like) of entry – in agreement with observations for several rod-like microorganisms[25,26].

Some novel aspects of the membrane wrapping investigations conducted in Chapters 2 and 3 are following:

- For non-spherical particles considering orientation effects, the numerical calculations predict generically two kinds of partially wrapped states with shallow and deep wrapping, and a discontinuous transition to complete wrapping.
- The continuum description of membranes employed in this work does not depend explicitly on the specific size of the nanoparticle, because the particle size only appears as a factor in dimensionless parameters. Thus these calculations allow the prediction of wrapping properties over a wide range of particle sizes. In contrast, molecular dynamics simulations with explicit lipid molecules are typically restricted to nanoparticle sizes comparable to the membrane thickness.
- The role of edge curvature and aspect ratio of nanorods is analyzed for the first time systematically; both parameters are shown to play an important role in particle wrapping.
- The thermodynamic approach allows a detailed prediction of reorientation effects. Three different kind of uptake modes are found to exist, (i) submarine like (ii) rocket-like, and (iii) a competition of submarine and rocket mode. In contrast, in dynamical simulations the dynamical aspects of particle reorientation are difficult to disentangle form energetic contributions.
- The thermodynamic description allows the calculation of exact phase boundaries with both continuous and discontinuous transitions, as well as the corresponding energy barriers at the transitions.

The results on membrane wrapping of non-spherical particles have strong implications in the design of drug delivery systems which target infected cells. Nanoparticles which have a flat side bind more easily to cells and can act as membrane binding sensors. Partially bound states as seen for the non-spherical particles can be beneficial to escape the immune system and thereby make sure that drugs stay for longer time in the blood stream as exhibited in experiments[27] by with filamentous polymerosomes which managed to evade the macrophages for longer times compared to spherical ones. These results also have strong implications in nano-

toxicology studies and furthermore help to shed light to the entry mechanisms to different viruses, pathogens. For example, the competing modes of budding seen in filamentous viruses[25,26] like Ebola and Marburg can be explained using results for wrapping of nanorods where due a close interplay between particle geometry and membrane properties, the particles show different budding modes.

Furthermore, as an application of the membrane wrapping calculations in a biological system we address host cell membrane and parasite contributions to malarial invasion into the human red blood cell in Chapter 4. A typical malarial parasite during invasion phase within the red blood cell, has an asymmetric egg-like shape and is called a merozoite. A numerical analysis of a mechanical model is conducted for parasite membrane adhesion and deformation, in order to predict the respective host and parasite energetic contributions to invasion, in particular the role of erythrocyte membrane-wrapping. The theoretical model is based on membrane curvature elasticity, surface tension, parasite adhesion energy, line tension, and active motor forces. Several aspects of the investigations reshape our thinking on how the malaria parasite may in fact enter the erythrocyte. Foremost: (i) Membrane-wrapping alone, as a function of parasite adhesive and shape properties, can be enough to account for the first key step of the invasion process, that of parasite reorientation and tight adhesive linkage between the two cells; (ii) parasite-stimulated reorganization of the erythrocyte cytoskeleton and release of parasite-derived membranes, which modify the properties of the target cell membrane, can account for a considerable energetic portion of actual invasion itself; (iii) contrary to the prevailing dogma, host-centered energetic factors can markedly reduce (though not eliminate) the expected contributions required by the parasite actin-myosin motor for invasion.

Some striking aspects of the investigations presented in Chapter 4 which contribute to understanding the invasion of a merozoite into the red blood cell are:

- For the first time, through EM tomography, a quantitative measure of the merozoite shape that is required to give accuracy in the wrapping calculations is ascertained. The asymmetric egg shape of the merozoite is a key feature, playing an essential role in the membrane energetics of both "reorientation" and "invasion" phase of entry.
- To date, whilst experiments have clearly demonstrated that merozoites reorient to their apex for successful invasion, the mechanism for reorientation has not been explained. The numerical calculations show that reorientation of the merozoite can be achieved exclusively by wrapping interactions requiring no active parasite energy-dependent process. This would be a key new observation in invasion biology.
- A systematic study is presented based on membrane parameters such as bending rigidity, membrane tension, and spontaneous curvature, as well as line tension and adhesion strength between the merozoite and the membrane. Such an approach allows us to perform a systematic study of the effect of mechano-elastic parameters on reorientation and invasion – a framework in the form of wrapping phase diagrams that provides detailed insight into energetic requirements of invasion. This is not only key to our own discussions but will be critical for further studies incorporating additional factors such as active cy-

toskeletal forces that require dynamic simulations, which can now be guided by the presented work.

- The theoretical model presented here allows the prediction of exact phase boundaries for thermodynamic transitions during invasion, corresponding spinodals, energy barriers and wrapping fractions at the wrapping transitions for the egg-shaped merozoite. These values cannot be accessed using dynamic simulations on the molecular length scale, stressing the importance of insights that can be provided for the first time.
- Finally, and of key importance for the field of parasite invasion biology, the model shows that motor forces whilst playing a significant role in the parasite invasion (and for which there are no existent quantitative experimental measurements) may not be as critical for invasion as previously thought. The role of active forces arising from the acto-myosin machinery is discussed, and numerical estimates for the required forces based on the wrapping model is presented. This radically reshapes our thinking of invasion and helps establish hypotheses for future direct experiments to measure the contribution of motor forces during invasion.

Combining these biophysical insights within a parasitological framework, drawing on a broad foundation of molecular and cellular evidence, we propose that invasion is a balance between parasite and host cell contributions, evolved towards maximal efficient use of biophysical forces between the two cells. These findings lay important foundations for defining the mechanisms that underlie invasion and will be of significant value in understanding and eventually targeting host-cell specific processes in malaria treatment. As a direct outcome of this work, the red blood cell itself will re-emerge as a major focus of research for understanding the process of invasion.

Techniques like patch clamping have been established to perform cellular recordings for a single cell and such methods have been extensively used as a standard tool in electrophysiological experiments. To understand cellular signaling between a large network of cells, one needs to perform intracellular recordings of electrical response from several cells simultaneously. Hence, much interests are driven towards developing devices for efficient intracellular recordings. Patterned biomaterial substrates [28,29] is sought as a common platform for studying various biomechanical and biochemical properties associated with cell signaling, cell-adhesion and elasticity, and proliferation of bio-networks for cell guidance. One promising technology in this direction is coupling three dimensional nano-structured interfaces with living cells. Particularly, interfaces with arrays of pillar-like structures acting as electrodes known as multi electrode arrays (MEA) have emerged as a promising candidate. However, to perform such experiments one has to ensure a effective coupling between the cell membrane and the nanostructure. Previous research [30,31], has shown that the engulfment of these pillars by cells are similar to the situation where cells engulf solid nanoparticles via membrane wrapping.

Thus in Chapter 5, as another application using the membrane deformation calculations in conjunction to experiments involving electrogenic cells grown on single electrodes, we aim to predict an optimal shape for a nanopillar engulfed by a cell. The deformation profile of the cell membrane engulfing nanostructures are

obtained by transverse sectioning of the cell and the pillar using a focused ion beam technique. Interestingly, the deformation profile describing the structural coupling not only depends on the pillar geometry; but also on whether the engulfment occurs near the periphery of cell or near the nucleus. Since the membrane at the periphery has less association to a cortex hence it responds like a bilayer membrane without any cortex. Thus using the Helfrich description, deformation profiles around a pillar at the edge of a cell are obtained and the numerical results are compared with the experimentally obtained membrane profiles. At intermediate heights the membrane wraps around the pillar to form deep engulfed states while at extremal heights which are either too high or low, the membrane wraps weakly around the pillar thus providing weak engulfment. Since, higher engulfment promises better coupling, the height of the pillars plays an important role for effective coupling. There exists a close association of the membrane with the cortex at the center of the cell. Hence a "cytoskeletal pressure" is incorporated in the theoretical model to compare the membrane deformation profiles around pillars engulfed closer to nucleus and find good agreement with the experimental observations. These results shall help to design efficient devices for interfacing cells to nanostructured interfaces and thereby conduct intracellular recordings to investigate cellular signaling in a network of cells.

Fluid membranes are soft surfaces at the boundary of cells which are characterized by mechano-elastic parameters namely, bending rigidity κ and membrane tension σ. Fluid interfaces that act as the boundary between two fluid phases like a oil-water interface or between a fluid and a vapor/gas phase like air-water interface and remain entirely governed by surface tension. Particles at such a fluid interface can deform the fluid interface either through direct interactions like particle weight[32–34] or electromagnetic fields[35–38] or through indirect interactions due to an particle heterogeneity[39,40] causing an undulating contact line thereby creating an excess area. Neighboring particles thus interact to minimize this excess interfacial area, which corresponds to lowering the energy of the system. By characterizing this particle-induced distortion field, how anisotropic particles direct, orient and self-assemble at a fluid interface via capillary forces is investigated in Chapter 6. Strong capillary forces that help to direct, orient and assemble anisotropic particles at an interface can lead to form loosely packed aggregates, open chains, capillary arrows, tile formations and other self assembled two-dimensional structures over several length scales[41–43].

Strength and directionality of capillary interaction between neighboring particles remains affected by both wetting characteristics and shape. A systematic investigation of the interfacial deformation due to single ellipsoidal and cuboidal particles for varying contact angles and aspect ratio is conducted. Interface deformations due to cuboidal particles create a weaker distortion field in comparison to ellipsoidal particles of same aspect ratio. For both particle shapes, particles assembling with either their longer edges parallel in a side-by-side orientation or with their shorter edges aligned in a tip-to-tip assembly undergo capillary attraction. However, the numerics suggests side-by-side assembly to be more stable in comparison to tip-to-tip assembly due to stronger capillary attraction. These results can be backed up by experimental observations where micron-sized ellipsoidal parti-

cles[44] self assemble preferentially in side-side fashion or even for larger macroscopic objects like the ellipsoidal shaped mosquito eggs forming raft-like[45,46] structures. Surprisingly, for a pair of ellipsoids and cube-like particles approaching each other in side-to-tip orientation we observed a near-field capillary repulsion. This replusive nature of the interaction is unique and promises implications in tailoring capillary assembly. Though, one can use multipole approximations for the interface particle-induced distortion field, and superpose these multipole contributions to obtain the interaction potential nature for approaching particles in the far field but to obtain the near-field nature of these interactions are elusive. The numerical results can not only predict the nature of the interactions but also quantify the near-field nature of them using effective power-law-like behavior for several particle shapes at varying contact angles. These results support existing experimental observations for approaching[44] ellipsoidal particles. The near-field repulsion for side-to-tip assembly for both particles and the interaction potential for cuboidal particles have not been yet experimentally observed. Therefore, the numerical results presented here can stimulate experiments directed at quantifying these interactions using single particle tracking techniques. Using the knowledge of interaction potentials, like the attractive and repulsive nature of capillarity and its dependence on physical properties like shape, aspect ratio and also structural and chemical composition shall help to facilitate controlled colloidal assembly of well-defined complex structures with widespread applications. For instance, the numerical investigations further suggest a capillary attraction between spherical particles to neighboring ellipsoidal particle and the strength of attraction to be proportional to the particle radius of spheres. This interesting observation can help to explain the suppression of the "coffee-ring effect" observed for evaporating particulate droplets containing mixtures of spheres and ellipsoids. Moreover, a fluid membrane in the continuum description is an interface-like two-dimensional surface characterized with a membrane tension and curvature-elastic constants hence in biological systems capillarity might induce membrane proteins[47–49], nanoparticles[50] and inclusions[51] to aggregate due to membrane-mediated interactions. Formation of membrane rafts[52] at small length scales comparable to 10-100 nm and the implications of many nanoparticle mediated interactions on a membrane for nano-toxicological studies are questions that remain still to be understood.

7.2 Future perspectives

The results on particle wrapping in this thesis provide a systematic approach using phase diagrams analogously to thermodynamic phase transitions. For a given combination of parameters, the phase diagrams provide information whether the particle is not attached to the membrane, partially wrapped, or completely wrapped. A natural extension of the results presented in this thesis are wrapping phase diagrams for multicomponent membranes. Modeling wrapping behavior of two-component membrane using a mesoscopic description can be based on two scenarios. (i) The strong-segregation limit, where a domain boundary distinctly separates two membrane domains e.g. in a three component lipid mixture[53]. The domains can have different bending rigidities and spontaneous curvature terms in addition to a line tension along the domain boundary. For such a system, deformation energies can be explicitly calculated using numerical approaches like shape equations[54] or using triangulated membranes[55]. (ii) The weak segregation limit, where molecules like membrane-bound receptors or endocytic proteins are incorporated into the lipid bilayer. A classic example of such a case would be receptor-mediated endocytosis,[56–58] where one assumes that a smooth distribution of the receptors provides a net gain in adhesion energy. Another example is the distribution of proteins like bar domains[59] and clathrins[49,60,61] which can provide a local spontaneous curvature contribution to facilitate membrane deformation. Theoretical models[57,58,62] for receptor-mediated endocytosis generally assume a two-state model for wrapping accounting only for a non wrapped and a fully wrapped state. Such models neglect the changes in membrane deformation energies due to a redistribution of receptors as wrapping proceeds. Assuming a smooth distribution function of the receptors in thermal equilibrium, it is possible to couple it via the local adhesive strength with the membrane wrapping energy. Membrane deformations and receptor distribution can be alternatively calculated employing numerical minimization by triangulated membranes. Another interesting direction to the research theme on membrane wrapping is to incorporate the role of cell cytoskeleton[63] by making a mechanistic model which accounts for a shear modulus term of the underlying cortical cytoskeleton. A model that includes the cytoskeleton is needed for example to understand the formation of a "phagocytic cup"[64] due to assembly of actin filaments. Apart from single particle budding, one may also look at cooperative effects during many particle budding.

At a fluid interface, interface-mediated interactions due to anisotropic non-spherical particles have been investigated. For systems investigated within this thesis, the fluid interface is assumed to have no preferential interfacial curvature and remain flat in absence of the particles due to null pressure difference across the fluid interface. To study capillary interactions at a curved interface[65–68] is a natural extension to this work. By calculating numerically the interactions at differently curved surfaces like cylinder ($H > 0, K = 0$), catenoid ($H = 0, K < 0$), spheres ($H > 0, K > 0$) one can estimate the contributions due to mean curvature H and Gaussian curvature K to capillary interactions.

References: Summary & Outlook

1 I. Canton and G. Battaglia, *Chem. Soc. Rev.*, 2012, **41**, 2718–2739.

2 C. L. Ting and Z.-G. Wang, *Soft Matter*, 2012, **8**, 12066–12071.

3 K. Yang and Y. Q. Ma, *Nat. Nanotechnol.*, 2010, **5**, 579–583.

4 K. Yang and Y. Q. Ma, *Aust. J. Chem.*, 2011, **64**, 894.

5 Q. Zhang and Y. Ma, *J. Chem. Phys.*, 2006, **125**, 164710.

6 S. Pogodin and V. A. Baulin, *ACS Nano*, 2010, **4**, 5293–5300.

7 J. Lin, H. Zhang, Z. Chen and Y. Zheng, *ACS Nano*, 2010, **4**, 5421–5429.

8 J. H. Hurley, E. Boura, L.-A. Carlson and B. Różycki, *Cell*, 2010, **143**, 875–887.

9 S. Mayor and R. E. Pagano, *Nat. Rev. Mol. Cell Biol.*, 2007, **8**, 603–612.

10 J. P. Best, Y. Yan and F. Caruso, *Adv. Healthcare Mater.*, 2012, **1**, 35–47.

11 S. Mitragotri and J. Lahann, *Nat. Mater.*, 2009, **8**, 15–23.

12 A. Schrade, Z. Cao, K. Landfester and U. Ziener, *Langmuir*, 2011, **27**, 6689–6700.

13 S. E. A. Gratton, P. A. Ropp, P. D. Pohlhaus, J. C. Luft, V. J. Madden, M. E. Napier and J. M. DeSimone, *Proc. Natl. Acad. Sci. U.S.A.*, 2008, **105**, 11613–11618.

14 J. A. Champion and S. Mitragotri, *Proc. Natl. Acad. Sci. U.S.A.*, 2006, **103**, 4930–4934.

15 V. V. Ginzburg, S. Balijepalli, K. A. Smith and A. C. Balazs, *Nanotechnologies for the Life Sciences*, 2009.

16 Z. G. Qu, X. C. He, M. Lin, B. Y. Sha, X. H. Shi, T. J. Lu and F. Xu, *Nanomedicine*, 2013, **8**, 995–1011.

17 L. Florez, C. Herrmann, J. M. Cramer, C. P. Hauser, K. Koynov, K. Landfester, D. Crespy and V. Mailänder, *Small*, 2012, **8**, 2222–2230.

18 Y. Zhang, S. Tekobo, Y. Tu, Q. Zhou, X. Jin, S. A. Dergunov, E. Pinkhassik and B. Yan, *ACS Appl. Mater. Interfaces*, 2012, 4099–4105.

19 N. Jana, *Phys. Chem. Chem. Phys.*, 2010, **13**, 385–396.

20 D. Pissuwan, S. Valenzuela and M. B. Cortie, *Biotechnol. Genet. Eng. Rev.*, 2008, **25**, 93–112.

21 L. Xu, H. Kuang, L. Wang and C. Xu, *J. Mater. Chem.*, 2011, **21**, 16759.

22 H.-J. Wu, J. Henzie, W.-C. Lin, C. Rhodes, Z. Li, E. Sartorel, J. Thorner, P. Yang and J. T. Groves, *Nat. Methods*, 2012, **9**, 1189–1191.

23 Y. Wang, K. C. L. Black, H. Luehmann, W. Li, Y. Zhang, X. Cai, D. Wan, S.-Y. Liu, M. Li, P. Kim, Z.-Y. Li, L. V. Wang, Y. Liu and Y. Xia, *ACS Nano*, 2013, **7**, 2068–2077.

24 Y. Wang, Y. Liu, H. Luehmann, X. Xia, D. Wan, C. Cutler and Y. Xia, *Nano Lett.*, 2013, **13**, 581–585.

25 S. Welsch, L. Kolesnikova, V. Krähling, J. D. Riches, S. Becker and J. A. G. Briggs, *PLoS Pathogens*, 2010, **6**, 9.

26 T. Noda, H. Ebihara, Y. Muramoto, K. Fujii, A. Takada, H. Sagara, J. H. Kim, H. Kida, H. Feldmann and Y. Kawaoka, *PLoS Pathogens*, 2006, **2**, 9.

27 Y. Geng, P. Dalhaimer, S. Cai, R. Tsai, M. Tewari, T. Minko and D. E. Discher, *Nat. Nanotechnol.*, 2007, **2**, 249–255.

28 G. Panaitov, S. Thiery, B. Hofmann and A. Offenhäusser, *Microelectronic Engineering*, 2011, **88**, 1840–1844.

29 F. Santoro, J. Schnitker, G. Panaitov and A. Offenhäusser, *Nano letters*, 2013, **13**, 5379–5384.

30 A. Hai, A. Dormann, J. Shappir, S. Yitzchaik, C. Bartic, G. Borghs, J. Langedijk and M. E. Spira, *Journal of The Royal Society Interface*, 2009, **6**, 1153–1165.

31 A. Hai, J. Shappir and M. E. Spira, *Nature methods*, 2010, **7**, 200–202.

32 M. M. Nicolson, *Math. Proc. Cambridge Philos. Soc.*, 1949, **45**, 288–295.

33 W. Gifford and L. Scriven, *Chem. Eng. Sci.*, 1971, **26**, 287 – 297.

34 D. Vella and L. Mahadevan, *Am. J. Phys.*, 2005, **73**, 817–825.

35 M. Oettel and S. Dietrich, *Langmuir*, 2008, **24**, 1425–1441.

36 M. Oettel, A. Dominguez and S. Dietrich, *Phys. Rev. E*, 2005, **71**, 051401.

37 A. Dominguez, M. Oettel and S. Dietrich, *J. Phys.: Condens. Matter*, 2005, **17**, S3387.

38 M. Nikolaides, A. Bausch, M. Hsu, A. Dinsmore, M. P. Brenner, C. Gay and D. A. Weitz, *Nature*, 2002, **420**, 299–301.

39 L. Yao, L. Botto, M. Cavallaro, Jr, B. J. Bleier, V. Garbin and K. J. Stebe, *Soft Matter*, 2013, **9**, 779–786.

40 J. Lucassen, *Colloids and Surfaces*, 1992, **65**, 131 – 137.

41 N. Bowden, A. Terfort, J. Carbeck and G. M. Whitesides, *Science*, 1997, **276**, 233–235.

42 K. J. Stebe, E. Lewandowski and M. Ghosh, *Science*, 2009, **325**, 159–160.

43 M. Grzelczak, J. Vermant, E. M. Furst and L. M. Liz-Marzán, *ACS Nano*, 2010, **4**, 3591–3605.

44 J. C. Loudet, A. M. Alsayed, J. Zhang and A. G. Yodh, *Phys. Rev. Lett.*, 2005, **94**, 018301.

45 Z. Saliternik, *Bulletin of Entomological Research*, 1942, **33**, 221–221.

46 J. Loudet and B. Pouligny, *Eur. Phys. J. E: Soft Matter Biol. Phys.*, 2011, **34**, 1–17.

47 P. A. Kralchevsky and K. Nagayama, *Adv. Colloid Interface Sci.*, 2000, **85**, 145 – 192.

48 B. J. Reynwar and M. Deserno, *Soft Matter*, 2011, **7**, 8567–8575.

49 B. J. Reynwar, G. Illya, V. A. Harmandaris, M. M. Mueller, K. Kremer and M. Deserno, *Nature*, 2007, **447**, 461–464.

50 S. Dasgupta, T. Auth and G. Gompper, *Soft Matter*, 2013, **9**, 5473–5482.

51 T. Auth and G. Gompper, *Phys. Rev. E.*, 2009, **80**, 031901.

52 K. Simons and D. Toomre, *Nature reviews Molecular cell biology*, 2000, **1**, 31–39.

53 T. Baumgart, S. T. Hess and W. W. Webb, *Nature*, 2003, **425**, 821–824.

54 S. A. Nowak and T. Chou, *Phys. Rev. E.*, 2008, **78**, 021908.

55 *G. Gompper and D. M. Kroll: in Statistical Mechanics of Membranes and Surfaces, ed. D. R. Nelson, T. Piran, and S. Weinberg (World Scientific, Singapore, 2004) 2nd ed.*

56 S. Zhang, J. Li, G. Lykotrafitis, G. Bao and S. Suresh, *Advanced Materials*, 2009, **21**, 419–424.

57 H. Gao, W. Shi and L. B. Freund, *Proc. Natl. Acad. Sci. U.S.A.*, 2005, **102**, 9469–9474.

58 S. Zhang, J. Li, G. Lykotrafitis, G. Bao and S. Suresh, *Adv. mater.*, 2009, **21**, 419–424.

59 B. Sorre, A. Callan Jones, J. Manzi, B. Goud, J. Prost, P. Bassereau and A. Roux, *Proc. Natl. Acad. Sci. U.S.A.*, 2011, **109**, 173–8.

60 H. T. McMahon and I. G. Mills, *Curr. Opin. Cell Biol.*, 2004, **16**, 379–391.

61 T. Kohyama, D. M. Kroll and G. Gompper, *Phys. Rev. E*, 2003, **68**, 061905.

62 A. Chaudhuri, G. Battaglia and R. Golestanian, *Phys. Biol.*, 2011, **8**, 9.

63 A. Boulbitch, R. Simson, D. A. Simson, R. Merkel, W. Häckl, M. Bärmann and E. Sackmann, *Phys. Rev. E*, 2000, **62**, 3974–3985.

64 S. Tollis, A. E. Dart, G. Tzircotis and R. G. Endres, *BMC Syst. Biol.*, 2010, **4**, 149.

65 J. Leandri and A. Wuerger, *J. Colloid Interface Sci*, 2013, **405**, 249–255.

66 A. Würger, *Europhys. Lett.*, 2006, **75**, 978.

67 C. Zeng, F. Brau, B. Davidovitch and A. D. Dinsmore, *Soft Matter*, 2012, **8**, 8582–8594.

68 C. Blanc, D. Fedorenko, M. Gross, M. In, M. Abkarian, M. A. Gharbi, J.-B. Fournier, P. Galatola and M. Nobili, *Phys. Rev. Lett.*, 2013, **111**, 058302.

Declaration of Individual Contribution

Article no. 1

Corresponding Thesis Chapter: Chapter 2 **Status**: Published

*S. Dasgupta, T. Auth, and G. Gompper, Wrapping of ellipsoidal nano-particles by fluid membranes, Soft Matter **9** (22), 5473-5482 (2013).*

The independent contribution of the candidate:

I have worked on wrapping of ellipsoidal nanoparticles by membranes with guidance from T.A. and G.G. All numerical computations, data analysis,and development of numerical techniques shave been done $\sim$ 80% by me. The interpretation of the data and preparation of the manuscript in majority has been done independently by me with guidance from T.A. and G.G.

Article no. 2

Corresponding Thesis Chapter: Chapter 3 **Status**: Published
*S. Dasgupta, T. Auth, and G. Gompper, Shape and Orientation Matter for the Cellular Uptake of Nonspherical Particles, Nano letters **14** (2), 687–693 (2014).*

The independent contribution of the candidate:

I have contributed $\sim$ 80% to all numerical calculations and analysis presented in this manuscript. The interpretation of the data and preparation of the manuscript in majority has been done by me with guidance from T.A. and G.G..

Article no. 3

Corresponding Thesis Chapter: Chapter 4 **Status**: Published

*S. Dasgupta, T. Auth, N. Gov, E. S. Zuccala, E. G. Hanssen, T. J. Satchwell, D. T. Riglar, A. M. Toye, T. Betz, J. Baum, and G. Gompper, Membrane-Wrapping Contributions to Malaria Parasite Invasion of the Human Erythrocyte, Biophysical Journal **107** (1), 43-54 (2014).*

The independent contribution of the candidate:

The project aims to present a complete biophysical model establishing the significance of erythrocyte membrane-wrapping contributions to the invasion of malarial merozoites using theoretical calculations of wrapping phase diagrams. I have compared the dimensions obtained from cryo-X-ray images taken by our experimental collaborators (J.B.) with an idealized egg shape that is used for the calculations. I have contributed substantially ($\sim$ 80%) to the numerical calculations, analysis and theoretical model development. Further analysis and graphical representations of numerical data to construct structural phase diagrams for wrapping have been performed by me. The interpretation of the data has been done jointly with my coauthors.

Article no. 4

Corresponding Thesis Chapter: Chapter 5 **Status**: Published

*F. Santoro, S. Dasgupta, J. Schnitker, T. Auth, E. Neumann, G. Panaitov, G. Gompper, and A. Offenhäusser, Interfacing Electrogenic Cells with 3D Nanoelectrodes: Position, Shape, and Size Matter, ACS Nano **8** (7), 6713-6723 (2014).*

The independent contribution of the candidate:

This collaborative project aimed at predicting optimal shapes of 3D nanoelectrodes at the cell interface, which requires a balanced approach using both experimental and theoretical expertise. The conception of this project with an interdisciplinary approach has been jointly done by me and the lead author and experimentalist, F.S., with support from our principal investigators G.G and A.O., respectively. I have performed numerical calculations for the cell membrane deformation at the very edge of the cell using the Helfrich description of membranes and made theoretical predictions for the optimal height of the nanostructures. The analytical calculations have been performed along with T.A. My independent contribution in regard to novel theoretical calculations in the manuscript is $\sim$ 50%. The manuscript was written by all authors, who also discussed the results.

Article no. 5

Corresponding Thesis Chapter: Chapter 6 **Status**: Published

*S. Dasgupta, M. Katava, M. Faraj, T. Auth, and G. Gompper, Capillary Assembly of Microscale Ellipsoidal, Cuboidal, and Spherical Particles at Interfaces, Langmuir **30**(40), 11873–11882 (2014).*

The independent contribution of the candidate:

This projects aims at characterizing interface-mediated capillary interaction potential between neighboring nonspherical particles at a fluid interface. The design and conceptualization of this project was done in independent capacity as a supervisor of M.K. and M.F. for their internship. I developed computational methods required to calculate the interface deformation around single particles and the capillary interaction between two particles. I wrote all scripts for data analysis and generating the graphical representations. M.K and M.F. both contributed to numerical results for single particle induced deformations using numerical code and scripts written under my direct supervision while numerical results for two particle assembly were performed by me. Apart from an active role of supervision in this project, my overall contribution to the theoretical calculations and analysis is $\sim$ 60% and to the design and planning of the problem is $\sim$ 80%. The manuscript was written by all authors, who also discussed the results.

Erklärung

Ich versichere, daß ich die von mir vorgelegte Dissertation selbständig angefertigt, die benutzten Quellen und Hilfsmittel vollständig angegeben und die Stellen der Arbeit - einschließlich Tabellen, Karten und Abbildungen -, die anderen Werken im Wortlaut oder dem Sinn nach entnommen sind, in jedem Einzelfall als Entlehnung kenntlich gemacht habe; daß diese Dissertation noch keiner anderen Fakultät oder Universität zur Prüfung vorgelegen hat; daß sie - abgesehen von unten angegebenen Teilpublikationen - noch nicht veröffentlicht worden ist sowie, daß ich eine solche Veröffentlichung vor Abschluß des Promotionsverfahrens nicht vornehmen werde. Die Bestimmungen dieser Promotionsordnung sind mir bekannt. Die von mir vorgelegte Dissertation ist von Prof. Dr. G. Gompper betreut worden.

1. S. Dasgupta, T. Auth, G. Gompper,
   Wrapping of ellipsoidal nano-particles by fluid membranes
   Soft Matter **9** (22), 5473-5482 (2013).

2. S. Dasgupta,T. Auth, G. Gompper,
   Shape and Orientation Matter for the Cellular Uptake of Nonspherical Particles
   Nano Letters **14** (2), 687–693 (2014).

3. S. Dasgupta, T. Auth, N. Gov, E. S. Zuccala, E. G. Hanssen, T. J. Satchwell, D. T. Riglar, A. M. Toye, T. Betz, J. Baum, and G. Gompper
   Membrane-Wrapping Contributions to Malaria Parasite Invasion of the Human Erythrocyte
   Biophysical Journal **107** (1), 43-54 (2014).

4. F. Santoro, S. Dasgupta, J. Schnitker, T. Auth, E. Neumann, G. Panaitov, G. Gompper, and A. Offenhäusser
   Interfacing Electrogenic Cells with 3D Nanoelectrodes: Position, Shape, and Size Matter
   ACS Nano **8** (7), 6713-6723 (2014).

5. S. Dasgupta, M. Katava, M. Faraj, T. Auth, and G. Gompper
   Capillary Assembly of Microscale Ellipsoidal, Cuboidal, and Spherical Particles at Interfaces
   Langmuir **30** (40), 11873–11882 (2014).

Jülich, den 25. Nov 2014